

TECHNICAL DIGEST

1 9 9 5

SPATIAL LIGHT
MODULATORS AND
APPLICATIONS

MARCH 14-16, 1995

SALT LAKE CITY, UTAH

1995 TECHNICAL DIGEST SERIES
VOLUME 9



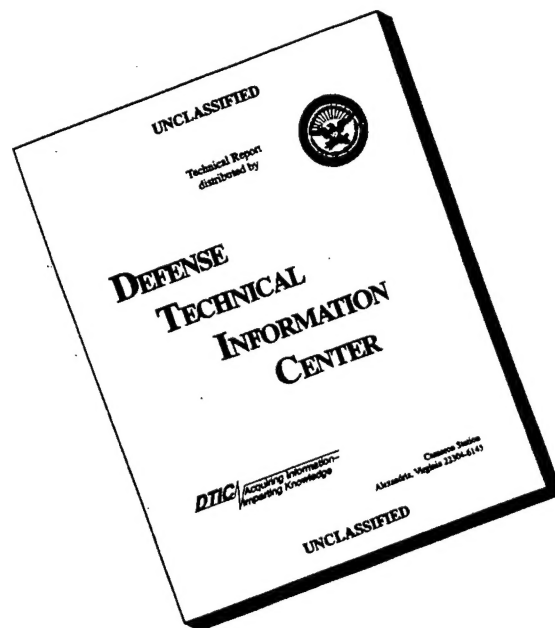
SPONSORED BY
OPTICAL SOCIETY OF AMERICA

DISTRIBUTION STATEMENT A

Approved for public release;
Distribution Unlimited

NOTED C

DISCLAIMER NOTICE



THIS DOCUMENT IS BEST QUALITY AVAILABLE. THE COPY FURNISHED TO DTIC CONTAINED A SIGNIFICANT NUMBER OF PAGES WHICH DO NOT REPRODUCE LEGIBLY.

CONFERENCE EDITION

*Summaries of the papers
presented at the topical meeting*

SPATIAL LIGHT MODULATORS AND APPLICATIONS

March 14-16, 1995
Salt Lake City, Utah

1995 Technical Digest Series
Volume 9

SPONSORED BY
Optical Society of America



19960325 100

DISTRIBUTION STATEMENT A

Approved for public release;
Distribution Unlimited

DTIC QUALITY INSPECTED 5

Articles in this publication may be cited in other publications. To facilitate access to the original publication source, the following form for the citation is suggested:

Name of Author(s), "Title of Paper," in *Spatial Light Modulators and Applications*, Vol. 9, 1995
OSA Technical Digest Series (Optical Society of America, Washington DC, 1995), pp. xx-xx.

Optical Society of America

ISBN

Conference Edition	1-55752-387-8
Postconference Edition	1-55752-388-6
(Note: Postconference Edition includes postdeadline papers.)	
1995 Technical Digest Series	1-55752-368-1

Library of Congress Catalog Card Number

Conference Edition	95-67803
Postconference Edition	95-67801

Copyright © 1995, Optical Society of America

Individual readers of this digest and libraries acting for them are permitted to make fair use of the material in it, such as to copy an article for use in teaching or research, without payment of fee, provided that such copies are not sold. Copying for sale is subject to payment of copying fees. The code 1-55752-368-1/95/\$6.00 gives the per-article copying fee for each copy of the article made beyond the free copying permitted under Sections 107 and 108 of the U.S. Copyright Law. The fee should be paid through the Copyright Clearance Center, Inc., 21 Congress Street, Salem, MA 01970.

Permission is granted to quote excerpts from articles in this digest in scientific works with the customary acknowledgment of the source, including the author's name and the name of the digest, page, year, and name of the Society. Reproduction of figures and tables is likewise permitted in other articles and books provided that the same information is printed with them and notification is given to the Optical Society of America. In addition, the Optical Society may require that permission also be obtained from one of the authors. Address inquiries and notices to Director of Publications, Optical Society of America, 2010 Massachusetts Avenue, NW, Washington, DC 20036-1023. In the case of articles whose authors are employees of the United States Government or its contractors or grantees, the Optical Society of America recognizes the right of the United States Government to retain a nonexclusive, royalty free license to use the author's copyrighted article for United States Government purposes.

Printed in the U.S.A.

Contents

Agenda of Sessions	v
LTuA MQW Spatial Light Modulators	1
LTuB SLM Applications	19
LTuC Poster Session	37
LWA Joint Session with Optical Computing	73
OWC Joint Plenary Session with Optical Computing	77
LThA SLM Structures	85
LThB SLM Materials	105
LThC Liquid Crystal: 1	125
LThD Liquid Crystal: 2	143
Key to Authors and Presiders	157

**SPATIAL LIGHT MODULATORS AND APPLICATIONS
TECHNICAL PROGRAM COMMITTEE**

Garret Moddel, *General Chair*
University of Colorado, Boulder

Geoff Burdge, *Program Chair*
Laboratory for Physical Sciences

Allan Craig
U.S. Air Force Office of Scientific Research

William Crossland
Cambridge University, U.K.

Uzi Efron
Hughes Research Laboratory

Sadik C. Esener
University of California, San Diego

Mary K. Hibbs-Brenner
Honeywell, Inc.

Jean Pierre Huignard
Thomson CSF, France

Takashi Kurokawa
NTT, Japan

John N. Lee
U.S. Naval Research Laboratory

Anthony L. Lentine
AT&T Bell Laboratories

Alexander Parfenov
Lebedev Physical Institute, Academy of Sciences, Russia

Cardinal Warde
Massachusetts Institute of Technology

TUESDAY

MARCH 14, 1995

RED LION EAST

8:20am

Opening Remarks

Garret Model, *University of Colorado-Boulder, Presider*

RED LION EAST

8:30am-10:00am

LTuA • MQW Spatial Light Modulators

Uzi Efron, *Hughes Research Laboratories, Presider*

8:30am (Invited)

LTuA1 • Providing optical I/O to electronic logic chips with multiple quantum-well diodes, Leo M. F. Chirovsky, *AT&T Bell Laboratories*. This paper is a review of the designs, the fabrication technologies, and the applications of optoelectronic chips realized by integrating p-i(MQW)-n diodes into electronic circuits to act as optical detectors and modulators. (p. 2)

9:00am

LTuA2 • 16×16 SLM with silicon CMOS drivers and III-V modulators, Mark Hansen, David Shih, Chi Fan, Sadik Esener, *Univ. California-San Diego*; Wei Chang, Eli Yablonovitch, *Univ. California-Los Angeles*; Uzi Efron, *Hughes Research Laboratories*. III-V MQW modulators are integrated with silicon CMOS drivers using gold ball flip-chip bonding. Various technical aspects of the integration are investigated experimentally. (p. 5)

9:15am

LTuA3 • High-yield low-cost Fabry-Perot modulators utilizing correctable partial antireflection coatings, K. W. Goossen, J. E. Cunningham, W. Y. Jan, J. Centanni, *AT&T Bell Laboratories*. We present reduced-finesse asymmetric Fabry-Perot modulators utilizing post-growth correctable partial antireflection coatings (PAR-ASFP). We achieve greater than 6.7:1 contrast over an entire 2 in. wafer at a single wavelength and drive voltage. (p. 9)

9:30am

LTuA4 • Compensation of thickness variations in a Fabry-Perot modulator array using a self-tuned Fabry-Perot structure, Phil Harvey, Sadik Esener, *Univ. California-San Diego*. We present a method to compensate for cavity-thickness variations using a holographic mirror, suitable for large arrays of Fabry-Perot devices. (p. 12)

9:45am

LTuA5 • Polarization rotation modulator in a strained [110]-oriented MQW, D. S. McCallum, X. R. Huang, Arthur L. Smirl, *Univ. Iowa*; D. Sun, E. Towe, *Univ. Virginia*. We use the optically induced nonlinearities that result from the inherent anisotropy of strained, [110]-oriented InGaAs/GaAs multiple quantum wells (MQWs) to demonstrate an all-optical modulator with a 25:1 contrast ratio using only 50 wells. (p. 16)

GRAND BALLROOM C

10:00am-10:30am

Coffee Break/Exhibits

RED LION EAST

10:30am-12:15pm

LTuB • SLM Applications

J. P. Huignard, *Thomson, CSF-LCR, France, Presider*

10:30am

LTuB1 • Optoelectronic hybrid system for rapid prototyping of paraxial diffractive elements, Harald Aagedal, Thomas Beth, Heiko Schwarzer, Stephan Teiwes, *Univ. Karlsruhe, Germany*; Frank Reichel, *Jenoptik Technologie GmbH, Germany*. A hybrid system for real-time prototyping of paraxial diffractive elements is proposed. Design concepts and implementations of the optical and electronic module of the system are given. (p. 20)

10:45am

LTuB2 • Speckle-free signal reconstruction with nonperiodic diffractive elements on liquid-crystal SLM, Stephan Teiwes, Heiko Schwarzer, Harald Aagedal, Michael Schmid, Thomas Beth, *Univ. Karlsruhe, Germany*; Frank Reichel, *Jenoptik Technologie GmbH, Germany*; Frank Wyrowski, *Berlin Institute of Optics, Germany*. A spherical signal phase is used for the iterative design of paraxial nonperiodic diffractive elements to avoid speckles in the signal reconstruction. The applicability of the method is validated by computer simulations and optical implementation with a liquid-crystal spatial light modulator (SLM). (p. 24)

11:00am

LTuB3 • Tunable holographic wavelength filter, M. C. Parker, S. T. Warr, R. J. Mears, W. A. Crossland, *Cambridge Univ., U.K.* We have demonstrated a new digital-filter architecture for single-mode fiber systems, combining a spatial-light-modulator-written dynamic hologram and a fixed grating. (p. 28)

11:15am (Invited)

LTuB4 • Properties and application of liquid crystal SLMs in JENOPTIK optical signal processing systems, Frank Reichel, *Jenoptik Technologie, Germany*. The parameters of optically addressable a-Si:H, MIS, Ge-Se and CdS-SLM with liquid crystals as light modulating layers and their technological dependence are discussed. The applications of spatial light modulators (SLM) in our OIPS300 incoherent-optical image processing system, the OFA050 optical autocorrelator, the PSI particle size measuring system, as well as in an optical microscope processor are presented. (p. 32)

11:45am (Invited)

LTuB5 • To be announced.

12:15pm

Lunch on Own

1:30pm-5:00pm

Free Time

GRAND BALLROOM C

7:30pm–10:00pm

LTuC • Poster Session

LTuC1 • Experimental investigation of free-space optical interconnects, A. J. Stevens, J. Gourlay, S. Samus, W. J. Hossack, D. G. Vass, D. C. Burns, *Univ. Edinburgh, U.K.* Ferroelectric liquid-crystal spatial light modulators displaying computer-generated patterns to produce reconfigurable holograms are compared with static holographic elements in optical interconnect systems. (p. 38)

LTuC2 • Switchable optical kinoforms, complex modulation holograms with twisted nematic liquid-crystal television, Yunlong Sheng, Luiz Gonçalves Neto, Danny Roberge, *Univ. Laval, Canada*. Continuous phase-only and full-complex holograms and filters are demonstrated with commercial twisted nematic liquid-crystal television, whose operating curve is experimentally optimized. (p. 42)

LTuC3 • Ferroelectric liquid-crystal optically addressed SLMs for binary-phase holograms, Dominic C. O'Brien, Garret Model, *Univ. Colorado–Boulder*. Ferroelectric liquid-crystal optically addressed spatial light modulators (SLMs) can be used to create programmable binary-phase computer-generated holograms. Operation and efficient addressing of these devices is examined. (p. 45)

LTuC4 • Diffraction properties of ferroelectric liquid-crystal optically addressed SLMs, Pierre R. Barbier, *Univ. Maryland*. The diffraction properties of ferroelectric liquid-crystal SLMs are discussed from an experimental prospective. In particular, the diffracted light polarization and intensity are analyzed. (p. 49)

LTuC5 • MIS model of optically addressed SLMs, Li Wang, Garret Model, *Univ. Colorado–Boulder*. We present a metal-insulator-semiconductor (MIS) model that interprets correctly the experimental data from optically addressed SLMs incorporating intrinsic a-Si:H and nematic liquid crystals. (p. 53)

LTuC6 • Photorefractive persistence and erasure in AlGaAs SLMs, S. R. Bowman, W. S. Rabinovich, D. S. Katzer, *Naval Research Laboratory*; C. S. Kyono, *Motorola*. Measurements of the pattern persistence and erasure in optically addressed, multiple quantum well, SLMs reveal carrier transport mechanisms which limit spatial resolution and sensitivity. (p. 57)

LTuC7 • Fundamental constraints on SLMs supporting $N \times N$ fanin/fanout, H. John Caulfield, Marius P. Schamschula, Leo Zhang, *Alabama A & M Univ.* Given the field of view, and the maximum fanin and fanout required, the pixel and overall size of the SLM are determined. (p. 61)

LTuC8 • Noise-induced switching and stochastic resonance in an optically addressed SLM, John P. Sharpe, Dominic C. O'Brien, Garret Model, *Univ. Colorado–Boulder*. The phenomenon of stochastic resonance is demonstrated using an optically addressed SLM. Results show good agreement with theory and computer simulation. (p. 65)

LTuC9 • Surface-normal optical modulation in thin-film silicon: is it feasible?, Michael Estes, Garret Model, *Univ. Colorado–Boulder*. We analyze the feasibility of amorphous and crystalline silicon materials for surface-normal optical modulators. Optically and electronically resonant structures are required for modulation. (p. 69)

GRAND BALLROOM A/B

1:30pm-3:00pm

LWA • Joint Session with Optical ComputingJohn N. Lee, *Naval Research Laboratory, Presider*

1:30pm (Plenary)

LWA1 • Future directions in "smart" quantum well SLMs and processing arrays, David A. B. Miller, *AT&T Bell Laboratories*. Integration of arrays of high-speed quantum well modulators with electronics, including hybrid integration with silicon, may exploit the best of optics and electronics. (p. 74)

David Miller received a B.Sc. in Physics from St. Andres University, and performed his graduate studies at Heriot-Watt University where he was a Carnegie Research Scholar. After receiving the Ph.D. degree in 1979, he continued to work at Heriot-Watt University as a Lecturer in the Department of Physics. He moved to AT&T Bell Laboratories in 1981 as a Member of the Technical Staff, and since 1987 has been a Department Head; currently of the Advanced Photonics Research Department. His research interests include optical switching and processing, nonlinear optics in semiconductors, and the physics of quantum-confined structures. He has published over 170 technical papers and 4 book chapters, delivered over 50 conference invited talks and over 20 short courses, and holds more than 30 patents.

2:15pm (Plenary)

LWA2 • Device-architecture interaction in optical computing, Ravindra A. Athale, *George Mason Univ.* Device technologies and processor architectures exert a strong influence on each other in optical computing. I will discuss examples of successful and unsuccessful interactions between these two communities. The role of the CO-OP in enhancing this interaction will be outlined. (p. 75)

Ravi Athale received his B.Sc. and M.Sc. degrees in Physics from Bombay University and IIT/Kanpur, respectively. He did his Ph.D. thesis work in Digital Optical Computing at University of California, San Diego. He worked at Naval Research Laboratory and BDM International before joining George Mason University faculty. He is a Fellow of Optical Society of America and a member of SPIE and IEEE/LEOS.

GRAND BALLROOM C

3:00pm-3:30pm

Coffee Break/Exhibits

GRAND BALLROOM A/B

3:30pm-5:00pm

OWC • Joint Plenary Session with Optical ComputingDemetri Psaltis, *California Institute of Technology, Presider*

3:30pm (Plenary)

OWC1 • History of optical computing: a personal perspective, Adolf W. Lohmann, *Weizmann Institute of Science, Israel*. The value of optics for signal transport and electronics for signal interaction will be discussed as well as how optical signal processing is instructive for optical computing. (p. 78)

4:15pm (Plenary)

OWC2 • Acoustic signal processing with photorefractive optical circuits, Dana Z. Anderson, *Univ. Colorado-Boulder*. Self-organized learning of temporal sequences is implemented with a photorefractive oscillator having a time delay element in the feedback path. (p. 81)

GRAND BALLROOM C

6:30pm-8:00pm

Conference Reception

RED LION WEST

8:30am-10:00am

LThA • SLM StructuresMary Hibbs-Brenner, *Honeywell, Inc., Presider*

8:30am (Invited)

LThA1 • Electrically and optically addressable spatial light modulators based on n-i-p-i doping superlattices, G. H. Döhler, P. Kiesel, M. Kneissl, N. Linder, K. H. Gulden, P. Riel, *Univ. Erlangen-Nürnberg, Germany*; X. Wu, J. S. Smith, *UC-Berkeley*. This paper reviews recent progress on n-i-p-i modulators. Electrical, nonlinear optical, and "smart optical" versions and their perspectives for future applications will be discussed. (p. 86)

9:00am

LThA2 • Design of an optically addressed SLM sensitive to 1.55- μ m write light, Li Wang, Garret Moddel, *Univ. Colorado-Boulder*; Geoff Burdge, *Univ. Maryland*. Design, experimental results, and fabrication issues for an optically addressed spatial light modulator (SLM) that incorporates an InGaAs-InP pin photodiode and ferroelectric liquid crystal are presented. (p. 89)

9:15am

LThA3 • Wedged liquid-crystal beam-steering device, Paul Searcy, Tami Hahn, Li Wang, Garret Moddel, *Univ. Colorado-Boulder*; John Wootton, Gary Waldman, Dave Holder, *Electronics and Space Corp.* A novel beam-steering device based on refractive index changes of nematic liquid crystals in a physical wedge is proposed and investigated. (p. 93)

9:30am

LThA4 • Spatial light modulation at photon-counting light levels, J. H. Hunt, R. B. Holmes, *Rockwell International Corp.* We report progress on the photon-counting SLM. The device, an avalanche photodiode which operates as an asymmetric Fizeau interferometer, achieves modulation of 80%. High-speed and multi-pixel operation is demonstrated. (p. 97)

9:45am

LThA5 • Epitaxial liftoff integration of a GaAs MQW modulator array onto Si VLSI for optical signal processing, W. Chang, R. Ranganathan, V. Arbet-Engels, E. Yablonovitch, *UC-Los Angeles*; M. Hansen, C. Fan, S. C. Esener, *UC-San Diego*; Uzi Efron, *Hughes Research Laboratories*. We report a novel self-aligned integration scheme for a GaAs/AlGaAs 16×16 multiple quantum well (MQW) modulator array on Si CMOS driver circuits employing the epitaxial liftoff approach. Such smart SLMs are expected to be valuable for optical signal processing. (p. 101)

GRAND BALLROOM C

10:00am-10:30am

Coffee Break/Exhibits

RED LION WEST

10:30am-12:00m

LThB • SLM MaterialsSadik Esener, *University of California-San Diego, Presider*

10:30am (Invited)

LThB1 • Electroholographic SLMs, Aharon J. Agranat, *Hebrew Univ. Jerusalem, Israel*. We present a generic architecture for spatial light modulators (SLMs), based on the use of the voltage-controlled photorefractive effect in paraelectric crystals, in which each pixel is a minute volume hologram. (p. 106)

11:00am

LThB2 • Optically addressed intrinsic MQW SLMs, W. S. Rabinovich, S. R. Bowman, D. S. Katzner, *Naval Research Laboratory*; C. S. Kyono, *Motorola*. We report large increases in the sensitivity of optically addressed multiple quantum well (MQW) SLMs that have been left intrinsic in the active region. (p. 110)

11:15am

LThB3 • Characterization of the optical quality and modulating properties of a PLZT modulator through Mueller matrix-imaging polarimetry, J. Larry Pezzaniti, Elizabeth A. Sornsin, Russell A. Chipman, *Univ. Alabama-Huntsville*; B. Mansoorian, *UC-San Diego*. The uniformity of the polarization-modulating properties of a wire-bonded PLZT SLM is evaluated using a Mueller matrix-imaging polarimeter. (p. 114)

11:30am

LThB4 • Spatial light modulation based on photo-induced change in the complex refractive index of bacteriorhodopsin, Hiroyuki Takei, Norio Shimizu, *Hitachi, Ltd., Japan*. $\pi/4$ phase shift exhibited by bacteriorhodopsin film at 633 nm was exploited in a Fabry-Perot cavity to accomplish spatial amplitude modulation at moderate intensities. (p. 118)

11:45am

LThB5 • Nonlinear optical image processing with bacteriorhodopsin films, John D. Downie, *NASA Ames Research Center*. The logarithmic transmission property of a bacteriorhodopsin film is exploited to facilitate the application of optical image processing operations to images with multiplicative noise. (p. 121)

12:00m-1:30pm

Lunch on Own

RED LION WEST

1:30pm-3:00pm

LThC • Liquid Crystal: 1Kristina Johnson, *University of Colorado-Boulder, Presider*

1:30pm (Invited)

LThC1 • Liquid crystal over silicon SLMs: emphasis on design for applications, Douglas J. McKnight, Kristina M. Johnson, H. Schuck, *Univ. Colorado-Boulder*; Steve A. Serati, *Boulder Nonlinear Systems*. This paper describes our recent binary and analog liquid crystal on silicon spatial light modulators (SLMs) and discusses how the final diffraction-based applications influence the device design. (p. 126)

2:00pm (Invited)

LThC2 • Ferroelectric liquid-crystal SLMs and their applications to information processing, Seiji Fukushima, Takashi Kurokawa, *NTT Opto-electronics Laboratories, Japan*. This paper reviews optically addressed SLMs containing ferroelectric liquid crystal and their applications to image processing, photonic switching, and optical measurement. (p. 130)

2:30pm

LThC3 • Optical image processing features of optically addressed liquid-crystal light modulators, Alexander V. Parfenov, *P. N. Lebedev Physics Institute, Russia*. This report is devoted to some of the physical mechanisms in liquid-crystal light modulators, which perform image processing functions. Attention is paid to applications in both coherent and incoherent light. (p. 134)

2:45pm

LThC4 • Optical characterization of stripe deformation in an electroclinic liquid crystal, J. R. Lindle, S. R. Flom, F. J. Bartoli, R. Shashidhar, B. R. Ratna, G. P. Crawford, *U.S. Naval Research Laboratory*. Spatially resolved optical measurements with micron resolution are reported for a chiral smectic A liquid crystal exhibiting quasibookshelf stripe deformation. (p. 138)

GRAND BALLROOM C

3:00pm–3:30pm

Coffee Break/Exhibits

RED LION WEST

3:30pm–5:00pm

LThD • Liquid Crystal: 2

William Crossland, *Cambridge University, U.K., Presider*

3:30pm (Invited)

LThD1 • Spatial light modulators: Russian research, development, and applications, Igor N. Kompanets, *P. N. Lebedev Physics Institute, Russia*. Some types of SLMs are discussed, especially the image converters and passive-addressed matrices on the base of ferroelectric liquid crystal for the fast input and the phase filtration of images. (p. 144)

4:00 (Invited)

LThD2 • Novel electroclinic liquid crystals for SLMs, B. R. Ratna, R. Shashidhar, *U.S. Naval Research Laboratory*. Development of chiral smectic A liquid crystal materials for spatial light modulators (SLMs) with analog phase modulation capability and fast response times will be discussed. (p. 146)

4:30pm

LThD3 • Liquid-crystal device performance degradation through selective adsorption of ions by alignment layers, Stephen H. Perlmutter, David Doroski, Garret Moddel, *Univ. Colorado–Boulder*. Selective adsorption of ions by alignment layers causes liquid-crystal device performance degradation by permanently increasing ion populations. (p. 148)

4:45pm

LThD4 • Responses of a SLM to pulsed-electron irradiation, E. W. Taylor, A. D. Sanchez, S. P. Chapman, S. A. De Walt, D. M. Craig, M. A. Kelly, M. F. Mitcham, *AFMC Phillips Laboratory*. The peak transient and residual attenuation observed in a ferroelectric liquid-crystal light valve exposed to pulsed-electron irradiation is presented and discussed. (p. 152)

RED LION WEST

5:00pm

Closing Remarks

Tuesday, March 14, 1995

MQW Spatial Light Modulators

LTuA 8:30 am-10:00 am
Red Lion East

Uzi Efron, *Presider*
Hughes Research Laboratories

PROVIDING OPTICAL I/O TO ELECTRONIC LOGIC CIRCUITS WITH MULTIPLE QUANTUM -WELL (MQW) DIODES (INVITED)

Leo M. F. Chirovsky
AT&T Bell Laboratories, Murray Hill, NJ 07974

The introductory paragraph to the Call for Papers for this Spatial Light Modulators (SLM's) Topical Meeting contains a very cogent definition of SLM's. In the context of that definition, the topic of this talk falls into the category of "highly integrated semiconductor 'smart' SLM's which spatially modify the intensity of a two-dimensional light distribution under the time-varying control of another spatial optical intensity distribution". The general purpose of these SLM's is to enable the construction of information processing systems which take advantage of the massive parallelism possible with free-space optical interconnects for very high data throughputs. The SLM's take the form of optoelectronic chips, which generate pixellated, parallel, synchronous, monochromatic, digital optical data streams. These chips usually also receive similar optical data streams, although the inputs do not need to be either digital, or pixellated or monochromatic or quite as synchronous. The circuitry on these chips can contain purely electronic components such as transistors, resistors, diodes, etc., but very importantly, need only one type of optoelectronic component - the p-i(MQW)-n diode, since it performs both Optical to Electrical (O/E) signal conversions and E/O conversions.

The p-i(MQW)-n diode can only be made in material grown by modern epitaxial growth techniques such as Molecular Beam Epitaxy (MBE) [1]. Like any p-i-n diode, when reverse-biased, it absorbs light efficiently at wavelengths shorter than the MQW absorption band-edge, producing a photocurrent, and thus performing an O/E signal conversion. With properly designed MQW structures, nearly ideal responsivities (one photocarrier pair per one photon incident) are possible with just a 1 μ m thick MQW stack and light at normal incidence. The photocarrier sweep-out times can be as short as ten to a hundred picoseconds, yielding very rapid responses, potentially allowing operations up to several GHz [2].

Due to a phenomenon called the Quantum Confined Stark Effect (QCSE) [1], in p-i(MQW)-n diodes, the absorption band-edge (and the exciton absorption peak near that edge) can be red-shifted several nanometers with several volts of reverse bias. As a result, the absorption of light incident on the diode can be strongly varied at certain wavelengths, by an applied voltage. At or very near the exciton peak wavelength, λ_0 , the absorption decreases with applied voltage; at wavelengths several nanometers longer, λ_1 , the absorption increases with applied voltage. Thus the intensity of light passing through the MQW Stack can be modified by an applied voltage, at λ_0 or λ_1 , and that is an E/O signal conversion. For instance, for p-i(MQW)-n diodes made in GaAs/AlGaAs material, having an $\sim 1\mu$ m

thick MQW stack, and an anti-reflection (AR) coating on the surface of incidence and a highly reflecting mirror on the opposite side of the diode, the intensity of reflected light, at λ_1 , can be modulated from $\sim 50\%$ to $\sim 10\%$ of an incident intensity $< 5\text{kW/cm}^2$, with a voltage swing of 7-10 Volts. The speed of modulation depends only on the speed with which the voltage swing occurs, and so, depends mostly on the abilities of drive circuits to charge the modulator (and any parasitic capacitance) while draining any opposing modulator photocurrent that is present.

The first optoelectronic chips which contained p-i(MQW)-n diodes and were used in system experiments, were arrays of Self Electro-optic Effect Devices (SEED's). These SEED's were actually circuits comprised only of p-i(MQW)-n diodes. They were so named because the operation, at λ_0 , of those early SEED's, such as the S-SEED's, depended on each diode's being both a detector (photocurrent producer) and a modulator simultaneously for optical and electrical bistability [1].

The system experiments with SEED arrays produced numerous insights - on the system level [3], such as 1) how to construct the free space opto-mechanics for long term stability, 2) how to generate and combine arrays of optical beams, 3) how to package chips, and most importantly 4) what novel system architectures best utilize the massive parallelism provided by free space optics; and on the chip level [4], such as 1) how to fabricate high-yield, reliable p-i(MQW)-n diodes, 2) how to deal with limited signal contrast, and 3) how to test large device arrays. Among the major achievements of the SEED technology was the demonstration of the ability to fabricate very large arrays, comprising up to 128x128 functioning p-i(MQW)-n diodes.

Two important shortcomings of SEED's also became apparent from those experiments - limited functionality and low switching speed. The first problem arose when studies of system architectures showed that flexibility in the system designs for many applications would increase dramatically if the functional complexity and variety between the optical inputs and the optical outputs increased beyond that of simple logic gates. The second problem stemmed from the fact that, although the input signal photocurrents appeared extremely quickly, they could not be made large enough to produce the required voltage swing across the modulators quickly. An S-SEED can sustain a data-rate, f , given by -

$$f = I_{ph} / 2C\Delta V, \quad (1)$$

where I_{ph} is the effective charging photocurrent, ΔV is the required voltage swing and C is the total device capacitance to be charged. (The factor of 2 arises from the fact that the switching-rate must be twice the data-rate.) For reasonably sized devices, $C\Delta V \sim 500\text{fC}$, but because of saturation and

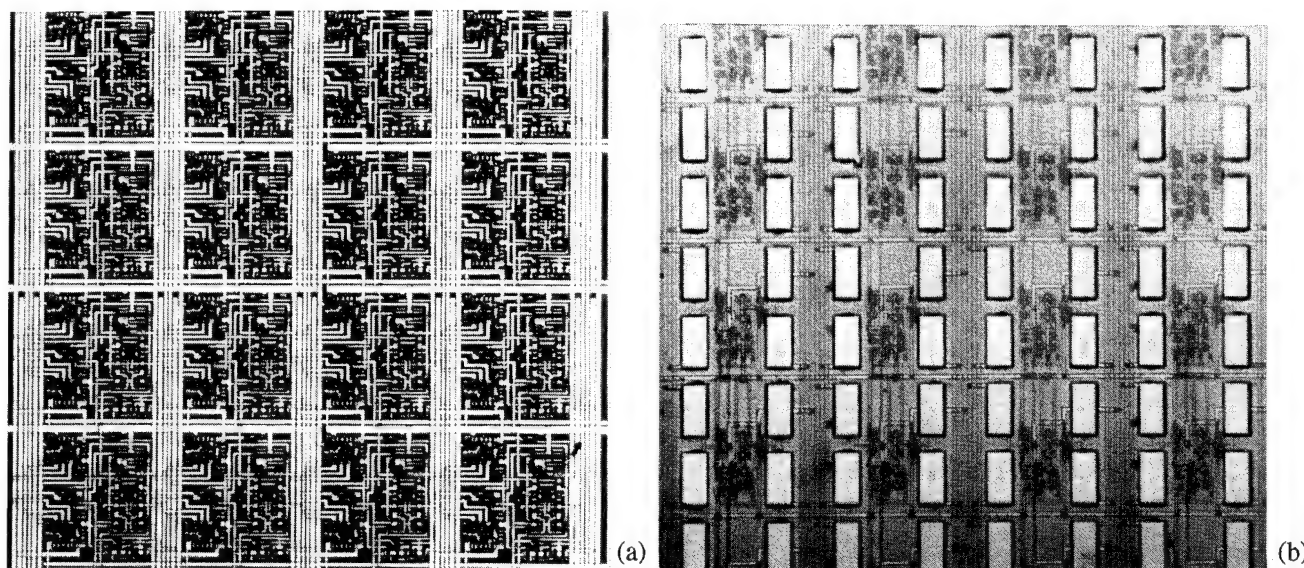


Figure 1. Photographs of 2x1 switching node arrays - a) a 4x4 array of nodes processed via the monolithic FET-SEED technology and used in the recent switching system prototype; b) a 4x4 array of nodes processed via the hybrid technology and designed for performance comparisons with the monolithic versions shown in (a).

heating effects and the need for optical gain, I_{ph} was limited to $\sim 10\mu A$ allowing a maximum f of ~ 10 Mbits/s. Since the SEED's, among many other things, were already electrical circuits, one solution to both of the above problems was the integration of p-i(MQW)-n diodes with transistors. Then functional diversity and complexity can come from electronic logic circuits; higher data-rates can come from an electronic amplification of I_{ph} by amplifier circuits. Once there is a suitable co-fabrication process, all issues can be resolved with the proper circuit designs, at least in principle.

The first decision made, in the quest for a suitable processing technology, was to co-fabricate the p-i(MQW)-n diodes with field-effect transistors (FET's) and not bipolar transistors, because FET's have lower input capacitance and FET circuits can latch dynamically. Then an elegant processing technology was developed [5] for a monolithic integration of the two components, whereby the epitaxial growth of the p-i(MQW)-n diodes was done p-side down so that FET's could be made on the surface in a thin n-i-n+ structure. Only one processing level was added to the processing sequence for SEED's. This optoelectronic technology became known as the FET-SEED technology. In one sense the FET-SEED circuits outgrew the name SEED, since they could no longer be construed as devices, no longer required bistability, and assigned to each p-i(MQW)-n diode the role of detector or modulator but not both. In another sense however they were still SEED's, since they still kept the very important attribute of SEED's, that the same identical component could be used for optical signal detection and transmission, so that effectively p-i(MQW)-n diode photocurrents still modify the states of p-i(MQW)-n modulators.

The monolithic FET-SEED technology fulfilled many of the expectations that developed with its inception, foremost of which were increases in functional sophistication and in

achievable data-rates, as compared to what was possible with plain SEED's. A large variety of circuit arrays were implemented and used in several system experiments as, for example, a 16 input by 16 output ATM switching system prototype which was operated at 155 Mbits/s/channel and so was capable of switching at video-rates [6]. The system consisted of 5 stages with one circuit array per stage such as the one shown in Figure 1a.

The circuit designs were divided into three sub-circuit categories - 1) optical signal receivers, 2) logic circuit families, and 3) optical signal transmitters. What logic circuit family to adopt is often dictated by the exact nature of the FET's available. Since initially only depletion mode MESFET's were made, the first preferred choice was the Buffered-FET Logic family (used for the circuits in Fig. 1a), with a voltage logic swing, ΔV_L , from +0.8V to -0.8V. Switching times, τ_{TO} , of ~ 140 ps were measured with simple ring-oscillator circuits [7] implying that at least the logic circuits should operate at data-rates up to 1 Gbit/s. All the circuitry needed to convert an optical input signal to a ΔV_L was then considered part of a receiver circuit, and all the circuitry needed to convert a ΔV_L to an optical output signal was then part of a transmitter circuit. Certain (often conflicting) constraints were placed on the receiver and transmitter circuit designs usually not imposed on such circuits in data transmission systems. These stemmed from the desire to make optoelectronic chips with large arrays of input and output ports, in order to exploit the very high degree of parallelism offered by free space optical interconnects. The goal was that these sub-circuits be as simple and small as possible (hopefully occupying areas no larger than $100 \times 100 \mu m$ and dissipating only a few mW of total power) and yet switch in 1 ns or less with sensitivities < -20 dBm. A study, comprised of a series of experiments [8-11] on individual test circuits, demonstrated that the

goal was indeed achievable, in particular, if 1) the optical signals are in the form of short RZ (return-to-zero) pulses such as from mode-locked lasers and 2) either the receiver or the transmitter latches dynamically (holds its state in the absence of a signal for a long time compared to a bit-period). Another set of analyses and experiments showed that one can deal with finite optical signal contrast not only by using differential signals but also with single-ended RZ optical signals, if one sacrifices dynamic range for a large reduction in the external laser power requirement [12-13].

Presently, the major weakness of the monolithic FET-SEED technology is its processing yield. The principal goal of this technology, and perhaps of any other SLM technology, is high aggregate data throughput, which will need to be in the range of 100's Gbit/s to 1Tbit/s to merit the widespread attention of system designers. Defined as the product of the number of parallel data channels and the data-rate/channel, such throughputs would require FET-SEED circuit arrays with hundreds, maybe thousands of I/O ports, handling data-rates of 0.1 to 1.0 Gbit/s. Although FET-SEED circuits have demonstrated the required speed and the fabrication yield of p-i(MQW)-n diodes is quite sufficient, the FET yield may not be, because many system applications are persistently asking for circuits with ever larger ratios of # of FET's to # of p-i(MQW)-n diodes, to increase the data-processing capabilities of the logic sub-circuits. Raw data throughput with little on-chip data processing appears to be wasteful. The more appealing concept is a VLSI-like electronic chip with SLM-like data throughput. An effort is underway to produce monolithic FET-SEED chips with ~10,000 FET's for a 256x256 ATM switch, but to proceed beyond that scale of integration would require a huge effort and expenditure of resources that may be unnecessary in light of a new approach. The Si CMOS technology is very advanced, so instead of trying to duplicate its high yields in epi-grown material, the wiser choice may be to use Si CMOS chips and to add a few thousand p-i(MQW)-n diodes to them to make very high data throughput optoelectronic chips. Recently, it was shown that, in fact, arrays of planar p-i(MQW)-n diodes (with both contacts on the same surface) can be flip-chip solder-bump bonded onto Si chips [14] and thereby hybrid-integrated into Si CMOS circuits. The diodes' substrate is then removed for stress relief and optical access, leaving each diode as a little island in a sea of CMOS circuits. To prove the efficacy of the new hybrid process, p-i(MQW)-n diodes were bonded to a Si chip with an array of CMOS circuits (shown in Fig.1b), designed to emulate the FET-SEED nodes in Fig. 1a. These first hybrid nodes were then successfully operated at data-rates up to 250 Mbits/s [15]. In the near future much larger hybrid circuit arrays will be attempted. The principal fabrication challenge in this approach is to develop high yield solder-bump processes with ever smaller bump pads, to decrease the p-i(MQW)-n diode capacitances, presently much greater than in the monolithic FET-SEED's.

In summary, data processing systems, which must deal with vast amounts of data, can benefit from the use of free space optical interconnects between optoelectronic chips, configured as SLM's to launch and receive arrays of high speed optical data streams. A particularly useful way of making such chips is to integrate arrays of p-i(MQW)-n diodes with electronic circuits, because 1) these diodes can be used both as input and output ports (so no other device integration is needed); 2) the diodes are quite amenable to integration with electronics; 3) the resulting circuits are very fast; and 4) large arrays are in the offing.

- [1] D. A. B. Miller, D. S. Chemla, T. C. Damen, T. H. Wood, C. A. Burrus, A. C. Gossard, and W. Wiegmann, "The Quantum Well Self-Electrooptic Effect Device: Optoelectronic Bistability and Oscillation, and Self-Linearized Modulation", *IEEE JQE*, V.21, 1462 (1985).
- [2] A. M. Fox, D. A. B. Miller, G. Livescu, J. E. Cunningham, and W. Y. Jan, "Quantum Well Carrier Sweep Out: Relation to Electroabsorption and Exciton Saturation", *IEEE JQE*, V.27, 2281 (1991).
- [3] F. B. McCormick, T. J. Cloonan, F. A. P. Tooley, A. L. Lentine, J. M. Sasian, J. L. Brubaker, R. L. Morrison, S. L. Walker, R. J. Crisci, R. A. Novotny, S. J. Hinterlong, H. S. Hinton, and E. Kerbis, "A 6-Stage Digital Free Space Optical Switching Network Using SEED's", *Appl. Optics* V.32, 5153-71 (1993).
- [4] L. M. F. Chirovsky, M. W. Focht, J. M. Freund, G. D. Guth, R. E. Leibenguth, G. J. Przybylek, L. E. Smith, L. A. D'Asaro, A. L. Lentine, R. A. Novotny, and D. B. Bucholz, "Large Arrays of Symmetric Self Electrooptic Effect Devices", *OSA Proceedings on Photonic Switching*, V.8, 56-59 (1991).
- [5] L. A. D'Asaro, L. M. F. Chirovsky, E. J. Laskowski, S. S. Pei, T. K. Woodward, A. L. Lentine, R. E. Leibenguth, M. W. Focht, J. M. Freund, G. D. Guth, and L. E. Smith, "Batch Fabrication and Operation of GaAs-AlGaAs Field-Effect Transistor - Self Electrooptic Effect Device (FET-SEED) Smart Pixel Arrays", *IEEE JQE*, V.29, 670-7 (1993).
- [6] A. L. Lentine, R. A. Novotny, T. J. Cloonan, L. M. F. Chirovsky, L. A. D'Asaro, G. Livescu, S. P. Hui, M. W. Focht, J. M. Freund, G. D. Guth, R. E. Leibenguth, K. G. Glogovsky, and T. K. Woodward, "4x4 arrays of FET-SEED embedded control 2x1 optoelectronic switching nodes with electrical fan-out" *IEEE Photonics Tech. Lett.*, V.6, No.9, (1994).
- [7] T. K. Woodward, R. A. Novotny, A. L. Lentine, L. M. F. Chirovsky, L. A. D'Asaro, S. P. Hui, M. W. Focht, G. D. Guth, L. E. Smith, and R. E. Leibenguth, "Ring Oscillator with Monolithically Integrated Read-out Based on GaAs/AlGaAs FET-SEED Technology", to be publ., *IEEE EDL*, Feb. 1995.
- [8] A. L. Lentine, L. M. F. Chirovsky, and T. K. Woodward, "Optical Energy Considerations for Diode-Clamped Smart Pixel Optical Receivers", *IEEE JQE*, V. 30, 1167-71 (1994).
- [9] T. K. Woodward, A. L. Lentine, and L. M. F. Chirovsky, "Experimental Sensitivity Studies of Diode-Clamped FET-SEED Smart Pixel Optical Receivers", *IEEE JQE*, V.30, 2319-24 (1994).
- [10] G. D. Boyd, G. Livescu, L. M. F. Chirovsky, A. L. Lentine, "Mode-locked Pulse Operation of GaAs/AlGaAs Field Effect Transistor - Self Electrooptic Effect Device Smart Pixels and Saturation Considerations", *Appl. Phys. Lett.*, V.65(24), pp.3108-10 (1994).
- [11] G. Livescu, G. D. Boyd, L. M. F. Chirovsky, R. A. Morgan, and T. Mullally, " ", *Opt. Lett.*, V. 19, Dec. 15, 1995.
- [12] T. K. Woodward, L. M. F. Chirovsky, R. A. Novotny, and A. L. Lentine, "Single-Ended Operation of FET-SEED Smart Pixels", Paper M3.3, Tech. Digest, LEOS Topical Meeting on Smart Pixels, pp.24-5, July 11-13, 1994.
- [13] L. M. F. Chirovsky, A. L. Lentine, T. K. Woodward, G. Livescu, and G. D. Boyd, "Nonuniformity Tolerance and Its Price for Different Modes of Operation of FET-SEED Smart Pixel Arrays", to be published in *Proceedings of OC'94*.
- [14] K. W. Goossen, A. L. Lentine, J. A. Walker, L. A. D'Asaro, S. P. Hui, B. Tseng, R. E. Leibenguth, D. P. Kossives, D. W. Dahringer, L. M. F. Chirovsky, and D. A. B. Miller, "4x4 Array of GaAs Hybrid on Silicon Optoelectronic Switching Nodes Operating at 250 Mbits/s", Postdeadline Paper PD2, LEOS Annual Meeting, Boston, MA (Nov., 1994).
- [15] A. L. Lentine et al., "8x8 Optoelectronic Switching Nodes Comprised of Flip-Chip-solder-Bonded MQW Modulators on Silicon CMOS circuitry", talk to be presented at PS'95, March 12-17, 1995.

16x16 SLM with Silicon CMOS Drivers and III-V Modulators

Mark Hansen, David Shih, Chi Fan, Sadik Esener
 University of California, San Diego
 Department of Electrical and Computer Engineering
 La Jolla, CA 92093-0407
 (619) 534-6226

Wei Chang, Eli Yablonovitch
 University of California, Los Angeles
 Electrical Engineering Department
 Los Angeles, CA 90024
 (310) 206-1034

Uzi Efron
 Hughes Research Laboratories
 3011 Malibu Canyon Road
 Malibu, CA 90265-4799
 (310) 317-5214

Introduction

Hybrid integration of III-V based optical devices, such as modulators, LEDs, and lasers, with silicon VLSI technology promises cost effective solutions to many optoelectronic challenges. It combines the low cost, high density, and high yield of silicon circuitry with the unique optical properties of III-V devices. Flip-chip bonding is a mature and commercial technology. It provides a means of reliable, rapid integration of these two types of devices.¹

In this paper, we report the results of a technological investigation of the integration of AlGaAs/GaAs and InAlGaAs/InGaAs multiple quantum well (MQW) modulators with silicon CMOS circuitry using flip-chip bonding. A 16x16 array of multiple quantum well (MQW) modulators and Si driver circuitry has been designed and fabricated. The devices are flip-chip bonded using gold balls as the bump technology. The gold ball technology is reliable and widely available. It can be readily used for hybrid integration on Si circuitry without any alteration of or addition to existing silicon IC fabrication processes.

We have investigated the epitaxial lift off (ELO) and total substrate removal (TSR) of AlGaAs/GaAs MQWs onto quartz substrates in the context of flip-chip bonding. Issues regarding the processing of modulator devices both before and after the thin film procedure have been examined. The InAlGaAs/InGaAs modulators, which operate near 1.06 μ m, are flip-chip bonded directly to silicon drivers as the GaAs substrate is transparent at this wavelength. The performances of the various approaches are to be presented.

Bump Technology

Various bump technologies were evaluated, with strong emphasis on rapid development and ease of prototyping. Many bump technologies require complex metallurgy and/or processing on the silicon and III-V circuitry. For instance, in order to use indium bumps on foundry fabricated silicon circuitry, additional metallization layers must be deposited on the silicon IC for use as a solder wetting surface.² However, reflowable flip-chip bumps such as indium have the advantage of self-alignment, allowing for accurate placement of large arrays. Additionally, indium or

solder bumps can be fabricated to small dimensions, yielding high density interconnects.

Gold balls can be quickly placed on standard silicon VLSI I/O pads with no extra silicon process steps. A common commercially available thermocompression ball bonder, adjusted to leave no wire tails, can be used to place the balls. This process has been shown to be reliable and quite cost effective.³ A major drawback of gold balls is their size, generally 50-100 μm , depending upon the ball bonding technology. The size of the bumps in this case will determine the minimum pitch and minimum pixel size of the bonded devices. Correspondingly, the capacitances for the bump and modulator will be high, a total of 4.2pF in our work, so the driver dimensions must also be made large in order to drive this load capacitance.

Si CMOS Driver

To evaluate the density limitation of hybrid device arrays, the emphasis on the design of the modulator driver circuit was to minimize the Si area used. Besides driving a capacitive load with a small photocurrent component (our high fill factor SLM has relatively low light input intensities), another requirement of the driver is a large voltage swing. Our modulator driver, therefore, consists of only four transistors, a two stage CMOS inverter with V_{dd} at 10V (Fig. 1 b). A 10V output swing is possible using standard 5V technology since the V_{GS} breakdown is typically above 12V with the 2 μm CMOS technology used.

The first inverter is driven by the five volt input signal. With the supply at 10V, an input high state will cause a weak output low state, since P1 as well as N1 will turn on. This first inverter stage is designed so that the output low state is low enough to ensure that N2 in the second stage does not turn on under this condition. When the input to the first stage is low, the first stage output reaches the rail voltage of 10V since N1 is completely off. The second stage inverter, therefore, has a rail to rail output swing of ten volts. This stage drives the MQW modulator. The silicon chip was fabricated through the MOSIS foundry service (Fig. 1 a).

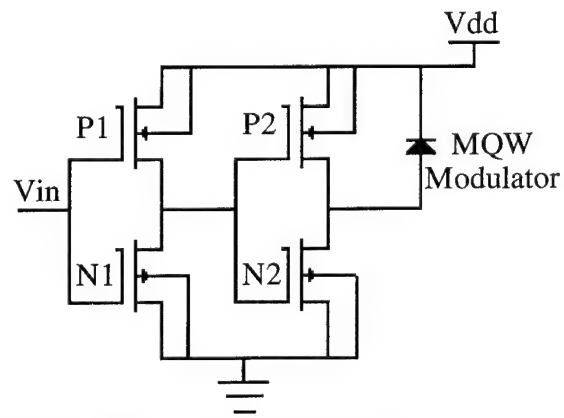
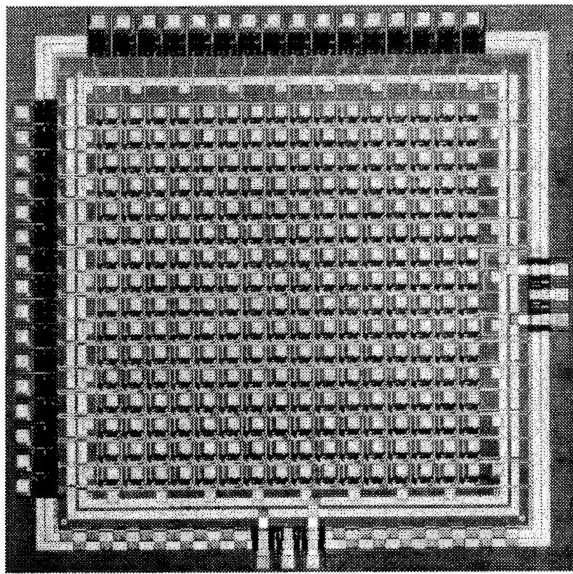


Fig. 1. (a) Photograph of 16x16 silicon CMOS driver array IC.
(b) Schematic of single driver

Modulator Material

Flip-chip bonded modulators must have light incident from the back side, since the front is in contact with the silicon driver and logic circuitry. A transparent substrate, or removal of an opaque substrate, is therefore required. We have investigated several material systems and processing approaches which address this requirement.

We have experimentally investigated strained well InAlGaAs/InGaAs MQW modulators operating at $1.06\mu\text{m}$.⁴ The MQWs are grown atop a step graded, strain relaxing buffer layer to compensate for lattice mismatch between the MQWs and the GaAs substrate. Since GaAs is transparent at $1.06\mu\text{m}$, after device processing, the modulator array is bonded directly to the Si driver. The lattice mismatch between substrate and MQWs is a disadvantage, however, since dislocations generated in the buffer layer may propagate to the MQWs, degrading modulator performance. The linewidth of the InAlGaAs/InGaAs exciton peak is generally wider than that of AlGaAs/GaAs MQWs. The full-width at half maximum of the exciton peak in our InAlGaAs/InGaAs material is around 20meV at room temperature.

AlGaAs/GaAs MQW material is lattice matched to the GaAs substrate. Hence, high quality modulator materials are more easily obtained. However, electroabsorption modulation occurs at a wavelength below the GaAs band edge, so the substrate is opaque. To separate the GaAs substrate and MQW material, epitaxial lift off (ELO)⁵ and total substrate removal (TSR)⁶ techniques have been investigated.

The ELO process involves a highly selective etch through a sacrificial AlAs layer. The lifted-off GaAs film is then bonded to a transparent substrate, in this case quartz. Large area high quality films are difficult to obtain due to water which remains between the substrate and the lifted off films, and surface contamination on the substrate. These can both result in poor bonding and affect the flip-chip process.

In the TSR technique, the GaAs wafer is first bonded to the transparent substrate. The GaAs substrate is then etched away, with a GaAs selective etch being stopped at an AlAs layer. However, the selectivity of the etchant is rather weak compared to AlAs selective etching. This places a tight constraint on the processing. In other words, either the AlAs etch stop layer has to be very thick, which degrades the quality of the device material on top of it, or the backside of the GaAs wafer has to be carefully lapped to be parallel with the AlAs layer.

Presently, bonding techniques using palladium, UV curable epoxy, and Van der Waals bonding are being investigated for the large area thin film process. The details and results of these experiments will be presented.

Modulator Array

The modulator material is processed into P-I-N diodes, with the N layer being common to all modulators in the array. This common layer approach reduces the number of bump interconnects required. This, in turn, increases the array density. Mesa isolation is used to electrically separate modulators. Due to the large size of the gold balls, planarization of the modulator array is not required. The distance from the top of the mesa to the bottom is small compared to the diameter of the balls. This simplifies the integration process.

The modulator array has the mirror image of the silicon driver bond pads for flip-chip bonding. The gold p-type contact on top of the mesa also serves as the

reflector for the modulator. Mirror surface roughening, and hence degraded modulator performance, from the annealed contact is avoided through the use of a thin SiO₂ layer between the gold reflector and the GaAs. Windows in the SiO₂ are opened for electrical contact. The efficiency of the Au/SiO₂ mirror will be evaluated and the results will be presented.

Summary

We are investigating the integration of III-V optoelectronic devices and Si circuitry via hybrid flip-chip bonding technology. Two types of MQW modulators, InAlGaAs/InGaAs and AlGaAs/GaAs, as well as their fabrication processes, are being examined in the context of flip-chip bonding. Various technical approaches have been taken. The comparison of the performance will be presented.

The gold ball technique for flip-chip bump bonding is also evaluated. The density of bonded devices is limited by the diameter of the ball, 90µm in our work. The pitch of our 16x16 SLM is about 200µm. The individual Si CMOS driver area is around 100µm x 50 µm, which drives a capacitance of 4.2pJ. The pitch decreases approximately linearly with bump size. The total capacitance, including the modulator and the bump, will be less than 50fF when the bump size becomes 10µm x 10µm. Minimum size CMOS inverters can be used to drive such a configuration. Using 2µm CMOS technology, for instance, the driver size would be 400µm², which results in a pitch spacing of 20µm. Further reduction in the bump size will have no effect on device density, since it would be determined by the Si IC technology.

References

1. H. B. Bakoglu, Circuits, Interconnections, and Packaging for VLSI, Addison-Wesley Publishing Co., 1990
2. S. Ray, K. Beckham, and R. Master, "Device Interconnection Technology for Advanced Thermal Conduction Modules", IEEE Transactions on Components, Hybrids, and Manufacturing Technology, August 1992, Vol. 15, No. 4, 432-7
3. C. Goodman and M. Metroka: "A Novel Multichip Module Assembly Approach Using Gold Ball Flip-Chip Bonding", IEEE Transactions on Components, Hybrids, and Manufacturing Technology, August 1992, Vol. 15, No. 4, 457-464
4. C. Fan, D.W. Shih, M.W. Hansen, S.C. Esener, et al. "Quantum-Confined Stark Effect Modulators at 1.06 µm on GaAs" IEEE Photonics Technology Letters, Dec. 1993, Vol. 5, No. 12, 1383-5.
5. E. Yablonovitch, T. Sands, D. M. Hwang, I. Schnitzer, and T.J. Gmitter, "Van der Waals Bonding of GaAs on Pd Leads to a Permanent, Solid-Phase-Topotaxial Metallurgical Bond." Applied Physics Letters, 1991, Vol. 59, 3159-61
6. K. W. Goossen, J. E. Cunningham, and W. Y. Jan, "GaAs 850 nm Modulators Solder-Bonded to Silicon", IEEE Photonics Technology Letters, 1993, Vol. 5, 776-8

High yield, low cost Fabry-Perot modulators utilizing correctable partial anti-reflection coatings

K.W. Goossen, J.E. Cunningham, W.Y. Jan, and J. Centanni

AT&T Bell Laboratories, room 4B-519, Holmdel, NJ 07733 (908) 949-6979

Many systems are contemplated that use surface-normal multiple quantum well (MQW) modulators to imprint data on optical beams. These include "smart pixel" digital processors,¹ as well as image processors that employ spatial light modulators. These modulators are typically p-i(MQW)-n diodes, grown by techniques such as Molecular Beam Epitaxy (MBE), wherein an integral multilayer mirror is produced underneath the MQW. By reverse biasing the diode the MQW's absorption is modified and hence the reflectivity of the device is modulated. In simple designs a perfect anti-reflection coating is placed on the surface so multiple reflections do not occur within the modulator. This has the advantage that no strict control of the overall thickness of the device is required.

Several years ago modulators employing multiple reflections to enhance modulation were demonstrated. In particular, the asymmetric Fabry-Perot modulator (ASFP) was shown.^{2,3} In this device the absorption of the MQW is tailored such that the integral mirror's reflectivity, when reduced by this absorption, can equal the surface reflectivity under appropriate bias to the diode. Then, the overall reflectivity of the ASFP is essentially zero. By changing the bias, the balance is disrupted and the overall reflectivity rises, so achieving high contrast. Although better

modulation is obtained, the device requires strict control of the layer thicknesses, reducing yield due to nonuniform crystal growth. Before this work the best achievement was greater than 2:1 contrast over an entire 2 inch wafer.⁴

Here we present the use of a partial anti-reflection (PAR) coating to achieve a lower finesse ASFP (PAR-ASFP). The reduced finesse makes ASFP's more tolerant to semiconductor growth nonuniformity (i.e., variations in semiconductor thickness across a wafer), and in addition adjusting the thickness of the PAR can correct for errors in the semiconductor thickness. Note that it is still necessary to achieve growth accuracy, i.e., the appropriate semiconductor thickness at the center of the wafer, and schemes to achieve growth accuracy by post-growth etching,⁵ would complement our technique. Note that compensation by adjusting the thickness of a post-growth deposited top dielectric mirror has been presented in [6], whereas our technique requires only one layer, and as shown below, lends itself to a wafer-scale process as opposed to a chip-by-chip basis.

We show in Fig. 1 a simplified model for the PAR-ASFP assuming a spectrally-independent absorption to more clearly show the affect of PAR thickness on FP resonance wavelength. In Fig. 1, the designed resonance is at 850 nm for a PAR thickness of 1400 Å. An index of 1.5 is assumed for the PAR layer. Note that a perfect anti-reflection layer would have an index near 1.9. If the semiconductor layer thicknesses are reduced by 1 %, the resonance shifts to shorter wavelengths by 8.5 nm. However, if for such a error in growth, the PAR layer is reduced to 900 Å, the resonance shifts back toward the design value of 850 nm. Similarly, for too thick semiconductor layers, if the PAR layer is made thicker the resonance shift is corrected for. Thus the very powerful principle of this design, *errors in semiconductor layer thicknesses (+ or -) are corrected for by changing the PAR thickness by the same sign (+ or -)*. This is powerful since the semiconductor layers, if grown by MBE, are always thicker in the center of

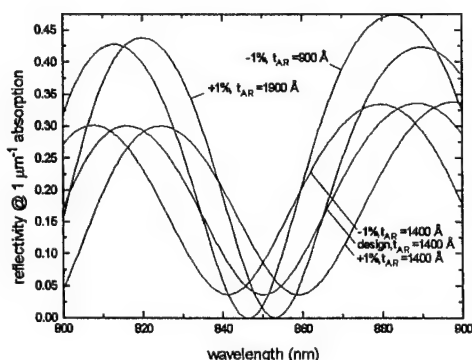


Fig. 1: Spectra of simplified (nonabsorbing) ASFP modulator with partial anti-reflection (PAR) coating of index 1.5 to illustrate correcting effect of changing PAR thickness.

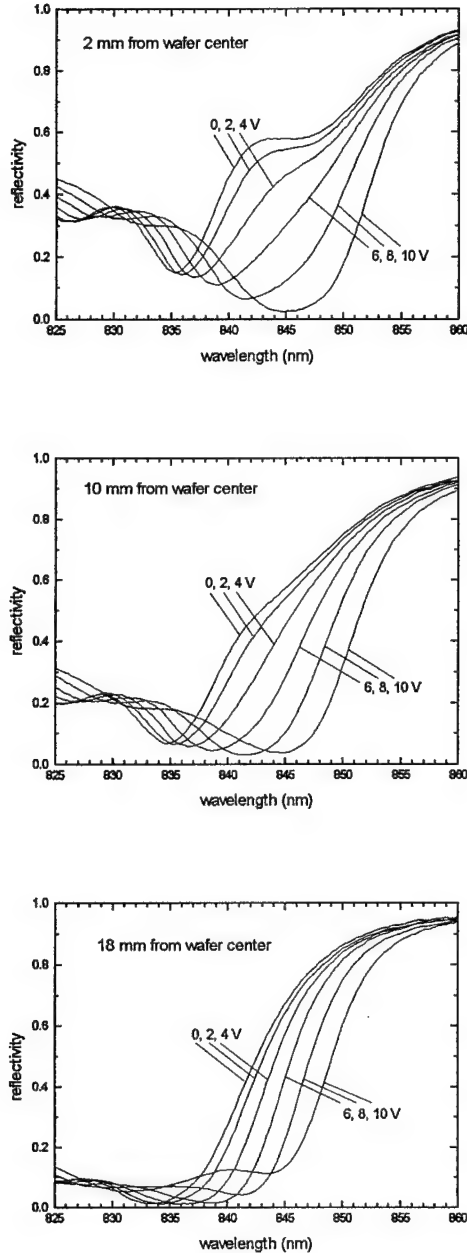


Fig. 2: Spectra of our sample for different biases for a device 2, 10, and 18 mm from wafer center. The (SiO_2) PAR thickness is 1600 Å. The F-P resonance is near 846 nm for the 2 mm plot. It is difficult to observe the F-P as it blue-shifts with wafer position due to the thinning of the crystal.

the wafer, since it is a geometric effect of the relation between the source crucibles and the wafer, which is typically rotated during growth. The PAR layer, if deposited using a technique such as evaporation, will similarly be thicker in the center. The PAR nonuniformity could be

accentuated and controlled by placing the wafer fairly near the evaporation boat, *thus automatically correcting for variations in semiconductor thicknesses*. Using PAR correction, we achieve greater than 6.7:1 contrast over the entire 2 inch wafer at a single wavelength.

Our device comprises of a n-type bottom multilayer mirror consisting of ten periods of $\text{AlAs}/\text{Al}_{0.15}\text{Ga}_{0.85}\text{As}$ (707/601 Å), followed by an intrinsic 72 period GaAs/AlAs (90/20 Å) MQW. Then a 1000 Å p $\text{Al}_{0.15}\text{Ga}_{0.85}\text{As}$ layer is grown, and finally a 50 Å p+ GaAs cap layer. After removing from the growth chamber, a 1600 Å SiO_2 layer is deposited by chemical vapor deposition. Note that the SiO_2 has an index of about 1.5, so forms a partial anti-reflection layer. The sample is designed so that the Fabry-Perot resonance is below the band edge of the MQW, so that when the exciton shifts under bias into the resonance, the cavity is nulled. Using the PAR dictates that the design employ a weak 10 period mirror. Note that our design uses minimal total semiconductor thickness, 2.2 microns compared to a typical ASFP thickness of 3.8 microns,⁴ so greatly reduces semiconductor growth cost, which depends on growth time. Gold contacts are made and 200x200 micron mesas etched around them to define the modulators.

In Figs. 2-3 we show the spectra at different biases for devices 2, 10, 18 and 24 mm from the center of the wafer, as measured at low intensity with a lamp/monochromator. As the distance is increased, the Fabry-Perot (F-P) resonance moves to shorter wavelengths. In Fig. 2, at 2 mm from wafer center, the F-P resonance can be seen near 846 nm, while the MQW exciton is near 835 nm. The F-P resonance is weaker and broader in the PAR-ASFP than in standard ASFP's due to the reduced finesse of the cavity. In Fig. 2, the usual behavior of ASFP's is observed, with the reflectivity dropping to near zero as the exciton shifts with bias into the F-P resonance. The F-P resonance becomes more difficult to see as it shifts with wafer position to shorter wavelengths near the exciton. High contrast is still achieved, though, until we move to a position 24 mm from wafer center.

Then in Fig. 4 high contrast is achieved for the device 24 mm from wafer center by thinning its PAR layer to 1200 Å. In accordance with the

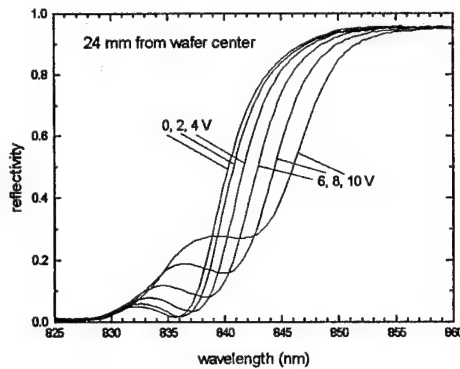


Fig. 3: Same as Fig. 2 for 24 mm from wafer center. Contrast is now quite degraded.

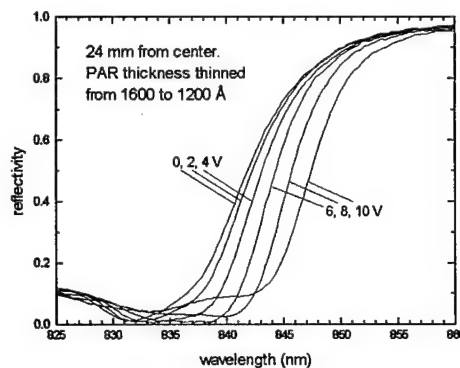


Fig. 4: Same as Fig. 3, after reducing the PAR thickness to 1200 Å. High contrast is now achieved, ostensibly due to a red-shift of the F-P upon reducing PAR thickness in accordance with the theoretical prediction of Fig. 1.

theoretical prediction of Fig. 1, this causes the F-P resonance to shift to longer wavelengths, and thus higher contrast is achieved. In Fig. 5, the contrast ratio spectra for 9 volts drive is displayed for the four wafer positions (solid lines), and for the 24 mm position after thinning the PAR (dotted line). Using PAR correction, greater than 6.7:1 contrast is achieved at 842.5 nm over the entire wafer.

Note that the theoretical prediction of F-P red-shift with PAR thinning is difficult to observe due to the broadness of the F-P. Nonetheless, the empirical result of increased contrast achieved for PAR thinning at the wafer edge is confirmed, with the manufacturing implications stated earlier.

In conclusion, it has been shown that low finesse, partial anti-reflection coated asymmetric Fabry-Perot (PAR-ASFP) modulators, may

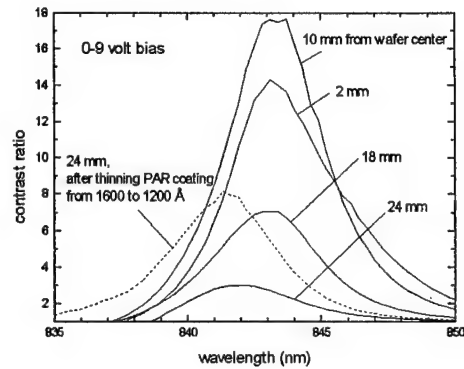


Fig. 5: Contrast ratio spectra for 0-9 volts bias for different wafer positions, and for the 24 mm position after PAR correction (dotted line). By thinning the PAR near the wafer edge, contrast greater than 6.7:1 is achieved over the entire 2 inch wafer.

achieve high contrast, and in addition, errors in growth may be corrected for by adjusting the PAR coating thickness. Too thin semiconductor layers are corrected for by reducing the thickness of the PAR layer. This leads to easy manufacturing, since both the semiconductor and PAR layers will naturally be thinner at the edge of a wafer. We achieve greater than 6.7:1 contrast over an entire 2 inch wafer at a single wavelength and drive bias.

REFERENCES

- [1] A.L. Lentine, F.B. McCormick, T.J. Cloonan, J.M. Sasian, R.L. Morrison, M.G. Beckman, S.L. Walker, M.J. Wojcik, S.J. Hinterlong, R.J. Crisci, R.A. Novotny, and H.S. Hinton, 1993 CLEO postdeadline session, (Optical Society of America, Washington, D.C.) paper CPD24, p. 48.
- [2] R.H. Yan, R.J. Simes, and L.A. Coldren, IEEE Phot. Tech. Lett. vol. 1, p. 272 (1989).
- [3] M. Whitehead, A. Rivers, G. Perry, J.S. Roberts, and C. Button, Elec. Lett. vol. 25, p. 984 (1989).
- [4] Chih-Hsiang Lin, K.W. Goossen, K. Sadra, and J.M. Meese, Appl. Phys. Lett., Sept., 1994.
- [5] L.A. D'Asaro, S.-S. Pei, J.M. Kuo, G. Livescu, R.E. Leibenguth, and P.-C. Chang, IEEE Summer Top. meeting Optoelectronic Materials Growth and Processing, July, 1994, p. 48.
- [6] Z. Karim, C. Kyriakakis, A.R. Tanguay, Jr., K. Hu, L. Chen, and A. Madhukar, Appl. Phys. Lett. 64, 2913 (1994).

Compensation of Thickness Variations in a Fabry-Perot Modulator Array using a Self Tuned Fabry-Perot Structure

Phil Harvey and Sadik Esener

University of California, San Diego
Department of Electrical Engineering,
La Jolla, Ca 92093-0407
(619) 534-8155

1.0 Introduction

Many optical modulators achieve improved performance when used in a Fabry-Perot (FP) configuration^[1-3]. This is due to the increased interaction of the light with the modulator active material. A conventional FP modulator consists of an active layer (electrooptic, electroabsorptive, or optically active material) acting as a cavity sandwiched between two dielectric or metal mirrors. To increase the interaction in the cavity, higher reflectance mirrors are required resulting in higher finesse cavities^[4]. However, as the finesse increases, the cavity thickness tolerance decreases. This proves to be a serious practical limitation when building large size and/or large arrays of FP modulators (e.g. wafer size). Only when fabrication techniques that create materials one monolayer at a time are used does it become possible to build uniform FP modulator arrays.

We propose another solution to the cavity thickness tolerance problem by replacing the input mirror with a holographic mirror, resulting in what we refer to as a Self Tuned Fabry-Perot cavity (STFP). In the recording of the holographic mirror, thickness nonuniformities of the FP cavity (including those from the electrooptic film and the substrate, if any), are automatically compensated. Also, by applying a voltage to the electrooptic material during recording, one can create a Normally-Off or a Normally-On state modulator.

2.0 Principle of Operation

An example of a modulator array having nonuniform EO film thicknesses is shown in Figure 3-1. We will analyze the optical transmission of the modulators assuming they have first a fixed Bragg reflector input mirror, and then a holographic mirror.

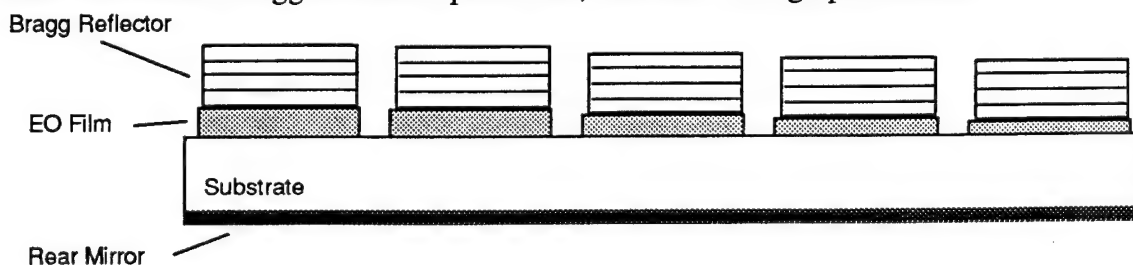


Figure 3-1 Example of a nonuniformly thick Fabry-Perot modulator array.

Fixed Bragg Reflector

Assuming all the modulators in the array have the same fixed phase ϕ_f , we can write the refractive index profile in the holographic layer as

$$n_{hol} = n_0 + n_1 \cos(Kz + \phi_f) \quad (3-1)$$

where n_0 is the average index, n_1 is the index modulation, $K=2\pi/\Lambda$ is the grating vector magnitude, and z is measured from the front surface of the hologram. Assuming a lossless rear reflector having a reflectivity of R_m , the transmission of each modulator can be expressed as

$$T = \frac{(1 - R_m)(1 - \eta)}{(1 - \sqrt{R_m \eta})^2 + 4\sqrt{R_m \eta} \sin^2 \left(k_{eo}(V) D + k_{hol} L + \left(\frac{\phi_f - \pi/2}{2} \right) \right)} \quad (3-2)$$

where η is the diffraction efficiency of the holographic mirror, $k_{eo}(V)=2\pi n_{eo}(V)/\lambda$ is the propagation constant through the EO film, $n_{eo}(V)$ is the EO film refractive index and is a function of the applied voltage V , D is the EO film thickness, $k_{hol}=2\pi n_{hol}/\lambda$ is the hologram's propagation constant, and L is the hologram thickness. The transmission is plotted in Figure 3-2 as a function of D with $\lambda=514\text{nm}$, $n_{eo}=n_{hol}=2.5$, $L=1.028\text{mm}$, $\phi_f=\pi/2$, and $R=\eta=R_m$.

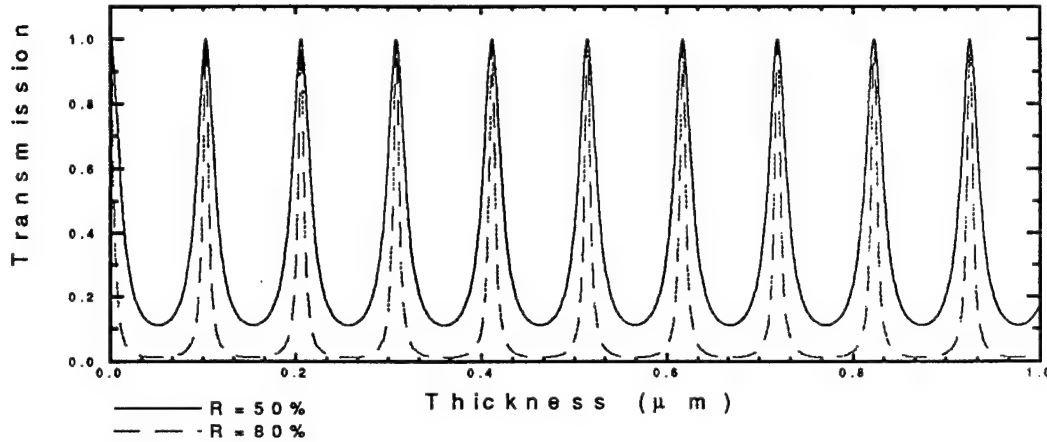


Figure 3-2 Transmission of a FP modulator with a fixed phase reflector as a function of EO thickness

Notice that the transmission is sensitive to EO thickness changes on the order of a few nanometers.

Recording a Holographic Bragg Reflector

To record the hologram, single beam illumination is used and due to the reflection off the rear mirror of the modulator, a sinusoidal interference pattern is created in the hologram. The spatial phase of the interference pattern in the hologram is

$$\phi_{ill} = -2(k_{eo}(V_{exp}) D + k_{hol} L) \quad (3-3)$$

where V_{exp} is the voltage that is applied to the EO film during exposure. This allows a phase bias to be recorded in the hologram. The recorded hologram will be a sinusoidal index modulation that may be shifted in phase to the illumination interference pattern, as is

the case in diffusion and trap-saturated photorefractive crystals. This results in a Bragg reflector having a spatial phase of $\phi_{\text{ill}} + \phi_{\text{hol}} = -2(k_{\text{eo}}(V_{\text{exp}})D + k_{\text{hol}}L) + \phi_{\text{hol}}$, where ϕ_{hol} is phase shift of the hologram. Plugging this Bragg reflector phase in for ϕ_f and setting $V=V_{\text{exp}}$ in Equation 3-2, we get

$$T = \frac{(1 - R_m)(1 - \eta)}{(1 - \sqrt{R_m \eta})^2 + 4\sqrt{R_m \eta} \sin^2\left(\frac{\phi_{\text{hol}} - \pi/2}{2}\right)} \quad (3-4)$$

Notice that the transmission is independent of the EO film thickness. For pure phase shifted holograms ($\phi_{\text{hol}}=\pi/2$), the transmission is 1, while for pure unshifted holograms ($\phi_{\text{hol}}=0$), the transmission is minimized.

Modulator Operation with the Recorded Compensation Holograms

The recorded hologram will have a fixed spatial phase $\phi_f = \phi_{\text{ill}} + \phi_{\text{hol}}$, provided that either it is chemically fixed or a low intensity optical beam is used which does not erase the hologram during operation. Equation 3-2 describes the transmission of the modulators as a function of the applied voltage V . For example, consider a quadratic transverse EO film having a refractive index $n_{\text{eo}}(V) = n + \frac{1}{2} n_{\text{eo}}^3 s_{12} \frac{V^2}{d^2}$, where s_{12} is a transverse EO coefficient, and d is the electrode spacing, then the transmission of the modulator is

$$T = \frac{(1 - R_m)(1 - \eta)}{(1 - \sqrt{R_m \eta})^2 + 4\sqrt{R_m \eta} \sin^2\left(\frac{\pi n_{\text{eo}}^3 s_{12} (V^2 - V_{\text{exp}}^2) D}{\lambda d^2} + \frac{\phi_{\text{hol}} - \pi/2}{2}\right)} \quad (3-5)$$

Now the EO film thickness, D , appears solely in the EO term in Equation 3-5. Figure 3-3 shows the transmission modulation (defined as the difference between the transmission at the voltage V and the transmission at zero volts) as a function of EO film thickness for an uncompensated FP modulator and a STFP modulator. The cavity parameters that we used were $R_m=\eta=80\%$, $n_{\text{eo}}=2.5$, $s_{12}=1.8 \times 10^{-16} \mu\text{m}/\text{V}$, $V_{\text{exp}}=0$, $d=40 \mu\text{m}$, $\lambda=514 \text{nm}$ and $\phi_{\text{hol}}=\pi/2$. As expected, the STFP transmission modulation is a slowly varying function, whereas it varies widely for the uncompensated structure. Thus, thickness variations of more than 10% can be tolerated using a STFP configuration. The reason that the transmission modulation is not constant for both configurations is because the interaction length in the active region is proportional to the thickness of the film.

The STFP parameters $V_{\text{exp}}=0$ and $\phi_{\text{hol}}=\pi/2$ yield, according to Equation 3-4, a transmission of 1 at $V=0$. However, this is not the optimal biasing point for transmission modulation, as is evident in Figure 3-3 for very low thicknesses. The optimal bias point can be achieved by (1) using photorefractive crystals and a moving grating recording^[5], or by applying a voltage to the EO film during recording.

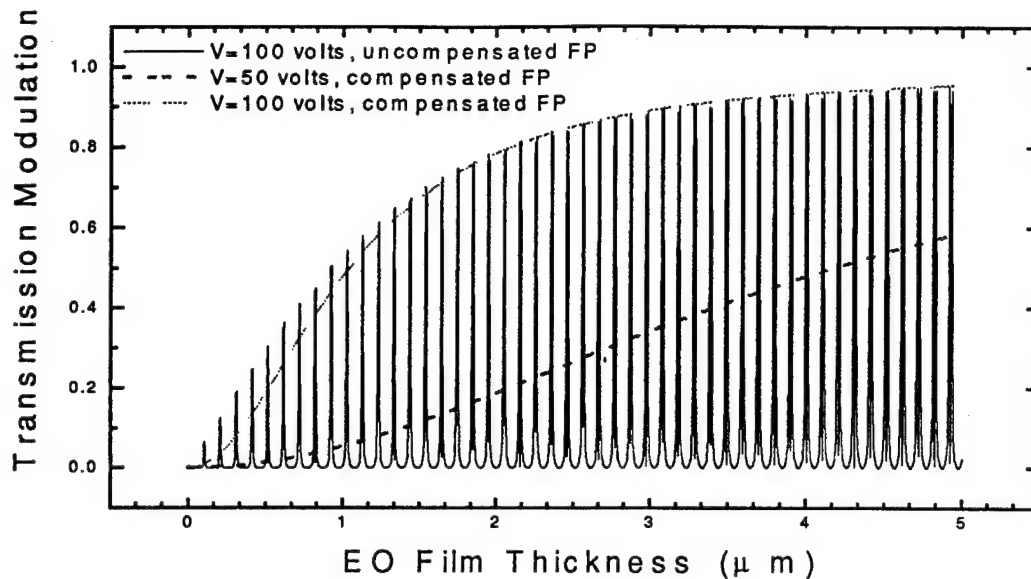


Figure 3-3 Transmission Modulation as a function of EO film thickness.

3.0 Experimental Proof-of-Concept

We have demonstrated the STFP concept using a highly nonuniform, 2 mm thick window glass cavity having an aluminum mirror on one side and a holographic mirror on the other. Only half of the glass plate had the mirrors, the other half was left bare to show the nonuniformity of the plate. The holographic material used was Dupont's HRF 352-25 photopolymer. After the polymer sheet was applied to the glass, it was exposed at normal incidence with a collimated 514 nm argon laser. Processing of the polymer consists of a short UV exposure and then a low temperature bake ($\sim 100^{\circ}\text{C}$).

The compensation effect was illustrated by comparing the normal incidence backreflections of the bare half to the mirrored half. The large thickness variations in the bare glass resulted in approximately 100 observable FP fringes within a 1" diameter backreflected beam. The mirrored part had less than 10 fringes. Ideally the mirrored part should have a uniform intensity, as predicted by Equation 3-4; however, the organic photopolymer experiences nonuniform distortions during post-processing, which results in a volume index modulation that is not identical to the exposure interference pattern. We are currently working on using photorefractive crystals as the holographic mirror, because they offer faithful recording of the intensity pattern.

4.0 References

1. D. R. Yankelevich, R. A. Hill, A. Knoesen, M. A. Mortazavi, H. N. Yoon and S. T. Kowel, *IEEE Photon. Technol. Lett.*, vol. 6, no. 3, pp. 386-389 (1994)
2. E. I. Gordon and J. D. Rigden, *Bell Syst. Tech. J.*, pp. 115-179 (1963)
3. R. H. Yan, R. J. Simes and L. A. Coldren, *IEEE Photon. Technol. Lett.*, vol. 2, no. 2, pp. 113-114 (1990)
4. J. M. Vaughan, *The Fabry-Perot Interferometer*, IOP Publishing Ltd., Bristol, England, pp. 89-134 (1989)
5. P. Yeh, *Introduction to Photorefractive Nonlinear Optics*, John Wiley & Sons, New York, p. 135 (1993)

Polarization Rotation Modulator in a Strained [110]-Oriented Multiple Quantum Well

D.S. McCallum, X.R. Huang, and Arthur L. Smirl

Laboratory for Photonics and Quantum Electronics, 100 IATL, University of Iowa, Iowa City, IA 52242
Tel.: 319 335 3461; Fax.: 319 335 3462

D. Sun and E. Towe

Department of Electrical Engineering, University of Virginia, Charlottesville, VA 22903
Tel.: 804 924 3960; Fax.: 804 924 8818

Optical modulators with a high contrast ratio are desirable for use in optical information processing applications. Devices based on semiconductor multiple quantum wells are of particular interest because of the possibility of combining modulators with detectors and electronic components on a single substrate to make high-speed smart-pixel arrays. However, it is difficult to obtain large contrast ratios in conventional MQW modulators, which function by using the quantum confined Stark effect to modify the absorption coefficient of the MQW. For example, a typical p-i(MQW)-n modulator has a contrast ratio of 3:1 to 5:1, although contrast ratios as high as 10:1 have been obtained. Fabry-Perot cavities have been used to increase the contrast ratio to 100:1, but at the expense of optical bandwidth.

Polarization rotation modulators offer the possibility of boosting the contrast ratio without significantly reducing the optical bandwidth.¹ Here, we present the first measurements of the nonlinear response of biaxially strained [110]-oriented quantum wells, and we show that the intrinsic optical anisotropy^{2,4} can be exploited to make a polarization rotation modulator (or switch) using as few as 50 wells that has a 25:1 contrast ratio while operating at room temperature. Our geometry is similar to, and our device performance is comparable to, that described in Ref. 1; however, in contrast to the structure described in Ref. 1, the MQW used here requires no post-growth processing. Moreover, by increasing the number of wells, it should be easily possible to increase the room-temperature contrast ratio to between 100:1 and 200:1.

Unstrained [110]-oriented QWs have an intrinsic anisotropy that is associated with the reduced symmetry of QWs grown on (110) surfaces compared with those on grown on (100) and (111) surfaces.² The optical anisotropy of unstrained [110]-oriented QWs (i.e., the difference between optical transition strengths for light polarized along the $[\bar{1}10]$ and $[001]$ directions) is approximately 8 %, but the anisotropy of an as-grown structure can be drastically increased by incorporating a biaxial tensile strain in the plane of the QWs.³ The origin of the anisotropy resides in the composition of the light-hole and heavy-hole states.^{2,3} More specifically, for $[100]$ and $[111]$ -oriented QWs, the light-hole and heavy-hole states are pure eigenstates of angular momentum, which correspond to the angular momentum eigenvalues $J_z = \pm 3/2$ or $J_z = \pm 1/2$, where z is the growth direction. By comparison, in $[110]$ -oriented QWs, the light-hole and heavy-hole states are mixtures of $J_z = \pm 3/2$ and $J_z = \pm 1/2$ components. As the strain is increased, the ratio of $J_z = \pm 3/2$ to $J_z = \pm 1/2$ contributions in each of the hole states changes, which changes the optical matrix elements for light polarized in the $[\bar{1}10]$ and $[001]$ directions, and thereby increases the anisotropy.

The structure which we studied was a p-i(MQW)-n diode grown on a semi-insulating substrate which was oriented 6° away from the $[110]$ direction towards the $[111]B$ direction.⁴ (The tilt towards the $[111]B$ direction was necessary to achieve good surface morphology.) A $1\text{ }\mu\text{m}$ thick n^+ GaAs buffer layer was grown on the substrate, and was followed by a 100 nm thick n type GaAs layer. The intrinsic region contained 50 periods of 6 nm wide $\text{In}_{0.13}\text{Ga}_{0.87}\text{As}$ quantum wells separated by 8 nm wide GaAs barriers. The structure was completed with a 100 nm thick p type GaAs cap layer. Although the sample had been processed into mesas with electrical contacts, these were not used in our studies and the diodes were left open-circuit. The anisotropy of the MQW was demonstrated by measuring the absorption coefficients for light polarized along the $[\bar{1}10]$ direction and the $[001]$ direction. The results are shown in Fig. 1. This

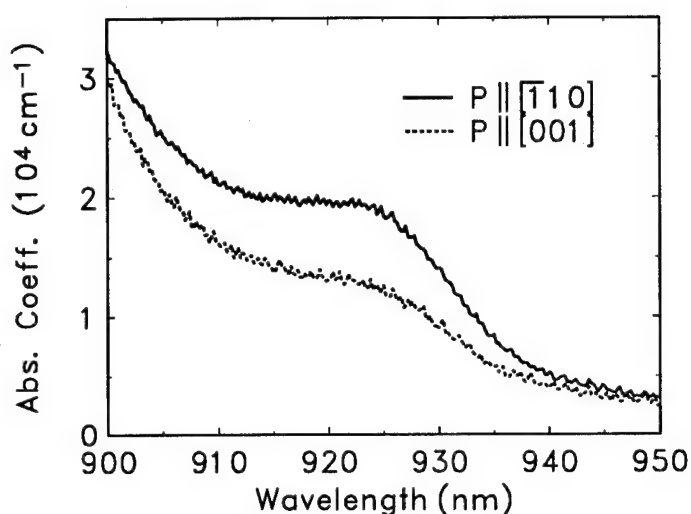


Fig. 1 Absorption spectra of [110]-oriented MQW for light polarized along the $[110]$ and $[001]$ directions.

the “off” state (and hence maximum contrast ratio) was obtained by adjusting the quarter wave plate and analyzer to minimize throughput in the absence of the pump. The quarter wave plate is necessary in this case because the anisotropy in the absorption coefficient is associated with an anisotropy in the refractive index which results in elliptically polarized light after the MQW.

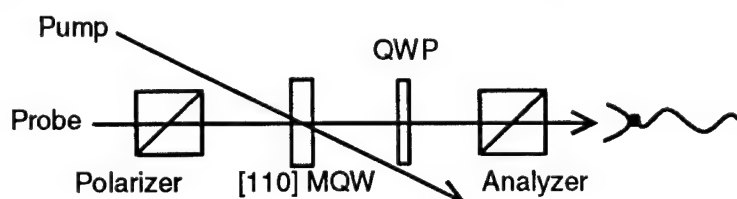


Fig. 2 Polarization rotation modulator using [110] MQW.

We demonstrated modulator operation and measured the contrast ratio. The pump and probe beams were generated by two independently tunable, synchronized, cavity-dumped, modelocked ps dye lasers, both of which generated pulses of approximately 2 ps duration. The lasers were operated at a repetition rate of 500 kHz. In the absence of the pump, the angle by which the probe was rotated upon passage through the sample was measured at a wavelength of 924 nm. The angle of rotation was measured to be 2.5° , which is in good agreement with the 2.8° predicted from the measured anisotropy in the absorption coefficients. The pump laser was set at 900 nm, approximately 25 nm to the blue of the excitonic line center. During modulator operation the probe pulse was set to arrive at the sample site approximately 30 ps after the pump. This delay was selected because a time-resolved differential transmission measurement showed that the maximum absorption coefficient change was obtained at this time, and hence the modulator would achieve its maximum transmission. To assess the effect of all previous pump pulses, differential transmission measurements were also made with the probe set to arrive in the MQW 50 ps before the pump. No significant transmission change was measured, indicating that the MQW had completely recovered between pulses. The transmission of the modulator in the presence of the pump is plotted as a function of wavelength in Fig. 3 (filled circles), as is the corresponding contrast ratio (triangles). Note that the plot of contrast ratio against wavelength has a peak which is significantly

measurement, in common with all the others described here, was performed at room temperature. The peak difference in absorption coefficients, $\Delta\alpha$, for orthogonal polarizations is $6.6 \times 10^3 \text{ cm}^{-1}$ near excitonic line center.

We built a polarization rotation modulator which has a similar principle of operation to that described previously.¹ The modulator consisted of the [110]-oriented MQW structure and a quarter wave plate between a polarizer and analyzer, as shown in Fig. 2. The MQW was positioned at the intersection of pump and probe beams with the probe polarization aligned at 45° to the MQW $[110]$ and $[001]$ directions. Minimum transmission in the “off” state (and hence maximum contrast ratio) was obtained by adjusting the quarter wave plate and analyzer to minimize throughput in the absence of the pump. The quarter wave plate is necessary in this case because the anisotropy in the absorption coefficient is associated with an anisotropy in the refractive index which results in elliptically polarized light after the MQW. Under pump illumination, photogenerated carriers partially bleach the exciton, which changes the polarization state of the light transmitted through the MQW, hence greatly increasing the fraction of probe light incident on the detector. The contrast ratio of the modulator is defined as the ratio of the transmitted probe fluence in the presence of the pump to that in the absence of the pump.

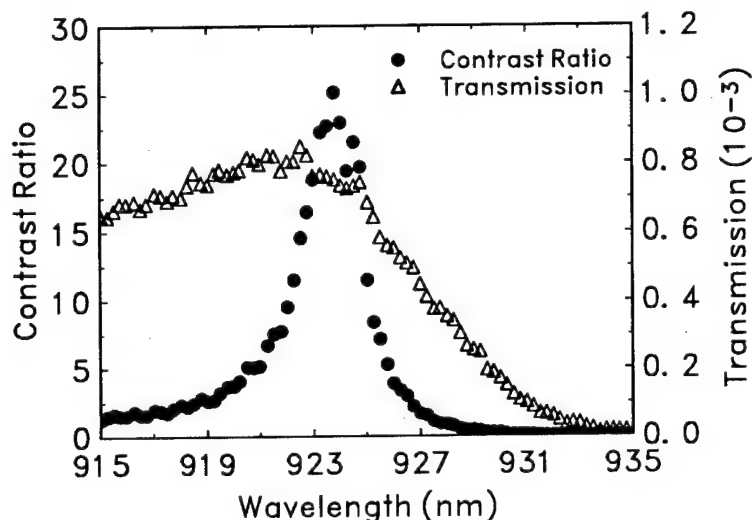


Fig. 3 Contrast ratio (filled circles) and transmission (triangles) as a function of wavelength for the [110]-oriented polarization rotation modulator.

however, is that it required a number of processing steps before the anisotropy could be obtained. Namely, a thin film containing the MQW was etched from the surface of the substrate and bonded to a piece of LiTaO₃. (The lift-off step was necessary because the GaAs substrate is opaque to the QW optical transitions.) The LiTaO₃ had been specially cut so that its expansion coefficient in one direction matched that of GaAs, but was ~ 3 times larger in the orthogonal direction. A uniaxial in-plane strain, and hence an anisotropy of the excitonic absorption, was produced by changing the temperature of the LiTaO₃ and GaAs/AlGaAs film. We emphasize that one of advantage of the approach reported here is that no post growth processing is required.

The peak contrast ratio obtained here is 25:1, compared to 330:1 reported in Ref. 1. It should be noted, however, that our sample contains only 50 QWs, compared to the 100 QWs in the previous result. Also, our measurements were made at 300 K, whereas the previous measurements were made at 200 K. As the temperature is reduced, the peak absorption coefficient of the MQW increases, which causes a larger absolute anisotropy of the absorption coefficients ($\Delta\alpha \approx 9.6 \times 10^3 \text{ cm}^{-1}$),¹ and hence a larger polarization rotation. For small probe transmissions, the contrast ratio is expected to increase quadratically with sample length and also with the anisotropy of the absorption coefficient.¹ Consequently, when compared on a per unit length basis at the same temperature, the biaxially strained [110]-oriented MQW modulator performs as well as the [100]-oriented modulator reported previously and also has the advantage of much simpler fabrication.

References

1. H. Shen, M. Wraback, J. Pamulapati, M. Dutta, P.G. Newman, A. Ballato, and Y. Lu, Appl. Phys. Lett. **62**, 2908 (1993).
2. Y. Kajikawa, M. Hata, T. Isu, and Y. Katayama, Surf. Sci. **267**, 501 (1992).
3. Y. Kajikawa and M. Hata, Superlattices and Microstructures **12**, 355 (1992).
4. D. Sun, E. Towe, M.J. Hayduk, and R.K. Boncek, Appl. Phys. Lett. **63**, 2881 (1993).

narrower than the plot of transmission against wavelength. This is caused by the narrow transmission bandpass of the quarter wave plate and analyzer combination.

A polarization rotation modulator with impressive performance has been previously demonstrated.¹ The anisotropy in the previous device was obtained simply and elegantly by externally applying a uniaxial in-plane strain to an otherwise optically isotropic [100]-oriented GaAs/AlGaAs MQW. The applied strain reduced the symmetry of the MQW, which resulted in different oscillator strengths for the excitonic absorptions experienced by normally-incident light polarized parallel to and perpendicular to the strain direction. One difficulty with this approach,

Tuesday, March 14, 1995

SLM Applications

LTuB 10:30 am-12:15 pm
Red Lion East

J. P. Huignard, *Presider*
Thomson CSF-LCR, France

Opto-electronic Hybrid System for Rapid Prototyping of Paraxial Diffractive Elements

Harald Aagedal, Thomas Beth, Frank Reichel*, Heiko Schwarzer, and Stephan Teiwes

Institute of Algorithms and Cognitive Systems, Department of Computer Science,
University of Karlsruhe, Am Fasanengarten 5, D-76128 Karlsruhe, Germany
Phone: ++49 721 9640013, Fax: ++49 721 696893

*) Jenoptik Technologie GmbH, Carl-Zeiss-Straße 1, D-07739 Jena, Germany
Phone: ++49 3641 65 3156, Fax: ++49 3641 65 3666

1 Introduction

Progress in developing and applying a young technology like diffractive optics for scientific or industrial purposes can be better supported by closely linking theory and practice. It is very helpful to validate theoretical reflections quickly by computer simulations and optical tests. However, to our knowledge, there does not yet exist a software system offering enough flexibility and comfortable handling to do extensive simulation experiments in diffractive optics. Such a system would help to concentrate on solving a given problem like the design of a diffractive element (DE) with a specific function.

Computer simulations are very useful for validating the functionality of a DE. Noise effects can be considered according to theoretical models but, very often, perturbing effects in an optical arrangement are difficult to predict. Perturbing effects have consequences on the quality of the optical function of a DE and may for instance be caused by disalignment of optical components, dust particles, optical unpreciseness of components and illumination wave. Hence, also the practical experiment is required to make reliable statements about the properties of a DE in an optical arrangement. Both aspects, computer-aided development

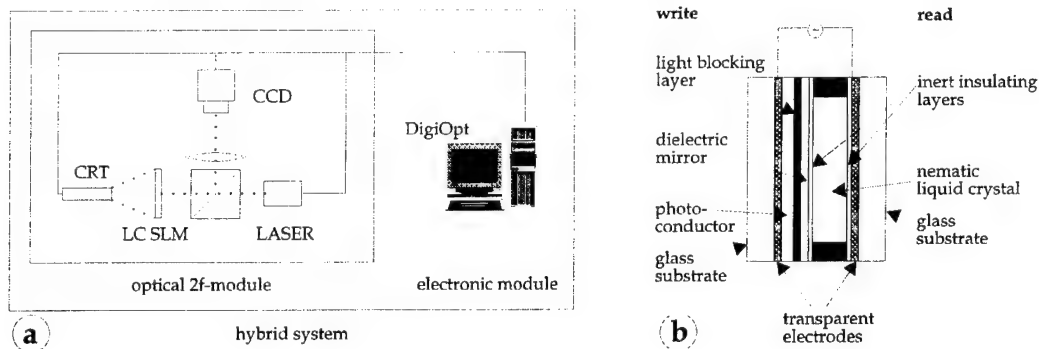


Figure 1: Architecture of opto-electronic hybrid system (a), Cross section of a liquid-crystal SLM (b).

and test of DEs with optical implementation facilities can be combined by an opto-electronical hybrid system consisting of an optical and an electronic module, as shown in Fig. 1(a). The electronic module basically consists of a computer which is a platform to run a software system for DE design, simulation of wave propagation or modulation processes, and the control of active components such as spatial light modulators (SLMs), mechanical adjustment components, or charge-coupled devices (CCDs). The function of the optical module is controlled by a computer addressing SLMs with certain DE distributions.

Unfortunately, the functionality of an optical system is strongly restricted by the arrangement and physical limitations of optical components. The functionality can principally be changed by rearranging the optical components, but this needs too much time and is therefore unacceptable to be realized in the optical module. For real-time applications the optical setup has to be a static one based on SLMs, where the functionality can be changed by "programming" them. The physical implementation of such systems causes problems since current SLMs are still in prototype stage. Their characteristics are influenced by many parameters

which are difficult to control simultaneously. Hence, it is sensible to reduce problems by choosing a simple optical arrangement for a hybrid system. We propose the use of a $2f$ - or $4f$ -setup with a SLM in the Fourier plane to do paraxial real-time experiments. The $2f$ -setup realizing an optical Fourier transform is a suitable system for examining the optical function of a DE by recording and checking the modulus of the impulse response.

Typical problem classes which can be treated by hybrid systems with optical $2f$ - or $4f$ -modules are optical free-space communications, beam shaping, pattern generation, and signal classification [1, 2, 3]. It is of fundamental interest how many and which functions can be implemented with that setup by programming the SLM.

In this paper, we present concepts and implementations for the optical as well as the electronic module of a hybrid system for rapid prototyping of paraxial DEs. First steps to connect a software system to a SLM-based $2f$ -system for DE design processes have been made. Experiences with that system are described by giving examples for design and test of different DE types.

2 Electronic module

The electronic module is a computer running the software system DigiOpt [4] being developed at the Institute of Algorithms and Cognitive Systems. DigiOpt is a prototype system for computer-aided design and test of paraxial diffractive optics. It provides the user with a large set of elementary operations for signal processing, wave propagation, and design of DEs in the paraxial domain. The essential concept is to perform a huge range of experiments by simply concatenating these elementary operations and looking at the results. There are also facilities to build complex operations from elementary ones by the aid of a system specific programming language.

DigiOpt is not only a tool for the design of paraxial DEs, it can also be interfaced to physical devices of an optical setup such as SLMs or CCDs. In this context, DigiOpt serves as a programming platform of the hybrid system. The optical function of the hybrid system can be changed with time by writing different DE distributions onto the SLM. Depending on the application, these distributions are pre-computed and stored in a data base or they can be generated in real-time. The programming language of DigiOpt is also a helpful tool to write programs for the hybrid system. In that case, the DE distributions are displayed on the screen as well as onto the SLM. The system output of the optical module is recorded by a CCD sending the data back to the computer for post-processing. This could be performed again on the DigiOpt system but also by other systems, e.g., artificial neural networks for signal classification.

Current SLMs are restricted to specified modulation domains. Normally, they are either amplitude- or phase-only modulating elements. In fact, optical DEs are generally defined by complex distributions which at first do not seem to be realizable by SLMs restricted to some modulation domain. Fortunately, modern coding techniques of diffractive optics [5] help to overcome that problem. The DigiOpt system offers direct and iterative operators to encode DEs with restriction to almost any modulation domain.

The DE design on the DigiOpt system can be performed according to formalized design principles. As an example, multifacet elements implementing point transforms can be exactly specified by a permutation assigning a certain location in the Fourier plane to each point in the input plane. Further specification parameters like element size, facet size, and modulation domain have to be considered in the design process. As an example, the design and test of a multifacet element are given in Fig. 3(a).

3 Optical module

The main item of the optical module is a SLM which can be used to cause diffraction effects. We apply a phase modulating nematic liquid-crystal SLM (LC SLM) developed and fabricated at Jenoptik Technologie GmbH. This SLM is installed in the input plane of a $2f$ -setup and can be optically addressed by means of a cathode ray tube (CRT), as depicted in Fig. 1(a).

The cross section of a nematic LC SLM is shown in Fig. 1(b). A LC SLM consists of several layers, where a monocrystalline silicon and a nematic LC layer play the most important roles. When voltage is applied, the silicon layer behaves as photosensitive material influencing the LC voltage. Thus, the index of refraction in the LC layer can be controlled by an exposure intensity distribution. The LC is a birefringent medium

characterized by large variations of the index of refraction if linearly polarized light of wavelength $\lambda_{\text{out}} = 550\text{nm}$ (green laser light) is used for *read out* (see Fig. 1(b)). These index variations cause a phase modulation on incoming illumination waves and can be used to achieve diffraction effects. A suitable wavelength for illumination of the silicon layer on the *write side* is $\lambda_{\text{in}} = 625\text{nm}$. This layer and the LC layer on the *read side* are separated by a multi-layer dielectric mirror reflecting the read light beam. Essential parameters

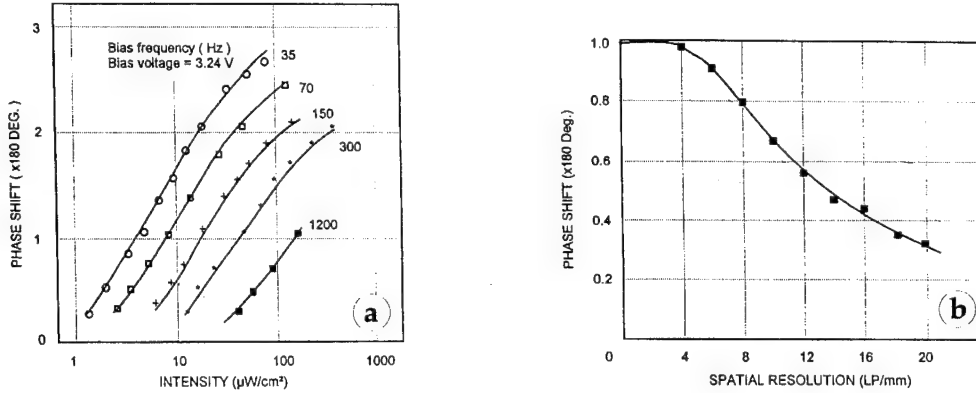


Figure 2: Influence of exposure intensity (a) and spatial resolution (b) on phase shift of LC SLM.

influencing the index of refraction are spectral sensitivity, spatial resolution, optical quality, thermal stability, and switching time. In order to build an efficient optical module, it is important to have full control on the phase shifts occurring in the LC layer. The maximal realizable phase shift is in particular a function of the exposure intensity on the write side and the spatial resolution of the structures projected onto the silicon layer. This is documented in Fig. 2. On the left, the phase dependence on the intensity for a fixed SLM operation voltage at various frequencies is sketched. Obviously, large phase shifts can only be generated by high exposure intensities together with low operation frequencies. However, this limits the switching time, i.e., the optical response time to an exposure pulse, of the SLM.

Fig. 2(b) illustrates that the phase shift decreases with higher spatial frequencies of grating structures projected onto the write side of the SLM. The limiting resolution capability is about 35 lines per millimeter. Also the temperature may have a significant influence on the phase if temperatures are lower than -20°C .

The phase shift caused by the LC SLM depends on many parameters which are not easy to control at the same time. However, phase shifts from 0 to 2π are needed to implement optical DE functions with a phase modulating SLM. If the maximal realizable phase is lower than 2π , unwanted effects arise. First of all, the diffraction efficiency decreases drastically. The reason is that a phase distribution with phase values $0 \leq \varphi < 2\pi$ always has a bias part leading to a dc-peak in the center of its Fourier transform. Secondly, the more the real part of the phase signal becomes dominant compared to the imaginary part, the more the effect of having a twin image in the Fourier transform grows. This effect is well-known from diffractive amplitude elements in *digital holography* [5].

4 Connection of optical and electronic module

In the $2f$ -module, shown in Fig. 1(a), the LC SLM is optically addressed by the DigiOpt system via a CRT. This offers the possibility to change the DE function in real-time. The module output is recorded by a CCD camera and captured by the DigiOpt system for further processing.

In order to drive the LC SLM correctly as pure phase modulator, it is important to realize phase shifts from 0 to 2π . Unfortunately, in our experiments, it turned out that the CRT does not offer enough light intensity to constrain the SLM to such phase shifts. As a result, a strong dc-term and a twin image appeared in the output plane of the $2f$ -setup leading to low diffraction efficiencies.

In our experiments, we designed DEs reconstructing a specified signal off-axis in order to avoid an overlap with dc-peak and twin image. Fig. 3 documents the results of optical tests performed on a LC SLM. In

Fig. 3(a), a 5×5 multifacet element which mirrors an incoming point image at the vertical axis, is shown. For the input distribution (b), the system output is obtained by computer simulation (c) and optically (d). In (e), a non-periodic DE for speckle-free signal generation is depicted, with the corresponding impulse response of the SLM in (f). Finally, we used a $4f$ -setup to show the applicability of LC SLMs for signal analysis purposes. A cosine-modulated Mexican-hat bandpass filter (g) is applied to an input image, containing the letter "P", for edge detection. The output of the optical $4f$ -module is shown in (h). These experiments

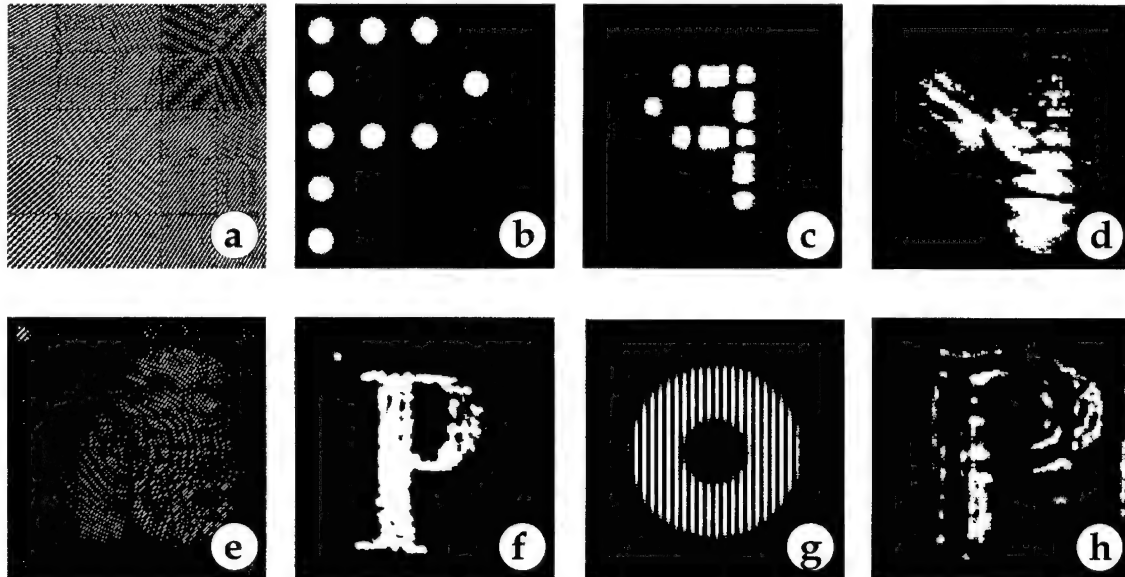


Figure 3: Implementation of different DEs on LC SLM. (a) multifacet DE, (e) non-periodic DE, and (g) Mexican-hat filter with system responses in (d), (f), and (h), respectively.

represent our first steps to build a computer-controlled hybrid system for paraxial DE design with optical real-time tests. Essential aspects which have to be tackled are the realization of 2π phase shifts with the LC SLM and the development of methods for automated alignment of optical components.

References

- [1] T. H. Barnes, T. Eiju, K. Matsuda, H. Ichikawa, M. R. Taghizadeh, and J. Turunen, "Reconfigurable free-space optical interconnections with a phase-only liquid-crystal spatial light modulator," *Appl. Opt.* **31**, 5527-5535 (1992).
- [2] J. Rosen, L. Shiv, J. Stein, and J. Shamir, "Electro-optic hologram generation on spatial light modulators," *J. Opt. Soc. Am. A* **7**, 1159-1166 (1992).
- [3] F. Reichel and W. Löffler, "Optical space frequency analysis for real-time pattern recognition," *Int. J. Optoelectronics* **9**, 99-109 (1994).
- [4] H. Aagedal, T. Beth, H. Schwarzer, and S. Teiwes, "Modern concepts for computer-aided design in diffractive optics," in *Proceedings of the International Optical Design Conference*, (OSA, Washington, DC, 1994), G. W. Forbes, ed. to be published.
- [5] F. Wyrowski, "Digital holography as part in diffractive optics," *Rep. Prog. Phys.* **54**, 1481-1571 (1991).

Speckle-free Signal Reconstruction with Non-periodic Diffractive Elements on Liquid-crystal SLM

Stephan Teiwes, Heiko Schwarzer, Harald Aagedal, Michael Schmid,
Thomas Beth, Frank Reichel*, and Frank Wyrowski**

Institute of Algorithms and Cognitive Systems, Department of Computer Science,
University of Karlsruhe, Am Fasanengarten 5, D-76128 Karlsruhe, Germany
Phone: ++49 721 9640013, Fax: ++49 721 696893

*) Jenoptik Technologie GmbH, Carl-Zeiss-Straße 1, D-07739 Jena, Germany
Phone: ++49 3641 65 3156, Fax: ++49 3641 65 3666

**) Berlin Institute of Optics, Rudower Chaussee 5, D-12484 Berlin, Germany
Phone: ++49 30 6392 3470, Fax: ++49 30 6392 3452

1 Introduction

The methods to generate intensity signals using diffractive elements bear importance for optical signal processing and printing applications. In principle, the diffractive element (DE) can be viewed as optical memory carrying encoded information about a signal wave $s(x)$, $x \in \mathbf{R}^2$, which can be generated in a certain output plane by illuminating the DE with a specified wavefront. The capability to generate a certain signal wave, defined in a *signal window*, is called the *optical function* of a DE. On one hand, a DE can be implemented as a passive optical component with a fixed optical function. Modern spatial light modulator (SLM) technology on the other hand allows adaptive implementations, where a computer addresses the optical device. The advantage is that the optical function of the DE can be changed with time. For this reason SLMs have a key role in the design of programmable opto-electronic devices for signal generation and processing.

The capability of a SLM to realize specified optical functions is restricted by its various physical parameters such as size, resolution, transmission mode (amplitude-only, phase-only), or switching time. The current SLM technology does not allow production of low-cost devices with a large high-resolution modulation area. Common devices do not offer more than about 1000×1000 pixels on an area of one square inch. For this restriction to a very limited *space-bandwidth product* (SBP), it is sensible to realize a desired optical function by a non-periodic DE in order to exploit the whole SBP. The reconstruction of signal waves using non-

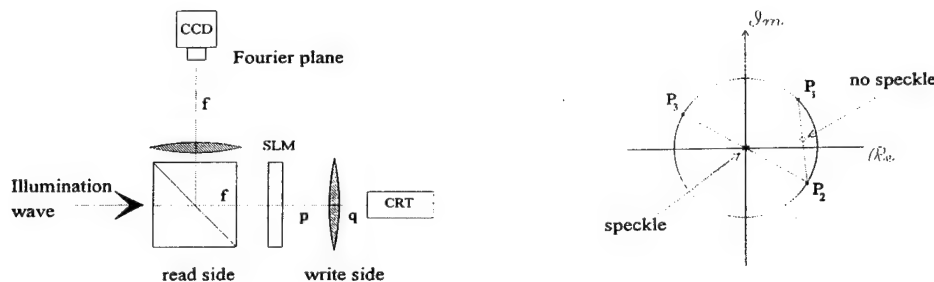


Figure 1: Optical 2f-Fourier setup with SLM for signal generation (left). Simple scheme for explaining interpolation between two phase-values in the complex plane (right).

periodic DEs usually suffers from *speckles*. The speckles can be identified as wavefront dislocations which are optical field locations with zero amplitude. In this paper, we present methods to design paraxial DEs overcoming the speckle problem. These elements can, for example, be implemented with a liquid-crystal SLM installed in the input plane of a 2f-Fourier setup as depicted in Fig. 1. A plane wave is assumed for DE illumination here, but other illumination wave could also be considered [1].

After briefly investigating the cause and effect of speckles, methods to find a smooth *band-limited* complex distribution carrying the information of a specified intensity signal, are presented. We describe an iterative algorithm to encode binary DEs generating a specified signal wave speckle-free in a signal window. The computer simulations and optical experiments with a liquid-crystal SLM are then presented validating the theoretical results.

2 Cause and effect of speckles

In many applications, only the intensity $|s(x)|^2$ of a signal wave is of interest. For the design process, $|s(x)|$ is assumed to be a band-limited signal amplitude represented by a two-dimensional field of discrete values sampled with Nyquist rate. This is due to the finite extent of the DE. The corresponding phase distribution $\arg(s(x))$ at first glance seems to be a parameter of freedom. If the phase is chosen to be constant, the (inverse) Fourier transform $S = \mathcal{F}^{-1}s$ can be encoded into a DE, but its diffraction properties are very bad. The reason is that the energy of $s(x)$ is concentrated around the origin in the Fourier plane resulting in badly-developed diffractive structures when designing a DE. To improve the diffraction efficiency, it is useful to spread the energy almost equally over the Fourier plane. This can be performed by introducing a diffusing phase distribution $\arg(s(x))$. Encoding of S then leads to a DE with well-developed diffractive structures.

An energy diffusion over the Fourier plane can be achieved by choosing $\arg(s(x))$ at random, but the impulse response of the corresponding DE contains a great amount of speckles, as shown in Fig. 2. This effect results from the fact that the random phase is not band-limited and behaves like a diffusor spreading the information of $|s(x)|$ over the whole Fourier plane ignoring the finite DE size. One could try to constrain a

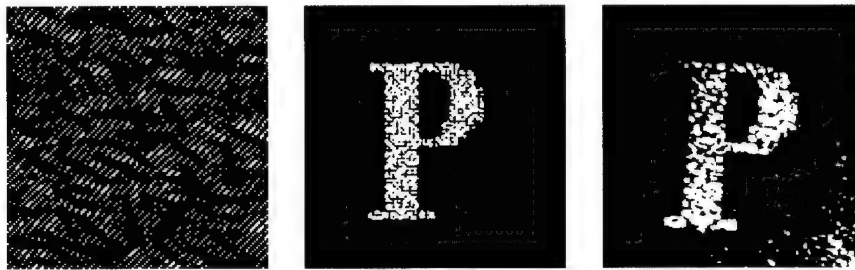


Figure 2: Binary diffractive element (left), computer simulated (center) and optical signal reconstruction intensities (right).

randomly chosen phase distribution to band-limitation by applying iterative techniques [2] and use this as the signal phase. In this case, encoding of the Fourier transform of $s(x)$ leads to a DE reconstructing the intensity distribution $|s(x)|^2$ with clearly less speckles. The reason for remaining speckles is well understood. Due to its random nature, the phase distribution contains consecutive sample points characterized by π -jumps, i.e., the phase values of samples differ by π . Let φ and $\varphi + \pi$ be the phase of two neighbour samples. Then a sinc-interpolation of the phase distribution leads to a zero crossing between the samples. A reasonable argument is given by Fig. 1(right). It represents two neighbouring samples by points on the circle of unity in the complex plane. If the phase difference between the two points is π , the origin representing zero amplitude, has to be crossed. The more the phase difference differs from π , the larger is the distance from the origin, which means that no zero crossing occurs.

Wyrowski states [2] that π -jumps in phase distributions can be eliminated by an iterative band-limitation if they are not caused by isolated point zeros [3]. In this case the iteration introduces soft topological phase deformations causing π -jumps to disappear after a few iterations. Compared to that, an isolated point zero is characterized by a particular phase distribution in its vicinity. Tracing the phase along a closed curve around the point zero leads to a 2π shift [3]. This situation cannot be changed by continuous phase deformations as caused by iterative methods. Consequently, the band-limited phase distributions can only be generated, if point zeros are strictly avoided. For our purpose, it is sufficient to realize a smooth distribution $\arg(s(x))$ containing no 2π -circle around any sampling point.

Methods to generate phase distributions without 2π -circles are described in [2, 4]. As an alternative, we propose the use of a spherical phase since it has natural band-limitation properties and no 2π -circles. Hence, a suitable phase distribution is given by $\varphi_{\text{sphere}}(x) = -\pi|x|^2/(\lambda f)$, where λ is the wavelength and f a focal length parameter which can be used to influence the band-limitation characteristic of the phase.

In general, the resulting signal $|s(x)|\exp(i\varphi(x))$ does not preserve the band-limitation previously defined for $|s(x)|$. To overcome this effect, iterative methods modifying phases successively in order to optimize band-limitation can be used. During the iteration process, the phase as a parameter of freedom may be changed in the signal domain to achieve band-limitation [2, 1]. The resulting complex distribution $s(x)$ will not have point zeros unless introduced by the starting phase $\varphi(x)$ for the iteration process. $s(x)$ will be used for the encoding process of diffractive Fourier elements.

3 Coding of binary diffractive elements

Given a band-limited complex distribution $s(x)$ carrying the signal information, a continuous diffractive amplitude element (DAE) can simply be defined by $G(u) = [\mathcal{N}\tilde{G}](u)$ with $\tilde{G}(u) = 2|S(u)|\cos(2\pi ux_0 - \Phi(u)) + B(u)$, $u \in \mathbb{R}^2$, where \mathcal{N} is a normalizing operator ensuring $\forall u : 0 \leq G(u) \leq 1$, $S = \mathcal{F}s$ is the Fourier transform of s , $\Phi = \arg(S(u))$, and $B(u)$ a suitably chosen function making \tilde{G} positive. However, these DAEs suffer from low diffraction efficiencies. Much better results can be achieved by using iterative coding techniques [6].

The iterative Fourier transform algorithm (IFTA) is a useful method to recover a Fourier transform pair $s(x)$ and $S(u)$ from partially known data on either or both functions [5]. The iteration moves back and forth between space (x) and frequency (u) domain to satisfy certain constraints on the distributions in both domains, respectively. These constraints are controlled by well-defined operators. Hence, the IFTA can basically be represented by the operator notation $s_{i+1} = \mathcal{X}\mathcal{F}\mathcal{U}\mathcal{F}^{-1}s_i$, where \mathcal{X} and \mathcal{U} represent operators to fulfil constraints in the x - and u -domain, respectively.

The iterative encoding of non-periodic DEs is identical to the problem of finding a Fourier pair s and S , where $|s(x)|^2$ is a given intensity signal and $S(u)$ is a (possibly quantized) amplitude-only or phase-only distribution. In an example, we want to design binary DAEs reconstructing the specified intensity signal without speckles.

In order to obtain a binary DE distribution, we have to introduce *amplitude freedom* in the x -domain. According to [6], $s(x)$ is defined in a window D at location x_0 and the corresponding conjugate signal $s^*(-x)$ in a window D^* at location $-x_0$, where x_0 is chosen to separate signal and conjugate from each other. As a result, we get a Hermitian distribution $\tilde{s}(x)$ which is characterized by a real-valued Fourier transform. The constraints introduced by an Operator \mathcal{X} in the x -domain are restricted to D and D^* . The amplitudes outside these windows are used as parameters of freedom. The operator \mathcal{X} is defined as

$$[\mathcal{X}\tilde{s}](x) = \begin{cases} \alpha|s(x)|\exp(\arg(\tilde{s}(x))) & : x \in D \\ \alpha|s(-x)|\exp(\arg(\tilde{s}(x))) & : x \in D^* \\ \tilde{s}(x) & : \text{otherwise} \end{cases}, \quad (1)$$

with the scaling factor α as given in [6]. After an inverse Fourier transform in the frequency domain, the concatenated operators $\mathcal{U} = \mathcal{U}_2\mathcal{U}_1$ are performed. The operator \mathcal{U}_1 ensures band-limitation and \mathcal{U}_2 binarizes $S(u)$ continuously.

$$[\mathcal{U}_1 S](u) = \begin{cases} S(u) & : x \in B \\ 0 & : \text{otherwise} \end{cases} \quad [\mathcal{U}_2 S](u) = \begin{cases} S(u)(1 - \gamma) + \gamma & : S(u) > 1 \\ S(u)(1 - \gamma) & : S(u) < 0 \\ \mathcal{Q}_2 S(u) & : \text{otherwise} \end{cases}. \quad (2)$$

The window B represents the DE area and γ is a parameter changing continuously with the number of iterations. It can be defined by $\gamma = i/n$, $i, n \in \mathbb{N}$, where i represents the number of the current iteration cycle and n the total number of iterations. The binary quantization operator \mathcal{Q}_2 is described in [6]. We emphasize on the importance of changing the coding operator \mathcal{U}_2 smoothly and continuously with the iteration cycles. Hard clip operators turn out to introduce isolated phase dislocations resulting in speckles again.

4 Experimental results

In Fig. 3(left) two DEs generated by the above coding method are shown. The IFTA start phase for the upper DE was chosen according to [4]. For comparison, we also performed a DE design with a spherical start phase, the result of which is depicted in Fig. 3 at lower left. The computer simulated signal reconstructions of both DEs are depicted in the middle column. Both DEs were implemented with an optically addressable liquid-crystal SLM in a $2f$ -setup, as sketched in Fig. 1. The binary DE distributions was projected directly onto the write side of the SLM by a cathode ray tube. The resulting diffraction patterns recorded by a CCD camera are given in the right column of Fig. 3. It turns out that slight disalignments in the optical setup lead again to speckle problems. Because of its smoothness, the spherical phase has a positive influence on the reconstruction quality of $s(x)$.

Acknowledgements: The authors would like to thank Miles J. Murdocca and Uma Y. Shama for their support.

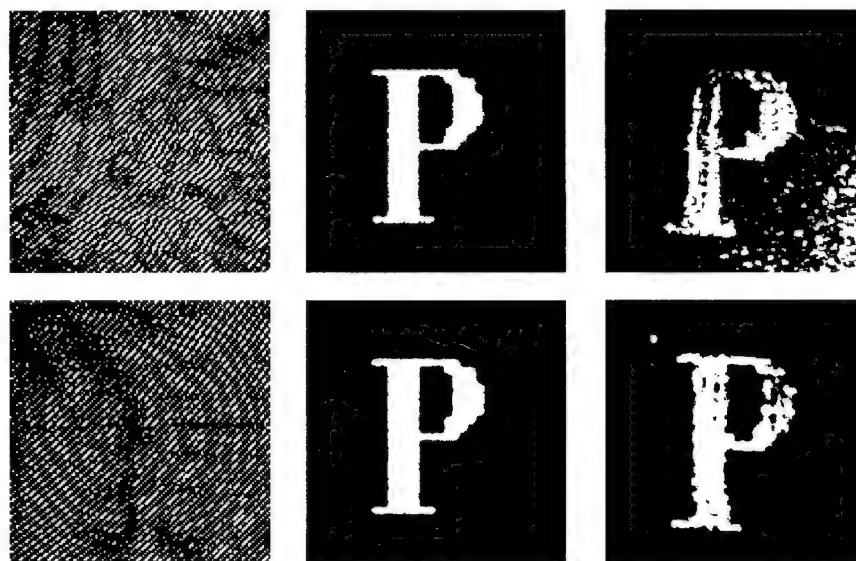


Figure 3: Binary DEs, intensities of computer simulated and optically reconstructed impulse responses.

References

- [1] H. Aagedal, T. Beth, S. Teiwes, and F. Wyrowski, "Design of non-periodic diffractive elements with respect to illumination wave," in *Technical Digest, Diffractive Optics: Design, Fabrication, and Applications*, Tech. Digest Ser. 1994, Vol. 11 (OSA, Washington, DC), 194–197 (1994).
- [2] F. Wyrowski and O. Bryngdahl, "Iterative Fourier-transform algorithm applied to computer holography," *J. Opt. Soc. Am. A* **5**, 1058–1065 (1988).
- [3] M. S. Scivier and M. A. Fiddy, "Phase ambiguities and the zeros of multidimensional band-limited functions," *J. Opt. Soc. Am. A* **2**, 693–697 (1985).
- [4] R. Bräuer, F. Wyrowski, and O. Bryngdahl, "Diffusers in digital holography," *J. Opt. Soc. Am. A* **8**, 572–578 (1991).
- [5] J. R. Fienup, "Phase retrieval algorithms: a comparison," *Appl. Opt.* **21**, 2758–2769 (1982).
- [6] F. Wyrowski, "Iterative quantization of digital amplitude holograms," *Appl. Opt.* **28**, 3864–3870 (1989).

Tunable Holographic Wavelength Filter

M.C. Parker, S.T. Warr, R.J. Mears and W.A. Crossland.

Department of Engineering, Cambridge University, Trumpington Street.

Cambridge CB1 2PZ, United Kingdom. Tel: +44 1223 332674.

1. Introduction

The high available bandwidth of optical fibres has led to a large interest in wavelength-division-multiplexed (WDM) networks. Such systems rely on the functionality provided by tunable sources, receivers and filters. Components must be quickly tunable over a large range, have a narrow-band channel response, low insertion loss and be robust and repeatable in their operation. Various wavelength filtering techniques have been previously proposed. These have been based on liquid crystal birefringent slabs [1], Fabry-Perot cavity filters [2], acousto-optic surface wave effects [3] and semiconductor resonant amplification [4]. A method of space-wavelength switching using a mechanically rotatable grating has also been demonstrated [5]. Such methods are generally analogue in operation and require complex calibration or control techniques.

2. Principle of Operation

The use of a fixed grating for reversible WDM demultiplexing is well known [6]. The spectral components of the input source are separated and distributed around the output plane so that selection of the correct spatial region allows any WDM channel to be isolated. If the grating pitch can be dynamically altered, the filter may be tuned to direct different wavelengths towards the same output fibre or detector. A ferro-electric liquid crystal spatial light modulator (FELC SLM) is capable of displaying an arbitrary binary phase holographic pattern which may be used as a dynamic grating.

However current SLM pixel pitches do not allow the source wavelengths to be diffracted through large enough angles for them to be sufficiently separated out from one another to enable high resolution tuning. This problem can be solved by the use of a SLM in conjunction with a fixed high resolution grating. The fixed grating provides large angular separation of the wavelengths, while the SLM provides the fine tuning of the system. The architecture chosen is a compact double-pass system, which minimizes optical components and ensures efficient recoupling of the light into the output SM fibre. The $2f$ architecture ensures that light coupling back onto the output fibre has a flat phase profile.

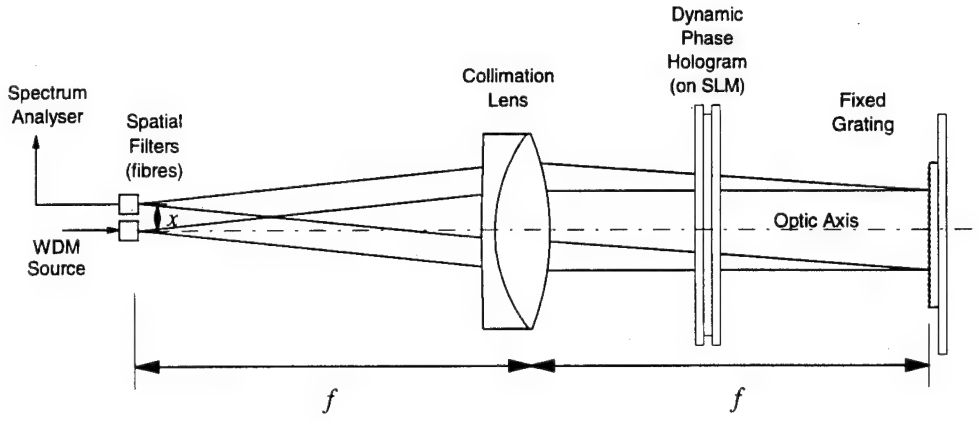


Figure 2.1: Wavelength tunable filter.

With reference to figure 2.1, the source light from the input fibre placed on the optical axis, is collimated by means of a lens and shone through a transmission SLM, such that the input angle of the light into the SLM is zero. The hologram displayed on the SLM acts as a grating which causes the light to be diffracted out of the SLM at angles $+\theta$ and $-\theta$ with respect to the input angle of the light. The angle θ has a wavelength dependence given by $\theta = n\lambda/ND_{slm}$ which causes the light to be angularly spread out. The wavelength is represented by λ , D_{slm} is the SLM pixel pitch, N is the number of pixels along one side of the SLM and n is an integer in the range $0 \rightarrow N/2$ representing the filter tuning. The angularly dispersed light continues onto a reflective fixed grating, where the angular separation of the light is increased by a greater amount. The grating causes the light to be further deviated by an angle $\pm\phi$, where $\phi = \lambda/D_f$ and D_f is the line-pair width of the grating. The reflected light passes once more through the SLM and is deviated once again by angles of $\pm\theta$. Thus the total deviation of the light is given by $\Phi = \pm\theta \pm \phi \pm \theta$. The light passes through the lens once again, and is launched back into the output fibre placed a distance x from the optical axis. The output angle (β) from the SLM is given by simple geometry as $\tan(\beta) = x/f$, so that for small β , we have $\beta \approx x/f$. But the output angle β is given by the input angle with all the angular deviations through the system added, so that $\beta = \Phi$. This gives us $x/f = \pm\theta \pm \phi \pm \theta$, so that ultimately we get

$$\lambda = \frac{x}{f \left\{ \frac{1}{D_f} \pm \frac{n}{ND_{slm}} \pm \frac{n}{ND_{slm}} \right\}}$$

For fixed values of x, f, N, D_{slm} and D_f , the selection of a particular wavelength to couple back into a fibre at x is determined by the variable n which is set by the hologram displayed on the SLM. The equation shows that multiple wavelengths will couple back into the fibre at x . This is a result of using binary phase holograms and gratings which always produce symmetric orders. Some of the wavelength solutions are the same as if only the fixed grating were there, but the SLM introduces tunable wavelength solutions above and below the fixed central wavelength. To achieve useful filtering, we need to design the filter so that only one of the tunable sidebands corresponds to the active spectral region.

3. Results

In this paper we will describe the construction of a proof of principle demonstration filter consisting of single-mode communications fibre for input and output (core $\phi = 10\mu\text{m}$) and a $f = 76.2\text{mm}$ achromat collimating lens.

The input source spectrum, figure 3.1, was provided by a Fabry-Perot laser diode coupled to a visible source used to aid with optical alignment of the system. The spectrum of this source was monitored on a Hewlett Packard MS90308 spectrum analyzer.

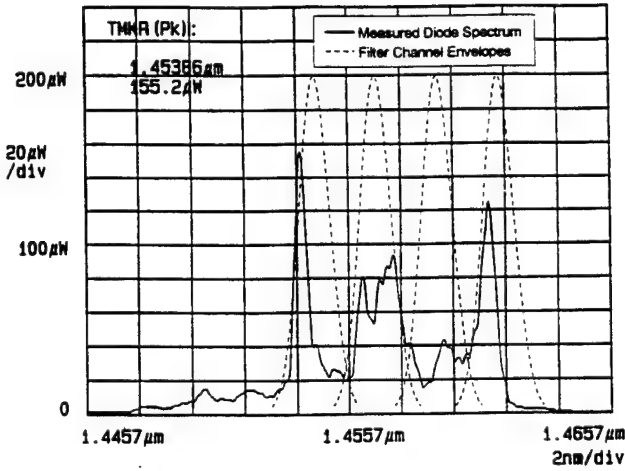


Figure 3.1: Diode laser input spectrum.

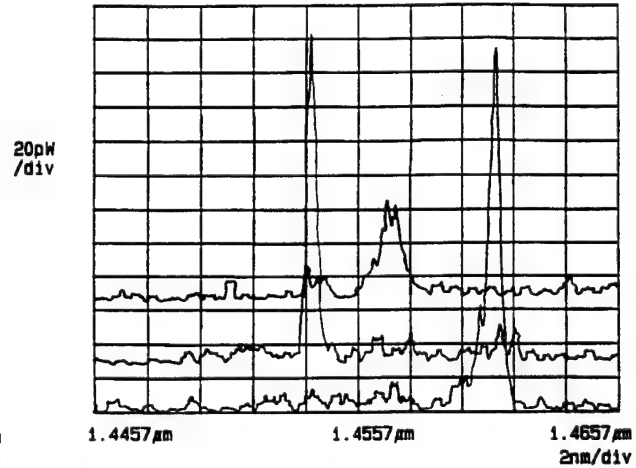


Figure 3.2: Filtered output spectra.

The SLM is a passive matrix-addressed glass cell with ITO contacts and 128×128 binary phase pixels within a $21\text{mm} \times 21\text{mm}$ active region. This device has been optimized for high transmission within the $1.5\mu\text{m}$ erbium window.

The fixed grating was made by oxidising a silicon wafer to a depth of $\frac{\lambda}{4}$ and etching grating lines with HF acid. The resulting structure was coated with aluminium to increase the reflectivity.

Various holograms were generated using simulated annealing [7] and displayed to isolate each of the 3 principle modes, figure 3.2. The channel response is Gaussian with an almost constant 2.5nm channel separation across the entire 160nm tuning range. However the input modes do not exactly coincide with the filter channels and have been attenuated by different amounts.

Although a filter of the type proposed has the potential for low loss operation, our demonstration exhibits a high insertion loss due to defects in the components used. These defects and the associated losses they introduce will be discussed.

4. Conclusions

In this paper we describe the concept and practical implementation of a new optically transparent method of wavelength filtering. The architecture we propose is digital in nature and therefore repeatable in operation. The design uses a dynamically reconfigurable computer-generated hologram for tuning and the inherent redundancy in such holograms makes it extremely robust.

We have demonstrated a filter with a 2.5nm channel spacing capable of tuning over a 160nm range in the erbium window. Such a filter has important applications in WDM systems and may also be useful in the design of an external cavity tunable laser.

References

- [1] H.J. Masterson, G.D. Sharp, and K.M Johnson. Ferroelectric liquid-crystal tunable filter. *Opt. Lett.*, 14:1249–1251, 1989.
- [2] J. Stone and L.W. Stulz. FiEnd filters: passive multilayer thinfilm optical filters deposited on fibre ends. *Electron. Lett.*, 26(16):1290–1291, 1990.
- [3] J. Frangen, H. Herrmann, R. Ricken, H. Seibert, and W. Sohler. Integrated optical, acoustically tunable wavelength filter. *Electron. Lett.*, 25(23):1583–1584, 1989.
- [4] T.L. Koch, F.S. Choa, F. Heismann, and U. Koren. Tunable multiple-quantum well distributed-Bragg reflector lasers as tunable narrowband receivers. *Electron. Lett.*, 25(14):890–892, 1989.
- [5] D.C. Griffiths and K.R. Preston. Space and wavelength filter for use in WDM-based optical switching networks. *Electron. Lett.*, 28(18):1729–1730, 1992.
- [6] E.E. Basch, editor. *Optical-Fiber Transmission*, pages 250–251. Macmillan, 1987.
- [7] S.E. Broomfield, M.A.A. Neil, E.G.S. Paige, and G.G. Yang. Programmable binary phase-only optical-device based on ferroelectric liquid-crystal SLM. *Electron. Lett.*, 28(1):26–28, 1992.

Properties and Application of Liquid Crystal Spatial Light Modulators in JENOPTIK Optical Signal Processing Systems

Frank Reichel

JENOPTIK Technologie GmbH, D-07739 Jena, Germany
Tel. (++49) 3641 65 3156, FAX. (++49) 3641 65 3666

1 Introduction

Spatial Light Modulators (SLM) used as components in optical signal processing systems are gaining ever greater importance. The application of SLM for performing optical Fourier transformations or optical correlations in real time pattern recognition are worth speaking of. Additionally, a new scope of application has been opened up by SLM in creating optical neuronal networks and optical memories.

Determined by their interesting electro-optical properties, such as electrically controlled optical activity, birefringence and scattering, liquid crystal layers are appropriate for defined changes of amplitude, phase, polarisation state and spectral composition of light beams.

It is our intention to describe and discuss in this paper the scope of properties and the application possibilities of optically addressable SLM. Specific attention is focused on the interpretation of SLM parameters as well as on LC-SLM properties influenced by different physical and technological processes. Furthermore, we want to describe and summarize the applications of SLM used in our incoherent-optical image processing system and in the optical autocorrelator serving for the for evaluation of particle image velocimetry (PIV) and laser speckle photographic (LSP) recordings.

2 LC-SLM structures

Matching of photoconductor and LC-layer impedances can be achieved by means of metal-insulator-semiconductor (MIS) structures. When applying voltage, a high-impedance state is generated in the semiconductor bulk over a certain time. Thus, it is possible to vary the LC voltage drop as a function of the exposure intensity. In literature SLM are described using as semiconductor Si [1] and GaAs [2].

If monocrystalline silicon is used as photosensitive material, the SLM can be regarded as a MIS structure. In this case the gate insulator comprises both the dielectric mirror and the LC-layer. If the voltage U_d of appropriate polarity is applied to the metal electrode a depletion region is developing in the semiconductor. This region is completely deprived of free charge carriers. As a result, the U_s part of the applied voltage U_d is dropping at the semiconductor. The minority carriers obtained by thermal ionisation and photo generation accumulate at the semiconductor - insulator interface and shield the outer field. Due to permanent carrier accumulation the depletion region is continuously decreased while the insulator voltage drop is increased. By constant alternation of depletion and accumulation phases, an exposure-dependent and d.c. voltage -free mean square voltage U_{rms} is obtained at the insulator if the voltages U_d and U_a as well as the pulse durations t_d and t_a were tailored appropriately.

Fig. 1a shows two experimental dependencies of the exposure intensity I^π as a function of the time t_d . I^π corresponds to the write intensities that gives an phase shift of the readout light $\Delta\phi = \pi$. Fig. 1b illustrates wavelength dependencies of the exposure intensity I^π for several depletion voltages.

Fig. 2a gives a survey of various processes influencing the resolution of the MIS SLM structure. The bipolar and unipolar diffusion are one of the possible limiting reasons. The main limitation of Si-MIS SLM resolution power seems to be based on the electric field spread in the layer system semiconductor - insulator (liquid crystal). Fig. 2b depicts the MTF calculated on the basis of the two-dimensional solution of the continuity equation (A) and the MTF obtained as a result of field spread calculated by solving the Laplace equation (B). Fig. 2b shows also a experimental MTF for a Schottky SLM structure (Au - n-Si - TiO_2/SiO_2 - LC-ITO) on the basis of n-Si (2000 Ωcm , wafer thickness = 180 μm), a 12-paired dielectric mirror and a nematic LC-layer (TN0403, thickness 6 μm)

Due to minor Si-wafer thicknesses (100 - 300 μm) layer stresses are playing an important role in coating processes with the TiO_x/SiO_y mirror. Various coating conditions were investigated and optimized in order to minimize deformations of the Si-substrate.

A homogeneous distribution of the isolation parameters of the MIS structure is necessary to achieve a uniform image reconstruction. Fixed and mobile charges at the "insulator - semiconductor" interface as well as charges inside the isolator impact the homogeneity. These charges can be introduced during the mirror coating process.

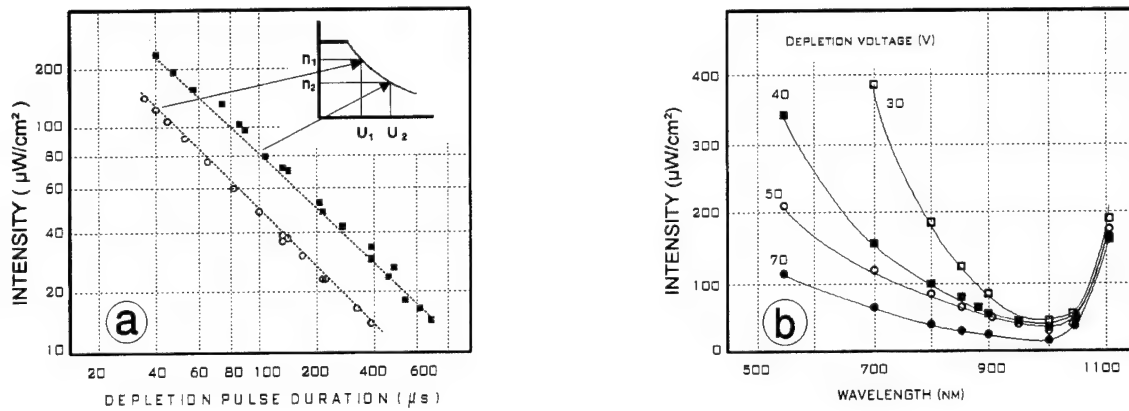


Figure 1: Intensity dependence on depletion pulse length (a) and write-in wavelength (b)

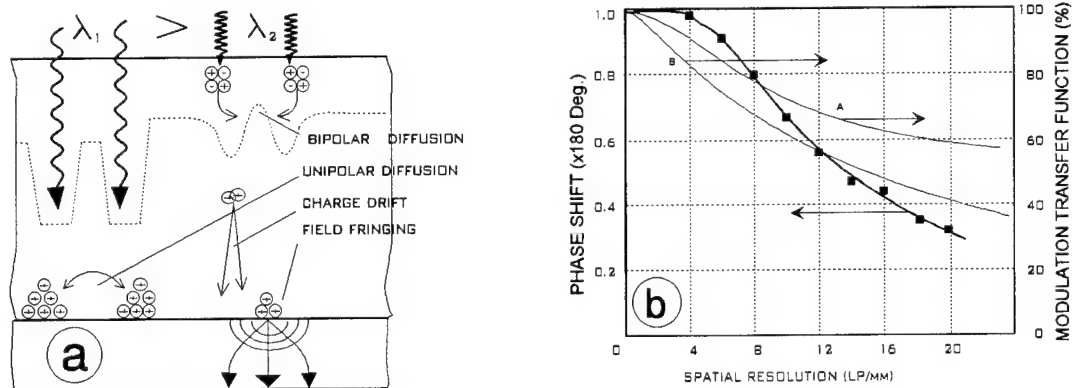


Figure 2: Illustration of resolution-limiting processes (a) and the modulation transfer functions (b)

Depending on the charge type, the capacity-voltage characteristic curve is shifted by changing the flat band voltage. Differences in the insulator capacity (mirror) are caused by variations of the effective dielectric constant ϵ_m of the mirror. The stoichiometry of the individual layers exercises a dominant influence on the effective dielectric constant ϵ_m . Especially, the composition of the TiO_x layers in the region of $x = 1.8 - 2$ can produce ϵ_{TiO} alterations ranging between 15 - 80. Thanks to the optimized coating technology, a homogeneous distribution of the dielectric parameters of the mirror layers is achieved across an area of approx. 15 mm diameter.

Additionally to the described MIS structures, high-impedance photoconductors are used. The main importance is attached to amorphous and polycrystalline layers. SLM with ZnS, CdS, amorphous chalcogenides (As-S-Se) as well as amorphous Si:H layers or a-SiC:H layers have been investigated. Thanks to the well-mastered a-Si:H technology good SLM parameters are achieved with a-Si:H layers [3,4].

As a photoconductor the light modulator uses PCVD deposited a-Si:H on ITO glass substrate. The CVD process with $\text{P}(\text{SiH}_4) = 20 \text{ Pa}$, $U(\text{AC}) = 380 \text{ V}$ and $U(\text{DC}) = 170 \text{ V}$ permits the deposition of a-Si:H layers with good adhesion.

The calculated and experimentally determined phase shift dependencies are shown in Fig. 3a. At a drive frequency of 100 Hz an illumination intensity of $I^\pi = 10 \mu\text{W}/\text{cm}^2$ is required to generate phase shifts of $\Delta\phi = 1\pi$. The spectral distribution of the sensitivity $1/I^\pi$ of 3 different a-Si:H layer thicknesses is given in Fig. 3b. As expected, the maximum of $1/I^\pi$ moves towards the long wavelength range when the layer thickness grows. Simultaneously, the absolute sensitivity increases. The cause is the minimization of the capacitive voltage distribution ratio, so that, with an operating point fixed at the $\Delta n = f(u)$ characteristic, an increased driving voltage must be applied. Thus, a lower illumination intensity is required. In the short wavelength region, the photoimpedance is determined mainly by the ITO - a-Si:H diode and less by the bulk. Hence, the layer thickness dependence is reduced.

In order to determine the resolution capability on the basis of the intensities of the zero order diffraction with and without grating $I_0(u)$ and $I_0(0)$, the diffraction efficiency η can be determined as a function of the spatial

frequency ν . In Fig. 4a, a respective behaviour of the resolution capability is demonstrated with 3 different LC layer thicknesses.

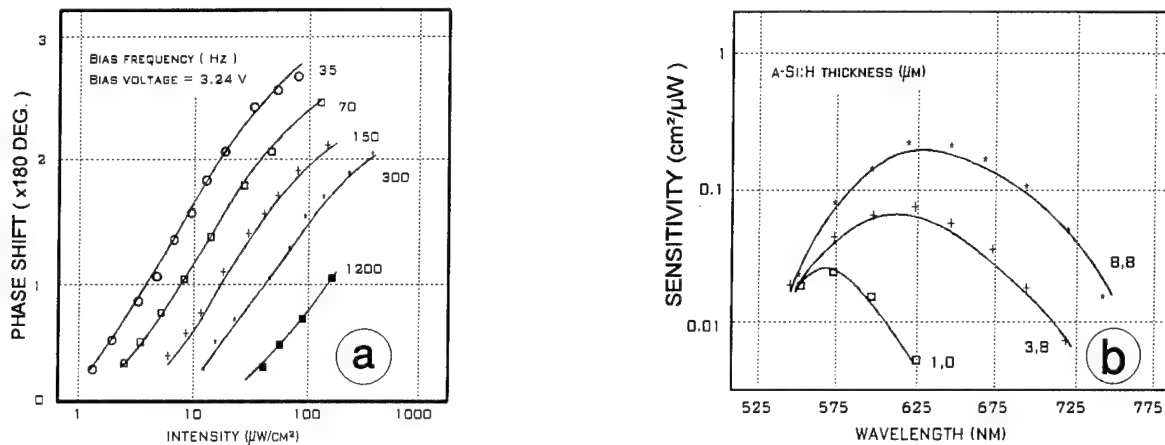


Figure 3: Dependence of phase shift on write intensity (a), a-Si:H-SLM spectral response (b)

The dynamic behaviour of a-Si:H SLM, i.e. the optical response to exposure pulses is determined by the voltage redistribution rate and the dynamics of the director change of the LC. The redistribution speed depends on the kinetics of the photoconduction. These times can be influenced by a number of technological parameters, such as CVD gas composition, a-Si:H "light saturation" state as well as SLM driving conditions.

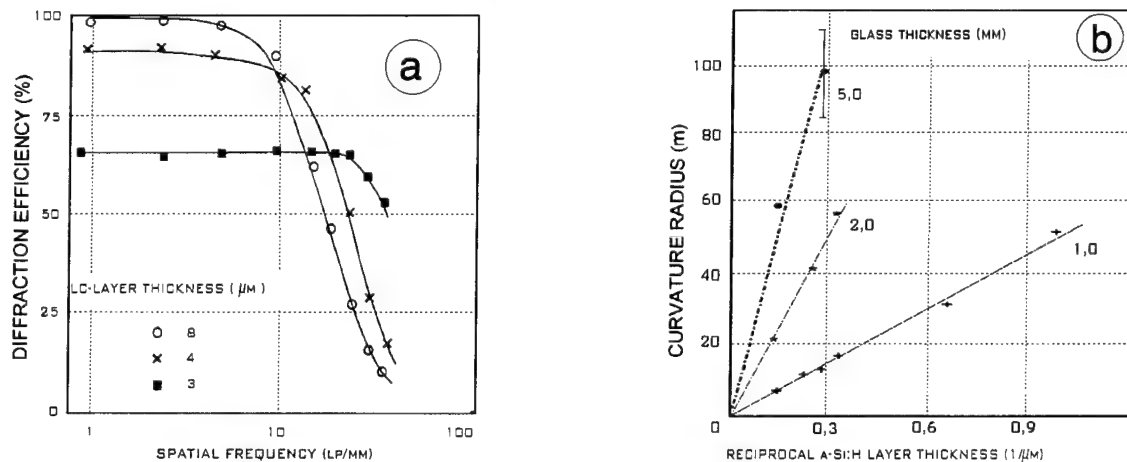


Figure 4: Modulation transfer function (a) and dependence of curvature radius (b) for a-Si:H SLMs

The main reason of the a-Si:H SLM curvature is the deformation of the coated glass substrate resulting from layer tensions and differences in the thermal expansion coefficient $\Delta\alpha$. The radius of curvature measured for different a-Si:H layer and glass substrate thicknesses is given in Fig. 4b.

During industrial uses, typical temperature differences are ranging in the interval of 5 to 50 deg C. They have essential influence on the stability since temperature dependent differences in the refractive index $\Delta n(T)$ as well as changes of the voltage distribution between semiconductor and LC layer can result. The measured results show that a sufficiently stable phase modulation can be achieved by an appropriate selection of the LC mixtures in respect of their resistance.

3 Application of LC- SLM

If the image processing tasks could be reduced to an object/pattern recognition in which the objects for testing are identified by extensive data, the transition from the object to the frequency space would offer a sensible solution. If, in addition, the object structures are characterized by multi-design, translation and rotation variances, then an

integral transformation, e.g. a Fourier transformation of the object function, can be seen as a useful aid in pattern classification.

The incoherent set-up [5] for optical space frequency analysis (OSFA) consists of different binary area radiators in the object-side focal plane of the Fourier lens O2 and a "point" detector on the optical axis, in the image-side focal plane of this lens. The known integrals of the spatial-frequency spectrum are obtained, if different light emitting geometries are sequentially connected and disconnected.

Fig. 5a shows the schematic diagram of an incoherent optically addressable Fourier processor for OSFA. The image information to be classified is projected by a camera lens O3 on to an optically addressable SLM. On the readout side, the switchable radiating face is projected by the lenses O2 via beam splitter Bs and reflective OASLM on to the single detector D. The detector arranged on the optical axis consists of an photomultiplier with preceding pinhole. An electrical addressed LC modulator (wedge-ring layout) with background lighting is used as readout radiating face. The beam splitter BS serves for the splitting of the optical path in order to visually control and align the camera towards the object. The electronic LC modulator control, the SLM activation, the piezo control, the data acquisition and analysis are carried out by means of a microprocessor.

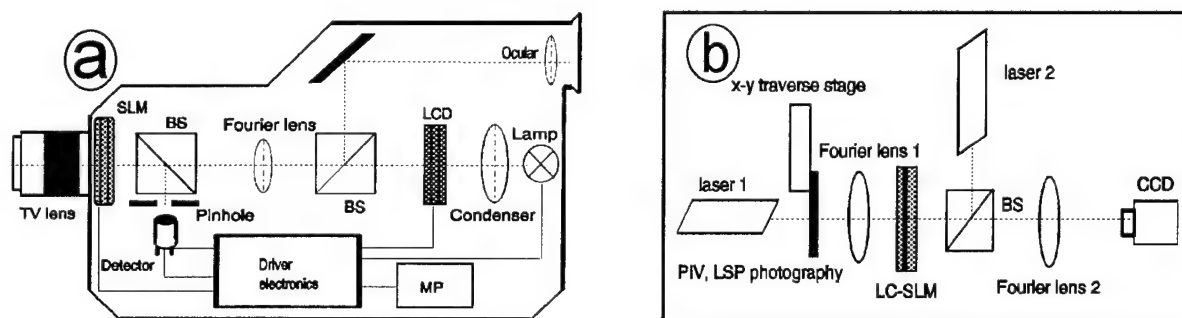


Figure 5: Architecture of the incoherent-optical image processing camera (a) and the optical autocorrelator (b)

In fluid mechanical research, recordings of complete velocity fields can be produced by photographic means. The same goes for the determination of mechanical shifts and deformations of surfaces.

An efficient evaluation of PIV or LSP photographic recordings cannot be made unless the position shifts of the particle images or speckles is computed with high speed and accuracy. This is commonly achieved by computing a few thousand two-dimensional autocorrelation functions of interrogation areas and determining the positions of the correlation peaks.

The two two-dimensional Fourier transformation can be made with optical set-ups [6]. In this version, the photographic transparency are exposed to laser light and the resulting Young's fringes are addressed to a SLM. Subsequently the optical Fourier transformation of the respective fringes is performed using a second laser source. The present paper deals with a compact optical autocorrelator which contains a nematic liquid-crystal SLM. This supports algebraic norm and second Fourier transform realisation at high speed and with comparatively simple hardware. Fig.5b presents a schematic illustration of the optical principle of this setup.

References

- [1] U. Efron, J. Grinberg, P. O. Braatz, M. J. Little, P. G. Reif, R. N. Schwartz. The silicon liquid-crystal light valve. *J. Appl. Phys.* **57**, 1356-1368 (1985).
- [2] D. Armitage, J. I. Thackara, W. D. Eades: Photoaddressed liquid crystal devices. *Liquid Crystals* **5**, 1389-1396 (1989).
- [3] P. R. Ashley, J. H. Davis: Amorphous Silicon Photoconductor in a Liquid Crystal Spatial Light Modulator. *Appl. Opt.* **26**, 241-246 (1987).
- [4] I. A. Abdulhalim, G. Moddel, K. M. Johnson, C. M. Walker: Optically addressed electroclinic liquid crystal spatial light modulator with an a-Si:H photodiode. *J. Non-Cryst. Solids* **115**, 162-164 (1989).
- [5] F. Reichel, W. Löffler, E. Gärtner. Using optical space-frequency analysis for real-time pattern recognition. *IEEE Micro* **14**, 49-60 (1994).
- [6] A. Vogt, F. Reichel, J. Kompenhans. A compact and simple all optical evaluation method for PIV recordings. *Proc. 7th Int. Symp. on Application of Laser Techniques to Fluid Mechanics, Lisbon, vol. 2*, 35.2.1-35.2.8 (1994).

Summary not available.

Tuesday, March 14, 1995

Poster Session

LTuC 7:30 pm-10:00 pm
Grand Ballroom C

Experimental Investigation of Free Space Optical Interconnects.

A.J. Stevens, J. Gourlay, S. Samus, W.J. Hossack,
D.G. Vass, and D.C. Burns.

Applied Optics Group,
Department of Physics,
The University of Edinburgh,
King's Buildings,
Edinburgh,
EH9 3JZ,
Scotland, UK

Phone : +44 (0)31 650 5270.
Email : andy.stevens@ed.ac.uk.

Introduction

Free space optical interconnects have applications in many optical systems such as crossbars, optical neural networks and telecommunications. The interconnect may be implemented in two ways; by the use of static holographic elements to fan out the input channels onto a modulating plane which allows only the appropriate channels to propagate^{1,2}, or by using a dynamic holographic element to provide direct interconnection^{3,4}. Ferroelectric liquid crystal over silicon spatial light modulators (FLC/VLSI SLM's) have been demonstrated to be suitable elements as both an amplitude modulating plane addressed by holographic elements, and as a phase modulating plane for encoding dynamic holograms. The aim of this paper is to assess the capabilities of FLC/VLSI SLM's in both these roles using experimental test systems. In order to do this, performance criteria such as scalability, diffraction efficiency, uniformity, contrast ratio, optical throughput, and switching speed shall be considered. Finally, the analysis of these results will provide an insight into the performance of future FLC/VLSI SLM's in optical free space routing systems.

256 Channel Static Hologram Interconnect

The classic matrix-matrix crossbar architecture (fig.1.) consists of an array of $n \times n$ input channels which are fanned out onto an $n^2 \times n^2$ modulating plane, and then fanned back in to an $n \times n$ output array. This allows any input channel to be routed to any output channel, along with broadcast capabilities. With FLC/VLSI SLM's as the modulating plane, each pixel acts as a *transparent window* when turned on (fig.2.), which means that the optical data stream can pass through without the liquid crystal being required to switch at the optical data rate. The pixels only need to switch within the channel reconfiguration time.

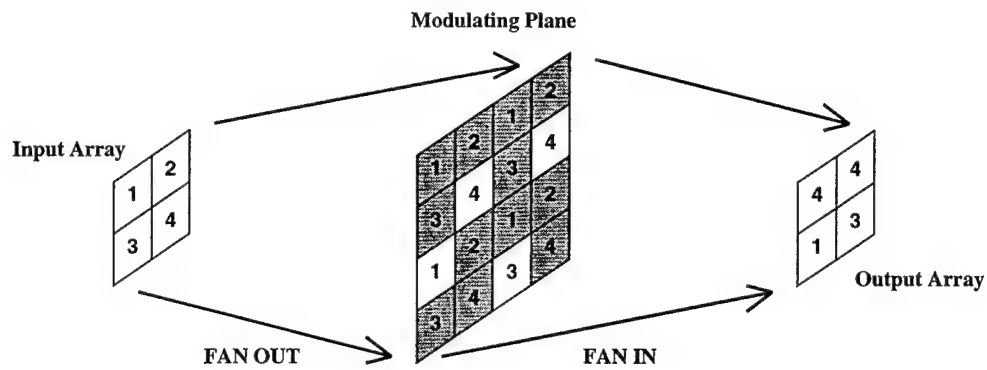


Figure 1: Schematic Model of Matrix-Matrix Crossbar.

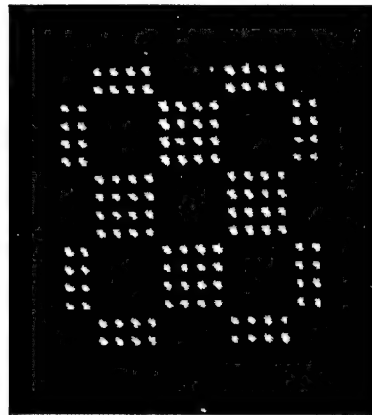


Figure 2: Static Fanout Hologram With 256 Spots Modulated By FLC/VLSI SLM.

In order to assess the performance of FLC/VLSI SLM's in this role, a test system has been constructed⁵ (fig.3.). By systematic investigation of the performance of this system we shall address the following; device and system scalability, contrast ratio and uniformity requirements, and space-bandwidth product issues.

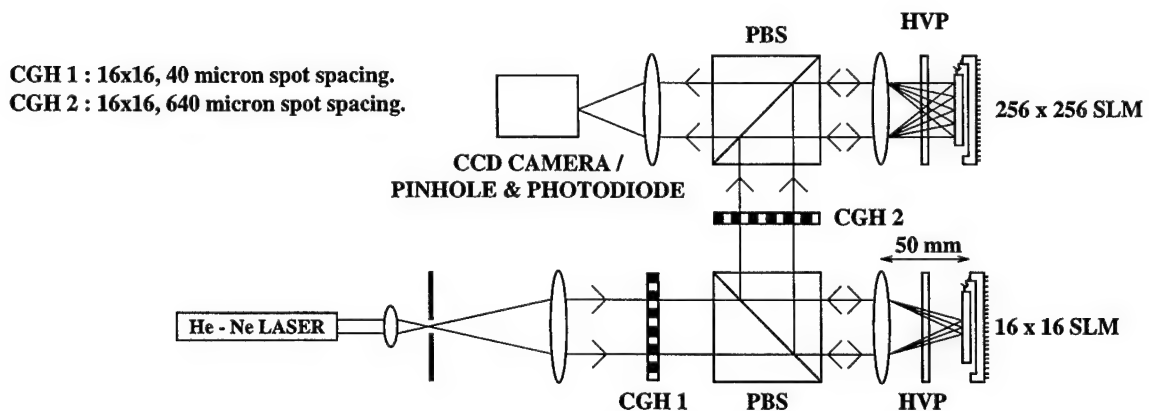


Figure 3: Experimental Test Bed For 256 Channel Interconnect.

Dynamic Holographic Interconnects

Many optical systems require dynamic holographic interconnects for the routing of signals and addressing of optical and electro-optic devices. Such systems require fast reconfiguration times and high diffraction efficiencies. It has previously been demonstrated that ferroelectric liquid crystals (FLC's) can be used to provide the 0 to π rad phase modulation required by binary computer generated holograms⁶. Furthermore it has also been shown that FLC/VLSI SLM's are capable of encoding and modulating FLC's so as to produce holographic interconnects⁷ (fig.4.). We shall present results of experiments using the test system illustrated in (fig.5.) to give a detailed analysis of the performance of this technology as a means of producing dynamic interconnects.

Finally, we will discuss the feasibility and estimated performance of asymmetric holograms produced by fabricating a $\pi/2$ phase pattern on the SLM coverglass, which, in conjunction with the π phase modulation achievable from the liquid crystal, may be used to produce asymmetric spot arrays.

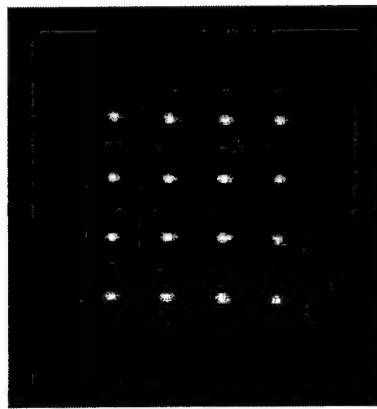


Figure 4: 4x4 Dynamic Holographic Fanout Using A Planarised FLC/VLSI SLM.

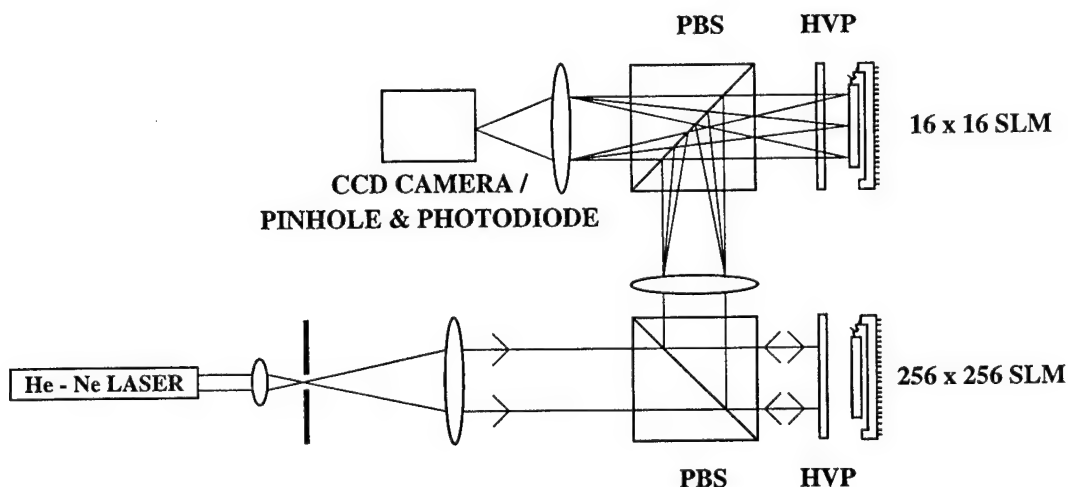


Figure 5: Experimental Testbed For Studying Dynamic Holographic Interconnects.

References

1. A.G. Kirk, W.A. Crossland, T.J. Hall. *A compact and scalable free space optical crossbar*. Proc. SPIE **1574** 137-141 (1991)
2. H.J. White, G.M. Proudly, et al. *Performance of a free space optical crossbar*. Presented at OC'94.
3. D.C. O'Brien, R.J. Mears, T.D. Wilkinson, W.A. Crossland. *Dynamic holographic interconnects that use ferroelectric liquid crystal spatial light modulators*. Applied Optics **33** 2795-2803 (1994)
4. Hirofumi Yamazaki, Masayasu Yamaguchi. *4x4 Free-space optical switching using real-time binary phase-only holograms generated by a liquid crystal display*. Optics Letters. **16** 1415-1417 (1991)
5. F.B. McCormick. *Generation of large spot arrays from a single laser beam by multiple imaging with binary phase gratings*. Optical Engineering **28** 299-304 (1989)
6. S.E. Broomfield, M.A.A. Neil, E.G.S. Paige, G.G. Yang. *Programmable binary phase-only optical device based on ferroelectric liquid crystal SLM*. Electronics Letters **28** 26-28 (1992)
7. J. Gourlay, S. Samus, P. McOwan, D.G. Vass, I. Underwood, M. Worboys. *Real-time binary phase holograms on a reflective ferroelectric liquid crystal spatial light modulator*. Accepted for Applied Optics.
8. T.D. Wilkinson, D.C. O'Brien, R.J. Mears. *Dynamic asymmetric binary holograms using a ferroelectric liquid crystal spatial light modulator*. Optics Communications **109** 222-226 (1994)

Switchable optical kinoforms, complex modulation holograms with twisted nematic liquid crystal television

Yunlong Sheng Luiz Gonçalves Neto and Danny Roberge

Université Laval, Centre d'Optique, Photonique et Laser,
Département de Physique, Québec, Canada G1K 7P4. sheng@phy.ulaval.ca

1. Introduction

Twisted nematic liquid crystal cell provides continuous phase modulation [1]. In this paper we explore this interesting property for implementation of switchable holograms and correlation filters.

Phase modulation of the commercial liquid crystal televisions (LCTV's) is cross coupled with amplitude modulation. The maximum phase shift can be less than 2π . An harmonic analysis shows that the coupled modulation holograms contain a kinoform term, which can dominate over the other diffraction orders in terms of energy. A new simple method is introduced for on-situ measurement of the phase and amplitude modulations of a spatial light modulator (SLM), that permits adjusting and optimizing the operating curve experimentally. The theory based on the Jones matrix calculus [2] is used for characterisation and optimization of the LCTV. Full complex modulation is obtained with two conjugated LCTV's. A number of optical Fourier and Fresnel kinoforms, complex valued holograms and various correlation filters are shown.

2. Phase-mostly holograms

2.1 Harmonic analysis

When a kinoform $\exp[j\phi(u,v)]$, with $0 \leq \phi \leq 2\pi$, is fed to a coupled-mode modulation SLM, the SLM provides the phase modulation $\phi'(u,v)$, which can be not equal to $\phi(u,v)$, and the coupled amplitude modulation $A(u,v)$. Both phase and amplitude are controlled through a single video signal, which is proportional to $\phi(u,v)$. The optical hologram $F'(u,v) = A(u,v)\exp[j\phi'(u,v)]$ on the SLM is a periodic function of $\phi(u,v)$ of period 2π and can be therefore expanded into the Fourier series with respect to $\phi(u,v)$

$$F'(u, v) = \sum_{m=-\infty}^{\infty} \alpha_m \exp [jm\phi(u, v)] \quad (1)$$

with the complex valued Fourier coefficients α_m

$$\alpha_m = \frac{1}{2\pi} \int_0^{2\pi} [A(\phi) \exp(j\phi'(\phi))] \exp(-jm\phi) d\phi$$

The term of $m = 1$ in Eq.(1) represents the original kinoform, whatever the modulation characteristics $A(\phi)$ and $\phi'(\phi)$ of the SLM. Other terms of $m \neq 1$ are not zero. They are superimposed on the on-axis reconstructed image, contributing to the noise. The energy distribution among the diffraction orders can be obtained by measuring the intensities of diffraction orders of an 1-D blazed phase grating coded on the SLM. One example shows that when the maximum phase modulation is 1.4π , and the maximum amplitude drop is 0.5, the kinoform term takes about 68% of the energy, the zero order takes about 21% and the rest (11%) goes to other orders [3]. The kinoform term is dominant in terms of energy.

2.2 Phase-mostly correlator

We built an optical correlator using the LCTV of the commercial Epson Crystal Image video projector. The twisted nematic LCTV panel has about 1 x 1 inch aperture and 220 x 320 pixels. This correlator is able to implement the phase-only matched spatial filters [3,4], composite filters[5], circular harmonic filters, the novel wavelet matched filters and the adaptive wavelet composite filters[6,7].

The phase-mostly filters are light efficient. Only about 10 μ W He-Ne laser power was used to avoid saturation of the CCD camera by the correlation peaks. One important issue of the electrically addressed SLM is the limited space bandwidth product (SBWP). Our experiments show that by using the on-axis kinoforms and phase-only filters (POF's), the SBWP of 200 x 200 pixels of the LCTV would suffice for some applications. The output SNR is high, since the on-axis POF yields bright narrow correlation peak, while the noise owing to the high diffraction orders is spread out in the correlation plane. Only the zero order yields an image of the input scene in the correlation plane. The experimental

results will be shown in the conference.

3. Optimization of the operating curve

The operating curve describes the coupled amplitude and phase modulation in the complex plane. For a given operating curve the optimal correlation filters can be designed [8]. We designed kinoforms with the Gerchberg and Saxton iterative method, that uses the operating curve as the constraint in the hologram plane, so that the mean square error of the reconstructed image is minimized [9]. However, the operating curve itself is a function of operation parameters and is to be optimized.

3.1 Measuring the phase modulation

We introduce a simple wedged shear plate interferometer for measuring the phase modulation of a SLM. The shear plate is a thick optical flat. Its front and rear surfaces are wedged along the vertical direction. The interference between the beams reflected from the front and rear surfaces of the wedged plate forms horizontal linear fringes. The two surfaces of the wedged plate are parallel in the horizontal direction. The SLM displays side by side two vertical bands of different gray level video signals. Because of the finite thickness of the plate, the beams reflected by the rear surface are laterally shifted in the horizontal plane with respect to the beams reflected by the front surface, resulting in an overlap between two beams of different gray levels in the middle region. The corresponding shift of the fringes in the middle region is proportional to the difference of phases between the two beams of different gray levels.

The wedged shear plate interferometer is extremely simple, stable and easy to align, permitting the on situ characterization and the optimization of the SLM.

3.2 Adjusting the operating curve

We measured the phase and amplitude modulations of the LCTV as a function of the angles ψ_1 and ψ_2 of the polarizer and analyzer and found out that when $\psi_1 = \psi_d + 16^\circ$, $\psi_2 = \psi_d + \alpha - 14^\circ$, where ψ_d is orientation of the front director of the liquid crystal and α is the twisted angle [10], the phase shift is approximately linear and the amplitude transmittance oscillates with increasing of the gray level. The operating curve becomes a perfect closed circle with the center of the circle slightly shifted from the origin in the complex plane. In the experiments encoding kinoforms on the LCTV we also found that when $\psi_1 = \psi_d + 16^\circ$, $\psi_2 = \psi_d + \alpha -$

14° the phase-mostly holograms give the best quality reconstructed images with the minimum intensity of the zero diffraction order spot.

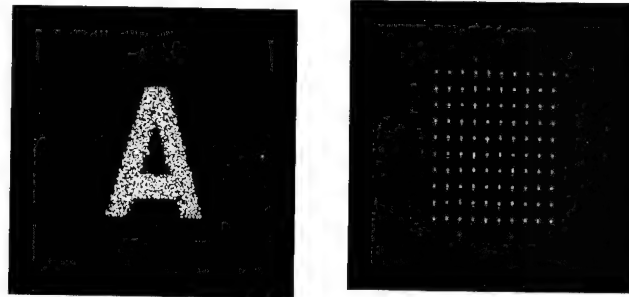


Fig.1 Images reconstructed from optical phase-mostly holograms

4. Complex modulation

The twisted nematic liquid crystal cell can be considered as a stack of birefringent slices whose extraordinary axes are normal to the incident light and rotate helically in the direction of light propagation. The complex transmittance of the polarizer-LCTV-analyzer sandwich can be obtained with Jones matrix calculus [2]. When the twist angle $\alpha \neq 90^\circ$ and $\psi_1 = \psi_d$ and $\psi_2 = \psi_d + \alpha$, the amplitude transmittance t and the phase shift δ as a function of β are given in Fig.2 with

$$\beta = \frac{\pi d}{\lambda} [n_e(\theta) - n_o]$$

where n_o and $n_e(\theta)$ are the indices of refraction of the liquid crystal, θ is the tilt angle of the liquid crystal molecules to the electrical field. The value of β is related to the applied voltage. The maximum value of β_{\max} occurs when the applied voltage is smaller than the threshold and the tilt $\theta = 0$. The minimum value $\beta = 0$ corresponds to the maximum tilt $\theta = 90^\circ$ when the applied voltage is maximum.

We obtained the full complex modulation [11] using two individual LCTV's, one in the phase-mostly regime, another in the amplitude-mostly regime. The residual amplitude in the first LCTV was compensated by coding the second LCTV, and vice versa.

In the phase-mostly regime, $\psi_1 = \psi_d$ and $\psi_2 = \psi_d + \alpha$, the phase shift δ is linear to β . When the brightness is turned to minimum, the residual bias voltage is determined by the manufacturer, that corresponds to $\beta = \beta_{\max}$. Rotating the polarizer and analyzer can shift the amplitude curve $t - \beta$ with respect to β_{\max} and optimize, therefore, the operating

curve, as shown in subsection 3.2.

In the amplitude-mostly regime $\psi_1 = \psi_d$ and $\psi_2 = \psi_d - \alpha + 90^\circ$, we increase the brightness so that the $\beta_{\max} = 2.75$ and the amplitude t is approximately linear to β , as shown in Fig.2. There is coupled phase modulation.

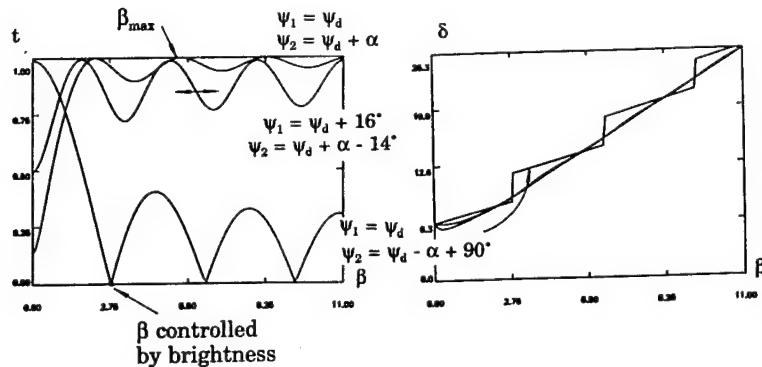


Fig.2 Amplitude t and phase δ as a function of applied voltage β for different ψ_1 and ψ_2

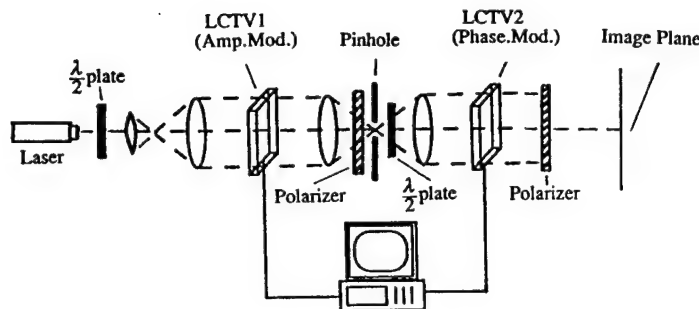


Fig.3. Real-time optical complex filter correlator

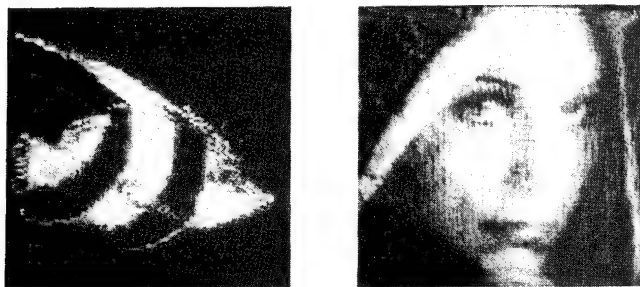


Fig.4 Reconstructed images of Fresnel complex holograms

For testing the optical complex modulation we used a separable 2-D hologram consisting of a 1-D vertical sinusoidal amplitude grating and a 1-D

horizontal blazed phase grating. The amplitude and phase of the 2-D complex grating are coded separately on two LCTV's. Its diffraction pattern consists of two peaks of the first order diffraction in vertical direction but shifted horizontally. The imperfections in the complex modulation leads to other orders of diffraction. Optical experiment shows that the complex modulation diffraction orders are dominant over the other orders in terms of energy.

A programmable optical correlator using one LCTV for input and two LCTV's for complex modulation is built, as shown in Fig.3. A number of kinoforms and complex modulation Fourier and Fresnel holograms are implemented, as shown in Fig.4.

We are looking for applications of our results to optical pattern recognition, neural networks, display holography and diffractive optics research.

References

1. N. Konforti, E. Maron and S. T. Wu, "Phase-only modulation with twisted nematic liquid-crystal spatial light modulator", *Optics, Lett.* **13**, 3, 251-253 (1988).
2. K. Lu and B. E. A. Saleh, "Theory and design of the liquid crystal TV as an optical spatial light modulator", *Opt. Eng.* **29**, 240-245 (1990).
3. Y. Sheng and G. Paul-Hus, "Optical on-axis imperfect phase-only correlator using liquid-crystal television", *Appl. Opt.* **32**, 29, 5782-5785 (1993).
4. S. S. Cotariu, S. E. Monroee Jr. and J. Knopp, "A live input, live filter, liquid crystal correlator" *Proc. SPIE*, vol. **1704**, paper 29 (1992).
5. D. Roberge and Y. Sheng, "Optical implementation of the phase-only composite filter using liquid crystal television", *Proc. SPIE* vol. **2237**, 196-203 (1994).
6. D. Roberge and Y. Sheng, "Optical wavelet matched filter", *Appl. Opt.*, **33**, 5287-5293 (1994).
7. D. Roberge and Y. Sheng, "Optical composite wavelet matched filters", *Opt. Eng.* **33**, 2290-2295, (1994).
8. R. Juday, "Correlation with a spatial light modulator having phase and amplitude cross coupling", *Appl. Opt.* **28**, 4865-4869 (1989).
9. L. Gonçalves, D. Roberge and Y. Sheng, "Programmable optical phase-mostly holograms with coupled-mode modulation liquid crystal television", *Appl. Opt.* accepted. (1994).
10. C. Soutar and K. Lu, "Determination of the physical properties of an arbitrary twisted-nematic liquid crystal cell", *Opt. Eng.*, **33**, 2704-2712 (1994).
11. D. A. Gregory, J. C. Kirsch "Full complex modulation using liquid crystal televisions" *Appl. Opt.*, **31**, 163-165 (1992).

Ferroelectric liquid-crystal optically addressed spatial light modulators for binary phase holograms

D.C.O'Brien, Garret Modell
 Optoelectronic Computing Systems Centre, Campus Box 525,
 University of Colorado, Boulder, CO 80309., USA. (tel 303 492 3330)

1. Introduction

Ferroelectric liquid crystal spatial light modulators have a robust binary (0 and π) phase modulation scheme [1], which can potentially be both polarisation independent and lossless using an optimised device [2]. This is ideally suited to displaying binary phase computer generated holograms (CGHs) [3], combining holographic elements with programmability.

Optical switches using such programmable holograms have many advantages over conventional techniques: Most switches connect all input ports to all output ports and block unwanted routes using an SLM working as a shutter. This causes high intrinsic loss, and failure of a single shutter causes incorrect routing. In a holographic switch potentially all the light can be 'steered' to the desired output using a programmable hologram. Damage to an area of the hologram causes degradation in the quality of connection, rather than failure. Results using electrically addressed devices for these applications are excellent [3], but the space bandwidth product (SBWP) is limited ($10^4 - 10^5$ compared with $\approx 10^9$ for a fixed CGH).

Optically addressed SLMs (OASLMs) offer the possibility of higher space bandwidth product if a high SBWP image can be written to the device. In this paper a means to accomplish this is described, and preliminary results of an investigation of OASLM binary phase performance presented.

2. Programming the OASLM

In most Fourier CGHs the hologram pattern is calculated over a 'base region' which is replicated over the entire area of the hologram during manufacture. The principle behind the technique described here is to replicate the pattern optically and write the resulting image to an OASLM, which is used as the holographic element. Figure 1 shows the system: The programming device is an electrically addressed SLM which displays the base pattern as an intensity image. This is then Fourier transformed and illuminates an array generator CGH. A further transform is taken, creating an array of replicated images at the Fourier plane of the

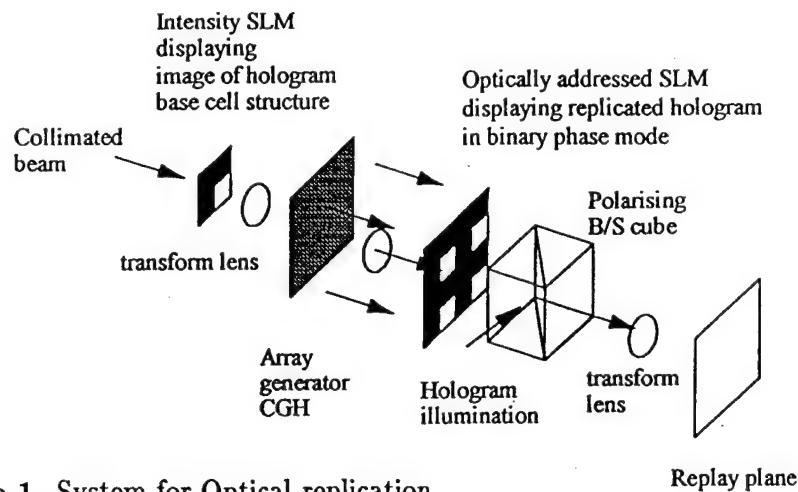


Figure 1. System for Optical replication

lens. This is written to the OASLM, which can be read in a binary phase mode: The device is rotated so the input polarisation bisects the angle between the two allowed states of the liquid crystal director, the output polarisation being orthogonal to the input as a consequence of the beamsplitter cube. This creates transmission of equal magnitude and opposite sign for each of the two states, independent of the crystal tilt angle and layer thickness. Such an experiment is described fully in reference [4].

The scheme above could be extended to independent addressing of the entire OASLM by using separate electrode structures for each replicated area: Sequential display of images and activation of areas would allow all points on the device to be independently addressed.

The experiment relies on OASLM devices operating in a robust binary phase mode, over large areas. In the experiment described in [4] a 4x4mm portion of the OASLM was used to record the binary phase hologram. Over larger areas the performance of the device degrades significantly. OASLM performance limits the utility of this scheme, and preliminary efforts to assess and improve device performance are described below.

3. Assessment of phase performance

A simple binary grating can be written to the OASLM, and should have no central (zero) order in its diffraction pattern if the device is operating in a binary phase mode. This provides a simple means to measure device performance. Figure 2 shows the apparatus: A collimated argon ion laser ($\lambda = 514nm$) illuminates an electrically addressed SLM which displays the grating. This is transferred to the writing surface of a ferroelectric liquid crystal OASLM using a 4f optical system. The device is read in reflection with a low intensity helium neon ($\lambda = 633nm$) collimated laser beam. A CCD camera is used to view the image on the device and its Fourier transform. Both read and write illumination are continuous.

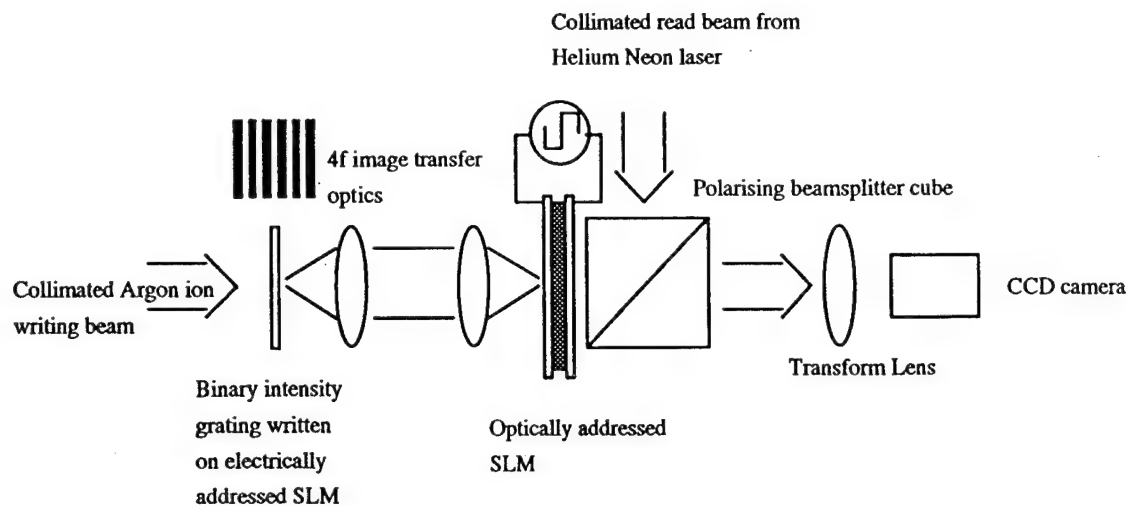


Figure 2. Assssment apparatus

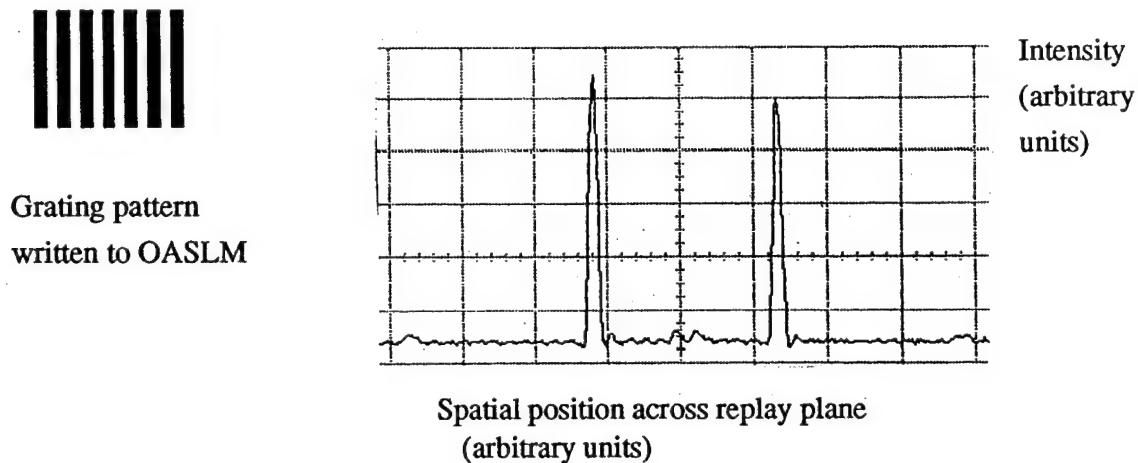


Figure 3. Schematic of grating and linescan through holographic replay

The OASLM device used is described fully in [5]. It consists of a PIN photosensor with an aligned layer of ferroelectric liquid crystal (SCE13). The device is driven in an integrating mode [6] using a 18 V peak to peak (-9 to +9 V) 6.3 kHz square wave, so that the phase pattern is present continuously. The writing beam intensity is $\approx 1.5 \text{ mWcm}^{-2}$ and the read beam $\approx 1.0 \text{ }\mu\text{Wcm}^{-2}$. The CCD camera is set to view an image of the device and a binary grating with a $320 \text{ }\mu\text{m}$ pitch is written to the OASLM, so that a good intensity image is obtained. The camera is then set to view the Fourier transform of the image, and the device is rotated through an angle approximately equal to the liquid crystal tilt angle so the zero order is minimised. The device should then be in a binary phase configuration. Figure 3 shows the grating pattern and a line scan through the holographic replay plane. The two peaks are the first orders, and the zero order of the diffraction pattern is approximately 6

% of the peaks, showing the device is operating close to binary phase (as a comparison the zero order would be approximately 2 - 3 % of the peaks for a typical electrically addressed device [3]). The optical transmission is 5-10 %, as the device is not optimised for binary phase modulation. Potentially lossless, polarisation independent phase modulation can be achieved using a liquid crystal with a 45 degree tilt angle and a quarter wave layer thickness [2]. This is a promising result, although the device is illuminated over an area 2.5 mm in diameter, and illumination over larger areas causes the zero order to increase rapidly. It compares favourably with the previous replication experiment which used a device with a homogenous amorphous silicon photoconductor, rather than a PIN structure. In both these cases good image transfer was obtained, but good phase performance was only achieved over a small area. Work to investigate the reasons for this and obtain good performance over larger areas is underway.

4. Conclusions

Previous experiments have demonstrated the principle of replication to increase SBWP, and show the potential to independently address large optically addressed devices. Such schemes place heavy demands on the OASLM devices, in terms of both the uniformity of the device, and the symmetry of the two phase states. The results presented here are the first using an OASLM with a PIN photosensor and are promising: Close to binary phase performance has been demonstrated, albeit over a small area of the device. Future work aims to extend the usable area and optimise devices for holographic applications.

References

- [1] S.E.Broomfield, M.A.A.Neil, E.G.S.Paige, and G.G.Yang. Programmable binary phase only optical device based on ferroelectric liquid crystal spatial light modulator. *Electronics Letters*, 28(1):26-27, 1992.
- [2] M.J.O'Callaghan and M.A.Handschy. Diffractive ferroelectric liquid-crystal shutters for unpolarized light. *Optics Letters*, 16(10):770-772, 1991.
- [3] D.C.O'Brien, T.D.Wilkinson, R.J.Mears, and W.A.Crossland. Dynamic holographic interconnects that use ferroelectric liquid-crystal spatial light modulators. *Applied Optics*, 33(14), 1994.
- [4] D.C.O'Brien, T.D.Wilkinson, and R.J.Mears. Computer generated holograms with large space bandwidth product. In *4th Int. Conf. on Holographic Systems, Components and Applications*. IEE, September 1993.
- [5] G.Moddel, K.M.Johnson, W.Li, R.A.Rice and L.A.Pagnano-Stuffer, and M.A.Handschy. High-speed binary optically addressed spatial light modulator. *Applied Physics Letters*, 55(6):537-539, 1989.
- [6] A.M.Gabor, B.Landreth, and G.Moddel. Integrating mode for an optically addressed spatial light modulator. *Applied Optics*, 32(17):3064-3067, 1993.

Diffraction Properties of Ferroelectric Liquid Crystal Optically-Addressed Spatial Light Modulators

Pierre R. Barbier

Laboratory for Physical Sciences - University of Maryland
8050 Greenmead Drive - College Park, MD 20740 - USA
E-mail: barbier@eng.umd.edu - Tel.: (301) 935-6441

1. Introduction

Ferroelectric liquid crystal (FLC) optically addressed spatial light modulators (OASLMs) exhibit high spatial resolution (≈ 50 -100 lp/mm) and short switching times (≈ 100 μ s) [1]. These devices can be used to produce dynamic holograms in optical computing [2] or phase conjugation applications [3]. To use FLC OASLMs in the diffractive mode it is important to understand their diffraction characteristics. In this paper we present OASLM diffraction efficiency measurements and analyze the switching behavior of the diffracted light as a function of the FLC grating characteristics. We then compare the experimental results with the results of the analysis and discuss the device limitations which affect the diffraction efficiency.

The analysis is based on the fact that in response to a write-light intensity grating FLC OASLMs form a birefringence-orientation grating which affects the polarization and intensity of the diffracted light. Moreover, even though they are bistable in steady-state, FLC OASLMs are operated in a transient analog manner to take advantage of the fast response of FLCs [4]. Consequently, when an intensity grating illuminates a OASLM the resulting FLC birefringence-orientation grating modulates in time the intensity and polarization of the diffracted light.

2. Optically addressed spatial light modulator

The OASLM used in this study incorporates a ferroelectric liquid crystal (FLC) birefringent layer and a hydrogenated amorphous silicon (a-Si:H) p-i-n photosensor sandwiched between two optical flats each coated with a transparent electrode [1, 5]. The OASLM is driven by applying a voltage waveform between the two electrodes and impressing a write image into the photosensor. Under the effect of the applied voltage and of the write light photocarriers are generated into the photosensor which modify locally the electric field and thus the orientation of the FLC.

The liquid crystal is a bistable surface-stabilized FLC (Merck ZLI 5014-100) obtained by appropriate surface treatment prior to OASLM assembly [1]. The molecules rotate by 45° (22.5° tilt angle) from one stable state to the other by applying a voltage larger than a threshold value. The thickness of the birefringent FLC is such that it forms a halfwave plate in reflection at 633 nm wavelength.

By convention when the voltage is positive the photodiode is forward biased and all the applied voltage drops uniformly across the FLC which orients to its *off* stable state. When the voltage is negative the photodiode is reverse biased. In the absence of write light no negative voltage forms across the FLC which remains in the off state. In the presence of write light into the a-Si:H photosensor electrons are photogenerated which drift to and accumulate at the FLC interface. These electrons build up locally a voltage across the FLC at a rate which is proportional to the write-light intensity [6]. The FLC eventually rotates under the influence of this negative electric field to its other bistable orientation, the *on* state. The on-switching time is inversely dependent on the write-light intensity [7]. In summary the OASLM forms an FLC birefringence-orientation replica of the write image during the negative voltage cycles of the drive waveform. This replica is reset (erased) during each positive voltage cycle.

The FLC orientation is read with a collimated 633 nm-wavelength laser beam which is linearly-polarized along one of the optical axes of the FLC in the off state (positive voltage). Because of the index of refraction discontinuity at the FLC/a-Si:H interface, 23% of the light is reflected back along the extraordinary axis of 16% along the ordinary axis (neglecting 4% transmission loss at the air/glass interface). The polarization of the light which is reflected back is identical to that of the incoming light where the FLC has not switched and is rotated by 90° where the FLC has fully switched. Thus, the read-out light carries a polarization replica of the write image. This polarization replica

can be converted into an intensity replica by filtering through a crossed analyzer [1].

If an intensity grating illuminates the photosensor and forms a birefringence-orientation grating in the FLC, the polarization of the reflected light is modulated between 0° and 90° with the same spatial frequency as the input grating. The diffracted light is composed of a combination of polarizations as discussed in part 5 and no polarizer is necessary to observe the diffracted light on contrary of imaging applications. Note that a grating can also be formed by interfering two laser beams into the a-Si:H photosensor through the FLC layer such as in the case of phase conjugation [3]. In this case even though the FLC orientation change the absolute polarization of the write beams, it does not affect their relative polarizations nor their interference pattern.

3. Experimental results

The OASLM is driven with a 500 Hz, 0/10 V square wave. Two collimated laser beams at 515 nm interfere forming a $100 \mu\text{m}$ -period sine intensity grating into the OASLM. The OASLM is read out with a low-intensity collimated beam at 633 nm linearly-polarized along the extraordinary axis of the FLC in the off state. The 1st order diffracted light is focused by a lens onto a fast photodetector. The diffraction efficiency is obtained by normalizing the diffracted intensity to that of the back reflected light intensity when the OASLM is off. In Fig. 1(a) the diffraction efficiency and in Fig. 1(b) the reflected light intensity (0th order) which has been filtered through a crossed analyzer are plotted versus time for various write light intensities.

From these experimental results the following observations can be made: 1) the diffraction efficiency increases with time, reaches a maximum and decreases when the write-light intensity is large; 2) immediately after the reset voltage pulse is applied, the diffraction efficiency rapidly peaks before switching off; 3) the crossed-polarized reflected light intensity increases with time until it saturates with a response time inversely dependent on the write-light intensity.

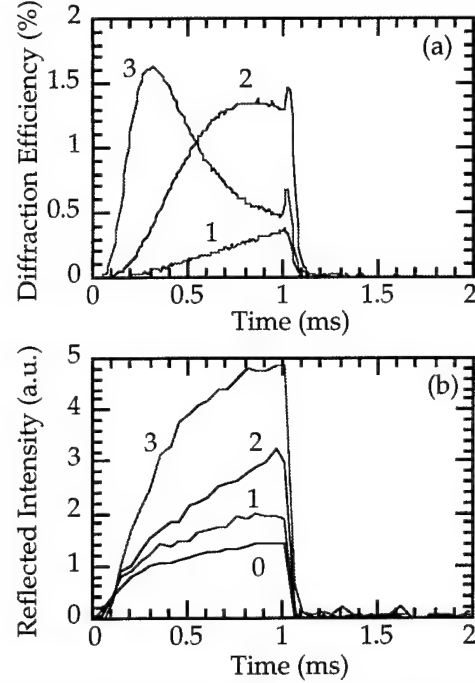


Fig. 1: (a) Diffraction efficiency and (b) crossed-polarized reflected light intensity versus time for 0 (0), 6 (1), 50 (2) and $100 \mu\text{W}/\text{cm}^2$ (3) write-light intensities. The OASLM was driven with 0 V from 0 to 1 ms and with 10 V from 1 to 2 ms.

4. Polarization of diffracted light

The output polarization of a linearly polarized light going through a birefringent plate can be calculated using the Jones matrix decomposition [8]. The FLC thickness d can be written such as $2\pi d \Delta n/\lambda = \pi + \delta$ where Δn is the birefringence, λ is the wavelength and δ is an angle representing the deviation from the perfect halfwave plate condition ($\delta=0$ in the case of a perfect halfwave plate). To simplify the calculation without restricting its physical meaning we assume that the input light is linearly polarized along the x axis ($\sigma_x=1, \sigma_y=0$) and that the FLC is oriented at an angle ϕ from the x axis. The output polarization is then

$$\begin{bmatrix} \sigma_x \\ \sigma_y \end{bmatrix} = \begin{bmatrix} \cos(\frac{\delta}{2}) \cos(2\phi) + i \sin(\frac{\delta}{2}) \\ \cos(\frac{\delta}{2}) \sin(2\phi) \end{bmatrix}. \quad (1)$$

As expressed in Eq. 1 the polarization of the output light is a combination of two linear polarizations. In the case of a perfect halfwave plate ($\delta=0$) the output polarization is linear and rotated by 2ϕ from the input polarization. In the case of a FLC with a 22.5° tilt angle ϕ varies be-

tween its two stable orientations 0 and $\pi/4$. When $\phi=0$ the output polarization is the same as that of the input light and when $\phi=\pi/4$ it has rotated by 90° . In the case of an imperfect halfwave plate, the output polarization is elliptical. When $\phi=\pi/4$ the elliptical polarization is oriented at 2ϕ with an ellipticity of $\tan(\delta/2)$.

Since surface stabilized FLC (SSFLC) is a bistable material it may form a binary birefringence pattern when operated in steady-state. When a grating is formed into the binary FLC the polarization of the output light and the diffraction efficiency of the grating can be calculated as in Ref. [8, 9]. However, FLC OASLMs are generally driven with a $\approx 1\text{kHz}$ voltage square wave in the reset mode [1]. In this case the switching dynamics of the FLC depends on the applied voltage and write light intensity. Thus the orientation ϕ of the FLC varies in time and in space between 0 and $\pi/4$. In imaging operation temporal averaging of this transient may be used to achieve gray levels [4].

5. Diffraction efficiency

When an intensity grating illuminates the photosensor of an OASLM, the FLC forms a birefringence-orientation grating which evolves in time but not in spatial frequency. Consequently the diffracted light varies temporally in intensity, in phase and in polarization but not in diffraction angle. Moreover, the diffracted light is linearly polarized if $\delta=0$, and is elliptically polarized if not. In any case to maximize the intensity of the diffracted light no analyzer should be used.

Assuming that the FLC forms a birefringence orientation grating, $\phi(z)$ along the z axis, the diffraction efficiency can be calculated by taking the sum of the diffraction efficiencies resulting from the two amplitude and phase gratings obtained by replacing $\phi(z)$ into Eq. (1). The diffraction efficiency for each polarization can be calculated using a computer by taking the Fourier transform of the transmission gratings $\sigma_x(\phi(z))$ and $\sigma_y(\phi(z))$.

The FLC birefringence-orientation grating is assumed to be binary or sinusoidal. The binary grating of period L is expressed by

$$\phi(z) = \begin{cases} \alpha & \text{if } 0 \leq z < L/2 \\ \beta & \text{if } L/2 \leq z < L \end{cases} \quad (2)$$

and the sine grating by

$$\phi(z) = \text{Max} \left[\left(\alpha \frac{\cos(2\pi z/L) + 1}{2} + \beta \right), \pi/4 \right]. \quad (3)$$

The parameter α corresponds to the maximum value of $\phi(z)$ below saturation at $\pi/4$. The parameter β corresponds to the minimum value of $\phi(z)$. The computed diffraction efficiencies are plotted versus α for $\beta=0$ in Fig. 2(a) and versus β for $\alpha=\pi/4$ in Fig. 2(b) in the case of a perfect halfwave plate ($\delta=0$) and that of a 20% imperfect halfwave plate ($\delta=0.2\pi$). Note that the computed diffraction efficiency of the perfect halfwave plate binary grating yield the same results as the analytically calculated $\text{sinc}^2(\alpha)$ function [10].

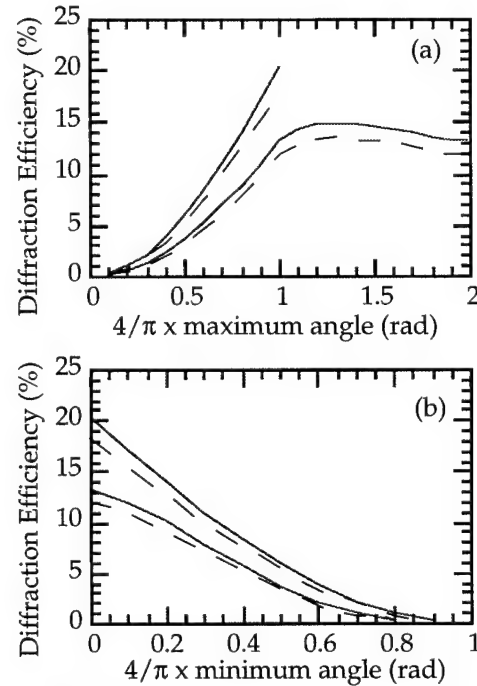


Fig. 2: Calculated diffraction efficiencies of a binary grating (top curves, Eq. (2)) and of a sine (bottom curves, Eq. (3)) birefringence-orientation grating versus maximum angle, α , for a minimum angle $\beta=0$ (a) and versus minimum angle, β , for a maximum angle $\alpha=\pi/4$ (b). The solid lines are for a perfect halfwave plate ($\delta=0$) plate and the dashed lines for a 20% imperfect halfwave plate ($\delta=0.2\pi$).

6. Discussion

As shown by the dashed curves in Fig. (2) the diffraction efficiency decreases slightly when the halfwave plate condition is not perfectly filled which occurs in the case of thickness deviation or of wavelength change.

As shown in Fig. 2 the diffraction efficiency of a sine FLC grating is significantly smaller than that of a perfect binary grating. In both cases the diffraction efficiency increases as the maximum orientation, α , of the FLC increases as shown in Fig. 2(a). After the sine grating saturates at an angle of $\pi/4$, the diffraction efficiency reaches a maximum and decreases. Saturation happens experimentally is the OASLM write-light intensity is large as shown in curve 3 of Fig. 1(b) [4]. This effect can be observed experimentally in Fig. 1(a) where in the case of the intense write light the diffraction efficiency peaks very rapidly in time as the FLC grating reaches an optimum distribution and then decreases as more and more of the FLC reaches $\pi/4$ (curve 3).

As shown in Fig. 2(b) if the FLC switches on in the absence of write light due to electrical effects in the OASLM the minimum angle β increases degrading the diffraction efficiency. This electrical dark turn-on of the FLC can be observed in curve 0 of Fig. 1(b). This effect may explain in Fig. 1(a) why the diffraction efficiency maximum in the case of the medium write-light conditions (curve 2) is less than that of the intense write-light conditions (curve 3). Electrical dark turn-on, i.e., an increase of β , is caused by capacitive or dark current effects in the OASLM [6] or by a poor visibility of the intensity fringes in the photosensor due to optics imperfections or to multiple reflections within the OASLM glass substrate [4, 7]. The electrical dark turn-on increases with operation time of the OASLM reducing its diffraction efficiency.

Immediately after a positive voltage is applied to reset the FLC to its off state the diffraction efficiency increases very rapidly before switching off. This is explain by the fact that FLC molecules rotate under the effect of a torque due to the interaction of the electric field and of the spontaneous polarization of the molecules [11]. This torque is larger when these two vectors are orthogonally oriented, i.e., when the FLC molecules are in between their bistable states, than when they are parallel. As a consequence, immediately after the reset voltage is applied the FLC molecules which are not oriented at $\pi/4$ switch rapidly to 0, i.e., β decreases rapidly to 0, resulting in a diffraction efficiency surge as observed in Fig. 2(a). This surge is eventually followed by a decay to 0 as the FLC switches off entirely.

7. Conclusions

An analysis of the diffraction properties of a birefringent-orientation grating was presented. The results of this analysis were used to explain the time dependence of experimental diffraction efficiency data of a FLC OASLM.

It was observed that even though FLCs are bistable, FLC OASLMs operate in transient forming a time-dependent analog birefringence-orientation grating. Consequently, the characteristics of the diffracted light are strongly time-dependent. The light diffracted off an OASLM is linearly polarized along a time-varying orientation in the case of a perfect FLC halfwave plate. The diffraction efficiency of a OASLM depends strongly on the minimum and maximum angles of the angular spread and on the profile of the grating. A sine grating which is closer to experimental conditions yields a lower diffraction efficiency than a binary grating. Both electrical dark turn-on which tends to rotate FLC molecules in the absence of write light and grating saturation at the maximum FLC orientation degrade significantly the diffraction efficiency. On the other hand deviation from the perfect halfwave plate conditions slightly affect the diffraction efficiency.

References

1. Model, G., Ch. 11, in *Amorphous and Microcrystalline Semiconductor Devices: Optoelectronic Devices*, J. Kanicki, Editor. 1991, Artech House, Boston, London., pp. 369-412.
2. Fukushima, S., T. Kurokawa, and M. Ohno, *Appl. Phys. Lett.* 58(8), pp. 787-789 (1991).
3. Mao, C.C., K.M. Johnson, and G. Model, *Ferroelectrics* 114, pp. 44-53 (1991).
4. Landreth, B. and G. Model, *SPIE Vol.* 1296, pp. 64-72 (1990).
5. Displaytech, Inc., 2200 Central Ave-Boulder, CO 80301,
6. Barbier, P.R. and G. Model, *Appl. Opt.* 31(20), pp. 3898-3907 (1992).
7. Landreth, B. and G. Model, *Appl. Opt.* 31(20), pp. 3937-3944 (1992).
8. O'Callaghan, M.J. and M.A. Hanschy, *Opt. Lett.* 16(10), pp. 770-772 (1991).
9. O'Callahan, M.J., personal comm., 1993.
10. Born, M. and E. Wolf, *Principle of Optics*. Oxford, Pergamon Press, 1987.
11. Towler, M.J., J.C. Jones, and E.P. Raynes, *Liquid Crystals* 11(3), pp. 365-371 (1992).

MIS model of optically addressed spatial light modulators

Li Wang and Garret Model

Department of Electrical and Computer Engineering
 Optoelectronic Computing Systems Center
 University of Colorado, Campus Box 425
 Boulder, CO 80309-0425
 Tel: (303) 492-1889, Email: model@boulder.colorado.edu

I Introduction

Optically addressed spatial light modulators (OASLMs) that incorporate nematic liquid crystal (NLC) light modulating layers find many applications in optical information processing due to their gray-scale capability. These devices are usually driven with sine or square-wave voltages at frequencies of 1-10 kHz that are beyond those to which the NLC can respond. The NLC responds to the rms value of the applied voltage across it. Some NLC OASLMs incorporate photosensors of hydrogenated amorphous silicon (a-Si:H) that offer high resolution and high sensitivity[1-6]. We have made some NLC OASLMs with intrinsic a-Si:H for phase-modulation applications. The observed behavior from these devices cannot be explaining using a resistor-capacitor circuit model in which the a-Si:H is treated as a photoconductor. Instead, a metal-insulator-semiconductor (MIS) model is found to fit the experimental data very well. The indium-tin oxide (ITO) electrode and the NLC layer in the OASLM form the respective metal and insulator layers. This MIS model can be used to optimize the thicknesses of the NLC and a-Si:H layers in an OASLM to obtain large phase or amplitude modulation.

II a-Si:H-ITO interface

The intrinsic a-Si:H that is used in a NLC OASLM is deposited on ITO-coated optical flats

by plasma-enhanced chemical vapor deposition and is slightly *n*-type. Between the intrinsic a-Si:H and the ITO electrode a Schottky barrier forms and prevents electrons from flowing freely from the ITO electrode into the a-Si:H. Fig. 1 shows a typical current-voltage curve for such a structure.

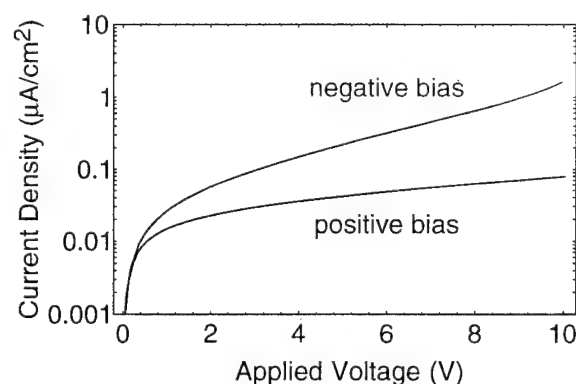


Fig. 1 Current-voltage characteristics of a 2.85- μm intrinsic a-Si:H on ITO. A Cr contact to the other side of a-Si:H is considered as the positive electrode.

The relatively small current density in negative-bias is limited by the other Schottky barrier between the a-Si:H and the Cr contact. It is not suitable to model the intrinsic a-Si:H layer as a photoconductor due to the rectifying behavior of the a-Si:H-ITO interface. This Schottky barrier is taken into account in the MIS model and is found to be important in modulating the voltage across the NLC in the OASLM under illumination.

III MIS model of NLC OASLM

The structure of the NLC OASLM we investigate is shown in Fig. 2(a). During the first half-cycle of a square driving wave, a negative voltage is applied to the NLC side. The a-Si:H-ITO Schottky barrier is under negative bias. Electrons in the intrinsic a-Si:H are swept out toward the a-Si:H-ITO interface and a depletion layer forms near the NLC-a-Si:H interface. When electron-hole pairs are generated by incident photons, holes move toward the NLC-a-Si:H interface under the internal electric field. The depletion width decreases and a very thin layer of holes builds up near the interface. If enough photogenerated holes are collected during this period, the depletion layer disappears and virtually all the applied voltage is dropped across the NLC. The voltage increase $\Delta V_-(t)$ across the NLC resulting from illumination is equal to the voltage decrease in the a-Si:H in magnitude. In the first half-cycle of the driving wave, the maximum obtainable voltage modulation is the voltage that is initially dropped across the a-Si:H layer. $\Delta V_-(t)$ is a function of the write-light intensity, the applied voltage, the thicknesses of the NLC and a-Si:H, and the effective density of localized gap states in a-Si:H. The a-Si:H can be fully depleted for a small effective density of localized gap states or a thin NLC.

During the second half-cycle of the square driving wave, a positive voltage is applied to the NLC side. Fig. 2(b) shows the corresponding charge distribution in a-Si:H without illumination. Because the positive-bias current through the Schottky barrier is so small (4×10^{-8} A/cm² at 5 V) the number of electrons that are injected from the ITO electrode into the a-Si:H is negligible. A very thin layer of electrons is created near the NLC-a-Si:H interface. A

depletion layer also forms near the a-Si:H-ITO Schottky barrier. If the a-Si:H layer is fully depleted during the first half-cycle of the

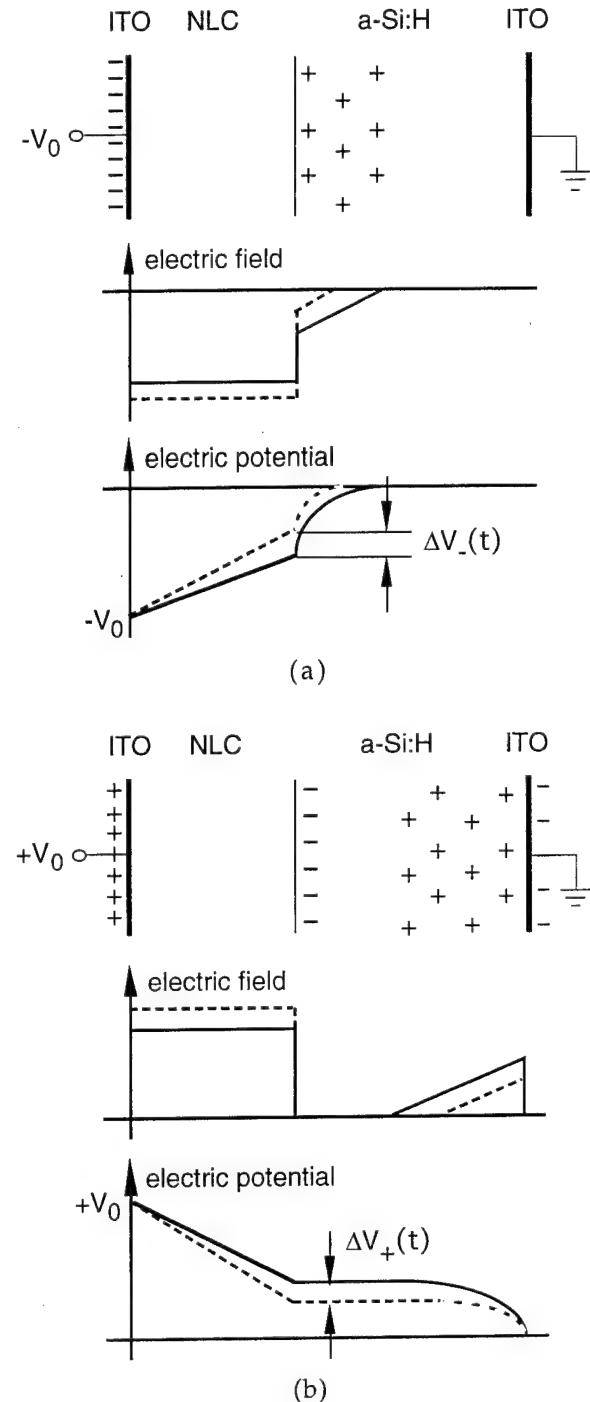


Fig. 2. Charge, electric field, and voltage distribution in the NLC OASLM under (a) negative, and (b) positive bias with (dashed lines) and without (solid lines) illumination.

driving wave, then no free electrons exist and the depletion region extends over the entire width of the a-Si:H layer. As is the case in Fig. 2(a), photogenerated electron-hole pairs reduce the depletion width and thus the voltage across the a-Si:H layer. The voltage increase $\Delta V_+(t)$ in NLC is indicated in Fig. 2(b). The rms voltage change in the NLC resulting from illumination during a full cycle of the driving wave can be calculated from $\Delta V_-(t)$ and $\Delta V_+(t)$.

If the a-Si:H-ITO interface is an ohmic contact instead of a Schottky barrier, then electrons can flow freely from the ITO electrode into the a-Si:H. When the NLC side is positively biased, the NLC layer is charged by the electrons flowing through the a-Si:H-ITO interface. All the applied voltage is dropped across the NLC. No voltage change across the NLC can be obtained by illumination during the second half-cycle of the driving wave. $\Delta V_+(t) \equiv 0$ in this case. Therefore the voltage modulation in NLC, thus the phase or amplitude modulation from the NLC OASLM would decrease significantly without the Schottky barrier at the a-Si:H-ITO interface.

Once the optical response of the NLC to the driving voltage is known, the phase or amplitude modulation from the OASLM can be calculated from this MIS model.

IV Experimental results

Fig. 3 shows the change of the extraordinary index in parallel-aligned NLC with the applied voltage for different thicknesses. The extraordinary index of the NLC for normal incident light decreases with the applied voltage because the tilt of the molecules increases with the electric field. Once the rms voltage modulation in the NLC is known, the phase modulation from the NLC can be calculated from

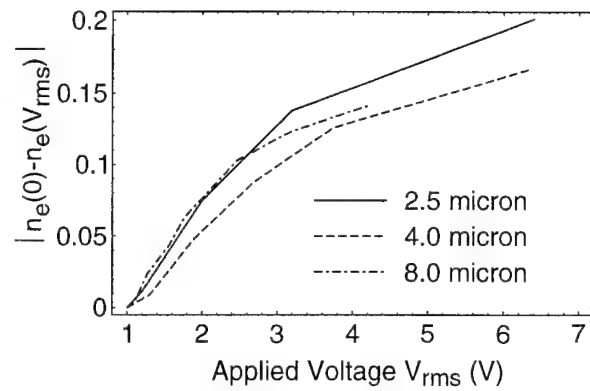


Fig. 3 Absolute change of the extraordinary index of parallel-aligned NLC with applied voltage V_{rms} . The thickness of each cell is shown in the figure.

this figure. It is interesting to note that the extraordinary index change in NLC depends only on the voltage, not on the thickness of the NLC or the applied electric field.

We made three NLC OASLMs with different NLC thicknesses. An intensity sinusoidal grating at 515 nm wavelength was written onto these devices. The maximum diffraction efficiency for a readout wavelength of 633 nm was obtained by adjusting the intensity of the grating, the rms voltage of the driving waveform, and the polarization of the read light with respect to the optic axis of the NLC. We calculated the corresponding phase modulation from the diffraction efficiency by assuming creation of a sinusoidal phase grating in the NLC layer. We simulated and obtained the phase modulation from the MIS model by adjusting the effective density of localized gap states in a-Si:H. The fitting value for this effective density is $7.5 \times 10^{13} \text{ cm}^{-3}$. This number is much lower than the density of states in a-Si:H because only a small fraction of these states can release and trap charge within one cycle of the driving wave. The device parameters, experimental and MIS-model results are listed in Table I.

Table I. Experimental results and simulation from the MIS model. The intrinsic a-Si:H is 4- μm thick. All the OASLMs are driven with a sine wave having rms voltage of 3.1 V.

thickness of NLC (μm)	2.5	4.0	8.0
maximum diffraction efficiency (%)	26	13	4.2
measured phase modulation (π)	0.80	0.50	0.27
phase modulation: MIS model (π)	0.81	0.58	0.25

The relationship between the needed density of photogenerated charge and a given phase modulation or diffraction efficiency for the NLC OASLM is also predicted from the MIS model. The write-light intensity corresponding to that diffraction efficiency should increase linearly with the driving frequency. Fig. 4 shows the experimental results from an OASLM that consists of a 3- μm intrinsic a-Si:H and 2- μm parallel-aligned NLC. The linearity between the write-light intensity and the driving frequency holds up very nicely from 0.5 to 10 kHz.

It is clear that the experimental data from

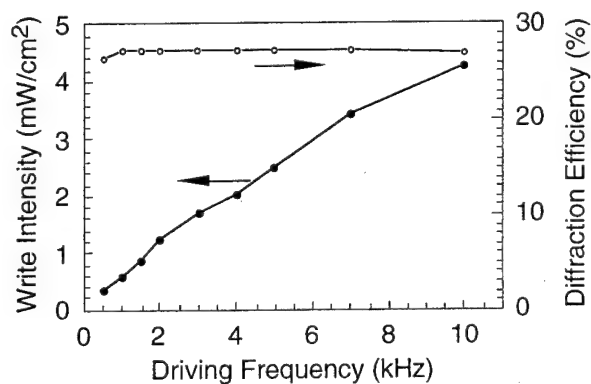


Fig. 4 Write light intensity at 515 nm wavelength and the corresponding diffraction efficiency at 633 nm wavelength versus the driving frequency. The NLC OASLM is driven under a square-wave with rms voltage of 2.8 V.

the NLC OASLMs can be interpreted correctly with the MIS model.

IV Conclusions

A MIS model for a NLC OASLM that incorporates photosensors of intrinsic a-Si:H is developed. It fits the experimental data very well. This model can be used to optimize the thicknesses of NLC and a-Si:H in the OASLM to obtain maximum phase or amplitude modulation and sensitivity. Very thin NLC and a-Si:H layers are often needed for OASLMs with high spatial resolutions[7]. At the same time, however, high sensitivity and large modulation favor relatively thick NLC and a-Si:H layers. This MIS model can be used together with the resolution model to design NLC OASLMs with overall high performance.

References

1. N. Mukohzaka, N. Yoshida, H. Toyoda, Y. Kobayashi, and T. Hara, *Appl. Opt.* **33**, 2804 (1994).
2. P. R. Ashley and J. H. Davis, *Appl. Opt.* **26**, 241 (1987).
3. R. D. Sterling, R. D. Te Kolste, J. M. Haggerty, T. C. Borah, and W. P. Bleha, *SID'90 Digest*, p. 327.
4. M. Powell, C. Powles, and J. Bagshaw, *SPIE Proceedings*, Vol. 936 (1988), pp. 68-75.
5. L. Samuelson, H. Wieder, C. R. Guarnieri, J. Chevallier, and A. Onton, *Appl. Phys. Lett.* **34**, 450 (1979).
6. J. Qiao, G. Han, P. Du, W. Han, W. Huang, and Z. Ding, in *Materials Research Society Symposium Proceedings*, Vol. 219 (1991), pp. 179-184.
7. W. R. Roach, *IEEE Trans. Electron Devices* **ED-21**, 453 (1974).

Photorefractive Persistence and Erasure in AlGaAs Spatial Light Modulators

S. R. Bowman, W. S. Rabinovich
Optical Sciences Division, Code 5640
Naval Research Laboratory, Washington, D. C. 20375-5320

D. S. Katzer
Electronics Sciences and Technology Division, Code 6850
Naval Research Laboratory, Washington, D. C. 20375-5374

C. S. Kyono
Motorola, MS #M350,
2200 West Broadway Road, Mesa, AZ 85202

Spatial light modulators have been demonstrated by a number of groups using GaAs/AlGaAs quantum well materials. These optical modulators utilize the enhanced electro-absorption and electro-dispersion associated with quantum confined excitons. Many of these devices use pixelated electrodes to apply a spatially varying electric field across the quantum well layer. We have investigated non-pixelated devices in which the applied field is varied through spatially modulated illumination. These optically addressed spatial light modulators (OASLM) are simple to fabricate and have demonstrated higher spatial resolution than pixelated devices.[1-4] Here we present recent experiments designed to determine the lifetime of the transient space charge distributions generated in GaAs/AlGaAs OASLM's.

Experiments were conducted on two similar OASLM devices. Both devices were fabricated from the MQW layers of a single wafer with 75 periods of 10 nm GaAs wells separated by 3.5 nm of $\text{Al}_{0.3}\text{Ga}_{0.7}\text{As}$ barriers. The MQW layer was sandwiched between two high resistivity cladding layers. These cladding layers consisted of 30 nm of low temperature (LT) grown $\text{Al}_{0.3}\text{Ga}_{0.7}\text{As}$. These LT layers were grown at a substrate temperature of 330 C and annealed at 580 C for 30 minutes. Low temperature AlGaAs grown under similar conditions has shown dark resistivities of $10^{12} \Omega\text{-cm}$ and trap densities higher than 10^{18} 1/cm^3 . [5] It was shown in a previous report that these LT cladding layer significantly improve the spatial resolution of these OASLM devices.[4]

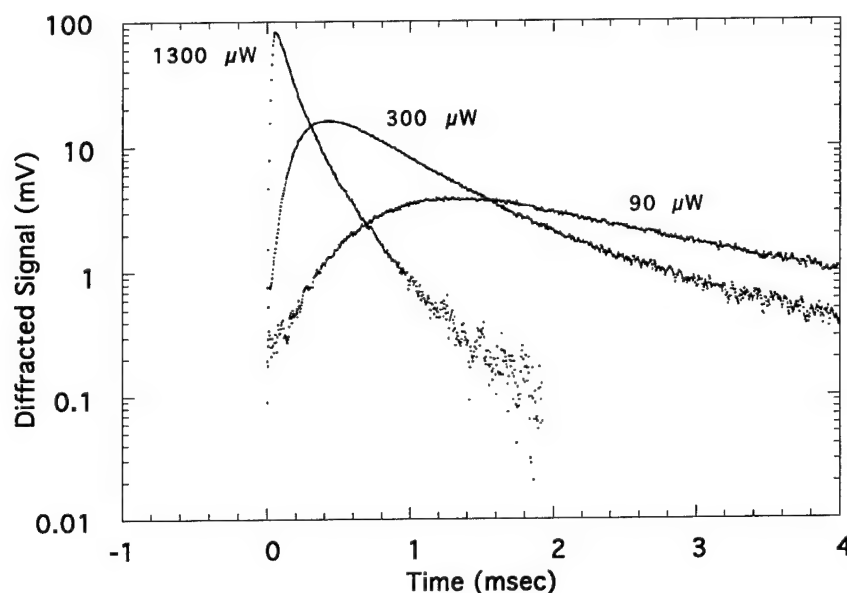
Both devices were fabricated using an epitaxial lift-off process and solid phase bonding to a quartz substrate coated with a transparent Cr/Pd/Au electrode. A 400 nm thick silicon nitride dielectric layer was then deposited on the top of the MQW followed by a Cr/Au transparent electrode. The 1 μm thick MQW layer of one device was made "semi-insulating" through proton implantation. A multiple step implantation process was used to generate a uniform defect density of approximately $4 \times 10^{16} \text{ 1/cm}^3$. The MQW layers in the other device were as grown "intrinsic" material. The details of the fabrication process and characterization of these devices have been reported elsewhere [3].

The testing of these devices used a CW titanium sapphire laser in a self-diffraction experiment. To produce a grating pattern on the OASLM's we used an achromatic interferometer arrangement. The beam from the Titanium sapphire laser was passed through a fixed Ronchi ruling and dispersed into many orders. The ± 1 orders were then recombined onto the OASLM using a telescope. When the laser was tuned near the electro-absorption peak and a square wave

voltage was applied to the OASLM, a transient spatial grating was created in the absorption and index of refraction of the quantum well. The first order diffraction of one of the pump beams was measured using a silicon PIN photodiode.

Under bright continuous illumination of the pump beams ($>1\text{mW/cm}^2$) these diffraction experiments show that the rise times of the transient gratings are proportional to pump intensity, see Figure 1. This is as expected since the build up of the space charge distribution which screens the applied field is limited by the rate of photocarrier production. Decay rates of the gratings were also observed to increase with CW pump intensity. This can be explained as a result of the partial illumination of the "dark" regions of the interference fringes or by non-unity fringe visibility.

Figure 1. Transient diffracted signal under continuous pumping at 852 nm. Field polarity flips at time = 0.



In order to study the effects of charge transport on the grating persistence, a series of pulsed pump/probe experiments were conducted. A traveling wave, acousto-optic modulator was used as a fast shutter for the titanium sapphire laser. Gratings were written onto the OASLM's with short ($\sim 200\text{ }\mu\text{sec}$) pump pulses. Grating persistence was then determined with a delayed $10\text{ }\mu\text{sec}$ probe pulses. Approximately 1 msec grating lifetimes were observed in both the intrinsic and the semi-insulating devices. Grating lifetime was found to rapidly decrease as the spatial period of the grating was reduced below $10\text{ }\mu\text{m}$, Figure 2. Grating persistence also decreased with increasing applied electric field.

These experiments are consistent with our previous observations that the CW grating strength in these devices also falls off rapidly below $10\text{ }\mu\text{m}$ grating periods. The experiments suggest that the observed grating decay is due to blurring of the initial space charge distribution in the LT cladding layers. Although the charges are trapped in defects in the LT layers, carrier migration is possible via trap-to-trap hopping mechanisms. Our results indicate that for speeds up to several kHz the sensitivity and spatial resolution of these devices will be limited by this grating decay mechanism.

Figure 2. Decay of the diffracted signal from the semi-insulating OASLM with ± 10 Volts applied.

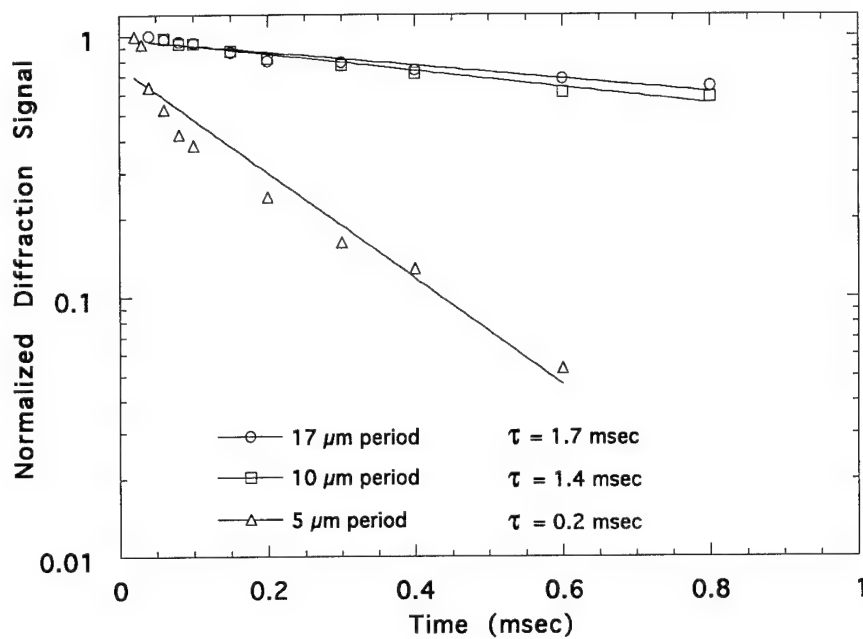
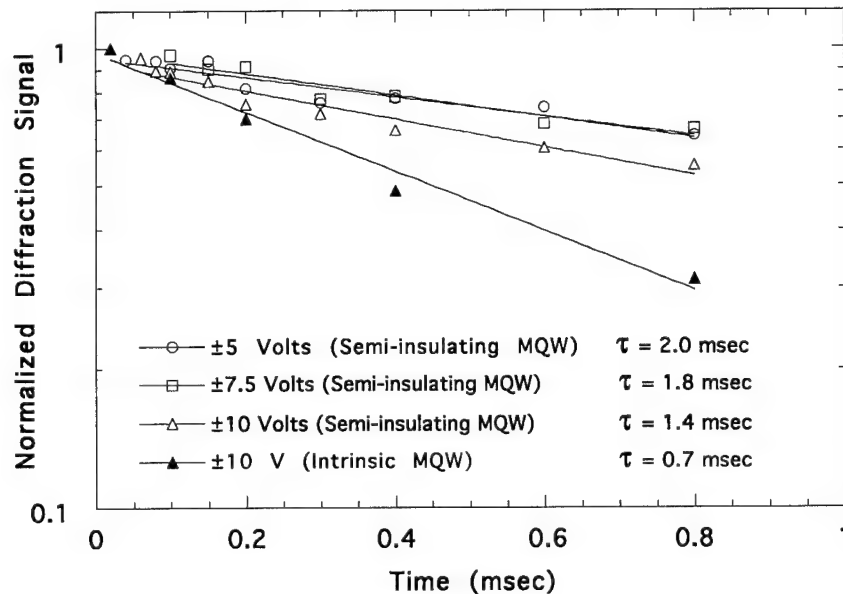


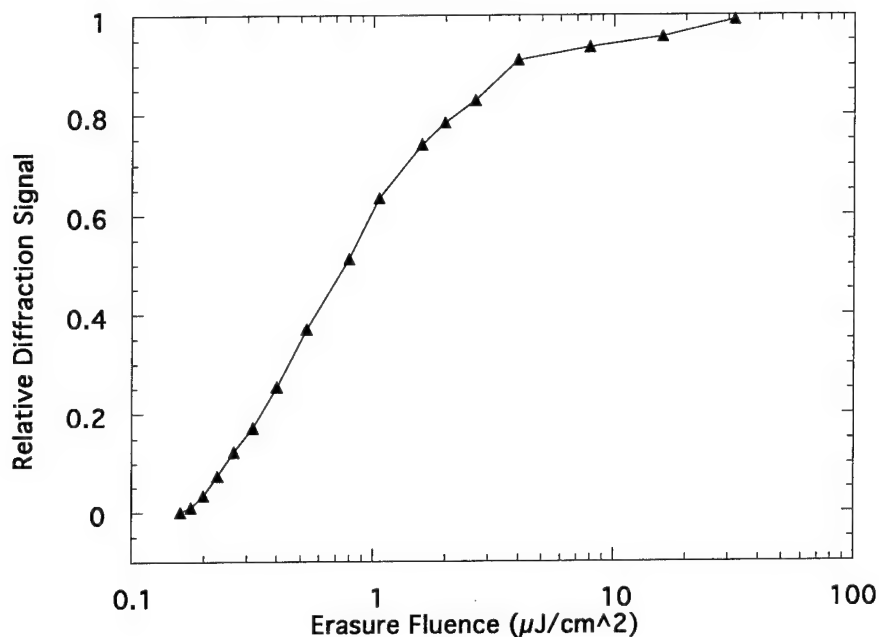
Figure 3. Decay of the diffracted signal from a 17 μm period grating.



The pump/probe experiments described above were performed with the OASLM in the dark. We observed that while the gratings in the OASLM's would completely decay in several milliseconds, a new grating could not be written until an erasure procedure was performed. In order to erase the previous space charge distribution it was necessary to reversed the polarity of

the applied field and illuminate the device. Simple polarity reversal does not appear to free the trapped carriers in the LT cladding layers. New photocarriers seem to be required to release the trapped carriers through recombination. A controlled uniform illumination experiment using a HeNe laser revealed that the required erasure fluence is approximately equal to the fluence required to write a grating, Figure 4.

Figure 4. Diffraction signal vs. uniform 633 nm exposure. The pump pulse fluence was $1 \mu\text{J}/\text{cm}^2$.



References

- [1] D. D. Nolte, D. H. Olson, G. E. Doran, W. H. Knox and A. M. Glass, "Resonant photodiffractive effect in semi-insulating multiple quantum wells", *J. Opt. Soc. Am. B* **7**, 2217 (1990).
- [2] A. Partovi, A. M. Glass, D. H. Olson, G. J. Zyzdik, H. M. O'Bryan, T. H. Chiu and W. H. Knox, "Cr-doped GaAs/AlGaAs semi-insulating multiple quantum well photorefractive devices", *Appl. Phys. Lett.* **62**, 464 (1993).
- [3] C. S. Kyono, K. Ikossi-Anastasiou, W. S. Rabinovich, S. R. Bowman, D. S. Katzer and A. J. Tsao, "GaAs/AlGaAs multi-quantum well resonant photorefractive devices fabricated using epitaxial lift-off", *Appl. Phys. Lett.* **64**, 2244 (1994).
- [4] S. R. Bowman, W. S. Rabinovich, C. S. Kyono, D. S. Katzer and K. Ikossi-Anastasiou, "High resolution spatial light modulators using GaAs/AlGaAs multiple quantum wells", *Appl. Phys. Lett.* **65**, 956 (1994).
- [5] Ashish K. Verma, Jay Tu, J. S. Smith, Hiroshi Fujioka and Eicke R. Weber, "Electrical characteristics of low temperature AlGaAs", *Journal of Electronic Materials* **22**, 1417 (1993).

Fundamental Constraints on SLMs Supporting N x N Fan-in/Fan-out

by

H. John Caulfield, Marius P. Schamschula, and Leo Zhang

The Center for Applied Optical Sciences

Department of Physics

Alabama A & M University

P. O. Box 1268

Normal, AL 35762

Tel. (205) 851-5870

The recent trend to use small SLMs (spatial light modulators) together with low f /numbers has stretched the capabilities of most SLMs¹. For common SLMs, such as those based on ferroelectric liquid-crystals or the electro-optic effect, possess a small field of view, usually no more than a 5° half-angle. Low f /numbers such as those approaching 1, with half-angles up to 45° greatly exceed the capabilities of such SLMs.

The transmittance of a given pixel of an SLM is strongly angularly dependent. This angular dependence is due to such factors as the thickness of the modulator along the optical axis, the obliquity of the illumination, the transmittance at the interfaces given by the Fresnel equations, and the physics of the birefringent materials.

What are the limits of the fan-in/fan-out capacity of an SLM? We can find some guidance from Gabor's "Theory of Communication."² Gabor introduces the concept of 'Logons'. A logon is a unit of information specified as a function of space and angle.

More precisely it is defined in terms of an area, a solid angle and the wavelength of the illuminating light,

$$L = A\Omega/\lambda^2.$$

Logons have the following properties: L is conserved by all diffraction limited optical systems, and optical systems can decrease but not increase L . $L = 1$ is equivalent to a single mode, a diffraction limited, or a spatially coherent beam. Most SLMs are designed for this specific case. LCTVs, now sometimes used in optical Fourier transform processors were designed to transmit one logon/pixel. Similarly Pockels cell electro-optic modulators were developed to amplitude modulate single light beams, usually plane wave or Gaussian beams, again $L = 1$.

Optical processors however have much higher logon numbers. For example take a field of view of 5° (HWHM), a value better than most SLMs but less than required by some optical processors. Further assume the area of a pixel $100 \mu\text{m}$ square and the area to be 10^{-2} cm^2 , and a wavelength of 500 nm . Thus $\Omega = \pi (5^\circ \cdot \pi/180^\circ)^2 = 0.024 \text{ Sterad}$. Now we have $L = 95600$ for one pixel, (allowing up to a 309×309 fan-in) and almost 1.5×10^9 logons for a 128×128 pixel SLM! In both cases this is a logon count much greater than 1. Even if we constrain the input beam to 1° , this still yields 3800 logons/pixel.

In Charts 1 and 2 we show the relationship between fan-in/fan-out (N) and the pixel and SLM sizes.

Given the size requirements given in Charts 1 and 2, how does one construct optical processors? The answer can be found in the expression defining the logon. For small angles, the number of logons is proportional to the area of the pixel and the square of the half angle. We may trade this angle for area. Thus we can conserve the number of logons if we adjust the length of the pixel sides inversely to the change in allowed half angle.

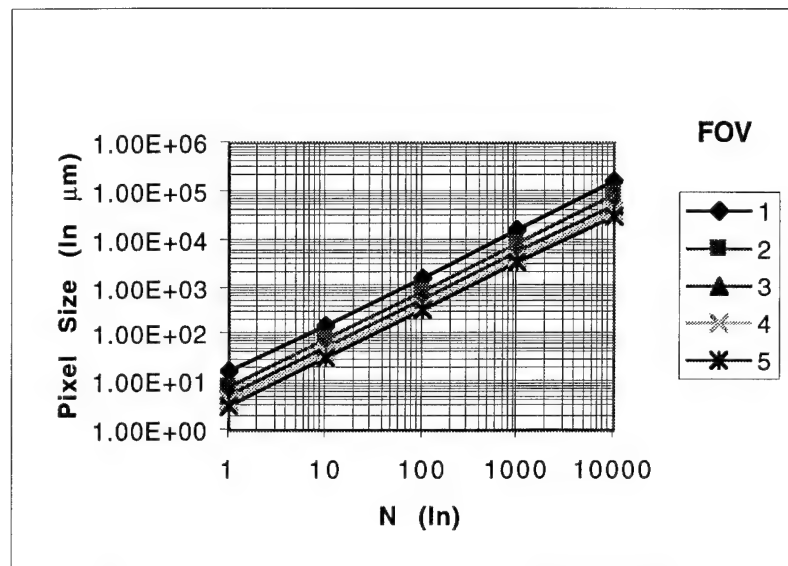


Chart 1) Pixel size (length of edge of square pixel) versus N, and field of view in degrees

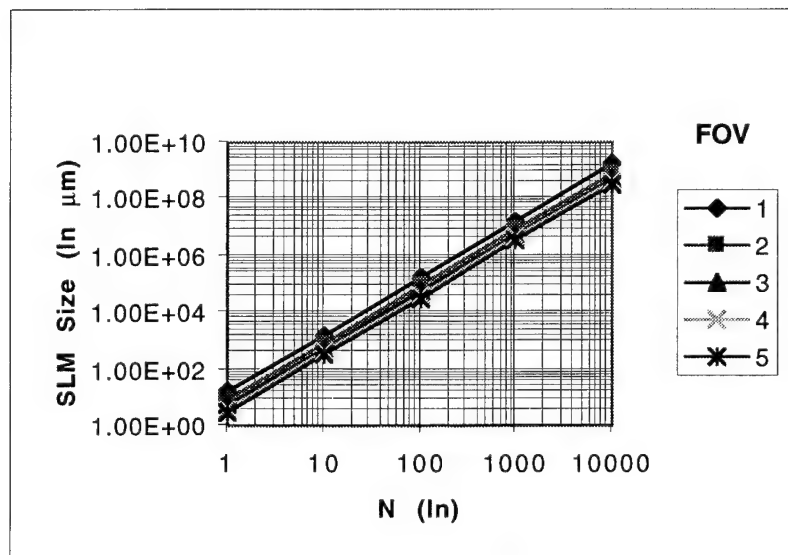


Chart 2) SLM size (length of side) versus N, and field of view in degrees.

A sample implementation for an optical processor using such a logon conserving transformation is shown in figure 1. It uses a pair of telescopes to increase 'beam' the diameter to reduce the field of view required by the SLM.

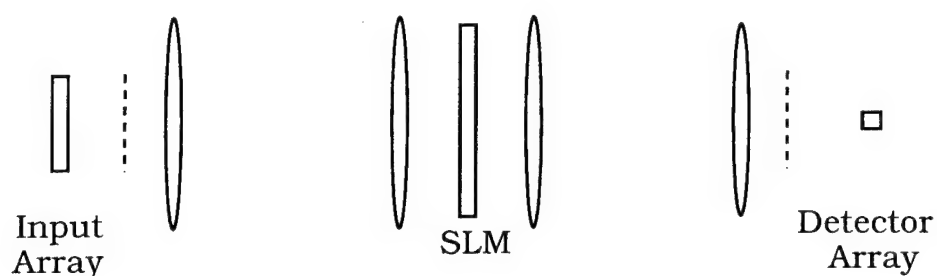


Figure 1) A logon conserving matrix vector multiplier. The dashed lines indicate the size and location of the virtual large field of view/small pixel SLM. We have omitted any cylindrical optics from this figure for clarity.

References

- ¹ John A. Neff, R. A. Athale, and S. H. Lee, "Two-dimensional spatial light modulators: a tutorial," *Proc. IEEE* **78**, 826-855 (1990)
- ² D. Gabor, "Theory of communication," *J. Inst. Elect. Eng.* **93**, 429-457 (1946)

Noise induced switching and stochastic resonance in an optically addressed spatial light modulator

John P. Sharpe, Dominic C. O'Brien and Garret Moddel

Optoelectronic Computing Systems Center, University of Colorado at Boulder, Boulder, CO 80309.

Since it was first adduced as a possible explanation for the periodic occurrence of the earth's ice ages [1] [2], the phenomenon of stochastic resonance has been extensively investigated, both theoretically and experimentally. An intuitive understanding of the phenomenon may be developed by considering figure 1(a) which shows a particle in a double potential well. Under a large periodic perturbation of the wells (1(b)) the particle can escape from well to well, and if we regard the particle position as the observable or signal then the power spectrum of this signal will exhibit a large peak at the perturbation frequency. Under large random forcing the particle also makes the transition between the two wells but this time in a random fashion and the output spectrum is typically Lorentzian. In the case where there is a small periodic perturbation the particle is unable to escape from the right hand well where it resides initially (fig 1(c)). However, if random noise is now added the particle can make the transition with a greater *probability* from right to left when the right well is higher and *vice versa* when it is in the left well. As may be imagined, if there is insufficient noise then no transitions are made while if the noise is too large then the random switching dominates. It is this notion of an optimum amount of noise coupled with a small periodic component in a nonlinear system that forms a definition of stochastic resonance.

The phenomenon has since been observed in many (bistable) physical systems, including nonlinear electronic circuits [3], ring lasers [4], nonlinear optical crystals [5] and semiconductor lasers [6]. It has also been observed in excitable systems, including the mechanoreceptors of crayfish [7]. Despite some tantalizing results in the literature [5] [8] it is not yet clear if the phenomenon can be usefully employed for signal-to-noise improvement in communications/computing systems.

Here we report observation of stochastic resonance in a novel physical system: the bistable optically addressed spatial light modulator (OASLM) [9]. This device comprises a thin film of surface stabilized SCE13 ferroelectric liquid crystal (FLC) atop a PIN photodiode amorphous silicon photosensor. In the particular device we use the FLC is aligned with rubbed silane, a technique which improves the bistability and resistance to degradation of the FLC [10]. Figure 2 shows the transfer function of the device, exhibiting a hysteretic or bistable behavior, corresponding to the double well potential discussed above [11]. Our experimental arrangement for observing stochastic resonance is shown in figure 3. A uniform light beam (dia. ~ 0.5 cm, $\lambda = 633$ nm, 0.5 mW/cm²) is incident on the OASLM through the polarizing beamsplitter, passes through the FLC, and is partially absorbed in the silicon and partially reflected from the silicon/FLC interface. The light thus simultaneously sets the electrical switching threshold of the OASLM and serves as the read light. Of course, it is not necessary to have an OASLM - a simple bistable FLC cell would be sufficient but the possibility of obtaining variable thresholds may be interesting to investigate, as we discuss below. The input signal to the OASLM is provided from the PC using a Data Translation DT-EZ board. The optical output from the OASLM is focussed onto a photodiode and the optical signal acquired using the same board.

A typical time series input and output from the OASLM is shown in figure 4. The noise is zero mean Gaussian, switching every 15 ms, and hence well within the switching capabilities of the OASLM (< 0.33 ms [9]). The underlying periodic signal has a period of 1.36 seconds and an amplitude of 0.6 V, insufficient to switch the OASLM by itself. One can see from the figure that the OASLM is more likely to switch when the underlying periodic signal is negative.

The optical signal is analyzed by computing the SNR, which is defined as the peak value of the power spectrum at the modulation frequency divided by the local noise background [3]. 2048 point samples were acquired and transformed using the FFT algorithm. For each noise variance this procedure was repeated 20 times with different noise realizations and the resulting power spectra averaged. Following reference [12] we thresholded the optical signal to give a true binary response prior to computing the FFTs. This permits a closer fit to simple theories of stochastic resonance. Figure 5 shows the SNR as a

function of the input noise deviation. We superimpose a theoretical curve (solid line), given by [13]

$$SNR(D) = \frac{Q}{D^2} \exp\left[-\frac{2\Delta U}{D}\right] \quad (1)$$

where D is the noise deviation, ΔU is the height of the barrier and Q is a constant. Since our potential well is asymmetric, we replace $2\Delta U$ with the sum of the well depths. As can be seen, the experimental results qualitatively follow the theory, exhibiting the characteristic swift rise and slow reduction in SNR with increasing additive input noise. Also superimposed on the graph is the result of a computer simulation, made using a simplified model of the OASLM response. Again, the qualitative agreement is good.

In conclusion, an optically addressed spatial light modulator can exhibit stochastic resonance using the bistable character of aligned FLC. This system is of potential interest on several counts. First of all, the switching threshold is determined by the optical intensity. Thus it would be possible, by using a space variant beam, to interrogate an input electrical signal using multiple thresholds simultaneously. Second, it may be possible to investigate coupling effects in stochastic resonance using the transverse diffusion of photoelectrons which occurs in these devices.

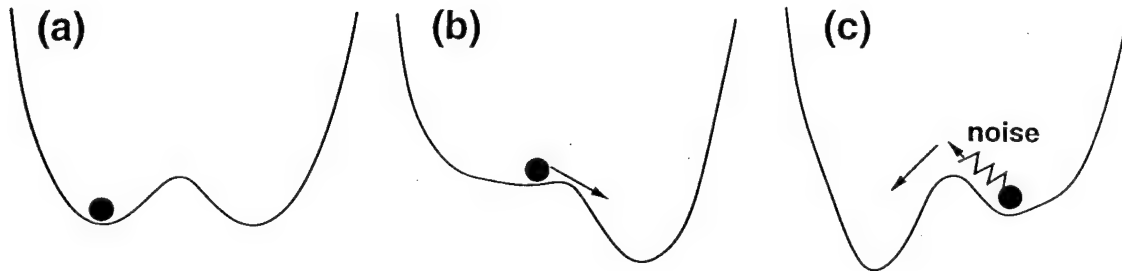


Figure 1. Particle in double potential well (see text).

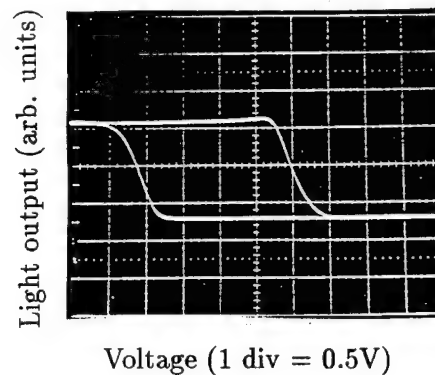


Figure 2. Hysteresis curve of OASLM. Obtained with $\lambda = 633 \text{ nm}$, 0.5 mW/cm^2 write/read light at an electrical driving frequency of 67 Hz. Experimental apparatus same as that of figure 3.

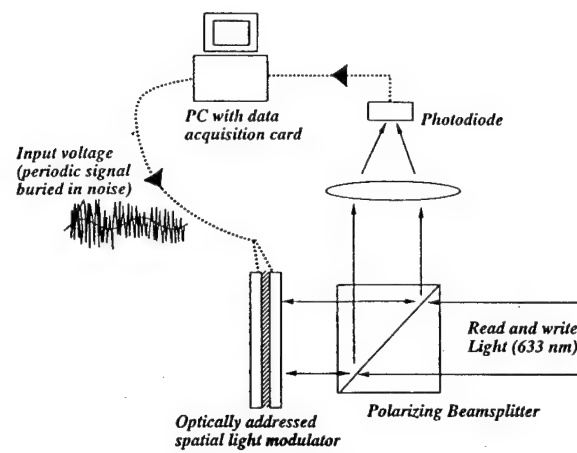


Figure 3. Experimental system.

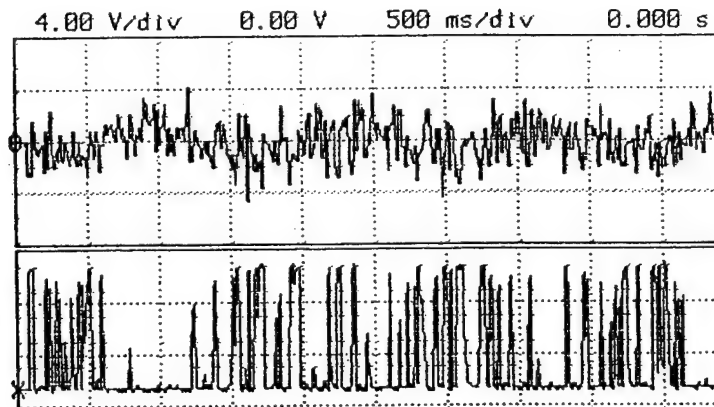


Figure 4. Typical input time series (top trace) and output from OASLM (bottom trace).

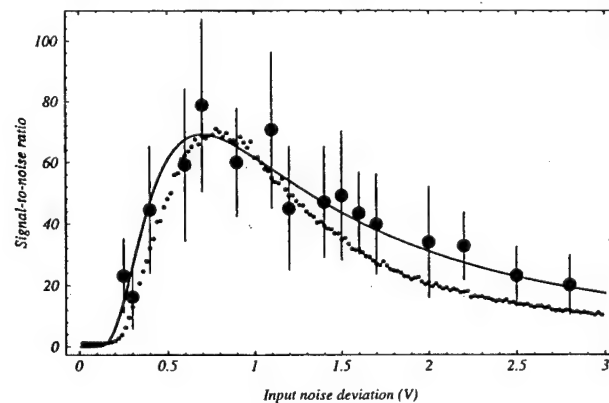


Figure 5. Signal to noise ratio as a function of the input noise deviation. Solid line is theoretical curve, dotted line is computer simulation.

References

- [1] R. Benzi, A. Sutera, and A. Vulpiani. The mechanism of stochastic resonance. *J. Phys A: Math. Gen.*, 14:L453-L457, 1981.
- [2] R. Benzi, G. Parisi, A. Sutera, and A. Vulpiani. Stochastic resonance in climatic change. *Tellus*, 34:10-16, 1982.
- [3] S. Fauve and F. Heslot. Stochastic resonance in a bistable system. *Phys. Lett.*, 97A:5, 1983.
- [4] G. Vemuri and R. Roy. Stochastic resonance in a bistable ring laser. *Physical Review A*, 39(9):4668-4674, 1989.
- [5] J. Grohs, S. Apanasevich, P. Jung, H. Issler, D. Burak, and C. Klingshirn. Noise induced switching and stochastic resonance in optically nonlinear CdS crystals. *Phys. Rev. A*, 49(3):2199-2202, 1994.
- [6] J. M. Ianelli, A. Yariv, T. R. Chen, and Y. H. Zhuang. Stochastic resonance in a semiconductor distributed feedback laser. *Appl. Phys. Lett.*, 65(16):1983-1985, 1994.
- [7] J. K. Douglass, L. Wilkins, and E. Pantazelou. Noise enhancement of information transfer in crayfish mechanoreceptors by stochastic resonance. *Nature*, 365:337, 1993.
- [8] D. Gong, G. Qin, X. Wen, and G. Hu. Comparison of signal to noise ratios by stochastic resonance device and by optimal linear filter. *Science in China (Ser. A)*, 36(4):431-436, 1993.
- [9] G. Model, K. M. Johnson, W. Li, R. A. Rice, L. A. Pagnano-Stauffer, and M. A. Handschy. High-speed binary optically addressed spatial light modulator. *Applied Physics Letters*, 55(6):537-539, 1989.
- [10] D. Doroski, S. H. Perlmutter, and G. Model. Alignment layers for improved surface-stabilised ferroelectric liquid-crystal devices. *Applied Optics*, 33(13):2608-2610, 1994.
- [11] S. H. Perlmutter, D. Doroski, B. Landreth, A. M. Gabor, P. R. Barbier, and G. Model. Tradeoffs in the design and operation of an optically addressed spatial light modulator. *Proc. SPIE*, 1562, Devices for Optical Processing:74-84, 1991.
- [12] T. Zhou and F. Moss. Analog simulations of stochastic resonance. *Physical Review A*, 41(8):4255-4264, 1990.
- [13] B. Macnamara and K. Weisenfeld. Theory of stochastic resonance. *Physical Review*, 39(9):4854-4868, 1989.

Surface Normal Optical Modulation in Thin Film Silicon: Is It feasible?

Michael Estes and Garret Model

Department of Electrical and Computer Engineering
University of Colorado, Campus Box 425
Boulder, Colorado 80309-0425
Tel: (303) 492-1889, Email: model@boulder.colorado.edu

I. Introduction

Unlike direct band gap materials such as GaAs, which exhibit very sharp and strong absorption at the band edge, indirect gap crystalline silicon has relatively weak band edge absorption and hence weak band edge nonlinearities[1]. Even hydrogenated amorphous silicon (a-Si:H) with its quasi-direct bandgap shows only moderate electro-optic modulation at its nominally 1.7 eV band edge[2, 3] due to disorder-induced tail states. In addition, both a-Si:H and c-Si are centrosymmetric materials so that there are no $\chi^{(2)}$ optical nonlinearities.

Silicon does, though, have some inherent advantages over conventional electro-optic materials: compatibility with conventional silicon electronics, ease of deposition over large areas, and well characterized behavior. Additionally, being an electronic material it has a potential speed advantage over liquid crystal modulators. The allure of all-silicon optoelectronics has motivated us to investigate its optical modulation potential. In the following sections we discuss basic requirements for surface-normal silicon modulators and review electro-optic modulation mechanisms in bulk and quantum confined silicon.

II. Material Requirements

The surface-normal geometry required for spatial light modulators severely limits the interaction length of light through the modulating layer. Since we do not expect the electro-optic properties of silicon to be strong, we require some resonance, either optical or electronic, to obtain sufficient modulation contrast.

A number of optically resonant structures have been proposed for III-V optical modulators. One promising structure is the active distributed Bragg reflector[4] in which the refractive index and absorption in alternating $\lambda/4$ layers are modulated to change reflectivity or

transmittivity. Figure 1 shows calculated reflection and transmission change for a 50 period a-Si:H or c-Si film in which the index of refraction in alternating $\lambda/4$ layers are modified by an amount $\Delta n = \Delta k$. The unmodulated layers are assumed to be of the same material (a-Si:H or c-Si). We assume subband gap wavelengths of 0.87 μm and 1.55 μm for the a-Si:H and c-Si, respectively. We see that we need electro-optic effects with $\Delta n, \Delta k > 10^{-3}$ to realize useful modulation contrast. In the following section, we will review electro-optic effects in silicon to assess the feasibility of obtaining such modulation.

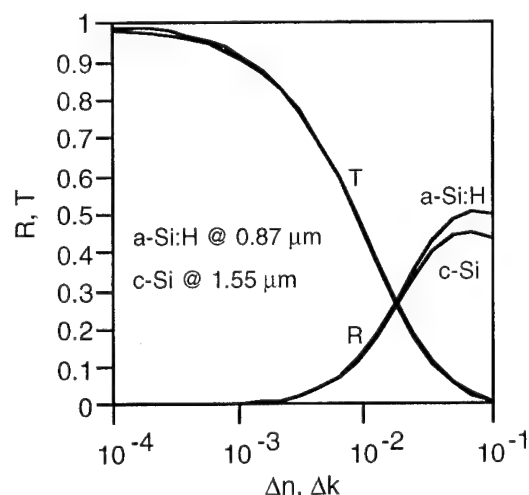


Figure 1. Calculated reflectivity (R) and transmittivity (T) of a-Si:H at 0.87 μm and c-Si at 1.55 μm in which alternating $\lambda/4$ layers are modified by $\Delta n = \Delta k$.

III. Optical Modulation Mechanisms in Silicon

A. Electric Field Effects

Under an applied electric field, carriers in a crystalline semiconductor may tunnel some distance into the band gap. This gives rise to an exponential absorption tail below the band edge and an oscillatory absorption above the band edge due to the spatial overlap of electron and

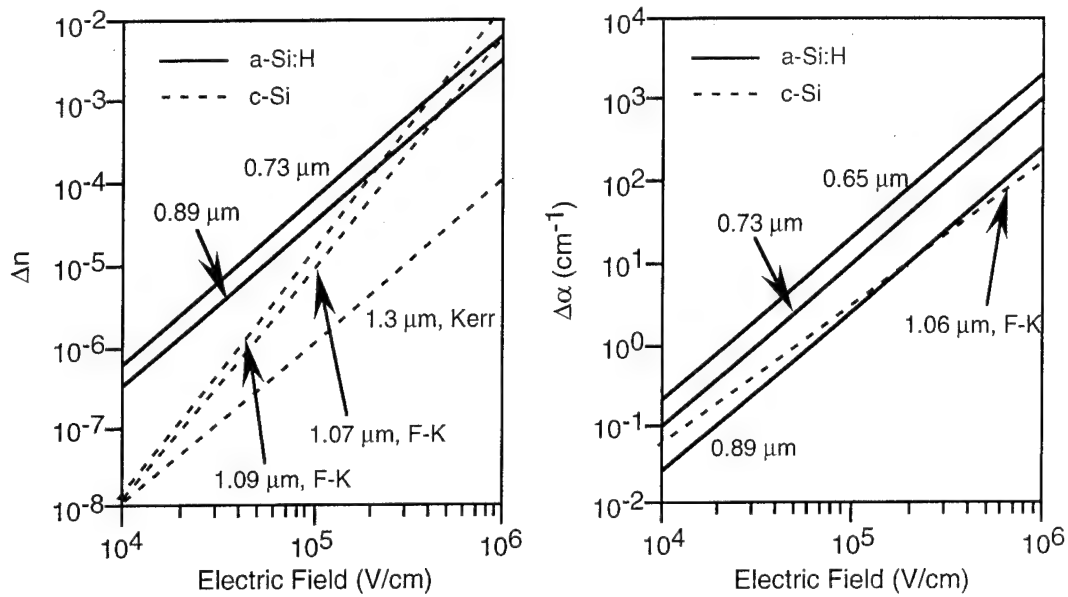


Figure 2. Electric field-induced change in the optical properties of bulk a-Si:H[2, 3] and c-Si.[5] Effects in a-Si:H are due to DC Kerr effect while those in c-Si are due to both DC Kerr and Franz-Keldysh (F-K) effects.

hole wave functions. This phenomenon is known as the Franz-Keldysh effect. The largest absorption change occurs for light very near the band gap energy. The Franz-Keldysh induced change in refractive index, Δn , and absorption coefficient, $\Delta\alpha$, for c-Si versus applied field are shown in Figure 2. The data shown in the Figure were extrapolated from results given by Soref and Bennett[5]. At the dielectric breakdown field of around 4×10^5 V/cm, $\Delta n \approx 10^{-3}$ and $\Delta\alpha \approx 50$ cm $^{-1}$ for 1.07 μ m light. The Franz-Keldysh effect in a-Si:H appears to be negligible[3].

Under high electric fields, the polarization response of a material becomes nonlinear. For centrosymmetric materials under an applied DC electric field the complex index of refraction changes quadratically with field by an amount

$$\Delta \hat{n}_x \approx \hat{n}_{x0} + \frac{1}{2} \hat{\chi}^{(3)} |E_x^{dc}|^2$$

where $\hat{\chi}^{(3)}$ is the third order nonlinear optical susceptibility and E_x^{dc} is the DC electric field along the x-direction. This is the DC Kerr effect. The change in optical properties due to the Kerr effect are shown in Figure 2 for c-Si and a-Si:H. In c-Si this effect is small and is independent of λ . [5] In a-Si:H, though, the Kerr effect is the dominant electro-optic mechanism, and seems to be resonantly enhanced near the band edge as shown by electroabsorption studies[2, 3]. At a field of 4×10^5 V/cm, we see maximum changes in

the optical constants of about $\Delta\alpha = 300$ cm $^{-1}$ ($\Delta\alpha/\alpha \approx 3\%$) at $\lambda = 0.65$ μ m and $\Delta n = 1.2 \times 10^{-3}$ at $\lambda = 0.73$ μ m in a-Si:H.

B. Free Carrier Absorption

The presence of free carriers in a semiconductor causes optical absorption below the band gap energy. The simple Drude model predicts a linear increase in absorption coefficient with the density of free carriers, N_e , as

$$\alpha(\omega) = \alpha_o(\omega) + \frac{4\pi N_e q^2 \tau}{cm_e n(\omega)},$$

where q is the elemental charge, τ is the carrier relaxation time, c is the speed of light, m_e is the carrier effective mass, and $n(\omega)$ is the index of refraction. Thus, by injecting high carrier densities we may modify the optical constants of silicon. The change in optical constants, Δn and Δk (complex index $\hat{n} = n + ik$), versus carrier concentration for a-Si:H and c-Si is shown in Figure 3.

In a-Si:H, free carrier absorption effects have been measured using picosecond pump/probe type experiments[6-8]. The problem in a-Si:H is that the carrier decay time is only ~ 1 psec[8] and becomes even shorter for carrier densities in excess of $N_e \approx 10^{21}$ cm $^{-3}$. Thus, it is very difficult in a device operating in steady state to inject carrier concentrations greater than around 10^{18} cm $^{-3}$,

though the high density of gap states may enhance below gap absorption by trapping carriers. There have been reports of increased steady state absorption due to filling boron-related defect states in the band gap of doped a-Si:H[9]. For 780 nm illumination, transmission through the a-Si:H film decreased from around 33% at low intensity to 25% at approximately 3 W/cm².

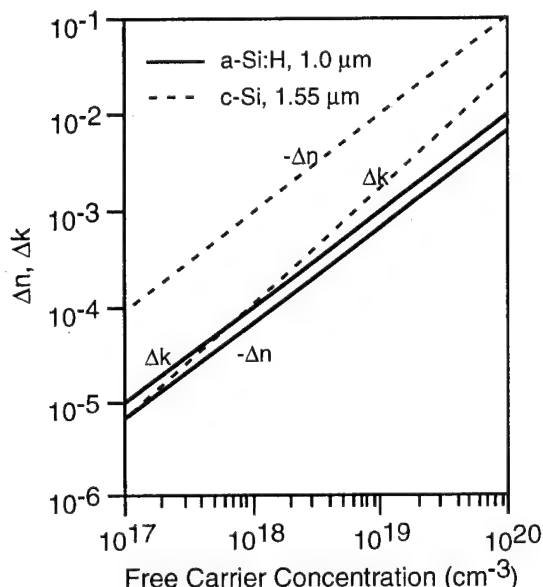


Figure 3. Free carrier absorption effects for bulk a-Si:H[7] and c-Si[5] for free electrons.

As Figure 3 indicates, free carrier absorption in c-Si is substantially greater than in a-Si:H. In addition, because the carrier lifetime is fairly long -- microseconds to milliseconds for clean silicon -- relatively high carrier densities may be realized in steady state. For a carrier concentration of $N_e \approx 10^{19} \text{ cm}^{-3}$ at $\lambda = 1.55 \text{ μm}$, $\Delta n \approx 10^{-2}$ and $\Delta \alpha \approx 100 \text{ cm}^{-1}$ [5]. Thus, for infrared modulation, free carrier effects in c-Si are reasonably large.

C. Modulation Effects in Quantum Confined Silicon

As we expected, optical modulation effects in bulk silicon are fairly small. In quantum confined silicon structures, however, we may expect some enhancement in the electro-optic properties of silicon due to sharpening of the absorption edge, confinement of excitons, or quantization of absorption levels.

Some enhancement of the Franz-Keldysh effect may be realized by using quantum confined c-Si structures[10], which would tend to blue-shift and sharpen the band edge absorption. In addition, confinement of excitons in quantum size structures would allow spectral shifting of the excitonic absorption edge with applied field due to the quantum confined Stark effect. Both of these effects are quite large in direct band gap semiconductors but would be weaker in indirect gap silicon. To our knowledge, no one has reported observation of these effects in silicon. Some theoretical studies have indicated a transition to a direct band gap in quantum sized silicon nanostructures[11]; however, the long luminescence lifetimes in nanoscale c-Si (eg., porous silicon) tend to refute this idea[12].

Another electro-optic effect that may be enhanced by quantum confinement is bandfilling. As the effective density of states at the band edge of bulk c-Si is around 10^{21} cm^{-3} , one would need a carrier concentration of 10^{21} cm^{-3} to observe an effective $2kT$ blue shift in the absorption. In silicon quantum dots, though, much lower carrier densities would be required because of quantization of the density of states function.

A major obstacle toward realization of devices based on quantum confinement effects in crystalline silicon is fabrication of uniform nanostructures. Since the energy levels in quantum structures are approximately proportional to $1/L^2$, where L is the size

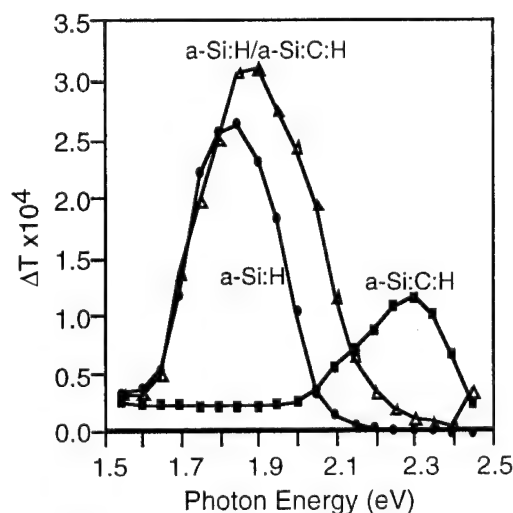


Figure 4. Measured change in transmittance of an a-Si:H/a-Si:C:H multilayer at an applied field of 10^5 V/cm along with equivalent spectra for films of a-Si:H and a-Si:C:H.

dimension, small nonuniformities in layer thickness or well width quickly wash out sharp absorption features.

To overcome problems associated with fabrication of c-Si quantum structures, some researchers have investigated quantum size effects in amorphous semiconductors. Very uniform multilayer films of amorphous semiconductors have been made using low temperature plasma enhanced chemical vapor deposition. The question is: are there quantum size effects in nanoscale a-Si:H? Though there is some experimental evidence to indicate there are quantum effects[13, 14], the overall enhancement in electro-optic properties is extremely small. This is probably due to the fact that the coherence length of carrier wave functions in amorphous semiconductors is on the order of an interatomic distance. Thus, very few of the carriers have sufficient coherence to resonate inside structures that are tens of atoms across. Figure 4 shows electroabsorption spectra for an a-Si:H/a-Si:C:H "multiple quantum well" structure grown by PECVD process. The structure consists of 50 layers of 3.1 nm thick a-Si:H wells between 13.3 nm thick a-Si:C:H barriers. We measured the Tauc gap of the a-Si:H at 1.72 eV and the gap of the a-Si:C:H at 2.10 eV. Note that the absolute change in transmission is small; we measured $\Delta T/T$ to be about 0.1% maximum for the multilayer at an applied voltage of 10 V over the nominally 1 μm thick film ($E \approx 10^5$ V/cm). The stronger electroabsorption signal from the multilayer arises from built-in fields within the silicon well layers. Electroabsorption in the multilayer appears to be mainly due to the a-Si:H well layers, though it is slightly blue-shifted from the bulk a-Si:H electroabsorption signal. This blue shift is likely due to spatial confinement of the a-Si:H layers, not quantum confinement[15]. Regardless, we see no evidence for quantum confinement effects in amorphous multilayers -- certainly, no significant enhancements are observed such as quantum confined Franz-Keldysh or Stark effects.

IV. Conclusions

Clearly, the electro-optic effects in bulk a-Si:H and c-Si are small. Device structures require optical and possibly electronic resonance to give useful contrast. Changes in the optical constants of $\Delta n, \Delta k > 10^{-3}$ are required. Electric field effects are not really strong enough for this

change. Free carrier effects in c-Si may be useful, though high carrier concentrations of $N > 10^{18} \text{ cm}^{-3}$ are required. Such high carrier concentrations will limit switching speed and sensitivity. Enhancement by quantum confinement does not appear to be possible in a-Si:H, but may be possible to some degree in c-Si. More work is needed to investigate the magnitude of these effects. A major issue in quantum confined material is fabricating very uniform nanostructures so that we may take advantage of the sharper and stronger absorption edge.

References

1. I. Galbraith and B. Ryvkin, J. Appl. Phys. **74**, 4145 (1993).
2. S. Al Jalali and G. Weiser, J. Non-Cryst. Solids **41**, 1 (1980).
3. G. Weiser, U. Dersch, and P. Thomas, Philos. Mag. B **57**, 721 (1988).
4. A. Obeidat, J. Khurgin, and S. Li, in Spatial Light Modulators and Applications **6**, March 15-17, 1993, 1993, Palm Springs, CA, pp. 182.
5. R. A. Soref and B. R. Bennett, IEEE J. Quant. Elec. **QE-32**, 123 (1987).
6. P. M. Fauchet, D. Hulin, A. Migus, A. Antonetti, J. Kolodzey, and S. Wagner, Phys. Rev. Lett. **57**, 2438 (1986).
7. C. Tanguy, D. Hulin, A. Mourchild, P. M. Fauchet, and S. Wagner, Appl. Phys. Lett. **53**, 880 (1988).
8. J. Tauc and Z. Vardeny, Solid State Mat. Sci. **16**, 403 (1990).
9. Y. Maeda, S. Yamamoto, and M. Migitaka, Appl. Phys. Lett. **59**, 390 (1991).
10. D. A. B. Miller, D. S. Chemla, and S. Schmitt-Rink, Phys. Rev. B **33**, 6976 (1986).
11. T. Takagahara and K. Takeda, Phys. Rev. B **46**, 15578 (1992).
12. Y. Kanemitsu, Phys. Rev. B **48**, 12357 (1993).
13. K. Hattori, T. Mori, H. Okamoto, and Y. Hamakawa, in *Amorphous Silicon and Related Materials*, edited by H. Fritzsche (World Scientific, Singapore, 1988), pp. 957.
14. M. A. Neifeld, in Spatial Light Modulators and Applications **6**, March 15-17, 1993, 1993, Palm Springs, CA, pp. 44.
15. T. Tiedje, B. Abeles, and B. G. Brooks, Phys. Rev. Lett. **54**, 2545 (1985).

Wednesday, March 15, 1995

Joint Session with Optical Computing

LWA 1:30 pm-3:00 pm
Grand Ballroom A/B

John N. Lee, *Presider*
Naval Research Laboratory

Future Directions in "Smart" Quantum Well Spatial Light Modulators and Processing Arrays

David A. B. Miller
AT&T Bell Laboratories
Holmdel, NJ
USA

Quantum well modulators and photodetectors are one attractive option for large scale integration of arrays of optical inputs and outputs in information processing systems. Optics is fundamentally attractive because it offers basic physical advantages in interconnections, and may allow novel architectures of information processing systems not well-suited to electronics alone. In the past, large arrays of quantum well devices have been used in experimental systems, and more recently technologies have emerged that have allowed "smart" arrays incorporating electronics both for added functional complexity and reduced optical energy requirements. The FET-SEED technology, for example, has integrated GaAs field effect transistors with quantum well modulators and detectors for high speed circuits with sophisticated functions, and has already been used to fabricate multi-project wafers for experimental use by a broad range of users.

Very recently, hybrid integration of quantum well devices with complex, mainstream, silicon circuits has become a practical reality. This advance opens up a broad range of new possibilities for systems. There is a serious prospect of large complex "smart" circuits, made from the most capable silicon circuits, and operating as fast as the silicon circuits themselves can run, but unconstrained by the usual difficulties of electrical interconnects. This possibility also raises challenges, at the optoelectronic device and electronic circuit level; for example, receiver circuits should occupy small areas and consume low powers so they can be made in large arrays, but they must at the same time be sensitive with low error rates with good immunity to the effects of neighboring circuits. The challenges and opportunities for research at the systems level are perhaps even greater. Such technologies raise the prospect of optical systems with functional complexity well beyond previous bounds and electronic systems with scales and topologies of interconnections also outside most previous experience. To give a sense of where such technologies could be, the talk will address a skeleton roadmap for how these technologies could progress in years to come.

Device-Architecture Interaction in Optical Computing

Ravindra A. Athale
George Mason University
4400 University Drive
Fairfax, VA 22030

Device technologies and processor architectures exert a strong influence on each other in optical computing. I will discuss examples of successful and unsuccessful interactions between these two communities. The role of the CO-OP in enhancing this interaction will be outlined.

Wednesday, March 15, 1995

Joint Plenary Session with Optical Computing

OWC 3:30 pm-5:00 pm
Grand Ballroom A/B

Demetri Psaltis, *Presider*
California Institute of Technology

THE HISTORY OF OPTICAL COMPUTING : A PERSONAL PERSPECTIVE

Adolf W. Lohmann

Michael visiting professor, Weizmann Institute of Science, Dept. of Physics of Complex Systems, Rehovot 76100, Israel.
Permanently : Universitat, Physikalisches Institut, Rommel Str. 1, 91058 Erlangen, Germany. (FAX 49 - 9131 - 15249).

For me the history of optical computing can be divided into several phases, which I will illustrate by examples. The phase transitions mark changes of my personal attitude towards optics in general and to information optics in particular.

PHASE 1 : From the Greeks to 1950.

Optics had been taught to me as a collection of phenomena, some of them nice - like the rainbow - , others not so nice, like the use of optics as a weapon by Archimedes. I tried to find intellectual structures behind the collection of phenomena. But my attempt [1] was deemed insufficient for a Masters thesis. In my second attempt I was forced to develop hardware, a two - layer lithographic grating structure [2]. It was a valuable experience.

PHASE 2 : Analog Processing (1950 - 60).

Gabor's holography was exciting. I tried to suppress the twin image by single sideband holography. The success was very modest only. But I learned to look at optics as a means for signal and image processing [3].

PHASE 3 : The signal amplitude changed gradually from analog to quantised and binary. The continuous space variable was fractured, or pixellated. Optical logic occurred in Theta Modulation [4]. What is now called wavelength division multiplexing was called 30 years ago lambda super-resolution. Hybrid mixtures of

digital and optical technologies became interesting, for example as computer generated holograms. The optical implementation of residue number algebra was tried in the FSU. That phase (1960 - 80) could be called perhaps "From analog to digital".

PHASE 4 : Now, during 1980 to 85, the optical community was courageous as seldom before, and never since. The digital optical computer was proclaimed as a goal. Parallelism was the magic term. The perfect shuffle was supposed to contribute to this movement. The relationship with the electronic community looked like the confrontation between David and Goliath. The experience was not always pleasant. But it was instructive. Gradually, a transition occurred into :

PHASE 5 : "Optics FOR Computing", or "Optics WITHIN the Computer".

That required the matching of technologies. Terms like optical packaging, from macro-optics to micro-optics became prominent. My own advice was - and still is - to use the existing classical macro-optics wherever sensible. You get high quality for a low price. I do not mean to use classical macro-optics exclusively. That would be as foolish as the opposite : to use only micro-optical arrays. Be tolerant and try hybrid macro-micro approaches.

PHASE 6 : (1995 - 2006)

Computation and communication will intermingle more and more. The former will remain dominated by electronics. After all, a silicon transistor costs less than a micro \$. Optics will progress as it has done already in the pure communications technology, from large distances to shorter distances.

We should not look at the future as a battlefield of technology replacements. Instead we should aim at HYBRID solutions, as it happened in the world of transportation. We have cars and trains which move on a 2D surface, just like electronic signals. The cars are self-routing, the trains under central control. And we have air traffic in 3D, with considerable topological advantages. Within the air traffic business there are two trends : to micro-planes (a mini-helicopter for everyone), and to macro-planes (1000 passengers, travelling from one conference to the next

conference). Again, tolerance is asked for.

The overall transportation system is not perfect, but it does function, largely because different technologies collaborate in a fairly sensible way. It does not require much fantasy to imagine how much worse the situation could be. Let us learn our lesson.

References :

- (1) "Duality in Optics", OPTIK 89 (1992) 93 - 97.
- (2) "The measurement of the absolute light phase by intensity measurements in the diffraction plane of a grating", Z. PHYS. 137 (1954) 362.
- (3) "Optical single sideband transmission, applied to the Gabor microscope", Opt. Acta 3 (1956) 97.
- (4) "Theta Modulation in Optics", Appl. Opt. 4 (1965) 399.

Acoustic Signal Processing with Photorefractive Optical Circuits

*Germano Montemazzani, Elizabeth Donley and Dana Z. Anderson
Department of Physics and Joint Institute for Laboratory Astrophysics
University of Colorado, Boulder CO 80309-0440*

Acoustic processing of audio and sonar by animals involves the temporal as well as spatial aspects of an incoming signal. We can presume that a bat, for example, acquires an entire spatial picture of its surroundings from its sonar returns rather than some empty series of blips that the untrained human ear derives from the sound of a ship's sonar; in effect the bat sees with its ears [1]. The barn owl makes equally impressive use of hearing with passive sonar to locate and capture prey in the dark. In these cases, and in speech recognition by humans, the sequential nature of the information plays an essential role.

This presentation looks at the use of dynamic holography for processing temporal and spatial-temporal information. We are motivated by the success of time-delay neural networks in speech recognition, [2, 3, 4] and by the evident structure of the sound processing mechanisms in bats and owls. Furthermore, as we look at the required processing, we will find them as well suited to holographic methods as many image processing tasks.

Our context for this presentation is the recognition of temporal sequences: Imagine listening to a radio as you tune across a short-wave band. It is easy to recognize a channel that carries Morse code, even if you do not know the code. That is because Morse code consists of a simple set of temporal features, (a dot, a dash, and two pause lengths) and a Morse signal is characterized by repeated occurrences of these features. It does not take long for the brain to identify these features as the dominant content of the received signal. We accomplish a similar task with a holographic optical system. This task characterizes a number of acoustical information processing problems and serves as a precursor for more complex systems.

Acoustic processing in animals employs both frequency and time domain operations. The short-time Fourier transform is part of the sound transduction mechanism itself (within the cochlea) and the time domain is served by delay line structures, at least in the bat and barn owl. The time domain is serviced by short and long term memory storage as well. For audio frequencies appropriate delays are in the milliseconds to seconds regime. We implement delays of this scale using a rotating photorefractive crystal [5].

As the delay line is an essential component in neural-like temporal signal processing it is perhaps worth describing the principle in some detail with the help of Figure 1. It shows a reference, or pump, wave and a signal wave incident on a crystal which is (slowly) rotating with the rotational axis along the pump wave. At a given moment $t = t_0$ the two waves form a holographic grating within the medium; the reference wave scatters off of the grating to reconstruct the signal at its incident polar angle defined as $\theta = 0$. In this specific geometry the reference wave continues to scatter off of the grating as the crystal rotates, but the grating rotates so the reconstructed signal sweeps out a cone in time, as

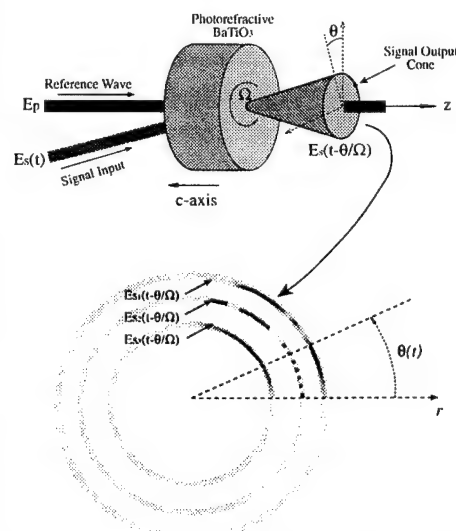


Figure 1. Photorefractive delay line having several parallel channels of delay.

indicated in the figure. In the meantime, a new grating is being written at every moment. Thus, the signal “now” reads out at $\theta = 0$, while the signal at increasingly earlier times reads out at increasingly larger angles. If we position ourselves at some angle θ , we will observe the signal at a time $t' = t + \theta/\Omega$, where Ω is the rotation rate of the crystal. If the delays are continuously read out, old gratings become erased as new ones are written, so the delayed signal experiences an overall decrease in time. Other than this fixed amplitude reduction (for a given delay time) the signal is reproduced in this system in amplitude, frequency and phase. In practice we use rotation rates of 0.5 to 2 rpm for total delays of up to about a second. Typically the desired delay region is sufficiently short that the arc is nearly a straight line.

One can use an array of inputs rather than a single one, and thereby have a collection of parallel delay lines. Figure 1 shows readout by the same reference beam used to record the grating. In our work we often use the phase conjugate of the reference to produce a phase conjugate of the signal.

In previous work we have used the photorefractive delay time to implement a time-delay neural network for word recognition [6]. Now we describe the mechanism for temporal feature extraction [7]. Schematically, our system consists of an optical resonator that contains two photorefractive crystals as processing elements (Figure. 2). The first crystal (gain crystal) provides the amplification necessary for oscillation. It is pumped by a Gaussian wave that carries the temporal information $S(t)$ of interest. The second crystal provides delay as we have described above: the rotation rate for this task is about one rpm.

The resonator field can build up in a number of spatial modes which are aligned along the time-delay coordinate. The delay line provides a (time-shifted) unidirectional coupling among the spatial modes. In this way, the spatial structure of the collection of all the modes, which we call collectively a chronomode, is modified each time it traverses the delay element. The equilibrium structure is determined by the temporal characteristics of the input signal $S(t)$.

In the gain crystal the interaction of the chronomode light with the pump wave $S(t)$ creates a photorefractive grating by a conventional two wave mixing process. This grating matches the particular chronomode spatial structure. It can be thought of as a matched filter, in the sense that it permits resonator oscillation only when the dominant temporal feature is present at the input.

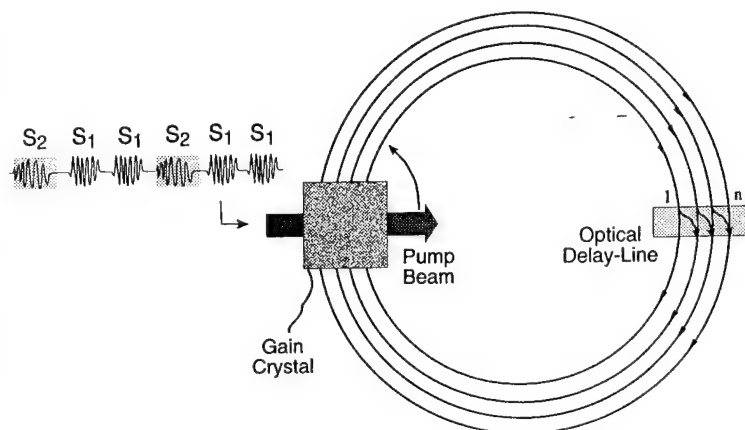


Figure 2. Schematic of a single temporal feature extractor.

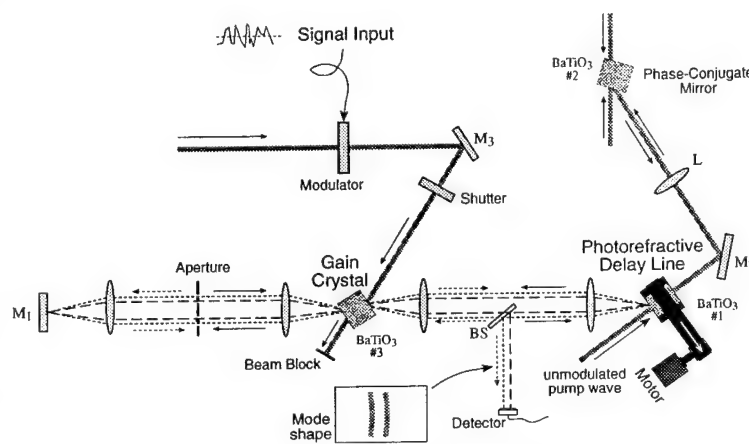


Figure 3. Experimental apparatus for temporal feature extractor.

Figure 3 shows the experimental implementation of the schematic of Figure 2. Note that the delay line is used with phase-conjugated readout using an additional photorefractive crystal in a four-wave mixing configuration.

In our experiments we have shown that a temporal feature occurring twice as often than other ones is chosen by the system with a response contrast ratio exceeding 10:1 [7]. An expanded version of the above system has also been developed, it contains a second ring resonator, and thus two chronomodes. The two chronomodes share the same gain crystal and compete for the pump energy. This competition forces different features in the input signal to be associated with different chronomodes. Figure 4a shows the two input signals applied alternately to modulate the input beam. Figure 4b shows an instantaneous image of the two elongated chronomodes in response to Signal 1. The lower chronomode responds most strongly. When Signal 2 is applied, in contrast, the upper chronomode oscillates strongly (Fig.4c).

In a Morse signal the letters of the alphabet are comprised of a short sequence of basic Morse features; words are comprised of a sequence of letters, and so on. By cascading temporal feature extractors like the one described here one can hope to extract the feature hierarchy contained in Morse code and other complex signals.

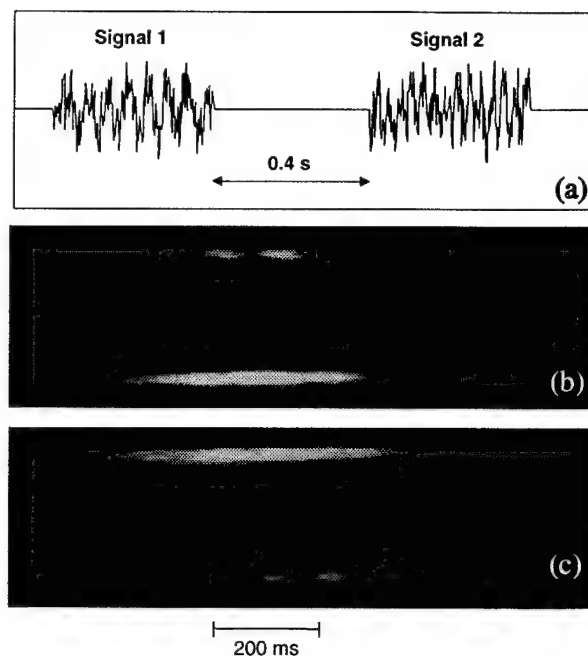


Figure 4. Temporal feature extraction. a) Two different temporal features shown repetitively with equal probability. b) Response of two modes to Signal 1 — lower ring responds most strongly. c) Response of two chronomodes to Signal 2 — upper ring responds most strongly.

References

1. N. Suga, in *Dynamic Aspects of Neocortical Function* G. Edelman, E. Gall, W. Cowan, Eds. (Wiley, New York, 1984) pp. 315-373.
2. D. W. Tank, J. J. Hopfield, *Proceedings of the National Academy of Sciences, USA* **84**, 1896 (1987).
3. K. P. Unnikrishnan, J. J. Hopfield, D. W. Tank, *IEEE Transactions on Signal Processing* **39**, 698 (1991).
4. A. Waibel, K. F. Lee, Eds., *Readings in Speech Recognition* (Morgan Kaufmann, San Mateo, Calif., 1990).
5. G. Zhou, D. Z. Anderson, *Optics Letters* **19**, 167-169 (1993).
6. G. Zhou, D. Z. Anderson, *Optics Letters* **19**, 655-657 (1994).
7. G. Montemazzani, G. Zhou, D. Z. Anderson, *Optics Letters* **19**, 2012-2014 (1994).

Thursday, March 16, 1995

SLM Structures

LThA 8:30 am-10:00 am
Red Lion West

Mary Hibbs-Brenner, *Presider*
Honeywell, Inc.

Electrically and Optically Addressable Spatial Light Modulators Based on n-i-p-i Doping Superlattices

G.H. Döhler, P. Kiesel, M. Kneissl, N. Linder, K.H. Gulden*, P. Riel*,

Institut f. Techn. Phys., University of Erlangen-Nürnberg, 91058 Erlangen, Germany
(*Present addr.: Paul Scherrer Institut, Badenerstrasse 569, 8048 Zürich, Switzerland)

X. Wu and J.S. Smith

Electronics Research Laboratory, University of California, Berkeley, CA 94720

In this paper three different versions of n-i-p-i based spatial light modulators will be discussed:

- 1) optically addressed modulators, based on the large non-linear absorption changes,
- 2) electrically addressed modulators with largely improved performance characteristics, and
- 3) optically addressed "smart modulators", consisting of a combination of fast detectors with gain with electro-optical modulators.

Semiconductors with a suitably designed periodic one-dimensional n-i-p-i doping structures exhibit large built-in electric fields. Due to an "indirect band gap in real space" electrons and holes in the n- and the p-layer are spatially separated. This results in (internal) recombination lifetimes of non-equilibrium electrons and holes which are generally by many orders of magnitude higher than those in the corresponding uniform bulk material [1].

Photo-generated electron-hole pairs are separated by the field within picoseconds. They partially screen the donor and acceptor space charge in the n- and the p-layers, respectively. Because of the long electron-hole recombination lifetimes weak excitation intensities are sufficient to induce large space charge densities and field changes, which, in turn are causing large changes of the optical absorption coefficient at photon energies close to the band gap [1,2]. In conventional n-i-p-i-structures, containing no quantum wells, the phenomena responsible for these absorption changes are the Franz-Keldysh effect in the high field regions and band filling within the doping layers [1,2,3,4]. If the i-regions consist of multiple quantum wells ("MQW-hetero-n-i-p-i") instead of the FKE the quantum-confined-Stark-effect (QCSE) [5] is responsible. This provides larger absorption changes at the expense of a spectrally more narrow photon energy window.

Although large nonlinear optical absorption changes of a few 10^3 cm^{-1} have been achieved at very low excitation densities (a few mW/cm) in both, homo- [3,4] and hetero-n-i-p-i structures [6,7], spatial light modulators based on direct optical modulation exhibit two major drawbacks:

- (a) Due to the long recombination lifetimes the recovery time for returning into the ground state is long (typically $> 1 \text{ ms}$).

(b) At high excitation level (i.e. at strongly reduced internal fields) thermally activated electron-hole recombination leads to an exponential decrease of the lifetimes. As a consequence the photoinduced absorption changes depend only logarithmically on the optical power [3,4,6,7].

Electrically addressed n-i-p-i modulators, in contrast, do not suffer from either of these problems. The problem which originally prevented the successful fabrication of electro-optical n-i-p-i modulators - the application of "selective n- and p-contacts", which connect to all the n- and all the p-doping layers, respectively - has finally been solved by using a shadow mask during MBE growth [8]. By the subsequent development of the "epitaxial-shadow-mask-MBE" (ESM-MBE) [9] miniaturisation became possible. As lifetimes are no longer determined by the "internal" recombination but by the RC-time constant miniaturization allows for very high modulation frequencies. A 3dB frequency of 40 MHz has been demonstrated for a $45 \times 45 \mu\text{m}^2$ modulator [10] and 3dB frequencies in the GHz domain are expected for structures with dimensions of less than $10 \mu\text{m}$.

Other advantages of electro-optical n-i-p-i modulators include large switching contrast and low insertion loss at small operation voltages within a wide spectral range resulting from the fact that high electric fields up to the breakdown threshold can be achieved by applying a small reverse bias voltage, whereas forward bias largely compensates the built-in fields [11].

For 1- and, particularly, 2-dimensional arrays of spatial light modulators it is usually preferable to address them optically. For this purpose "smart pixel" arrays, with each pixel composed of a detecting component and a modulating component are most suitable. By using novel photoconducting detectors (or switches) which provide large output currents [12] at low optical input power (or energy) in combination with n-i-p-i modulators [13] we have been able to demonstrate smart pixels [14] operating at high speed ($< 2 \text{ ns}$) low switching energy ($< 2 \text{ pJ}$) and high contrast (> 4) up to 2 mW output power [15].

The specific advantages of this concept compared with S-SEEDs [16] and FET-SEEDs [17] will be discussed.

References

- [1] G.H. Döhler "Doping Superlattices ("n-i-p-i Crystals")", IEEE QE-22, 1682-1695 (1986)
- [2] P.P. Ruden and G.H. Döhler "Low-Power Non-Linear Optical Phenomena in Doping Superlattices", Proceedings of the 17th Intern. Conf. on the Physics of Semiconductors, J.D. Chadi and W.H. Harrison, Eds. (Springer, N.Y., 1985), 535-538
- [3] T.B. Simpson, C.A. Pennise, and B.E. Gordon, "Optically Induced Absorption Modulation in GaAs Doping Superlattices", Appl. Phys. Lett. 49, 590 (1986)

- [4] P.P. Ruden and J.A. Lehman, "Nonlinear Optical Properties of n-i-p-i Superlattices", *Nonlinear Optical Materials and Devices for Photonic Switching*, N. Peyghambarian, Editor, Proc. SPIE 1216, 190 (1990)
- [5] D.A.B. Miller, D.S. Chemla, T.C. Damen, A.C. Gossard, W. Wiegmann, T.H. Wood, and C.A. Burrus, "Band-Edge Electroabsorption in Quantum Well Structures: The Quantum- Confined Stark Effect", *Phys. Rev. Lett.* 53, 2173 (1984)
- [6] A. Kost, H.C. Lee, Y. Zou, P.D. Dapkus, E. Garmire, "Band-edge absorption coefficients from photoluminescence in semiconductor multiple quantum wells", *Appl. Phys. Lett.* 54, (14),1356 (1989)
- [7] H. Ando, H. Iwamura, H. Oohashi and H. Kanbe, "Nonlinear absorption in n-i-p-i MQW Structures", *IEEE J. of Quant. El.* 25 (10), 2135 (1989)
- [8] G.H. Döhler, G. Hasnain, and J.N. Miller "In situ Grown-in Selective Contacts to n-i-p-i Doping Superlattice Crystals Using Molecular Beam Epitaxial Growth Through a Shadow Mask", *Appl. Phys. Lett.* 49, 704-706 (1986)
- [9] X. Wu, M. Thomas, J.S. Smith, J.R. Whinnery, K.H. Gulden S. Malzer, P. Kiesel, M. Kneissl, and G.H. Döhler, "Inter-digital laterally contacted hetero-nipi band-filling modulator fabricated by shadow mask MBE regrowth technique", *IEEE Lasers and Electro-optics Society Annual meeting*, paper OE9.2, San Jose, Nov. (1992)
- [10] N. Linder, T. Gabler, K.H. Gulden, P. Kiesel, M. Kneissl, P. Riel, X. Wu, J. Walker, J.S. Smith, and G.H. Döhler, "High Contrast Electrooptic n-i-p-i Doping Superlattice Modulator", *Appl. Phys. Lett.* 62, 1916-1918 (1993)
- [11] P. Kiesel, K.H. Gulden, A. Höfler, M. Kneissl, B. Knüpfer, N. Linder, P. Riel, X. Wu, J.S. Smith, and G.H. Döhler, " High speed and high contrast electro-optical modulator based on n-i-p-i doping superlattices", *Superlattices and Microstructures* 13, 21-24 (1993)
- [12] P. Riel, P. Kiesel, M. Ennes, Th. Gabler, M. Kneissl, G. Böhm, G. Tränkle, G. Weimann, K.H. Gulden, X.X. Wu, J. S. Smith, and G.H. Döhler "N-i-p-i-based High-Speed Detectors and Bistable Switches with Gain" *SPIE Proceedings*, 1675, 242-254 (1992)
- [13] G.H. Döhler, P. Kiesel, H. Lin, P. Riel, K. Ebeling and J.N. Miller "A n-i-p-i based new concept for optical logic gates" *SPIE Proceedings* 1283, 103-117 (1990)
- [14] P. Kiesel, K.H. Gulden, A. Höfler, B. Knüpfer, M. Kneissl, P. Riel, X. Wu, J.S. Smith, and G.H. Döhler, "Bistable Opto-optical Switches with High Optical Gain Based on n-i-p-i Doping Superlattices" *Appl. Phys. Lett.*, 62, 3288, (1993)
- [15] M. Kneissl, P. Kiesel, P. Riel, K. Reingruber, K.H. Gulden, S.U. Dankowski, E. Greger, A. Höfler, B. Knüpfer, and G.H. Döhler, "Demonstration of Extremely Low Switching Energies Using New n-i-p-i Based Smart Pixels", in *Quantum Well and Superlattice Physics V* , G.H. Döhler and E.S. Koteles, Editors, Proc. SPIE 2139, 115 (1994)
- [16] A.L. Lentine, H.S. Hinton, D.A.B. Miller, J.E. Henry, J.E. Czunningham, and L.M.F. Chirovsky, "Symmetric Self-Electrooptic Effect Device: Optical Set-Reset Latch, Differential Logic Gate, and Differential Modulator/Detector" *IEEE J. Quantum Electronics* 21, 1928 (1989)
- [17] T.K. Woodward, A.L. Lentine, L.M.F. Chirovsky, S.S. Pei, J.M. Freund, L.A. D'Asaro, M.F. Focht, E.J. Laskowski, G.D. Guth, L.E. Smith, "Operating Characteristics of GaAs/AlGaAs FET-SEED Smart Pixels", *IEEE IEDM*, 655 (1992)

Design of an optically addressed spatial light modulator sensitive to 1.55- μm write light

Li Wang and Garret Moddel

Department of Electrical and Computer Engineering
Optoelectronic Computing Systems Center
University of Colorado, Campus Box 425
Boulder, CO 80309-0425
Tel: (303) 492-1889, Email: moddel@boulder.colorado.edu

Geoff Burdge

Laboratory for Physical Sciences
University of Maryland
College Park, MD 20740

I Introduction

Most optically addressed spatial light modulators (OASLMs) utilize photosensors of hydrogenated amorphous silicon (a-Si:H), Si, GaAs, CdS, CdSe or other photosensors which are sensitive from visible to near IR wavelengths ($< 1.1 \mu\text{m}$). Some applications such as correction of atmospheric turbulence in the eye-safe region of the spectrum for free-space optical communication demand OASLMs that have high sensitivity at 1.55 μm , high frame rate ($> 1 \text{ kHz}$), and high resolution (MTF = 50% at 40 lp/mm). Ferroelectric liquid crystal (FLC) has very fast response and FLC OASLMs can be operated at frame rates of a few kHz[1]. An IR-OASLM with an $\text{In}_{0.53}\text{Ga}_{0.47}\text{As-InP}$ photosensor and an FLC light modulating layer is being developed in our laboratories. The design, preliminary experimental results, and practical issues for such an IR-OASLM will be presented and discussed.

II Photosensor material

We have investigated various types of IR photosensors which include thermal, internal photoemission, organic, and photon detectors. Among them, intrinsic semiconductor photosensors offer good performance in terms of responsivity

and dark current. The photosensor in the IR-OASLM should be sensitive at 1.55 μm , but also have as large an energy bandgap as possible to avoid the excessive thermal current and large dark conductivity that are associated with narrow-bandgap semiconductors.

OASLMs that incorporate photosensors of crystalline Si or GaAs are biased alternately in erase and write periods[2-4]. In the write period, the dark current must be sufficiently low that the device does not switch on in the absence of illumination. A reverse-biased *pin* photodiode is similar to the OASLM in the write period in its dark current generation mechanism. Therefore a semiconductor that is used to make IR *pin* photodiodes with low dark current could also be used in the IR-OASLM. InGaAs-InP *pin* photodiodes have dark currents from 5×10^{-5} to as low as $4 \times 10^{-8} \text{ A/cm}^2$ [5-7]. InGaAs films also have a large absorption coefficient at 1.55 μm wavelength (8000 cm^{-1}). Therefore we choose InGaAs-InP as the photosensor for the IR-OASLM.

III IR-OASLM structure

One of the possible IR-OASLM structures that is used in Si and GaAs OASLMs is

illustrated in Fig. 1(a). The intrinsic InGaAs is slightly n -type. The n^+ -InP wafer serves as the ohmic contact to the intrinsic layer.

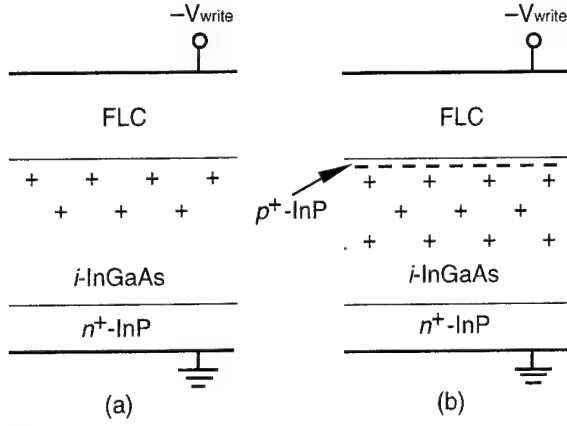


Fig. 1 Two possible structures of the IR-OASLM: (a) without, and (b) with a p^+ -InP layer.

When a positive erase-voltage V_{erase} is applied to the device, an electron accumulation layer forms near the FLC-InGaAs interface and the voltage across the FLC is equal to V_{erase} . The FLC layer is considered to be in its off-state. When a negative write-voltage $-V_{\text{write}}$ is applied, the electrons are swept out and a depletion layer forms in the InGaAs layer. The initial voltage in the FLC during the write period should be close to zero volts so that the FLC remains in its off-state in the absence of write light. Fig. 2 shows this initial voltage in a $1\text{-}\mu\text{m}$ FLC and the corresponding depletion width for $V_{\text{write}} = 5\text{ V}$ (assuming a thick InGaAs layer). It is clear that to keep the FLC in its off-state in the absence of write light the residual doping in InGaAs must be very small ($< 10^{13}\text{ cm}^{-3}$ for less than 1 V in FLC) and the InGaAs layer must be very thick ($> 20\text{ }\mu\text{m}$). Unfortunately, InGaAs can be grown only on InP wafers in thin-film form with residual doping $\geq 5 \times 10^{14}\text{ cm}^{-3}$. Most of the write voltage is dropped in the FLC layer if the

IR-OASLM incorporates only such an intrinsic InGaAs. In this case the FLC would switch to its on-state even in the absence of write light.

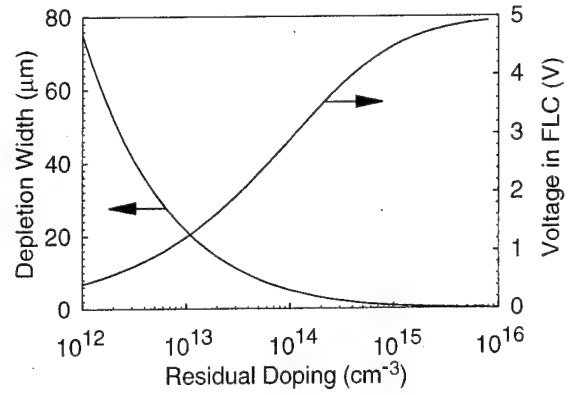


Fig. 2 Calculated depletion width in InGaAs and the initial voltage in the FLC versus residual doping in InGaAs. $V_{\text{write}} = 5\text{ V}$ is assumed.

The large initial voltage in the FLC can be reduced by depositing a thin layer of p^+ -InP on top of InGaAs, as shown in Fig. 1(b). InP is the preferred material over InGaAs for the reason discussed in Section V. When the voltage V_{erase} is applied to the device, electrons flow toward the p^+ -InP layer and holes in p^+ -InP are swept out or recombine with electrons. As a result a sheet of ionized acceptors are left in the p^+ -InP layer with charge density of $-\epsilon_{\text{lc}} V_{\text{erase}} / d_{\text{lc}}$, where ϵ_{lc} and d_{lc} are the dielectric constant and thickness of the FLC layer, respectively. When the voltage V_{write} is applied to the device, electrons in the intrinsic layer are swept out as in the configuration of Fig. 1(a). However, the acceptors *remain* ionized in the p^+ -InP layer, which lowers the potential at the interface and *reduces* the voltage in the FLC layer. Thus the initial voltage across the FLC during the write period can be adjusted by changing V_{erase} in the erase period. Fig. 3 shows the value of V_{erase}

that is needed to keep the initial voltage in a 1- μm FLC layer zero volts for a 3- μm InGaAs layer and $V_{\text{write}} = 5$ V. The corresponding depletion width in the InGaAs layer is also shown. With low residual doping, the InGaAs layer is fully depleted and V_{erase} is slightly larger than V_{write} . When the doping level increases, however, the depletion width decreases and the corresponding required V_{erase} grows and a very asymmetric driving waveform is needed.

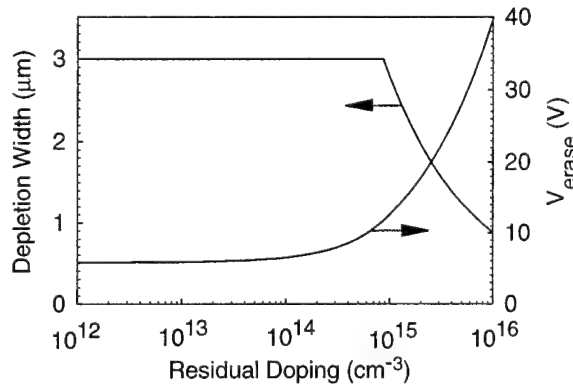


Fig. 3 Calculated depletion width in InGaAs and the required V_{erase} to keep the voltage in the FLC zero volts in the write period versus residual doping in InGaAs. $V_{\text{write}} = 5$ V is assumed.

A photosensor that consists of a thin p^+ -InP (< 100 nm) layer on top of a few micron intrinsic InGaAs layer is required in the proposed IR-OASLM. An InGaAs layer with low residual doping is desirable to reduce the asymmetry in the driving waveform.

IV IR-OASLM characterization

An IR-OASLM with the structure of Fig. 1(b) was assembled and tested. The SCE13 FLC is 1 μm thick, the 0.1 μm p^+ -InP layer has a doping concentration of $2 \times 10^{17} \text{ cm}^{-3}$, and the 1.9 μm intrinsic InGaAs $\sim 10^{16} \text{ cm}^{-3}$ [8]. The write light

(1.55 μm) is incident from the FLC side. Fig. 4 shows the transient response with a read light of 633 nm. The IR-OASLM can be operated at frame rates from 0.3 to 5 kHz. Its sensitivity at 1.55 μm is $\sim 1 \text{ mW/cm}^2$ and the best contrast ratio is 2:1.

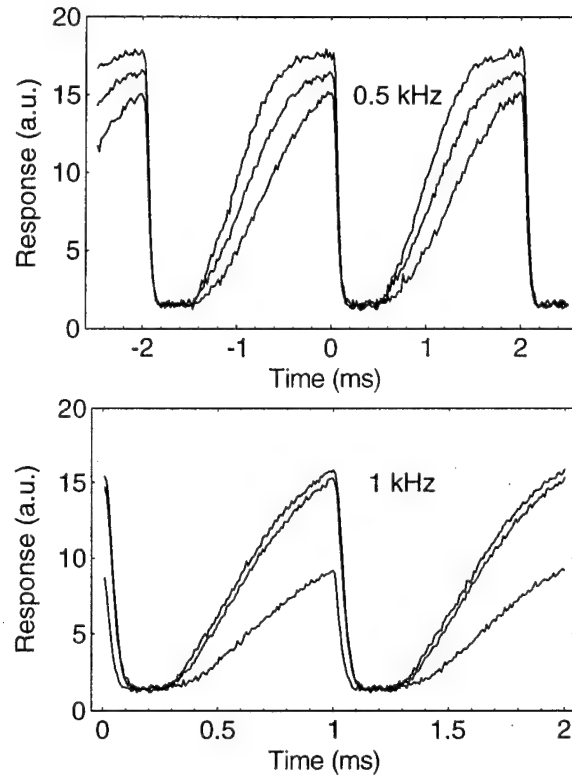


Fig. 4 Intensities of reflected read light from the IR-OASLM at frame rates of 0.5 and 1 kHz for write-light intensities of 0 (lowest curves), 1 (middle curves), and 2.5 mW/cm^2 (upper curves).

The partial switch-on of the FLC layer in the absence of write light is due to the large dark current from the InGaAs-InP photosensor. The frame rate of the IR-OASLM is limited by the switching speed of the FLC layer. In this test device the spatial resolution is very poor because of substantial charge spreading at the FLC-photosensor interface. We have also found that the FLC layer is not uniform. This is caused by the bow or warp in the photosensor, which is due

to the minor lattice-mismatch and thermal expansion difference between InGaAs and InP.

V Practical issues

An IR-OASLM that incorporates an InGaAs-InP photosensor has been demonstrated. The resolution, uniformity, and contrast ratio have to be investigated and improved to make practical devices.

From our recently developed resolution model[9] we have found that the carrier mobility and trapping time at the FLC-photosensor interface have to be very small for high resolution (diffusion length must be less than $3\text{ }\mu\text{m}$ for resolution of 10 lp/mm). One solution is to deposit a thin layer of a-Si:H on top of the p^+ -InP. The photogenerated minority carriers in InGaAs are holes. The hole mobility in a-Si:H is very small ($\sim 0.01\text{ cm}^2/\text{V s}$) and the charge spreading can be significantly reduced. The key to the success of this technique is to avoid having excessive dark current generated at the a-Si:H-InP heterojunction. Because the energy bandgap of InP (1.35 eV) is much larger than that of InGaAs (0.75 eV), it is expected that an a-Si:H-InP heterojunction[10] would result in much smaller dark current than an a-Si:H-InGaAs heterojunction.

A uniform gap between the optical flat and the photosensor is necessary for an IR-OASLM with large active area. The flatness of the photosensor could be improved by thinning and polishing the backside of InP wafer before bonding. An epitaxial liftoff technique offers another possibility[11].

The contrast ratio of the output from the IR-OASLM can be improved by reducing the dark

current from the photosensor. This may be accomplished by using high quality InGaAs-InP photosensors. The contrast ratio can also be improved by increasing the frame rate so that the amount of charge generated by the dark current in each write period is reduced.

Reference

1. G. Moddel, in *Spatial light modulator technology: materials, devices, and applications*, edited by U. Efron (Marcel Dekker, New York, 1994), pp. 287-359.
2. U. Efron, J. Grinberg, P. O. Braatz, M. J. Little, P. G. Reif, and R. N. Schwartz, *J. Appl. Phys.* **57**, 1356 (1985).
3. D. Armitage, J. I. Thackara, and W. D. Eades, *Appl. Opt.* **28**, 4763 (1989).
4. M. C. Hebborn and S. S. Makh, *SPIE Proceedings*, Vol. 825 (1987), pp. 19-23.
5. A. Zemel and M. Gallant, *J. Appl. Phys.* **64**, 6552 (1988).
6. S. Kagawa, K. Inoue, I. Ogawa, Y. Takada, and T. Shibata, *Japn. J. Appl. Phys.* **28**, 1843 (1989).
7. K. W. Carey and S. Wang, *J. Crys. Growth* **98**, 90 (1989).
8. The InGaAs-InP photosensor was grown by Professor Gary Robinson at Colorado State University.
9. L. Wang and G. Moddel, *Opt. Lett.* **19**, December 1, 1994.
10. S. Wu and D. Haneman, *J. Appl. Phys.* **74**, 5904 (1993).
11. W. K. Chan, A. Yi-Yan, and T. J. Gmitter, *IEEE J. Quan. Electron.* **27**, 717 (1991).

Wedged Liquid Crystal Beam Steering Device

Paul Searcy
Tami Hahn
Li Wang
Garret Moddel

Department of Electrical and Computer Engineering
Optoelectronics Computing Systems Center
University of Colorado, Campus Box 425
Boulder CO, 80309-0425
moddel@boulder.colorado.edu (303) 492-1889

John Wootton
Gary Waldman
Dave Holder

Electronics and Space Corporation
Advanced Development Center
8100 W. Florissant Ave.
St. Louis MO 63136

Introduction

Liquid crystals have long been investigated for non-mechanical beam steering devices. Previous work has approached beam steering by using an electrically addressed cell with multiple electrodes arranged in stripes. By creating a series of steps in the index of refraction profile, the beam experiences an effective wedge and is steered in a particular direction [1]. The discrete nature of the steps creates a substantial amount of scattering which can be reduced by the addition of a resistive region between electrodes to interpolate neighboring voltages [2]. Another method of beam steering is to create a voltage drop along one electrode which produces

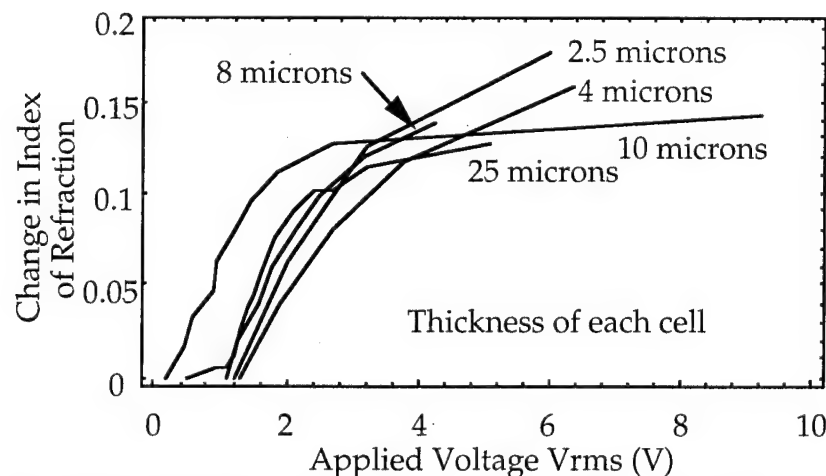


Fig. 1 Refractive index change to normally incident light of anti-parallel aligned nematic liquid crystal with applied voltage.

distortion. The approach is based on the finding that, for nematic liquid crystal (NLC) cells, the change in refractive index is dependent only on voltage and is independent of thickness [4]. Thus, within the variability from one experimental cell to another, the refractive index varies with the voltage rather than with electric field, as is shown in Fig. 1. Because of this thickness-independent change, a NLC

continuous phase profiles [3]. The steering angle is limited by the product of the change in index and thickness of the cell divided by the length of the cell. This creates a trade-off between switching speed and steering angle since the nematic relaxation time is proportional to the thickness squared.

We have taken a different approach to create beam steering with no diffractive loss and very little optical

wedge, depicted in Fig. 2, would exhibit a uniform change in refractive index for a particular voltage across the non-parallel electrodes. A beam transmitted through such a wedge would undergo a continuously varying refraction angle as a function of applied voltage. In this way, a beam could be deflected by simply varying a single voltage signal applied across the wedge.

Initial Results

The first design consists of a blazed grating with a blaze angle of 26.75° and a $50\text{ }\mu\text{m}$ pitch as one electrode to conveniently create a series of wedges, which were then filled with NLC. Anti-parallel alignment layers on both the grating surface and the optical flat were formed by the oblique evaporation of SiO_x . By reflecting the beam back through the NLC we were able to increase the steering angle by approximately a factor of two. One disadvantage of using a diffraction grating is the diffraction pattern that forms from the grating spacing. The grating produces a pattern of diffracted orders which change in intensity as a function of applied voltage but do not move from their respective positions. We demonstrated a change in direction of the refracted energy by approximately 28° through these diffracted spots with an applied voltage of 3.1 V_{ac} .

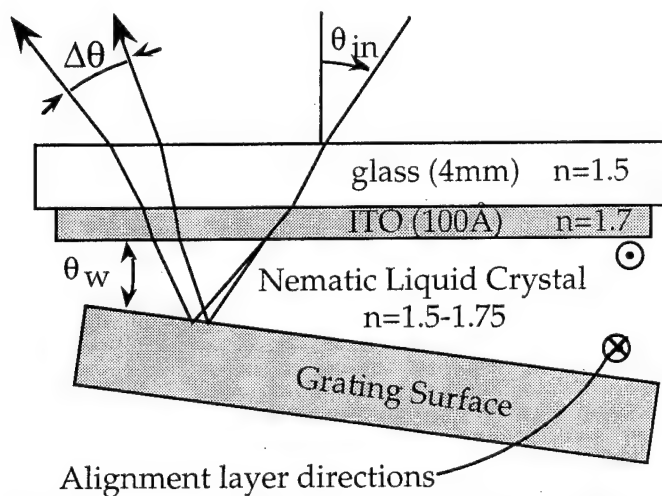


Fig. 2. Single wedge of a diffraction grating device used in reflection mode.

In an attempt to eliminate the discontinuous output by diffracting through a single wedge, we focused the incoming light onto as small a region as possible. We were successful in minimizing the diffractive effects of the grating at the expense of rather severe distortions of the refracted beam. The distortions arise from the fact that the incident ray angles are not linearly mapped to the output angles.

Modeling

A simple simulation, based on Snell's law, was

developed to minimize the distortions of the beam and maximize the steering angle ($\Delta\theta$) as a function of incident angle (θ_{in}), wedge angle (θ_{wedge}) and change in index of refraction (Δn). As can be seen in Fig. 3, when illuminated by a range of angles corresponding to a converging beam a wedged device creates a more divergent cone of rays. The divergence of the output cone depends on incident angle, change in index of refraction and wedge angle. By calculating the deflection angle of the refracted beam and comparing that angle to the amount of beam distortion we were able to determine the optimal wedge and incident angles. Fig. 3 shows the dependence of the steering angle on the wedge and incident angles for a change in

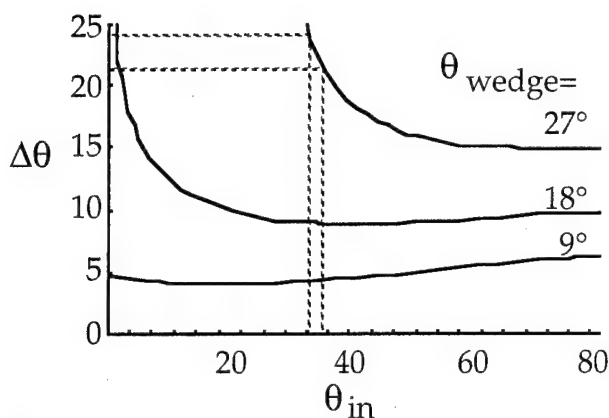


Fig. 3. Calculated beam steering angles versus incident angle for three wedge angles.

nematic liquid crystal index (Δn) of 0.225.* Although the beam steering angle increases by a factor of about three between $\theta_{\text{wedge}} = 9^\circ$ and 27° , the flat region which corresponds to low distortion (as is discussed below) becomes smaller.

To minimize distortion while maximizing steering angle we developed a figure of merit as a function of input and wedge angles. This number is calculated by dividing the change in the beam steering angle as a function of input angle by the steering angle ($\Delta\theta$):

$$\text{Figure of Merit} = F = \frac{d\Delta\theta(\theta_{\text{in}})}{d\theta_{\text{in}}} \frac{1}{\Delta\theta}$$

The smaller F values correspond to either greater beam steering angle or a smaller slope to the beam steering curve in Fig. 3. Ideally, we would have $F = 0$, which would correspond to a perfect mapping for all input angles to linearly shifted output angles. However, the next best case would be a linear dependence of $\Delta\theta_{\text{out}}$ on θ_{in} , which would give a simple $F = \text{constant}$ where the constant = slope/steering angle. This kind of distortion can be corrected for by the addition of elements in the optical train that would provide a transverse magnification of either the incident or refracted rays. (Examples of such elements are a cylindrical lens pair or an anamorphic prism pair.) If F is not a constant over the range of input angles then it is more difficult to correct the aberration. The calculated figure of merit versus three different wedge angles is shown in Fig. 4. Using Fig. 4 as our criterion for selecting the best operating region, we discover that although the amount of beam steering is the largest with a large wedge angle the distortion for convenient

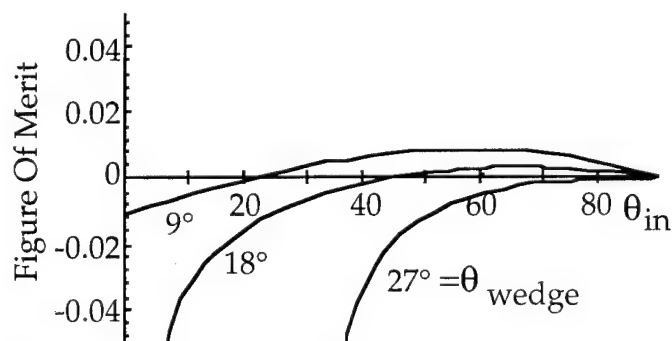


Fig. 4. Figure of merit versus wedge and incident angles.

incident angles (less than 30°) is much lower for smaller wedge angles. The 9° wedge device with an incident angle of approximately 20° appears to be optimal.

Improved Devices

Based upon this analysis we built a "lean-to" structure to create a wedged region of liquid crystal sandwiched between an ITO-coated substrate and a microsheet glass "roof." The alignment layers in the

* Merck specifications for nematic liquid crystal E7.

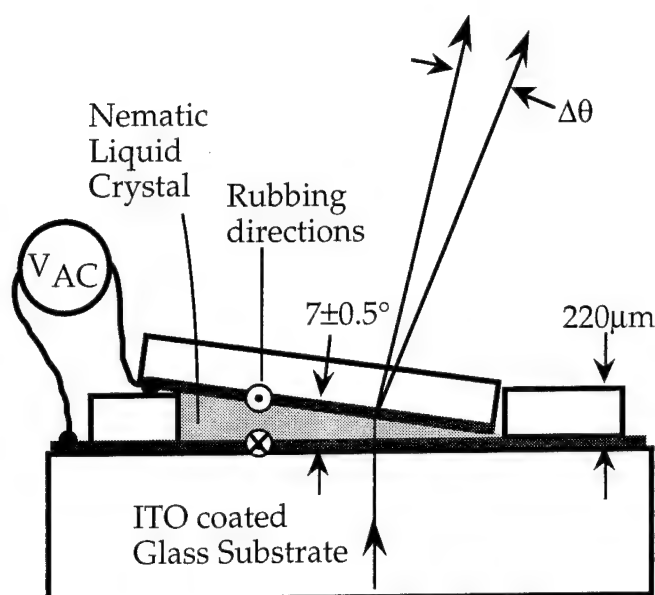


Fig. 5. Schematic of "lean-to" device.

cell are anti-parallel rubbed nylon as shown in Fig. 5. The point of contact between the two electrodes is insulated with 2 μm silica spacers suspended in epoxy. In order to investigate the thinnest region of liquid crystal possible the epoxy was intentionally not used along the entire length of the wedge. By leaving portions of the wedge-substrate bond unfilled with epoxy, the liquid crystal was able to fill the thinnest regions of the cell allowing us to investigate those regions with the fastest time response.

The relaxation time of 500 msec corresponds to a thickness of 7 μm as

calculated by [5]: $\tau = \frac{\eta d^2}{\pi^2 k}$. In this

equation η = viscosity of the liquid crystal, d is the thickness of the cell and k is an elastic constant.

An additional wedge of a very mild angle (0.064°) was built that gave effectively no optical distortion and beam steering over a large (4 cm^2) aperture but of limited steering angle. (0.015°)

We have presented a new type of beam steering device in which the steering angle can be controlled by varying a single voltage level. We demonstrated continuous steering over 2° from a device with a wedge angle of 7° with relatively no distortion and no diffractive losses.

References

1. P.F. McManamon, E.A. Watson, T.A. Dorschner, and L.J. Barnes, "Applications look at the use of liquid crystal writable gratings for steering passive radiation," *Optical Engineering* **32**, 2657-2664 (1993).
2. W. Chan, L. Ning, S.T. Kowel, and P.F. Brinkley, "The liquid crystal adaptive lens: aberration correction," *Photonic Neural Networks*, 1773, (SPIE) p.468-475 (1992).
3. G.D. Love, J.V. Major, and A. Purvis, "Liquid crystal prisms for tip-tilt adaptive optics," *Optics Letters* **19**, 1170-2 (1994).
4. L. Wang and G. Moddel, "MIS model of optically addressed spatial light modulators," *Spatial Light Modulators*, Salt Lake City, (1995).
5. P.G. de Gennes. *The Physics of Liquid Crystals* (Oxford: Clarendon Press, 1974).

Spatial Light Modulation at Photon-Counting Light Levels

J. H. Hunt and R. B. Holmes

Rockwell International Corporation, Rocketdyne Division, MS/JA01

6633 Canoga Ave, P O Box 7922, Canoga Park, CA 91309-7922

818/586-4614 E-Mail: jhhunt@APMAIL.APLAN.rdyne.rockwell.com

Recently, there has been a great deal of interest in the use of avalanche photodiodes (APD) for spatial light modulation.^{1,2,3} We report improved performance of our all-optical spatial light modulation with an avalanche photodiode. Modulation is performed with the APD operating as an asymmetric Fizeau interferometer with refractive index modulated by optically-initiated, avalanche-induced heating. Modulation of 80 % is achieved with optically optimized APDs. We demonstrate multiple-pixel operation, as well as free-carrier induced modulation.

When an incoming photon is absorbed by the avalanche photodiode (APD) under applied voltage, a localized avalanche of charge carriers is created as shown in Figure 1.

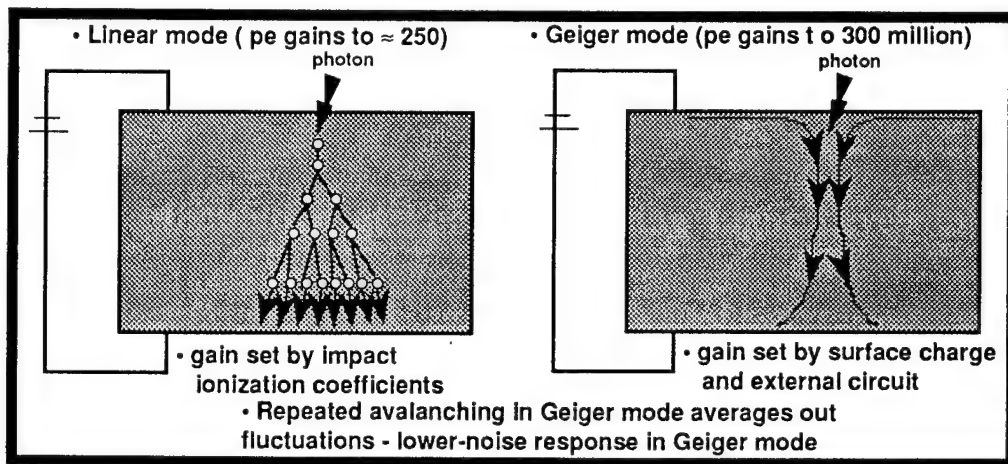


Figure 1. APD modes of operation.

The electrical response alters the local optical properties (index of refraction) of the diode, allowing it to act as a spatial light modulator. The process, shown schematically in Figure 2, depends on the size and duration of the avalanche, these being controlled by the external electrical circuit.

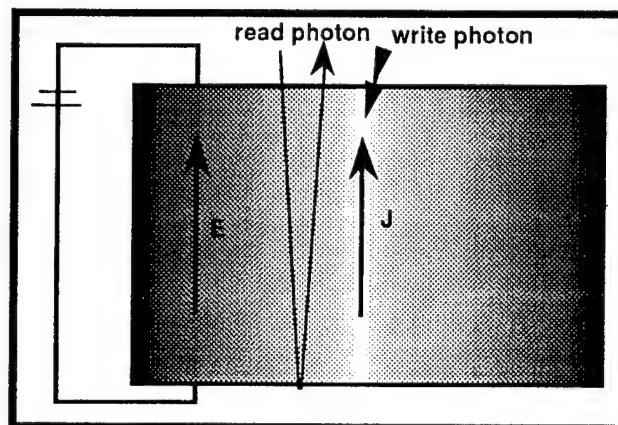


Figure 2. Schematic of Modulation Process

The avalanche process can possibly alter the optical properties of the device via four mechanisms.¹ First, Joule heating results from the localized current of charge carriers. Second, free-carriers alter the refractive index directly as a plasma and indirectly by changing the local conduction band structure of the diode. Third, the avalanche produces secondary photoemission. Fourth, the external voltage may electrically alter the refractive index of the material. In the experiments presented herein, Joule heating is found to completely explain the observed modulation of light. This thermo-optic modulation is observed even when a single photon initiates the response.

Two distinct modes of operation were tested. These are shown in Figure 3.

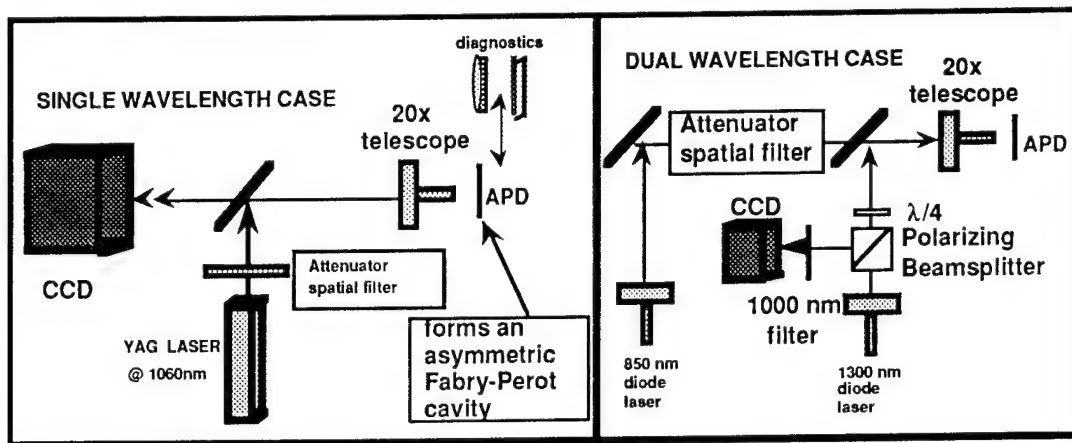


Figure 3. Experimental Set-up

In the first mode, the modulation is both written and read with light at 1064 nm in 750 ns duration pulses. In this mode, the lower limit intensity was constrained by the detection limit at the readout camera. The optical power was reduced to intensities as low as 1 nW, corresponding to 54 APD-absorbed photons per pulse. Based on these results, it is believed that the APD response will produce light modulation with write laser intensities of single-absorbed-photon levels.

Figure 4 below shows the single wavelength results. Figure 4a shows the image produced from subtracting images taken with the ADP voltage on and off. The light region due to the modulation. Figure 4b shows two subtracted images with the voltage off to show a null result.

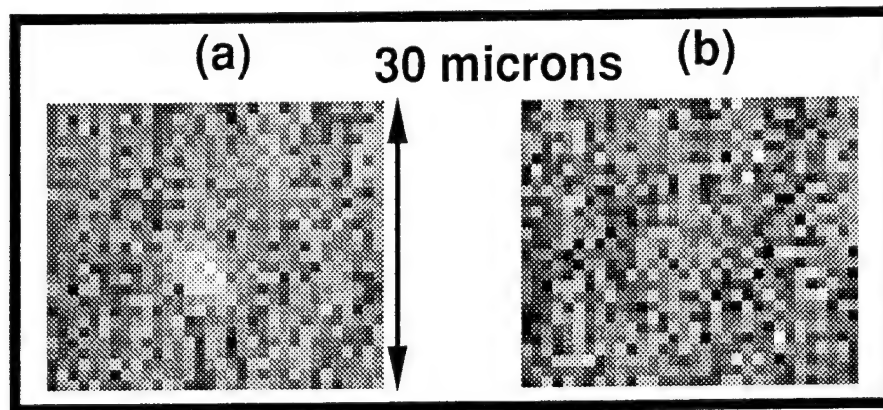


Figure 4. Single Wavelength Results

In the second mode, the modulation is written with a beam at 850 nm and read with a beam at 1300 nm. The 850 nm light is pulsed with 10 ns duration (FWHM) and the 1300 nm reading pulse of 15 ns is delayed by up to 100 ns from the writing pulse.

We present digitized camera images which show evidence of light modulation in both modes. In either mode, the APD voltage is varied to optimize response. In the dual wavelength mode, the write-read pulse delay is also varied. Experiments to date have been conducted with read/write frame rates of 20 kHz and optical spot diameters in the 3 micron range (FWHM). In both modes a read-out camera operating at 30 Hz was used to integrate signal.

Next are shown are the higher contrast modulation results. The result shown in Figure 5 is obtained under conditions similar to that of the first phase of the experiment. An overvoltage of 15 Volts was used with a 40 ns write-read delay with the optimized device near room temperature. Good results were also obtained by temperature tuning the unoptimized APD which had a thermoelectric cooler for temperature control. The figure clearly shows the high contrast modulation; the contrast modulation is measured at $78 \pm 8\%$. Contrast modulation of up to 98% (2:1) was observed at photon-counting light levels relative to the off state, with 50 nanosecond delays between the read and write beam and 6 nanoJoules of electrical energy per bit. This result is ascribed to Joule heating.

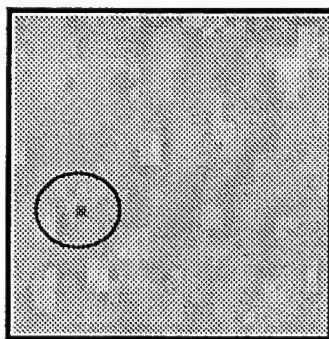


Figure 5. Improved contrast modulation with optimized device

The next measurement shown is the demonstration of high-speed modulation. For this measurement, the read and write pulses are shortened to 3 ns FWHM and are overlapped in time. The load resistance is reduced to 5 k Ω , giving a total resistance of about 10 k Ω . An operating voltage of about 40 V was used, giving a current of 4 mA, which should result in a free-carrier density of about $6.4 \times 10^{16} \text{ cm}^{-3}$, assuming a filament size of 2 microns in width and a carrier saturation velocity of 10^7 cm/sec . The predicted phase change should be is given by $\Delta\phi = 2.2 \times 10^{-2}$ radians/mA. The off-state reflectivity for the optimized device is about 12 % at room temperature, so inspection of Eq.(1) indicates that a phase change of about 0.022 radians should give at most a 7 % change in reflectivity (from 12.0 to either 12.9 or 11.1 % overall reflectivity). This is in relatively good agreement with the 8 % that is actually observed, as shown in Figure 5. Frame rates of 1 MHz or more are expected with this technology, based on published frame rates for APDs. The corresponding throughput of the device is 2.5 Terabits/sec/cm². The contrast modulation is clearly visible in the difference between the read beams with APD on and off and the ratio of the two (after smoothing and removal of highest and lowest pixels in image) clearly shows the result as well.

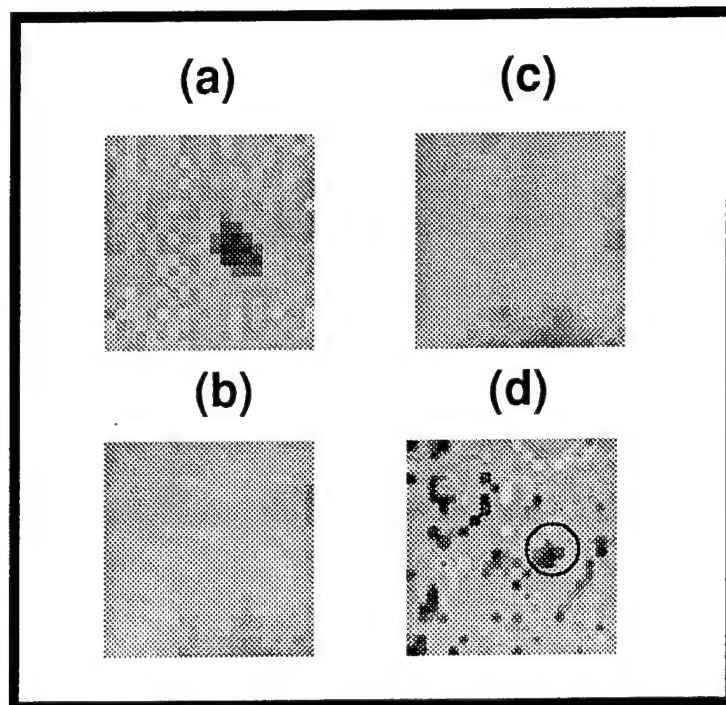


Figure 5. Contrast modulation @ 33 MHz. (a) 850 nm write beam; (b) 1300 nm read beam with APD off; (c) 1300 nm read beam with APD on; (d) ratio of (b) to (c).

Multi-resel images were also formed and observable modulation was found in this case too. A sample read-out image is shown with an image of the write beam in Figure 6. The image was taken with a 70 ns electrical pulse duration and an overvoltage of 20 V. The write beam is at relatively high light levels. The read-out image is smoothed in post-processing to eliminate camera noise.

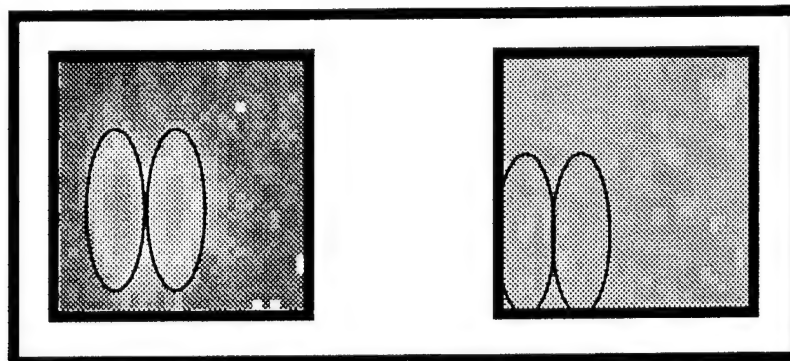


Figure 6. Demonstration of multi-pixel operation. The left image is the write beam, the right image is the read-out beam.

There are several potential applications. We will discuss these applications and means for their implementation.

References

1. J. H. Hunt and R. B. Holmes, Appl. Phys. Lett. **64**, pp. 2925 (1994).
2. G. Cocorullo, M. Iodice and I. Rendina, Opt. Lett., **19**, pp. 420-422 (1994).
3. Y. M. Liu, X. Xiao, P. R. Prucnal and J. C. Sturm, Appl. Opt. **33**, pp. 3871-3874 (1994).

Epitaxial Liftoff Integration of a GaAs Multiple Quantum Well Modulator Array onto Si VLSI for Optical Signal Processing

W. Chang, R. Ranganathan, V. Arbet-Engels, E. Yablonovitch
M. Hansen*, C. Fan*, S.C. Esener*, Uzi Efron**

UCLA, Electrical Engineering Department, Los Angeles, CA 90024-1594

*UCSD, Department of Electrical and Computer Engineering, La Jolla, CA 92093-0407

**Hughes Research Laboratories, Malibu, CA 90265

Introduction

The need for increased processing speed in advanced computing systems is straining the limits of purely electronic systems. Opto-electronic systems may represent the future form of implementation of high throughput data processing systems. The components that are selected for Opto-Electronic data processing systems have to meet the requirements of both high speed and low power dissipation. GaAs/AlGaAs Multiple Quantum Well (MQW) Spatial Light Modulators (SLM) exhibit low switching power and very high speed. Moreover, they operate at voltages which are compatible with Si VLSI technology¹. These make them attractive in high density optical information processing systems such as optical correlators. Thin film integration between Si integrated circuits and MQW modulators can be done by Epitaxial Lift-Off (ELO) technique. A major advantage of ELO is that Si circuitry and GaAs MQW modulators can be optimized individually and then integrated together resulting in improved yield and performance.

In this paper we report a novel self-aligned ELO integration scheme for a 16x16 reflective GaAs/AlGaAs MQW array on Si VLSI technology. The alignment of the MQW array on the Si driver circuitry was accomplished by controlling the respective aqueous surface tensions on lifted-off GaAs thin films and on the underlying bonding substrate surface.

Experiments

Reflective (normally-off) GaAs MQW modulators which contain 60 periods of (90Å)GaAs/(40Å)Al_{0.15}GaAs MQW's were fabricated. The driving voltage and operating wavelength were at 10Volts and 840nm, respectively. Foundry fabricated Si circuits, (MOSIS), designed with 2µm CMOS design rules served as drivers to the MQW array. The active area of the array had an effective fill factor of 97.3% and was composed of a 16x16 array containing 188µm×188µm pixels spaced on a 193µm pitch.

Most of the ELO processing procedures have been described in detail in other references². The form of integration in this experiment consists of the detachment of a fabricated array of GaAs MQW modulators from their substrate by under-cutting a thin sacrificial layer from between substrate and modulators. This thin film is then transferred onto the Si driver chip. The typical surface roughness on CMOS chips (MOSIS-2µm-technology) is about 1.8µm. It is essential to planarize this circuit topography before marrying the MQW modulators to the CMOS substrate. A variety of planarization schemes have been discussed elsewhere³. In this research work, a polymeric planarization coating which can reflow at 200°C and smooth out the surface was spun onto the Si chip

prior to thin film bonding. The degree of surface roughness was reduced by a factor of 10 after this coating. A 1500Å Au film reflector was then patterned onto the driver circuit array.

By controlling the respective aqueous surface tensions, of the planarization coating (hydrophobic, with wetting angle $> 90^\circ$) and the Au mirror (hydrophilic, with wetting angle $< 10^\circ$), the lifted-off film can be locked⁴ onto the surface pattern formed by the Au mirror. The modulators array is then "Self-aligned" onto the Si driver circuit when its surface pattern is exactly matched to the Au reflector. The processing sequence is shown in Figure 1. The major advantage of this self-aligned ELO is that Si circuits and GaAs MQW modulators can be fabricated and tested separately before brought together. The alignment of all the modulator array to the underlying driver circuitry can be done at the full array scale, or even at the wafer scale. After bonding the aligned lifted-off film onto the Au mirror, anti-reflection coatings and interconnection metallization were deposited, as diagrammed in Figure 2. The "floorplan" of the integrated chip is illustrated in Figure 3. After bonding the modulator diodes onto the Si driver circuitry, they do not exhibit any degradation. The performance of modulator array together with optical measurements will be presented in the conference.

The availability of a self-aligned epitaxial lift-off and bonding process, for modulator arrays, on planarized Si driver circuitry, may be extremely valuable in future dense, high speed, opto-electronic data processing systems.

References:

1. D. S. Chemla, D. A. B. Miller and P. W. Smith, *Optical Engineering*, vol. 24, no. 4, 556 (1985).
2. E. Yablonovitch, T. J. Gmitter, J. P. Harbison, and R. Bhat, *Appl. Phys. Lett.* **51**, 2222 (1987).
3. A. Ersen, I. Schnitzer, E. Yablonovitch and Tom Gmitter *Solid-State Electronics*, vol. 36, no. 12, 1731 (1993).
4. I. Pollentier, P. Demeester, P. Van Daele, D. Rondi, G. Glastre, A. Enard, and R. Blondeau, in *Proceedings of InP and Related Compounds*, (Cardiff U. K., 1991).

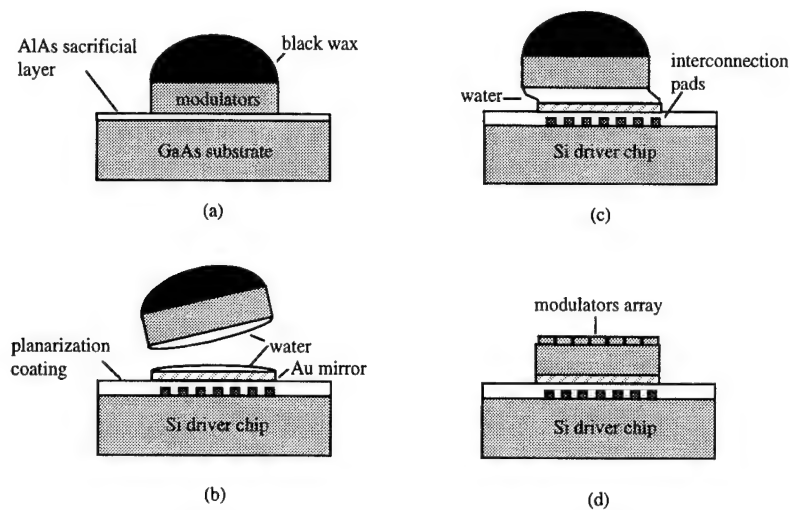


Figure 1: Self-aligned epitaxial lift-off thin-film integration. (a) Defining modulator array by mesa etching to AlAs sacrificial layer and selectively wax covering; (b) Lifted-off modulator array is brought together with the Si driver chip. Notice that water only adheres to hydrophilic surfaces. (c) Surface tension of water locks the thin film with respect to the underlying Au reflector. (d) The modulator array is self-aligned and bonded on to the Si chip.

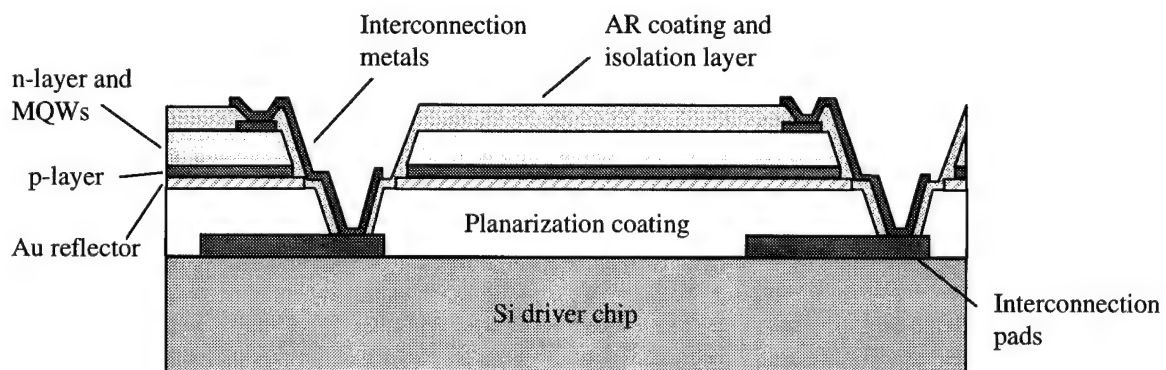


Figure 2: An illustration of thin film interconnection scheme between Si driver circuits and GaAs MQW spatial light modulators.

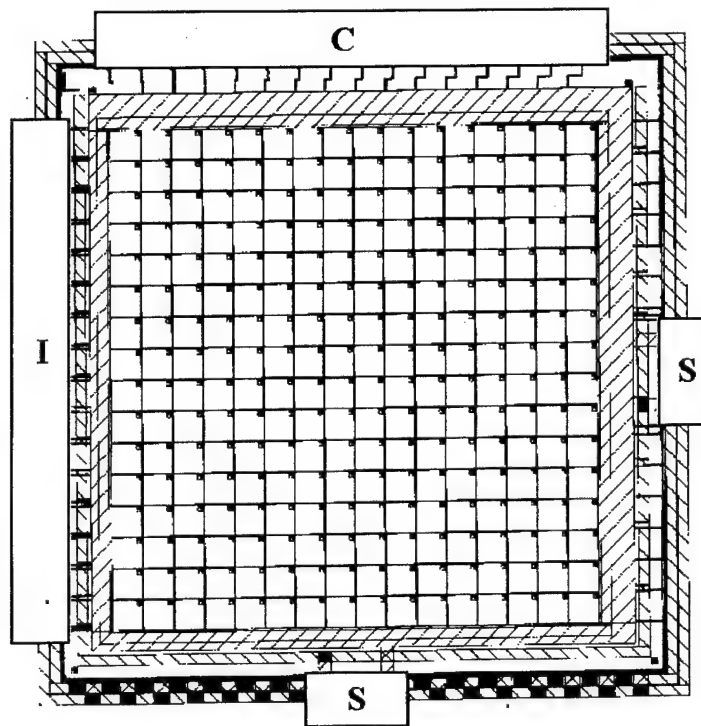


Figure 3: The “floorplan” of our 16x16 MQW-SLM integrated onto Si driver circuitry. C: Control signal inputs. I: Input signals. S: Sources, including external biases and GND.

Thursday, March 16, 1995

SLM Materials

LThB 10:30 am-12:00 m
Red Lion West

Sadik Esener, *Presider*
University of California-San Diego

ELECTROHOLOGRAPHIC SPATIAL LIGHT MODULATORS

Aharon J. Agranat
 Division of Applied Physics
 The Hebrew University of Jerusalem
 Jerusalem 91904, ISRAEL.
 AGRANAT@SHUM.CC.HUJI.AC.IL
 TL. 972 - 2 - 584710

Electroholography:

We present a new generic architecture for spatial light modulators (SLM), based on the concept of electroholography (EH). The pixel of the EH-SLM is a minute prestored volume hologram, the diffraction efficiency of which is controlled by a locally applied electric field.

The concept of EH is based on the use of the voltage controlled photorefractive (VC-PR) effect in paraelectric PR crystals which can be described as follows⁽¹⁾: In the paraelectric phase, the electrooptically induced birefringence depends quadratically on the electric field, and is given by

$$\Delta n = (1 / 2)n_0^3 g \epsilon_0^2 \epsilon^2 (E_0 + E_{sc})^2 \quad [1]$$

where Δn is the induced birefringence, n_0 is the refractive index; g is the quadratic electrooptic coefficient; and it is assumed that the (dc or low frequency) polarization is in the linear region: $P = \epsilon_0 \epsilon E$, where E is the electric field and ϵ is the dielectric constant (assuming $\epsilon \gg 1$). If E is given by $E = E_{sc} + E_0$, where E_{sc} is the photoinduced space charge and E_0 is the externally applied field, then the photoinduced changes in the birefringence which contribute constructively to the diffraction⁽¹⁾ are given by

$$\delta(\Delta n) = n_0^3 g \epsilon_0^2 \epsilon^2 E_0 E_{sc} \quad [2]$$

It can be immediately seen that the information carrying spacecharge field is transformed into a refractive index field only in the presence of an externally applied electric field. Thus, the use of the quadratic electrooptic effect enables an analog control of the PR index changes.

It should be noted that in the paraelectric phase ϵ becomes very large slightly above the transition temperature, (Typically: $\epsilon = 10^4 - 10^5$ for $T - T_c \approx 5K$). Thus, moderate spacecharge and externally applied fields induce a large photorefractive effect. It is necessary, therefore, to set the work point of a VC-PR device close to the phase transition temperature.

The VC-PR effect was originally observed in potassium tantalate niobate (KTN) crystals. However, in KTN, the ferroelectric phase transition becomes first order for Nb concentrations above 30% per mole (for which $T_c < 220K$). In the vicinity of a first order phase transition the optical quality deteriorates significantly. Consequently, the work point for devices based on the VC-PR effect in KTN cannot exceed 230K. This difficulty was overcome in a new PR crystal, potassium lithium tantalate niobate (KLTN), which was recently developed (2). KLTN samples with $T_c \approx 295K$ with high optical quality at room temperature were grown(3) opening the way for developing EH devices.

The Electroholographic Pixel:

The basic characteristics of the EH pixel are as follows:

- (a) Diffraction efficiency: The diffraction efficiency of an EH pixel can be estimated from experimental observations in 1 mm thick KLTN holograms and was found to be $\approx 90\%$ for a 100μ thick under an electric field of $1kV/cm$.
- (b) Switching time: Due to the critical slowing down of the dielectric response close to T_c , the switching time of the EH pixel is limited to $0.5 MHz$.
- (c) Spatial resolution: In order to maintain large diffraction efficiency in the EH pixel its thickness should be $\approx 100 \mu$ (in KLTN based devices). This requirement limits the spatial resolution to $\approx 10 lp/mm$ in devices in which the electrodes are deposited on the surface of the SLM. Special processing technology which will enable etching deep grooves into the KLTN crystal so that electrodes can be deposited on the side of the pixel, will remove this difficulty. This technology is currently under development.

(d) Storage density: Each EH pixel is a minute volume hologram with theoretical storage density of 10^{13} gratings/cm³. In practice the storage density is lower and a realistic number for a $100^3 \mu^3$ pixel is 1000 gratings.

(e) Analog switching: As can be seen in [2] the diffraction efficiency is continuously controlled by the external field. Therefore, the EH pixel can be operated in either analog or digital mode.

Electroholographic SLM Architectures:

The VC-PR effect is a natural tool for constructing electrically addressed SLMs. The possibilities opened up by the fact that the EH pixel is a minute volume hologram are demonstrated in the following two special purpose designs.

(a) The Fiber Linked EH-SLM: In several optical parallel computing designs, a SLM with large selectivity is required, whereas only a small number of pixels are 'on' in parallel, (typically 10-100 are 'on' out of 10^4 - 10^5 pixels). Normal SLMs suffer from very low efficiency under such constraints. The FL-SLM described schematically in Figure 1 overcomes this difficulty. The hologram in each pixel is created by the interference pattern of the light supplied by the fiber and traveling in the substrate, with the reference beam. During operation the light supplied by the fiber reconstructs the reference beam in the 'on' pixels defined by the electric signal V_i . Thus, the light emerges only from 'on' pixels.

(b) The EH Artificial Neural Network: The EH ANN is a device in which the SLM and the interconnecting network are integrated into one unit - the EH page (Figure 2). The principle of operation of the EH-ANN is described in detail in (4). Its main features are (a) it enable the construction of very large networks of approximately 10^5 neurons each connected to 10^3 - 10^4 other neurons with full selectivity; and (b) it enables real-time integration of complex receptive fields from full video images.

References:

1. A. J. Agranat, V. Leyva, And A. Yariv, Opt. Lett. **14** , 1017 (1989).
2. A. J. Agranat, R. Hofmeister, And A. Yariv, Opt. Lett **17** , 713 (1992).
3. R. Hofmeister, Caltech Ph.D. Thesis (1993).
4. A. J. Agranat , Physica A **200** , 608, (1993).

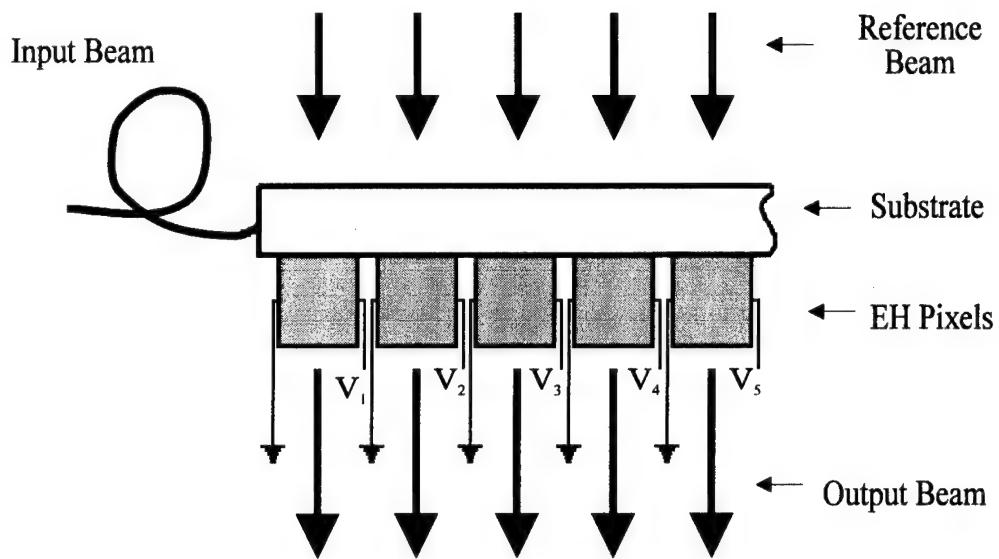


Figure 1: The Fiber Linked SLM

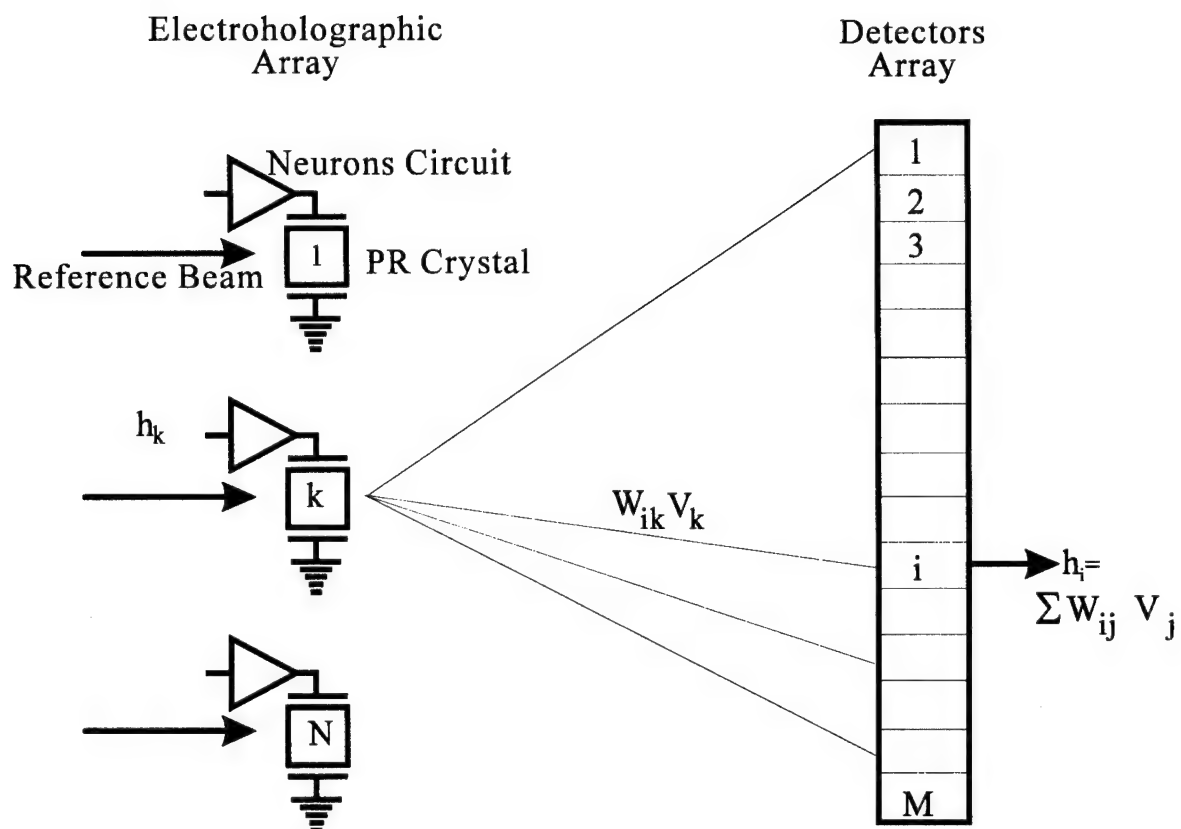


Figure 2: Schematic description of the Electroholographic neural network.

**Optically addressed intrinsic multiple quantum well
spatial light modulators**

W. S. Rabinovich, S. R. Bowman
Optical Sciences Division, Code 5640
Naval Research Laboratory, Washington, D. C. 20375-5320

D. S. Katzer
Electronics Sciences and Technology Division, Code 6850
Naval Research Laboratory, Washington, D. C. 20375-5374

C. S. Kyono
Motorola MS# M350
2200 West Broadway Road
Mesa, AZ 85202

Introduction

Recent demonstrations of perpendicular geometry GaAs/AlGaAs multiple quantum well (MQW) structures as optically addressed spatial light modulators (OASLM) have shown that these devices can offer high speed [1] and high resolution [2].

All MQW OASLMs to date have had deep traps distributed throughout the MQW region. These "bulk" traps have been thought necessary to decrease the dark conductivity of the MQW layers so that screening is largely due to photogenerated, and not background, carriers. In addition, the bulk traps were included to restrict the lateral diffusion of carriers which degrades OASLM resolution. Both these motivations are valid for parallel field geometry MQW OASLMs where photogenerated carriers drift and are trapped within the quantum well layers [3].

This reasoning may not, however, apply in the perpendicular geometry for the following reasons: Materials grown by molecular beam epitaxy (MBE), can have an unintentional doping on the order of 10^{14} carriers/cm³. This doping concentration is sufficient to screen only about 10% of the high fields applied to these materials in the perpendicular geometry (~50 kV/cm). Any further screening must be by photocarriers or thermally generated carriers, of which there are few due to the large band gap of GaAs. Thus background carrier screening may not be a problem in good quality materials

Recent work also suggest that bulk traps may not be necessary to maintain OASLM resolution. Theoretical calculations indicate that the screening carriers accumulate in an extremely thin (5

nm) region at the semiconductor-insulator interface[4]. In addition, experimental measurements of MQW OASLMs indicate that the transit time of the carriers across the quantum well region is approximately 300 psec[5], so the carriers spend most of each voltage cycle at the interface. These results indicate that the resolution performance of MQW OASLMs in the perpendicular geometry may be largely controlled by the trap concentration of thin layers at either end of the MQW region.

In this talk we examine the hypothesis that MQW OASLMs with surface, but no bulk, traps can show similar resolution to those with bulk traps. We show that these intrinsic MQW OASLMs offer superior performance to semi-insulating devices.

Device Structure

Three OASLMs were fabricated from two wafers. The MQW region in both wafers was grown by MBE to the same specification: 75 periods of 10 nm GaAs wells separated by 3.5 nm of $\text{Al}_{0.3}\text{Ga}_{0.7}\text{As}$ barriers. Wafer 1 had, in addition, high resistivity cladding layers at both ends of the MQW region. These cladding layers consisted of 30 nm of low temperature (LT) grown $\text{Al}_{0.3}\text{Ga}_{0.7}\text{As}$. The wafers were fabricated into three devices. For each we used epitaxial lift-off to remove the 1 μm MQW from its growth substrate. It was then attached, using solid phase bonding, to a quartz substrate coated with a transparent Cr/Pd/Au electrode. A 0.4 μm silicon nitride dielectric layer was then deposited on the top of the MQW followed by a Cr/Au transparent electrode.

Two devices were fabricated from wafer 1. The first device, designated SI/LT, was proton implanted to provide bulk traps and had low temperature AlGaAs layers to provide surface traps. The second device, designated, INT/LT, was not proton implanted and thus had only surface traps due to the low temperature AlGaAs layers present in this wafer.

The third device was fabricated from wafer 2. It was not proton implanted and had no low temperature AlGaAs layers. It was designated INT.

Optical Evaluation

Electroabsorption was measured in all three devices at room temperature in a Fourier transform spectrometer at voltages that varied from 0 to 10 Volts. Each device showed strong electroabsorption at about 850 nm.

The spatial resolution of the devices was determined by measuring the diffraction efficiency as a function of grating period. For the SI/LT and INT/LT samples, diffraction was measured at 852.5 nm, near the peak of the diffraction. For the INT sample the diffraction was measured at 856 nm because the peak diffraction fell at this slightly longer wavelength. Figure 1 shows diffraction efficiency for all three samples. As we demonstrated in an earlier work [2] the SI/LT maintains relatively high diffraction efficiency down to periods as short as 5 μm . However, as the figure shows, the INT/LT device's diffraction efficiency falls off only slightly faster with smaller

grating period even though it contains no intentional traps in the MQW region. The INT sample which has no intentional traps in either the bulk or at the surface shows only a very weak diffraction at the longest grating period, and no measurable diffraction below 30 μm . This constitutes strong evidence that the resolution of MQW OASLMs operated in the perpendicular geometry is determined predominantly by traps at the interface between the MQW region and the dielectric and that the traps in the bulk MQW play little part. The weak diffraction from the INT sample may be due to unintentional trap sites or surface traps.

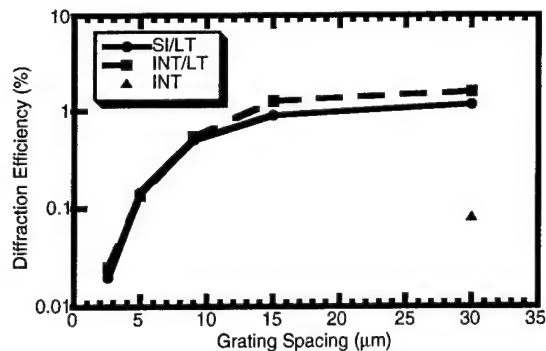


Figure 1
Diffraction efficiency vs. grating period for all three samples

Next we evaluated the temporal performance of the devices. In perpendicular mode MQW OASLMs each voltage flip of the applied AC field constitutes a new cycle for the device. The speed at which the device can be run is determined by the time for the diffraction to reach its peak value. Figure 2 shows the diffraction pulses for both the SI/LT and INT/LT samples for the same absorbed power of 43 mW/cm^2 . The INT/LT device rises and decays approximately 4 times faster than the SI/LT yielding a proportionally higher sensitivity. With no traps in the MQW region of the INT/LT sample it is much more likely for a photogenerated carrier to make it all the way across the well and fully participate in screening.

The amount of energy for the INT/LT sample to reach peak diffraction is 0.08 $\mu\text{J}/\text{cm}^2$. This means that the SI/LT sample needs approximately 8 photons to produce one carriers worth of screening, while the INT/LT sample needs only about 2 photons. The maximum efficiency possible would be 0.5 photons per carrier since each absorbed photon produces an electron-hole pair.

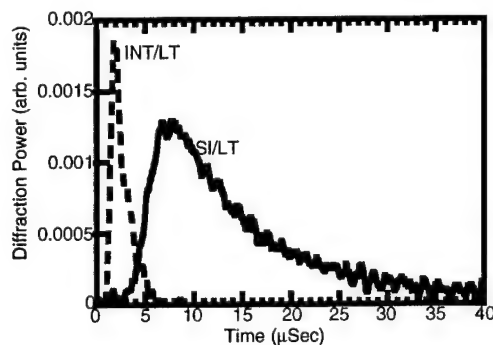


Figure 2
Diffracted power vs time for samples with low temperature layers.

Conclusion

Contrary to prior work on MQW OASLMs we have shown that bulk traps are not necessary and are in fact detrimental to the performance of these devices. Samples with the MQW region left as grown and with highly resistive LT AlGaAs layers show comparable resolution performance, larger diffraction efficiencies and more than four times the sensitivity of materials with bulk traps and LT layers. This high sensitivity should allow these materials to work at lower light levels and at speeds higher than 1 MHz without the heating problems that would be present in less sensitive devices.

Acknowledgments

The authors acknowledge the support of the Office of Naval Research.

References

- [1] A. Partovi, A. M. Glass, D. H. Olson, G. J. Zydzik, H. M. O'Bryan, T. H. Chiu and W. H. Knox, "Cr-doped GaAs/AlGaAs semi-insulating multiple quantum well photorefractive devices", *Appl. Phys. Lett.* **62**, 464 (1993).
- [2] S. R. Bowman, W. S. Rabinovich, C. S. Kyono, D. S. Katzer and K. Ikossi-Anastasiou, "High resolution spatial light modulators using GaAs/AlGaAs multiple quantum wells", *Appl. Phys. Lett.* **65** (1994).
- [3] D. D. Nolte, D. H. Olson, G. E. Doran, W. H. Knox and A. M. Glass, "Resonant photodiffractive effect in semi-insulating multiple quantum wells", *J. Opt. Soc. Am. B* **7**, 2217 (1990).
- [4] S. L. Smith and Lambertus Hesselink, "Transport modelling of multiple quantum well photorefractive devices" in OSA Annual Meeting Technical Digest, Vol. 16, 1993 (Optical Society of America, Washington, DC 1993), p.60
- [5] Daniel Mahgerefteh, Ergun Canoglu, Ching-Mei Yang, Elsa Garmire, Afshin Partovi, T. H. Chiu, A. M. Glass, G. J. Zydzik, "Picosecond response of a Cr-doped GaAs/AlGaAs semi-insulating multiple quantum well photorefractive device" in Conference on Lasers and Electro-optics, Vol. 8, 1994 (Optical Society of America, Washington, DC 1994), p.265

Characterization of the optical quality and modulating properties of a PLZT modulator through Mueller matrix imaging polarimetry

J. Larry Pezzaniti, Elizabeth A. Sornsin, Russell A. Chipman

University of Alabama in Huntsville

Physics Department

Huntsville, AL 35899

Tel. (205) 895-6417 ext. 318

Fax. (205) 895-6873

Email: sornsinb@email.uah.edu or chipmanr@email.uah.edu

B. Mansoorian

University of California, San Diego

Department of Electrical and Computer Engineering

1 Introduction

The Physics Department at the University of Alabama in Huntsville (UAH) in collaboration with the Electrical and Computer Engineering Department of University of California, San Diego (UCSD) has applied Mueller matrix imaging polarimetry[1] to quantifying the polarization modulating properties of PLZT spatial light modulators. The purpose of this study was to evaluate the optical quality of a wire-bonded transmissive PLZT (9/65/35) modulator array, the uniformity of modulation across pixels, and the cross-talk between adjacent pixels.

The Mueller matrix imaging polarimeter measures *Mueller matrix images* of spatial light modulators[2,3], polarization optics[4], or entire optical systems[5]. For this work, the imaging polarimeter was configured to measure 128x128 Mueller matrix images across individual pixels of the modulator. The Mueller matrix image contains all of the polarization altering properties of PLZT, including the magnitude of retardance, the orientation and ellipticity of the retardance, and the depolarization, a measure of how much the modulator scrambles the transmitted polarization state. This paper presents mappings of these polarization altering properties across pixels of the modulator when a half wave voltage is applied.

The next section presents the maps of the polarization altering properties of the PLZT modulator and interprets the information contained in them. The concluding section describes future directions using this metrology to study state-of-the-art PLZT smart spatial light modulators.[6][7][8]

2 Magnified Polarization maps of PLZT modulator pixels

Figure 1 shows a schematic of the PLZT modulator array. The modulator pixels are on $500\mu m$ centers and the electrode separation is $40\mu m$. The surface of the PLZT wafer is covered with silicon dioxide and openings are made where the metallic electrodes touch the PLZT wafer. The pixel electrodes are laid out at 45° to the horizontal, defining the optical axes of the individual modulators. Mueller matrix images were measured across single pixels (highlighted in Figure 1) of the PLZT modulator. The following sections describe the various mappings of the polarization properties of the device.

2.1 Retardance of PLZT modulator

Specification of retardance requires three parameters: a magnitude, an orientation and an ellipticity. The magnitude specifies the optical path length difference between the fast and slow polarization states. The orientation and ellipticity describe the type of retarder. For example a linear retarder, such as a quarter wave linear retarder, has an ellipticity equal to 0, and an orientation parallel to the retarder's fast axis. A circular retarder has an ellipticity equal to 1; the orientation then refers to the handedness of the fast circular polarization state, either right or left. For an elliptical retarder, the orientation and ellipticity define the polarization ellipse of the fast elliptical polarization state.

Ideally, each pixel of the PLZT modulator would display linear retardance oriented at 45° , and this retardance would be spatially uniform in the area between the electrodes. In other words, the retardance ellipticity would be uniformly equal to 0, and the retardance orientation would be uniformly equal to 45° .

2.1.1 Map of retardance magnitude of a single PLZT modulator pixel

Figure 2 shows a gray scale contour map of the variations of retardance between 0° and 180° . The retardance remains high ($\sim 40^\circ$) as far as $75\mu m$ away from the active region of the modulator. This residual retardance is caused by electric fields extending to neighboring pixels $500\mu m$ away and fringing fields. This effect is a potential source of cross-talk.

The spatial average of retardance between the electrodes is 165° . The retardance magnitude changes abruptly at several locations between the electrodes. In some places the retardance magnitude changes as much as 60° within $10\mu m$. These abrupt changes are caused by nonuniform electric fields between the electrodes. The variation of the electric field may be caused by damage to the PLZT from excessive electric field strength, impurities in the PLZT, large non-uniformities in the PLZT, and/or areas where contact has been broken between the electrode and the PLZT.

2.1.2 Retardance orientation and ellipticity

Figure 3 maps the orientation of the fast axis of retardance across the pixel. Ideally the retardance would be oriented at 45° , uniformly across the pixel. Between the electrodes, the average orientation of the retardance is 45° , but it varies from 25° to 50° . The orientation of the fast axis of retardance tends to align with the orientation of the electric field lines. The electric field lines between the electrodes appear striated. The orientation of the retardance of the PLZT surrounding the intended modulation area is nearly 45° , except for the zones outside area between the electrodes at 1 o'clock and 7 o'clock. In the latter area, the retardance orientation of $15\text{-}20^\circ$ may be caused by fringing electric fields originating from the corners of the electrodes.

Figure 4 maps the ellipticity of the retardance. The ellipticity is very small, less than 0.02, between the electrodes. The outlying areas have ellipticities of as high as 0.15.

2.2 Depolarization of PLZT modulator

Figure 5 is a mapping of the depolarization index of the PLZT modulator. The depolarization index is a figure of merit describing the polarization scrambling (scatter) properties of a sample. A depolarization index of 0 indicates that the sample is non-depolarizing, and a depolarization index of 1 indicates that the sample completely depolarizes the light. In modulators, light that is depolarized contributes to noise. From the map we see that the area between the electrodes depolarizes a greater fraction of the light than the surrounding (non-modulated) area. The edges of the etched away SiO_2 strongly depolarizes the light (the depolarization index is as high as 0.1). Additional data reduction of the Mueller matrix image can determine which polarization states are depolarized the most.

3 Conclusion

We conclude by describing other measurements which can be done with this technique. The future direction of this work is to apply Mueller matrix imaging polarimetry to study strain in flip-chip bonded PLZT [7], electrostriction induced strain, electric field confinement between pixels [8], and to determine PLZT grain size effects on depolarization and scattering.

The implementation of smart spatial light modulators requires a marriage between electronic processing materials (e.g. Si, GaAs) and light modulation materials (e.g. Ferroelectric ceramics, liquid crystals, III-V semiconductors, Si). Silicon/PLZT integration technologies offer a means to realize smart spatial light modulators, since PLZT can be integrated with Si, in which logic (smart) circuits can be fabricated. One approach to combining Si with PLZT is a hybrid integration technique using flip chip bonding. For example, two promising approaches currently under investigation for bonding Si thin films onto bulk PLZT are as follows: (1) a commercially available thin ($2\text{-}4\mu m$) Si film of very high quality is bonded onto a PLZT wafer with an interface layer of Al_2O_3 , and driver circuits are fabricated onto the Si film after bonding, and (2) driver circuits are implemented in a commercially available Si wafer which is then bonded onto bulk PLZT.

Several effects can be studied with Mueller matrix imaging polarimetry:

(1) flip-chip bonding induced strain:

Flip-chip bonding is applied to connect the outputs from logic signal processing circuits in bulk Si to the driver circuits on the Si thin film that is bonded on bulk PLZT. The bonding involves heating the Si and PLZT substrates to 300 ° C, liquifying an array of solder bumps, and pressing the substrates together until they are cooled. As the substrates cool, strain occurs between the substrates because of different thermal expansion coefficients of Si and PLZT.

(2) Electrostriction induced strain:

An electric field applied to a 9/65/35 PLZT material induces strain in the crystal due to the electrostriction effect. Since the PLZT is clamped tightly to the Si substrate, expansion of the PLZT increases its stress. Since clamping (solder bonds) strengths are not uniform across the device, the amount of stress across the device due to this effect is not uniform. Both electrostriction and the EO effect in 9/65/35 PLZT are quadratic in the electric field strength, and the birefringence due to electrostriction can be 60% as large as the birefringence from the EO effect.

(3) Electric field confinement

The longitudinal electric fields applied to the PLZT substrate are not confined to the pixel windows, i.e. the electric fields can spread into the interpixel spaces. If adjacent pixels are too close, the electric fields addressing one pixel influence the neighboring pixel, and cross-talk between the pixels occurs.

(4) Depolarization and scattering from PLZT grains

PLZT is usually fabricated as a hard pressed polycrystalline cubic lattice with grain sizes on the order of $5\mu m$ to $6\mu m$. The crystalline molecules are somewhat randomly oriented, and the quality of the wafers varies from vendor to vendor. The smaller grains and the random orientation of the molecules are expected to cause scatter and depolarization.

References

- [1] Mueller matrix imaging polarimetry, submitted to Opt. Lett., (1994).
- [2] J.L. Pezzaniti, R.A. Chipman, Opt. Lett. **18**, 1567 (1993).
- [3] J.L. Pezzaniti, R.A. Chipman, Opt. Lett. **18**, 2071 (1993).
- [4] J.L. Pezzaniti, R.A. Chipman, Appl. Opt. **33**, 5080 (1994).
- [5] J.L. Pezzaniti, R.A. Chipman, *Polarimetry: Radar, Infrared, Visible, Ultraviolet, and X-Ray*, R.A. Chipman and J. Morris, eds., Proc. SPIE **1317**, 280 (1990).
- [6] A. Ersen, S. Krishnakumar, V. Ozgur, J. Wang, C. Fan, S. Esener, S. H. Lee, Appl. Opt. **31**, 3950 (1992).
- [7] B. Mansoorian, G. Marsden, V. Ozguz, C. Fan, S. Esener, *OSA Proc. Spatial Light Modulators and Applications*, 1993 Tech. Dig. Series **6**, 128 (1993).
- [8] T. Lin, A. Ersen, J. H. Wang, S. Dasgupta, S. Esener, S. H. Lee, Appl. Opt. **29**, 1595 (1990).

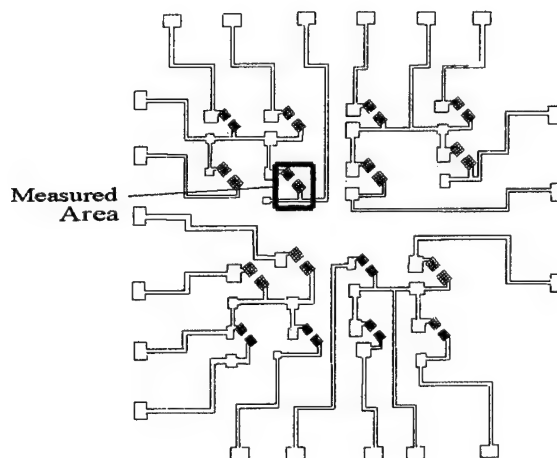


Figure 1: Schematic of PLZT array.

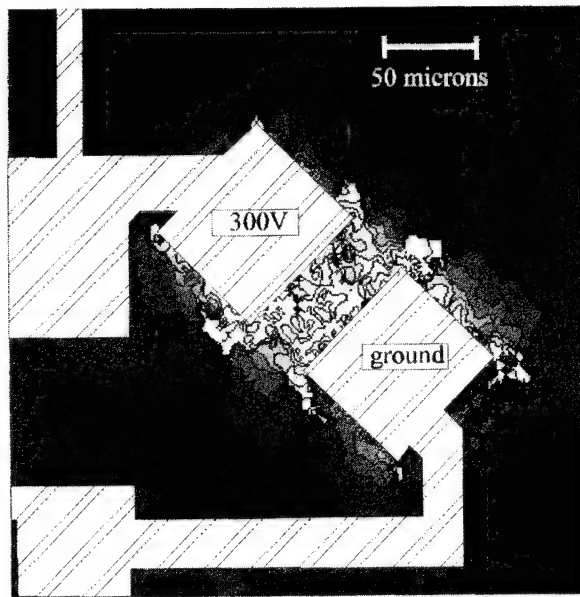


Figure 2. Map of retardance magnitude across one pixel of a wire bonded PLZT modulator (300V applied half wave voltage). Average retardance is near half wave. Zones 5 - 15 microns in diameter show sharply reduced retardance. This structure looks like striation between crossed polarizers. Retardance of nearly 40 degrees extends 100 microns away from the intended active region.

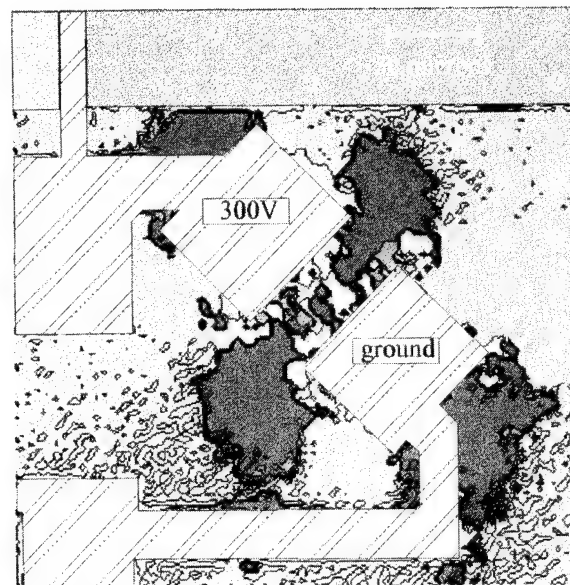


Figure 3. Retardance orientation of PLZT pixel. Orientation is nominally at 45 degrees, parallel to the electric field lines between the electrodes.

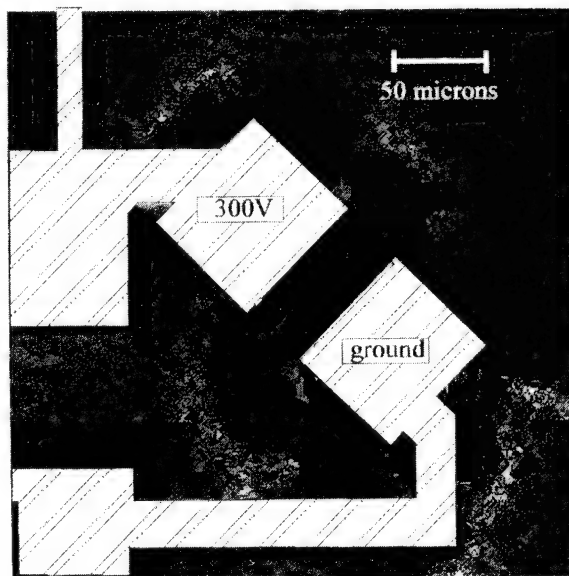


Figure 4. The modulator is expected to display linear retardance. The ellipticity is zero within the active region as expected.

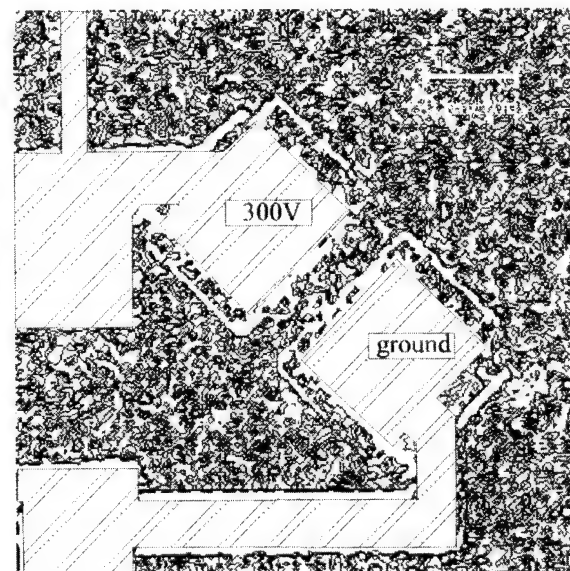


Figure 5. Ideally the modulator would preserve the degree of polarization of the light, i.e. the depolarization would equal 0. The depolarization of the PLZT varies between, and appears to be larger within the active region.

Spatial light modulation based on photo-induced change in the complex refractive index of bacteriorhodopsin

Hiroyuki Takei and Norio Shimizu

Advanced Research Laboratory, Hitachi, Ltd.

Hatoyama, Saitama, 350-03 Japan Tel:81-492-96-6111

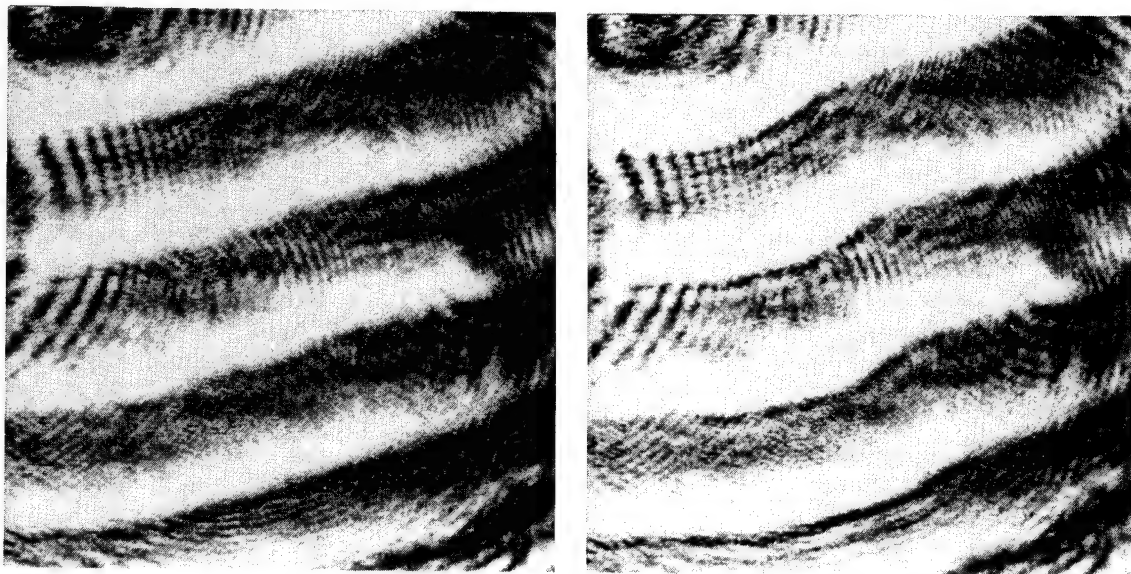
Bacteriorhodopsin (bR) is a photosensitive molecule found in the cell membrane of *Halobacterium halobium*. It has a large extinction coefficient of $6.3 \times 10^4 \text{ M}^{-1} \text{ cm}^{-1}$ at 568 nm. A chromophore, which is responsible for absorption, undergoes rapid isomerization upon photon absorption. In tens of μs , the M photo-intermediate whose absorption maximum is at 412 nm forms. Irradiation of the M photo-intermediate results in regeneration of the original B state. Thus, bR has a potential as a photoreversible photochromic material. It is characterized by a high quantum efficiency of over 60%, exceptional cyclical durability of more than million cycles, and excellent mechanical stability over several years.

Photo-induced changes in the absorption spectrum are accompanied by changes in the refractive index which are particularly large at 0.4% in the far red region (Ref. 1). We have formed thin bR film with little absorption or scattering. When the film was inserted into the Fabry-Perot cavity and irradiated uniformly by 792 nm light, interference fringes were observed. The fringes shifted upon photochemical reaction of the bR film (Ref. 2).

We have since then investigated the possibility of constructing a photo-addressable spatial light modulator. In particular, we have attempted to modulate light whose wavelength coincides with the absorption edge of bR around 633 nm. Irradiation of bR by 633 nm light induces photochemical reaction which is accompanied by changes in the absorption spectrum as well as refractive index. This will enable us to construct a spatial light modulator with a non-linear input-output response.

The effect of absorption to the transmission characteristics of the Fabry-Perot cavity was first examined. An appropriate optical density for bR film had to be determined to achieve a good on-off contrast ratio. An optically thick film would exhibit a greater phase shift upon photochemical reaction, but an optically thin film with little optical loss has an advantage in producing sharper interference fringes. Three films with transmissions of 23, 39, and 64 % at 633 nm were prepared. The transmission property of the Fabry-Perot cavity containing these films were calculated by the Airy formula, and good agreement with experimentally observed interference fringes was confirmed. The optically thinnest film resulted in fringes with the best contrast ratio.

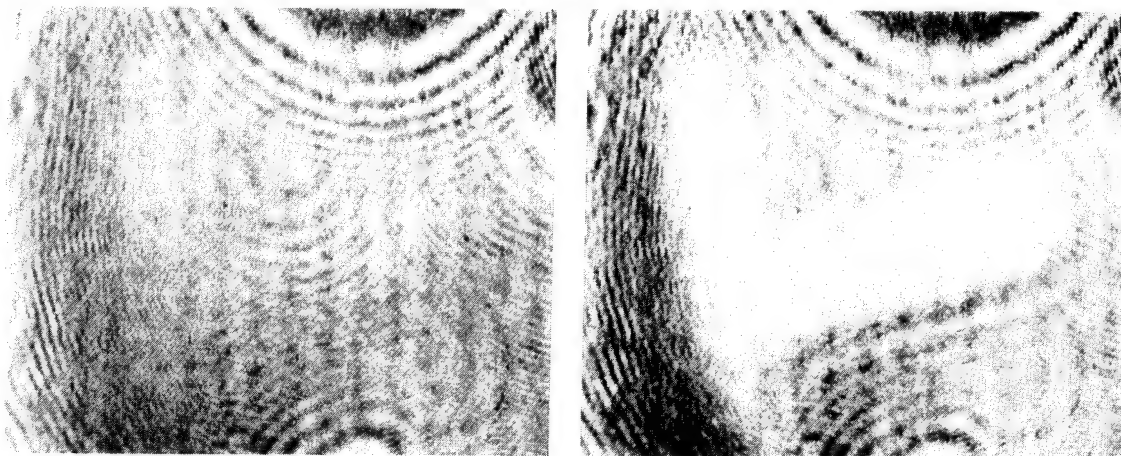
The photo-induced phase shift was measured with the film that exhibited the best fringes. In Fig. 1 (a), the entire bR film was irradiated by attenuated 633 nm light. In Fig. 1 (b), M was locally accumulated by brief irradiation. The fringe shift reflected a phase shift of $\pi/4$.



(a) (b)
Figure 1 Photo-induced shift of interference fringes

We proceeded to demonstrate spatial light modulation with this bR film. The cavity mirrors were set parallel to each other, and the cavity gap was adjusted in such a way to maximize the cavity transmission upon the M formation. Figure 2 provides two photos showing spatial light modulation of the cavity. In Fig. 2 (a), the bR film is in the B state. In Fig. 2 (b), the bR film was briefly irradiated in an L shaped region. Accumulation of the M photo-intermediate lead to an increase in the cavity transmission from 26 to 74%. This was in good agreement with calculations based on the Airy formula whereby changes in the absorption and refractive index were taken into account.

It is still necessary to examine effects of other parameters such as the mirror reflectivity and wavelength dependence. Dynamic switching characteristics have yet to



(a) (b)
Figure 2 Spatial light modulation

be examined. We foresee, nonetheless, that further investigation of the bR optical properties will lead to the construction of a spatial light modulator that exhibits a non-linear input-output response at moderate intensities of tens of mW/cm^2 . Combined with the memory effect of bR, the bR non-linear optical device will be particularly suited for implementation of an optical neural network.

Ref. 1 D. Zeisel and N. Hampp, "Spectral relationships of light-induced refractive index and absorption changes in bacteriorhodopsin films containing wildtype BR_{WT} and the variant BR_{D96N}," J. of Phys. Chem. **96**, 7788-7792 (1992).

Ref. 2 H. Takei and N. Shimizu, "Nonlinear optical properties of a bacteriorhodopsin film in a Fabry-Perot cavity," Opt. Lett. **19**, 248-250 (1994).

Nonlinear optical image processing with bacteriorhodopsin films

John D. Downie
NASA Ames Research Center
M/S 269-3
Moffett Field, CA 94035

Tel.: (415) 604-3588
e-mail: downie@ptolemy.arc.nasa.gov

The transmission properties of bacteriorhodopsin film spatial light modulators are used to perform nonlinear optical image processing operations on images with multiplicative noise. A logarithmic amplitude transmission characteristic of the film permits the real-time optical conversion of multiplicative noise to additive noise, which is then linearly filtered out in the Fourier plane of the transformed image. We present experimental results for different image and noise situations, including deterministic noise and speckle.

Images with multiplicative noise characteristics present special challenges for many applications including optical correlation and image restoration. A well-used approach in such situations is to logarithmically transform the original noisy image. This nonlinear operation on the image separates the noise from the underlying object function by producing a new image with additive noise. Traditional linear filtering techniques can then be applied for purposes of image restoration, reconstruction, etc. For some optical processing applications such as correlation, it may be efficient to perform the logarithmic preprocessing of the images optically. Bacteriorhodopsin (BR) is an organically-derived material that demonstrates many desirable properties for use as a real-time optically addressed SLM for optical processing applications^{1,2}. In a recent paper, we showed that certain BR films exhibit a logarithmic transmission property in intensity and demonstrated the efficient conversion of a speckle image into a transformed image with the appropriate additive noise characteristics³. Here we present data illustrating that the amplitude transmission properties of some films also exhibit behavior that is logarithmic over a large dynamic range. We use this effect to transform images in amplitude to allow subsequent coherent linear optical filtering to eliminate the unwanted noise which cannot be entirely removed using the same filters on the original images.

BR is a protein molecule found in the photosynthetic system of a salt-marsh bacterium called *Halobacterium salinarum*. The BR molecule is located in a cell membrane commonly called the purple membrane (PM). Effectively, BR is used by the bacterium to directly convert sunlight into chemical energy. The absorption of light also initiates a photocycle in the BR molecule. The characteristics of this photocycle make it a potentially useful material as an optically-addressed SLM. This is especially true since the photocycle continues to operate after the BR is extracted from the bacterium in the form of 2-dimensional crystalline sheets of PM and suspended in various solutions in the preparation of films. In the dark, the molecule is initially in the bR state, which has an absorption spectrum peaked at about 570 nm. Upon absorption of a photon, the molecule passes through several intermediate states via thermal relaxation until it reaches the M-state. In this state the peak absorption wavelength is in the blue region at about 412 nm. Thus images may be recorded in a BR film by exploiting this photochromic property. The image lifetime can be controlled by chemical means², among others. Images can be erased by exposure to blue light which directly returns the molecule to the bR-state. Thus BR films can be used as real-time, erasable optical photographic or holographic films which require no development process, although in general the images recorded are not permanent. The film spatial resolution is ~2000 line pairs/mm due to the small molecular size of BR.

The film used in this experiment was prepared from the wildtype form of BR by Bend Research, Inc. After extraction, the PM material was suspended in a polymer solution and deposited on an optical substrate. The film was dried in a controlled humidity environment to lower the water content. Chemical additives were introduced to the solution to produce a pH of about 9, which lengthened the M-state lifetime (image lifetime) to ~8 seconds. The film was sealed between the substrate and another glass plate to protect the film and to ensure a uniform thickness across the aperture of 1 inch diameter. The film thickness was approximately 100 μm and the optical density (OD) of the film in the bR state at the absorption peak wavelength of 570 nm was 2.5.

The light transmission characteristics of the film at one wavelength were measured experimentally using a variable-strength write beam and a weak read beam. Both beams are plane waves from an Argon ion laser at 514.5 nm. The film is first exposed to the write beam causing photoconversion of part of the bR state population to the M-state. In a steady-state condition, the read beam is passed through the film, and the transmitted intensity is measured with a photodetector. The data describing the relationship between transmitted amplitude or modulus of the read beam $A_{\text{read,trans}}$ and the incident power density of the write beam E_{write} is given in Figure 1. The amplitude data was obtained by taking the square root of the transmitted intensity data. The amplitude transmission is very close to logarithmic over most of the range of write beam power density, ie.

$$A_{\text{read,trans}} = K \log(E_{\text{write}}) + c \quad (1)$$

for some constants K and c . Thus in general the transmittance of the weak readout beam is controlled by the intensity of the write beam. The logarithmic transmittance relation displayed by this BR film is exactly that required for the proper transformation of images with multiplicative noise such that the image component and the noise component are additive in the Fourier transform plane⁴. It is also important that the dynamic range of the write power over which this property holds is large (> 2 orders of magnitude).

When a signal $s(x,y)$ is corrupted by additive noise $n(x,y)$ such that the observed quantity $r(x,y) = s(x,y) + n(x,y)$, it is often possible to filter out the noise in the Fourier plane of a coherent optical processor, provided that the Fourier transforms $S(u,v)$ and $N(u,v)$ are sufficiently separated in the frequency domain. However, if the observed image $r(x,y)$ is multiplicative such as

$$r(x,y) = s(x,y)n(x,y), \quad (2)$$

then filtering techniques in the Fourier plane of a coherent optical processor become much less effective because the image transform is given by

$$R(u,v) = S(u,v) * N(u,v) \quad (3)$$

where $*$ represents convolution. In this case the Fourier transforms $S(u,v)$ and $N(u,v)$ are convolved and impossible to separate, making it more difficult to isolate the original signal $s(x,y)$. In general, there are many examples of images with multiplicative noise, including speckle images formed when coherent radiation illuminates a rough object, and uneven conventional illumination of an arbitrary object. Applying a logarithmic transform to $r(x,y)$ yields

$$\log[r(x,y)] = \log[s(x,y)] + \log[n(x,y)] \quad (4)$$

and then traditional Fourier domain filtering can be used to remove as much noise as possible. The resultant image $\log[s(x,y)]$ can either be viewed or used as it is, or possibly transformed again in an exponential manner to recover $s(x,y)$, if desired. While the logarithmic transformation and filtering operations are relatively straightforward to accomplish digitally, there may be circumstances where it is desirable to perform the filtering operation optically, such as with the input of images to an optical correlator system for pattern recognition purposes. For an all-optical processing system, we would of course want to perform the logarithmic operation optically as well. The transmission properties of the BR film studied here allow the easy implementation of that transformation in a parallel fashion, with a simple and versatile optical system.

The optical system used in our experiments is shown in Figure 2. An Ar^+ laser beam at wavelength 514.5 nm is collimated and split into two arms with a non-polarizing beamsplitter. Each beam is controlled with an electronic shutter. With shutter A open and shutter B closed, the write beam is passed through the object which consists of an image pattern with multiplicative noise. Lens L_1 images the object function onto the BR film. The image is encoded in real-time by the photoconversion of BR molecules from the bR ground state to the M-state. Shutter A is then closed, shutter B is opened, and we transmit the much weaker read beam through the BR film. Lens L_2 performs the Fourier transform of the transmitted field, and Lens L_3 reimages the transmitted read beam onto the CCD detector. In general, a filter is inserted at the Fourier plane to remove the unwanted noise which is the Fourier transform of $\log[n(x,y)]$.

The first nonlinear image processing experiment conducted involves an image composed of two crossed Ronchi gratings. The dynamic range of the image (for transmission to light at 514.5 nm) is about 1.5 in density. The original image and the image transmitted by the BR film are shown in Figure 3. The original image is nearly binary since it is the multiplication of two binary grating patterns. The transformed image passed by the BR film clearly is more representative of the addition of the two gratings. We then performed a simple filtering operation on both images. Using the system in Figure 2, we placed a spatial filter in the Fourier plane to block the components of the vertical grating (vertical lines) in an effort to remove it from the image. The filter consists of two thin opaque horizontal strips, one on either side of the central dc location, which blocks only the components from the purely vertical grating. The results from the experiments are shown in Figure 4. The image obtained after filtering the original multiplicative image is in Fig. 4a. The vertical grating is not completely removed from this image because the filter allows transmittance of the convolutional cross-terms that still contains information of that image component. However, as seen in Fig. 4b, we are able to completely remove the vertical grating from the logarithmic image using this filter. This is because no cross-terms are present in the Fourier transform and thus the vertical grating is completely blocked by the filter while only the horizontal grating component is passed.

Another demonstration experiment involves the filtering of an image corrupted by speckle noise. The statistical properties of speckle noise have been thoroughly studied in the past, and it is well known that the image intensity generally follows a negative exponential probability density function (pdf)⁵. An image model that has been widely used to describe speckle images is the multiplicative model given in Eq. 2 in which the noise $n(x,y)$ has the negative exponential pdf. Logarithmic transformation not only makes the noise additive but also converts it to zero-mean, constant-variance noise which can presumably be filtered out to a greater degree than the multiplicative noise in the original speckle image. Of course to obtain the exact transformation of Eq. 4 for an arbitrary original

speckle pattern, we would require that the logarithmic transformation of the BR film possess an infinitely large dynamic range. This is obviously impossible, but fortunately Kato and Goodman found that for an original pattern (prior to submersion in speckle noise) with a dynamic range of 1 order of magnitude or less, then a logarithmic transformation with a dynamic range of 2.0 orders of magnitude will be sufficient to change the speckle noise to additive noise⁶. Figure 1 shows that the dynamic range of the BR film logarithmic transformation is greater than 2.0 orders of magnitude, and is thus adequate for this purpose.

The speckle image that we used in our experiment was obtained by placing a binary "X" pattern in contact with a transparent random phase object. Thus the original image had speckle noise, but the noise in the transformed image had the characteristics of random additive zero-mean noise. We then performed filtering operations on both the original and transformed images. The filter used was a simple circular aperture placed at the Fourier plane whose diameter was adjusted to be just large enough to pass the Fourier transform of the "X" object and to block all higher spatial frequencies. The resulting images obtained after the filtering operations are shown in Figure 5. We are unable to filter out the speckle noise from the original image because of the convolution of the noise spectrum with the spectrum of the "X" object. Instead, this filtering operation merely seems to enlarge the scale size of the speckle noise in the processed image. On the other hand, we are able to filter out a substantial amount of the noise from the logarithmically transformed image as shown in Fig. 12b, which is relatively uniform in intensity. This again confirms the satisfactory performance of the BR film acting as an amplitude logarithmic transformer.

We have demonstrated the use of a bacteriorhodopsin film as an optical logarithmic image transformer with application to coherent optical image processing of images with multiplicative noise properties. The photochromic behavior of our BR film was shown to possess logarithmic amplitude transmission characteristics over a dynamic range of greater than 2.0 orders of magnitude. Given the real-time recording and erasure capabilities of BR, this material may be well suited for high-throughput optical image processing operations. This would be especially important for all-optical systems such as optical correlators.

References

1. C. Bräuchle, N. Hampp, and D. Oesterhelt, "Optical applications of bacteriorhodopsin and its mutated variants," *Advanced Materials* **3**, 420-428 (1991).
2. R. R. Birge, "Photophysics and molecular electronic applications of the rhodopsins," *Ann. Rev. Physical Chemistry* **41**, 683-733 (1990).
3. J. D. Downie, "Optical logarithmic transformation of speckle images with bacteriorhodopsin films," in press at *Opt. Lett.*
4. A. V. Oppenheim, R. W. Schaffer, and T. G. Stockham, Jr., "Nonlinear filtering of multiplied and convolved signals," *Proc. IEEE* **56**, 1264-1291 (1968).
5. J. W. Goodman, *Statistical Optics*, (John Wiley & Sons, New York, 1985), Chap. 7, p. 350.
6. H. Kato and J. W. Goodman, "Nonlinear filtering in coherent optical systems through halftone screen processes," *Appl. Opt.* **14**, 1813-1824 (1975).

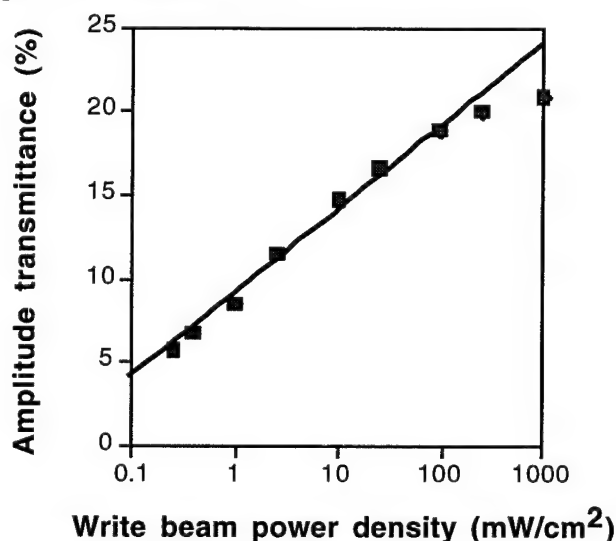


Figure 1: Transmittance of read beam amplitude as a function of write beam power density for wildtype bacteriorhodopsin film. Both beams have wavelength 514.5 nm. The boxes are experimentally measured data points while the solid black line is the best fit logarithmic curve.

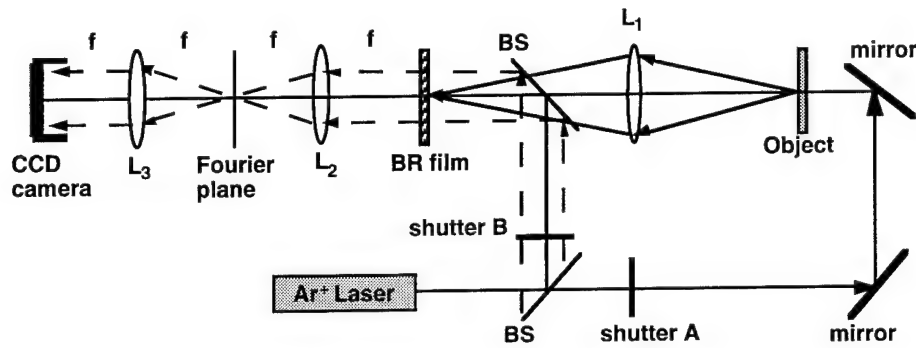


Figure 2: Optical set-up for logarithmic transformation and subsequent Fourier plane spatial filtering of images with multiplicative noise. Shutter A is opened during image recording process in BR film, and shutter B is opened during the read process and image processing operation. Argon laser used wavelength is 514.5 nm.

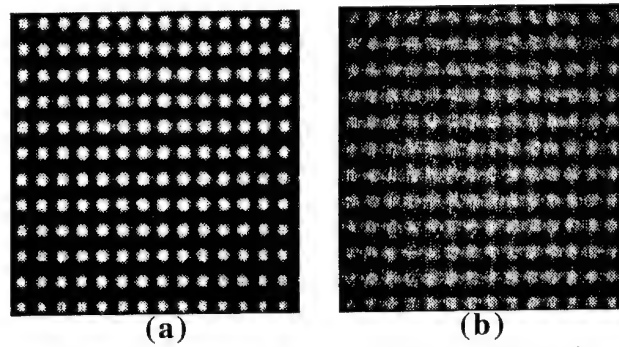


Figure 3: (a) Original unfiltered input pattern of multiplicative crossed gratings (b) Unfiltered image of logarithmically transformed crossed gratings pattern transmitted by BR film.

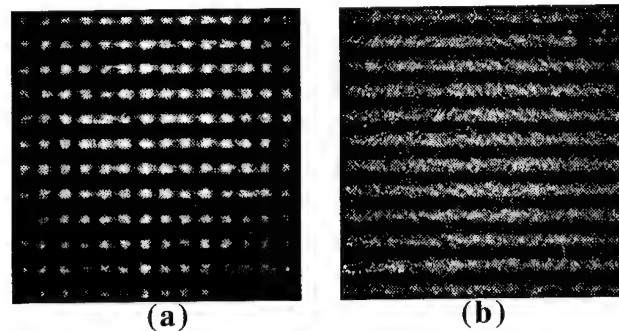


Figure 4: (a) Output image after filtering of original multiplicative crossed-grating image. (b) Output image after filtering of logarithmically transformed version of crossed-grating image.

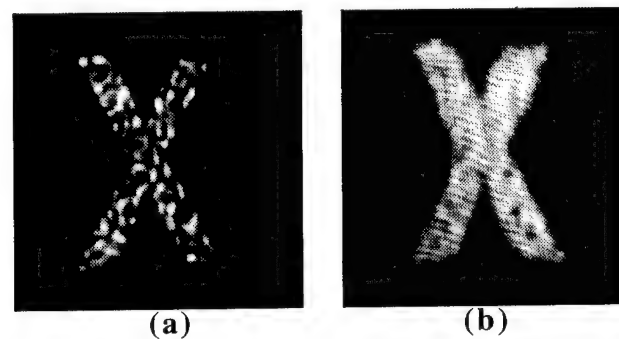


Figure 5: (a) Output image after filtering of original pattern of "X" with speckle noise. (b) Output image after filtering of logarithmically transformed version of same pattern.

Thursday, March 16, 1995

Liquid Crystal: 1

LThC 1:30 pm-3:00 pm
Red Lion West

Kristina M. Johnson, *Presider*
University of Colorado-Boulder

Liquid crystal over silicon spatial light modulators: emphasis on design for applications

Douglas J. McKnight[†], Steve A. Serati[‡], Kristina M. Johnson[†], and Miller H. Schuck[†]

[†] Optoelectronic Computing Systems Center, University of Colorado at Boulder, Campus Box 525, Boulder, Colorado 80309-0525, (303) 492 0958

[‡] Boulder Nonlinear Systems, 1898 South Flatiron Court, Boulder, Co.

1. Introduction

Liquid crystal on silicon spatial light modulators are made by placing a thin layer of liquid crystal directly on top of a silicon chip. For a recent review of this technology see, for example, reference [1]. We have constructed a 256 by 256 binary spatial light modulator (SLM) for an optical correlator application which uses a chiral smectic C (SmC*) ferroelectric liquid crystal as the light modulating layer [2]. This device is currently the subject of our planarization experiments. We have also made a 128 by 128 analog SLM and in this summary we present some early results from this device.

2. Binary spatial light modulators

Binary liquid crystal on silicon spatial light modulators use chiral smectic C (SmC*) liquid crystal materials such as BDH SCE13 as the light modulating layer. The liquid crystal material is addressed by a silicon chip which is designed to drive each of the reflective mirror/electrodes in the array to one of two voltages, typically 0V and $\approx 5V$. In the addressing scheme that we use the transparent electrode on the cover-glass is maintained midway between these two voltages. The liquid crystal is thus addressed with an electric field which is switchable in direction but which has a constant magnitude. The liquid crystal responds by switching between two states with tilt angles of $\pm 22.5^\circ$. Typically the thickness of the liquid crystal is chosen such that a double pass through the layer yields a total retardance of an odd number of half waves, preferably one. Each pixel can be viewed as an independently rotatable half-wave plate which can be switched into two states separated by a total angle of 45° .

In theory binary amplitude modulation with a lossless "on" state can be performed at the design wavelength by orienting the SLM between crossed polarizers with one of the switchable LC orientations aligned parallel to one of the polarizers. Binary phase modulation is performed by aligning the bisector of the two switched-state optical axes with one of the polarizers. The output light, when analyzed, has a phase difference of π introduced between the two switched states. This method of producing phase modulation is robust in the sense

Pixel Pitch	21.6 μ m
Fill-factor	79%
Flat fill-factor	60%
Diffraction efficiency	15%
Throughput into zero order	3.4%
Demonstrated frame load time	43 μ s
Simulated frame load time	27 μ s
Contrast ratio	70:1 zero order (10:1 imaged)
LC switching time	75 μ s

Table 1. Specifications of, and results from, the 256 by 256 binary SLM.

that the phase difference is not affected by liquid crystal switching angle, layer thickness or wavelength (though the optical throughput is).

Applications of binary SLMs include diffractive based applications such as optical correlators and beamsteerers and image based applications such as information displays. The device parameters which are important to optimize are not typically the same for the two types of application. For instance, a diffractive application will usually benefit from a small pixel pitch and a high frame rate, but may not require the device to function under intense illumination. For diffractive applications the proportion of output light which is in the central output order is usually important. This quantity is maximized by designing as flat a pixel mirror as possible within the limits set by constraints such as the pixel pitch and silicon design rules.

We developed a binary SLM for diffractive applications [2] and its specifications are summarized in table 1. The “diffraction efficiency” specification is found by illuminating the silicon backplane with a laser beam and measuring the fraction of the incident light which is reflected into the zero-order replica. The pixel design was chosen to maximize this parameter. To improve the diffraction efficiency and reflectivity of the device we are currently performing experiments on planarization techniques to improve the flatness of the pixels.

We are using a spin coated polymer to create a flat surface on top of the silicon backplane. The cured polymer can achieve planarities (defined as $1 - b/d$ where b is the step height before planarization and d is the step height after planarization) greater than 0.9. Recent results have shown step heights on an unplanarized device were reduced from 1.1 μ m to 25nm after planarization over a 100 μ m by 100 μ m area. This flat layer can then be plasma etched to form vias to the former metal pixel mirror/electrodes. The vias will be filled with a suitable conductor and highly reflective metal mirrors will be laid on top of the filled vias.

3. Analog spatial light modulators

Certain fast liquid crystals can display analog tilts as a function of the applied electric field. These materials include smectic A via the electroclinic effect and smectic C* through the distorted helix ferroelectric effect [3]. An analog tilt can be used to perform analog amplitude modulation by the same choice of device and analyser orientations as described above for the binary device. Typically, though, analog materials offer a lower tilt at the low voltages which are readily achieved on silicon backplanes thus leading to a reduced throughput in the “on” state. Reorientation of the device such that the polarizer bisects the range of available LC

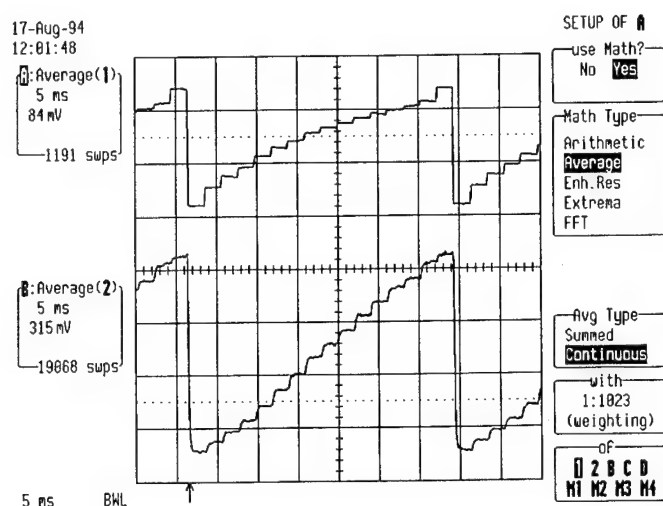


Figure 1. The intensity output from a group of pixels on the analog SLM switching through a succession of 16 gray scales. The lower trace is the output intensity and the upper trace is proportional to the analog input voltage that was applied. The response is not quite linear so a correction was estimated and applied to the input signal thus generating the approximately linear output scale shown here. The timebase is 5ms per box.

director angles allows us to perform “bipolar amplitude” modulation—the analog of the binary phase modulation available with binary devices. Continuous phase modulation can be achieved by using a passive retarder.

We have made a 128 by 128 pixel analog silicon backplane with pixels placed on a $40\mu\text{m}$ pitch, each of which uses a single transistor for dynamic data storage. The silicon chip is interfaced with a driver board which writes a frame of analog data to the SLM in $100\mu\text{s}$.

The analog backplane was used to address the distorted helix ferroelectric liquid crystal Hoffmann la Roche 9807. We observed a tilt of the macroscopic liquid crystal director of $\pm 11^\circ$. We show an example of the analog response in figure 1. Optical Fourier transforms resulting from binary and sinusoidal grating patterns written on the analog SLM are shown in figures 2a and 2b respectively. The first and third harmonics of the binary grating can be seen, but, as expected, the sinusoidal grating results in a transform with only the first-order peaks visible.

At the conference, we will report our most recent results from the analog devices and the results of our planarization efforts. We expect this will include measurements of device planarity over the entire chip, via etching and mirror formation results, and optical performance measurements of planarized devices.

References

- [1] K. M. Johnson et al. Smart spatial light modulators using liquid crystals on silicon. *Journal of Quantum Electronics*, 29(2):699, 1993.
- [2] Douglas J. McKnight, Kristina M. Johnson, and Roylann A. Serati. 256 x 256 liquid-crystal-on-silicon spatial light modulator. *Applied Optics*, 33(14):2775–2784, 1994.

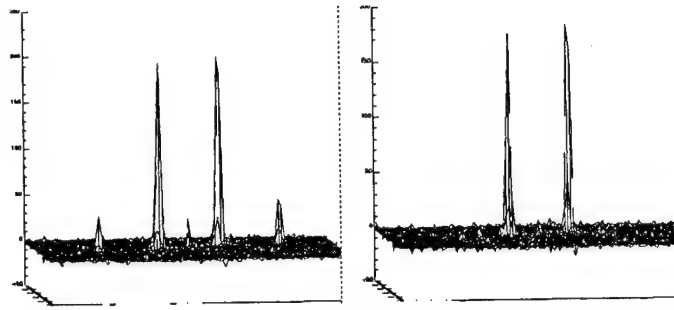


Figure 2. Contour plots of the optical Fourier transform of the analog SLM when it was displaying a binary stripe pattern (left), and a sinusoidal stripe pattern (right). The SLM was operated in bipolar amplitude mode.

- [3] J. Funfschilling and M. Schadt. Fast responding and highly multiplexible distorted helix ferroelectric liquid crystal displays. *Journal of Applied Physics*, 66(8):3877, 1989.



Figure 3. A greyscale image displayed on the 128 by 128 analog SLM.

Ferroelectric liquid crystal spatial light modulators and their applications to information processing

Seiji Fukushima and Takashi Kurokawa

NTT Opto-electronics Laboratories

3-1, Morinosato Wakamiya, Atsugi-shi, Kanagawa 243-01, Japan

TEL +81-462-40-3244, E-mail fksm@aecl.ntt.jp

1. Introduction

There has been increasing interest in optical processing because it is two-dimensional and massively parallel. One of the most important devices for optical parallel processing is the optically-addressed spatial light modulator. Providing logic and memory functions, it would be used to implement flexible processing. We have developed a ferroelectric liquid crystal spatial light modulator (FLC-SLM) with these kinds of functions and fast response.¹ This paper describes the device and some of its uses in information processing.

2. FLC-SLM

A surface-stabilized FLC is suitable for providing logic and memory functions since it has optical bistability and its optic axis of birefringence can be switched by applying an electric pulse. Our FLC-SLM has a sandwich structure consisting of an a-Si:H photoconductor (PC), a dielectric mirror (DM), and an FLC, as shown in Fig. 1. The FLC layer modulates the polarization of the read beam coming through a polarization beam splitter (PBS). The readout beam polarization is switched according to the write intensity that controls the voltage across the FLC through photoconductivity. The FLC-SLM thus outputs and stores a positive image for a positive electric pulse and a negative image for a negative pulse. The stored image can be read out at any time. Typical features include a clear aperture of 12x12 mm, a resolution of 75 line pairs/mm (lp/mm), a sensitivity of 200 $\mu\text{W}/\text{cm}^2$, a contrast ratio of 60:1, a response time of 70 μs , and a storage period of two months.

For holographic applications we improved the resolution of the FLC-SLM. Resolution is dependent on PC thickness because the photo-induced carriers spread into the dark region. Although a thinner photoconductor is preferable for higher resolution, such a device will not perform adequately because the capacitive current flowing into the dark area of the PC switches the FLC unexpectedly. The PC should, therefore, at least a few μm thick. Figure 2(a) shows how resolution depends on PC thickness: as the PC becomes thinner the resolution becomes higher. The best resolution so far observed at the modulation transfer function (MTF) of 50% was 300 lp/mm (or 1.7 μm). This value was obtained from an FLC-SLM with a PC thickness of 1.7 μm . MTF dependence on spatial frequency measured for the modulator with the best resolution is shown in Fig. 2(b). Diffracted light was still observed at the spatial frequency of 400 lp/mm.

3. Applications

3-1 Image processing

We have used these kinds of FLC-SLMs in many applications (Table 1). The FLC-SLM satisfies cascading requirements such as the single wavelength addressing and the light amplification; hence, it can perform flexible parallel image operations. All 16 Boolean functions for two binary images can be performed using three cascaded FLC-SLMs.² Input images A and B are encoded by the two modulators into four Boolean functions $A'B'$, $A'B$, AB' , and AB in the time domain. Some of the four encoded outputs are superposed to provide any Boolean

function. The measured contrast ratio was 10:1 and the processing rate was 300 frames a second.

The frame rate of the FLC-SLMs is higher than the television rates, so they can be applied to image encryption.³ A transmitter performs a parallel exclusive-or function between the input and key images and a receiver performs the same function between the enciphered image and the same key image. Despite the simplicity of this encryption principle, the enciphered image can be deciphered only by a receiver that has the same key as the transmitter.

Detection of a moving object is also performed by the parallel exclusive-or operation. When the present image is compared with the stored image, the moving object appears against the background as a bright pattern.⁴ This kind of processing would reduce the bandwidth of visual communications.

Edge detection is a well-known, classical optical processing that uses a Fourier transform of a lens. The previous processing, however, lacks programmability in the choice of the filters. Now it has flexibility when the Fourier transform pattern is incident on the FLC face and the filtering pattern is written on the PC face.⁵ Figure 3 shows experimental results obtained when the original image was a cat ornament and the functions were edge enhancement and horizontal edge enhancement. The arbitrary directional boundaries were detected in real time.

Real-time construction and reconstruction of Fresnel holograms has been achieved by using a high-resolution FLC-SLM.^{6,7} In that work a cycle of hologram operation was 560 Hz and the light energy was about 100 nJ/cm². For optical phase conjugation, a mirror-free FLC-SLM that accepts light beams from both sides was manufactured. This modulator compensated the aberration in the path and was used to demonstrate one-way image transmission.⁸

3-2 Photonic switching

Free-space photonic switching can be nonblocking and have large parallelism. If a pitch or a direction of a holographic grating are controllable, the light beam propagation can be controlled easily. To implement photonic switching a segmented FLC-SLM whose electrodes are patterned into 3x3 independent segments was developed.⁹ The gratings in the nine segments are recorded by the interference pattern from the laser diode, and the input signal beams are diffracted according to the grating. The structure of this kind of switch (Fig. 4) enabled 9x9-channel nonblocking switching.

3-3 Optical measurement

Our FLC-SLM has also been used to make optical measurements.¹⁰ Velocity was measured by using a double-exposure speckle pattern technique. The two speckle patterns are recorded on an FLC-SLM and the composite pattern is analyzed by an optical correlator. The correlator output exhibits straight fringes whose pitches are inversely proportional to the displacement of the object. As the exposure interval is known, the velocity can be calculated.

4. Conclusion

The FLC-SLMs and their applications were reviewed. They have been applied to wide range of processing that includes image processing, photonic switching, and optical measurement.

References

1. S. Fukushima, T. Kurokawa, and M. Ohno, *Appl. Opt.* **31**, 6859 (1992).
2. S. Fukushima and T. Kurokawa, *IEEE Photon. Technol. Lett.* **3**, 682 (1991).
3. S. Fukushima, T. Kurokawa, and Y. Sakai, *IEEE Photon. Technol. Lett.* **3**, 1133 (1991).

4. H. Suzuki, S. Fukushima, and A. Nagatsu, paper ThQQ2, OSA Annual Meeting, New Mexico, 1992.
5. A. Nagatsu and H. Suzuki, paper MZZ9, OSA Annual Meeting, Toronto, Canada, 1993.
6. S. Fukushima, T. Kurokawa, and M. Ohno, Appl. Phys. Lett. **58**, 787 (1991).
7. S. Fukushima and T. Kurokawa, Jpn. J. Appl. Phys. **33**, 5747 (1994).
8. S. Fukushima and T. Kurokawa, IEEE J. Quantum Electron. **29**, 613 (1993).
9. H. Yamazaki, M. Yamaguchi, K. Hirabayashi, S. Fukushima, and T. Ito, IEEE/LEOS Annual Meeting, San Jose, 1993, pp. 492-493.
10. Y. Kobayashi, T. Takemori, N. Mukohzaka, N. Yoshida, and S. Fukushima, Appl. Opt. **33**, 2785 (1994).

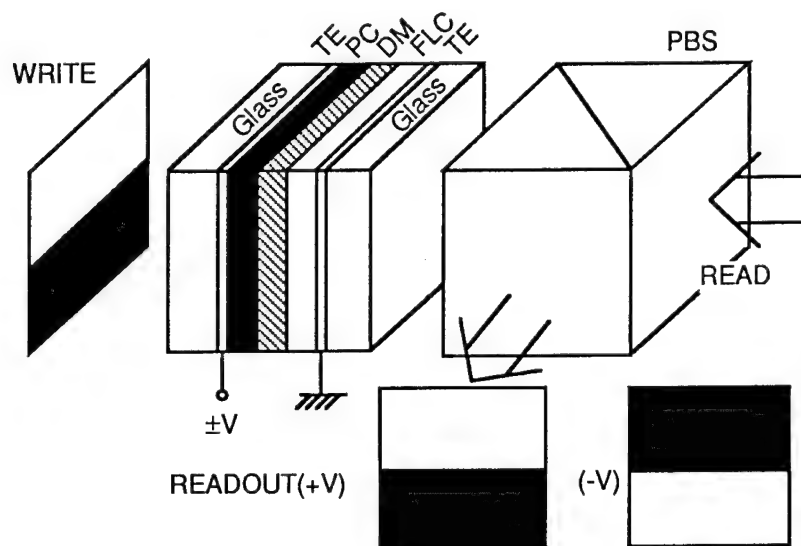


Fig. 1 Structure of an FLC-SLM. TE: transparent electrode.

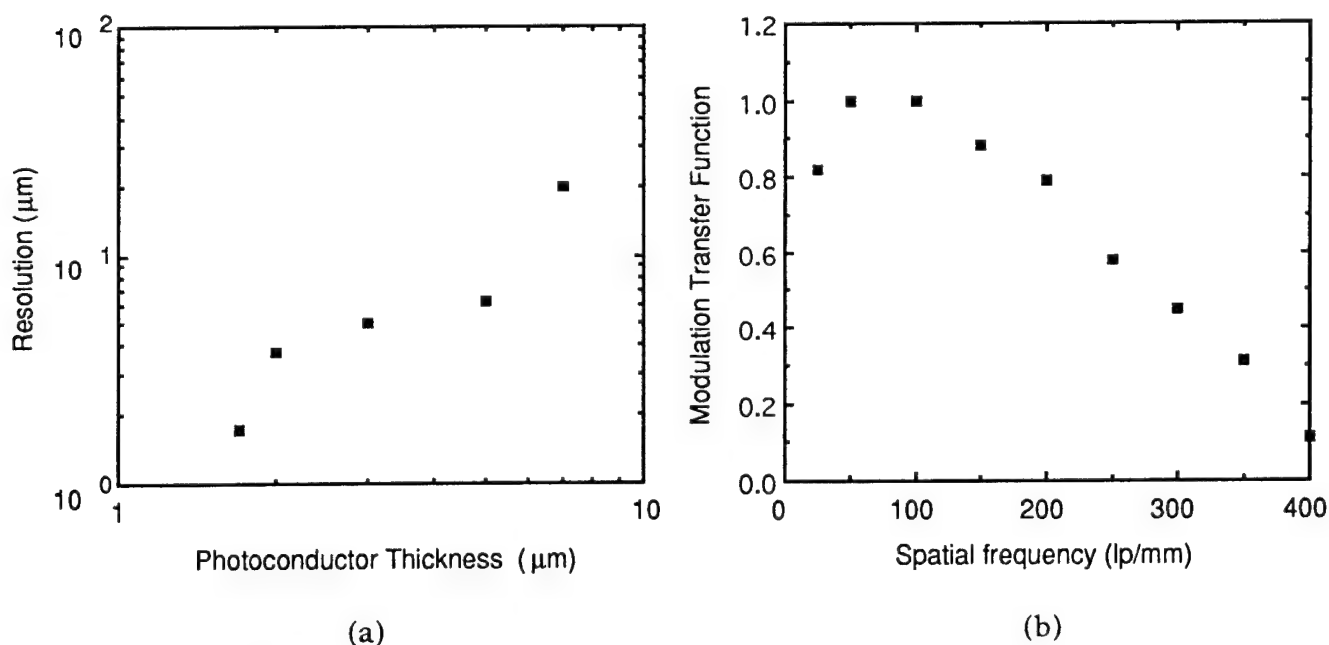
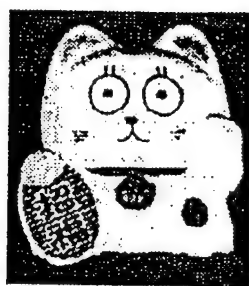


Fig. 2 (a) Resolution dependence on photoconductor thickness.
(b) Modulation transfer function vs spatial frequency.

Table 1 Applications of FLC-SLMs.

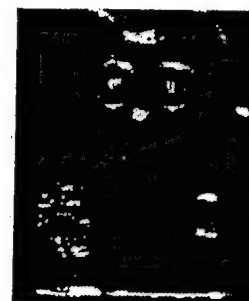
Category	Applications	FLC-SLM function utilized
Image processing	Boolean functions	Bipolar operation
	Image encryption	Bipolar operation
	Motion detection	Memory
	Edge detection	Thresholding
	Real-time holography	High resolution
	One-way imaging	High resolution
Photonic switching	Nonblocking holographic switch	High resolution
Optical measurement	Velocity measurement	Memory



(a)



(b)



(c)

Fig. 3 Results of edge detection. (a) Original, (b) edge enhanced, (c) horizontal edge enhanced.

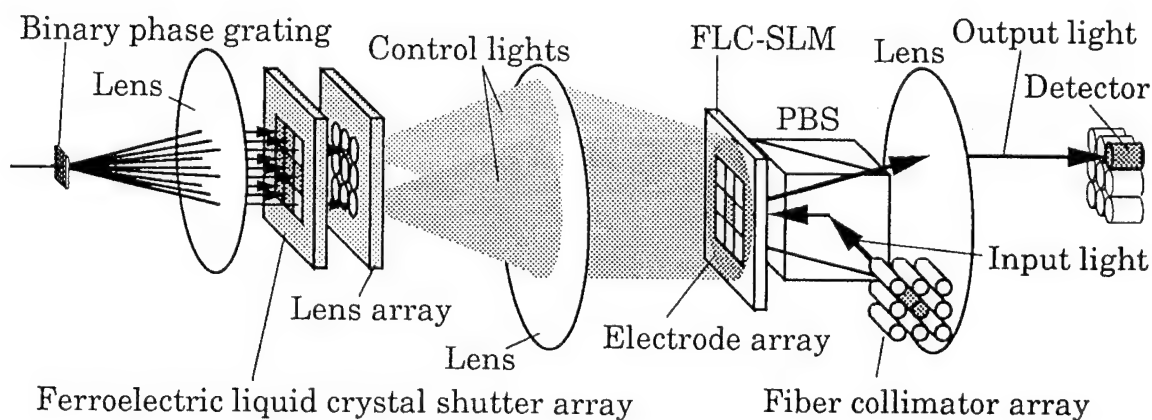


Fig. 4 Structure of a nonblocking photonic switch.

OPTICAL IMAGE PROCESSING FEATURES OF OPTICALLY ADDRESSED LIQUID CRYSTAL LIGHT MODULATORS

Alexander V.Parfenov

Levedev Physics Institute, Leninsky 53, Moscow, 117924, Russia
phone 7-095-1326664

Spatial light modulators (SLM) are considered as the main elements of optical data processing systems. Liquid crystal SLMs (LC SLM) have high performance parameters, and are normally used in optical systems as image transducers and optical filters. Whereas LC SLMs are able to increase the list of their applications due some image processing features. These features are appeared when SLM internal structure properly taken into account during SLM construction. Combination of these features with high performance SLM parameters could improve a flexibility and productivity of optical methods and is able to simplify optical setup.

Most discussed features are divided into two main classes: a) based on electrophysical properties of SLM structure (created due to presence of a few factors in various layers of structure); b) based on properties of electrooptical effects in LC only.

Through first group we are listing: moving-objects selection feature, image-subtraction possibilities, etc.

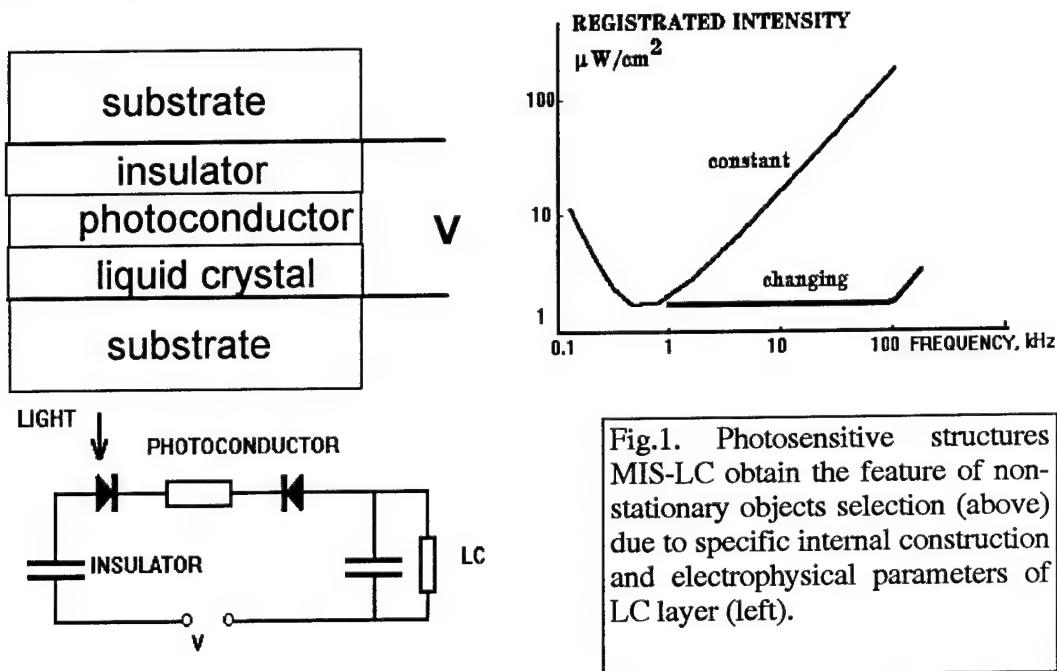


Fig.1. Photosensitive structures MIS-LC obtain the feature of non-stationary objects selection (above) due to specific internal construction and electrophysical parameters of LC layer (left).

Moving objects selection consists in ability of SLM to registrate the nonstationary objects (moving and flashing) at lower (a few order of magnitude) intensity rather than stationary ones. The cause of this effect is internal construction of SLM based on metal-insulator-semiconductor structure (MIS)-LC. Internal electrical asymmetry (appearing due to illumination of one side of semiconductor layer in SLM) leads to the transient DC component of (initially AC) electrical current in the structure. The characterical time of this transient flow is determined by electrical leakage through LC layer. This time (10-100 ms) is mostly responsible for electrooptical effect time, as well as related parameters of SLM in discussed regime.

This SLM being included in input plane of the optical correlator is capable to extract from input scheme only moving objects with typical velocity between 0.01 mm/s and 10-100 mm/s (in dependance of brightness of the images this region can be wider).

Through second group we are considering: nonlinear self-filtration of images in SLM, spectral (in wavelength domain) selection of input images, contour enhancement (for some variants), image contrast enhancement, optical lock-in-amplifier, etc.

Spatial response of LC SLM significantly depends of parameters of LC layer and material itself and before all of thickness and dielectric anisotropy. Homeotropical alignment of LC molecules with positive dielectric anisotropy leads to loss of electrooptical response in homogeneous electrical field perpendicular to LC layer. The transverse electrical field is created in LC layer when the image is projected on SLM and leads to inclination of LC molecules and appearance of specific spatial response, which is characterised by the absence of the lowest part of the spectra of transferred images (contour enhancement). The shape of MTF for the lowest frequencies observed significantly determined by energy of LC anchoring to the surface (which permitted to measure this energy for various techniques of homeotropic alignment -- as observed it is close to 10^{-5} erg/cm²), while the highest frequencies are influenced by the thickness and dielectric anisotropy. The mechanism of this mode is illustrated by Fig.2., whereas the sample of MTF, specific for such type of structures is presented in Fig.3.

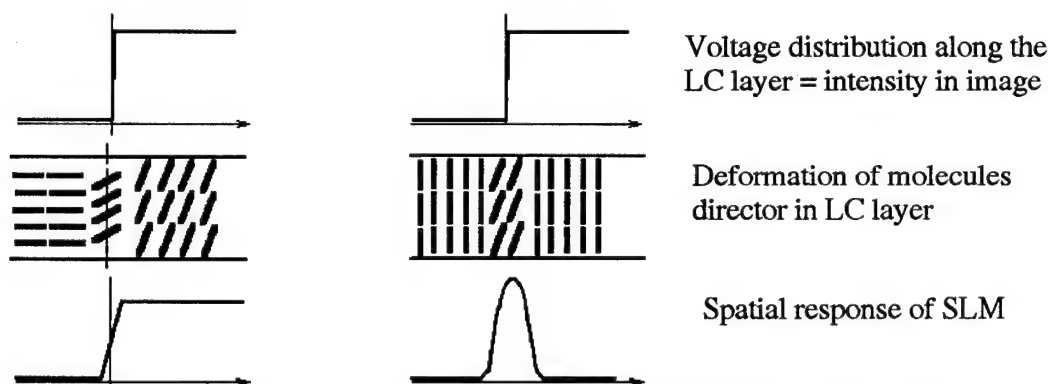


Fig.2. The formation of spatial response in SLM with LC of different alignment (homogeneously -- left, homeotropically -- right).

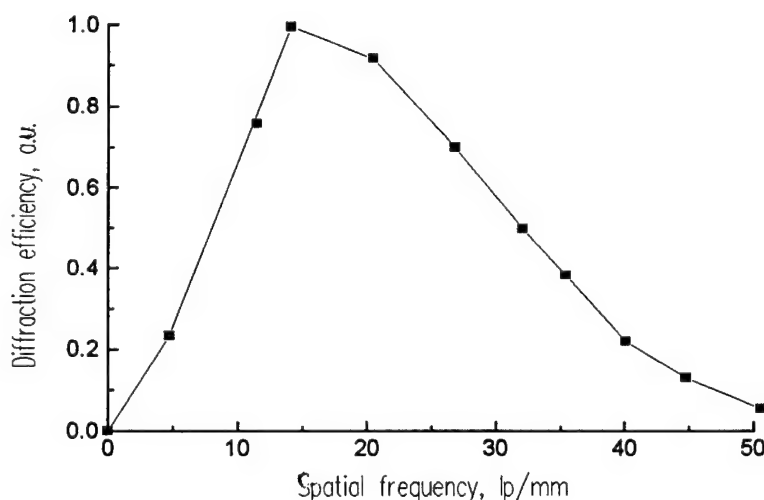


Fig.3. Spatial response curve for SLM based on amorphous silicon photo-sensitive layer and LC with dielectric anisotropy +23, aligned homeotropically.

This feature being applied to optical image processing allows to diminish in the spatial spectrum the intensity of the lowest frequencies. As the contrast of SLM with homeotropic alignment usually exceeds value 100:1 this suppression can significantly influence on signal-to-noise ratio in whole image processing scheme.

Self-filtration of images can be observed with SLM in spatial frequencies' plane or in image one. In first case SLM should be established in focal plane of lens creating an Fourier-spectrum on photosensitive layer of SLM, as depicted in Fig.4.

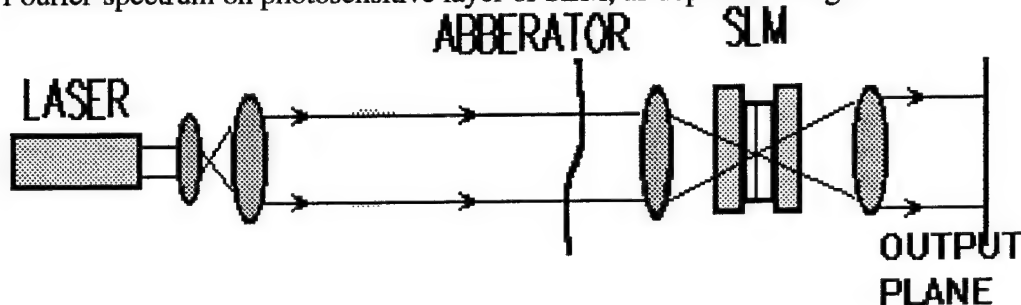


Fig.4. Experimental scheme for self-filtration image processing feature demonstration: input image is presented here as phase-only object (abberator).

Fourier-spectrum is regularly characterized by huge dynamic range of intensity in accordance to presence of various spatial structures in the input image (main power nevertheless is usually in zero order of spectrum). When this distribution is projected on photosensitive layer of SLM each spatial component of this spectrum gives rise to some change in SLM transmission locally (both phase and intensity transmission can be changed when proper LC effect and environment are choice, also linear change as well as nonlinear one is possible). Then this transmission spatially modulates the input spectrum. The process results in nonlinear changes in spectral (spatial) components' ratio. It means that the image transmitted through SLM with discussed features will be spatially filtered.

This is the case of the nonlinear spatial filtration in contrast to usually discussed linear spatial filtration. Here each spatial component gets the phase and/or amplitude factor according to its intensity, while in linear case it should get this factor according to its spectral position.

This feature can be used, e.g. for filtration of images which energy is known *a priori*, and frequency spectrum is unknown, or very approximatively.

It is important that order of linearity or nonlinearity can be easily settled in most experimental cases. This operation is based on the dependance of sensitivity of SLM on the magnitude and frequency of applied voltage. It means that experimentalist can change and settle the reasonable contrast of output image without significant difficulties.

In one of the demonstration optical experiment we used amorphous-Si based SLM with sensitivity near $50 \mu\text{W}/\text{cm}^2$ and spatial resolution near 50 lp/mm. Application of twist effect in LC leads to amplitude thresholding characteristic of SLM. This allowed us to suppress by two-three orders of magnitude the intensity of lowest spatial frequencies' components in the input image and to realize contour enhancement in this image.

We used the ITO patterned glass as input phase object. The period of this pattern was close to $200 \mu\text{m}$, the thickness of ITO layer was estimated as low as $0.1 \mu\text{m}$, i.e. phase modulation of the pattern was as small as 0.01 rad. and the pattern can not be observed without usual in such cases difficulties. Nevertheless nonlinear filtration, when

zero order has been suppressed in approximately 100 times, revealed apparently the existing phase-only pattern as amplitude one with contrast up to 10:1. This experiment is illustrated by Fig.5, where scanned pictures of the unfiltered and filtered images are shown as well as track of intensity distribution of filtered image.

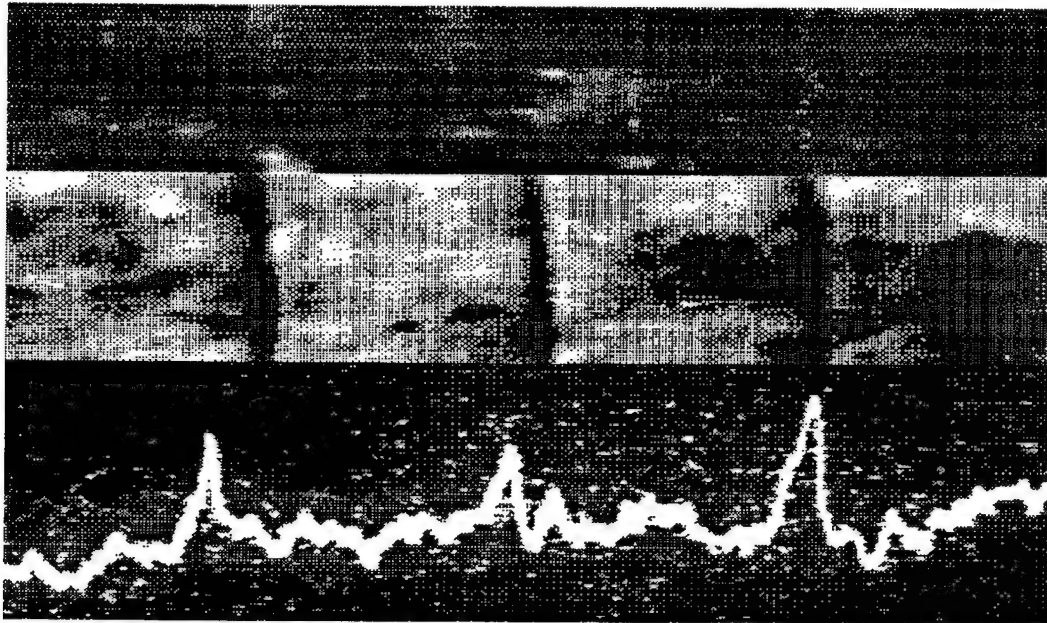


Fig.5. From up to bottom : the nonfiltered image, filtered one and track of intensity distribution in filtered image, measured in output plane.

In case of opposite alignment of polarizers (around the SLM) we realized the suppression of higher frequencies, considering this operation, e.g., as extraction of plane wave component from initial complicated wavefront (which consists one of the main task for adaptive optics application).

Important feature of suggested mechanism is concluded in insensitivity to displacement of the image in input plane.

Conclusion. We consider a number of the physical mechanisms in LC SLM which lead to features in optical response of SLM, which can be directly applied for optical image processing, adding the flexibility to this processing and enhancing the signal-to-noise ratio. In addition to disclosed above a few other mechanisms for image temporal and spatial filtration are discussed.

Acknowledgments. The fruitful collaboration with Prof.I.Kompanets, Prof.N.Kovtonjuk, E.Abeles, Dr.A.Naumov, Dr.S.Kotova, P.Vashurin is acknowledged with great pleasure.

Optical Characterization of Stripe Deformation In an Electroclinic Liquid Crystal

J. R. Lindle, S. R. Flom, F. J. Bartoli,

Optical Sciences Division

R. Shashidhar, B. R. Ratna, and G. P. Crawford

Center for Biomolecular Science and Engineering

Naval Research Lab

Washington DC 20375-5338

202-404-7374/(FAX) 202-404-8613

Recently the electroclinic effect in chiral smectic A (Sm A) liquid crystals has been the subject of increased study because of its potential for spatial light modulators with fast response and greyscale operation. For this application, a large contrast ratio is desirable and often essential. However, it has been observed¹ that, when smectic A liquid crystals are subjected to an electric field and viewed between crossed polarizers, they exhibit distinctive periodic stripe domains due to a voltage deformation (kink) of the bookshelf geometry.² The molecular alignment is reported to alternate between stripes, reducing the contrast ratio and imposing performance limitations on electrooptic devices based on these materials. In this investigation, we report spatially resolved measurements on a smectic A liquid crystal, performed using a novel technique to probe the optical properties with micron resolution. The effect of the stripe

formation on the electrooptic properties of the Sm A liquid crystal KN125 is investigated.

The electric-field-induced stripe domains were experimentally characterized by measuring the transmission of KN125, interposed at an angle of 22.5° between crossed polarizers. A tuneable Ar^+ laser was focused on the sample with a $4\text{ }\mu\text{m}$ $1/e^2$ diameter, and the sample translated perpendicular to the optical beam with one-micron resolution. The position and orientation of the sample and optical components were controlled using computer automated high-precision optical stages. Due to the strict spatial tolerances required in this measurement, the orientation of the sample relative to that of the light polarization and polarizing optics was varied by rotating the polarizer and analyzer while maintaining a stationary sample orientation. A variable-wavelength half-wave plate (Soliel-Babinet compensator) was used in conjunction with a polarizer to rotate the polarization of the laser, because rotation of a polarizer can translate the laser beam. The orientation of the Soliel-Babinet compensator and analyzer pair was computer controlled with 0.001° accuracy, while the sample was mounted on a precision X-Y translation stage.

The result of an x-scan across a $15.4\text{ }\mu\text{m}$ thick sample is shown in Fig. 1. A quasi-periodic modulation of the transmission associated with the stripe geometry was observed. This modulation, observed with the monochromatic laser source, is not as large as one would expect from microscopic observations made using white light. As shown in the figure, the position of the stripes can be determined with micron resolution, permitting optical measurements to be made within a given stripe domain. Fig.2 shows the transmission results for applied voltages of 0 and 10 V as a function of angle; the position corresponds to a valley in the x-scan. The tilt angle can be determined for a given stripe domain from the angular shift in the transmission minimum with voltage. A comparison of the angular position of the transmission minimum for

a peak with that of an adjacent valley would give the "kink" angle. The voltage dependence of the tilt and kink angles will be discussed.

In conclusion, we have performed spatially resolved measurements of the optical properties of the stripe domains in an electroclinic liquid crystal which permits an independent determination of the true optical tilt angle and the kink angle. The implications of these findings on device design and performance will be discussed.

References

1. A. B. Davey and W. A. Crossland, *Ferroelectrics* **114**, 101 (1991).
2. K. Sharp, G. Andersson, T. Hirai, A. Yoshizawa, K. Hiraoka, H. Takezoe, and A. Fukada, *Jpn. J. Appl. Phys.* **31**, 1409 (1992); P. A. Williams, Ph. D. Dissertation, University of Colorado (unpublished).

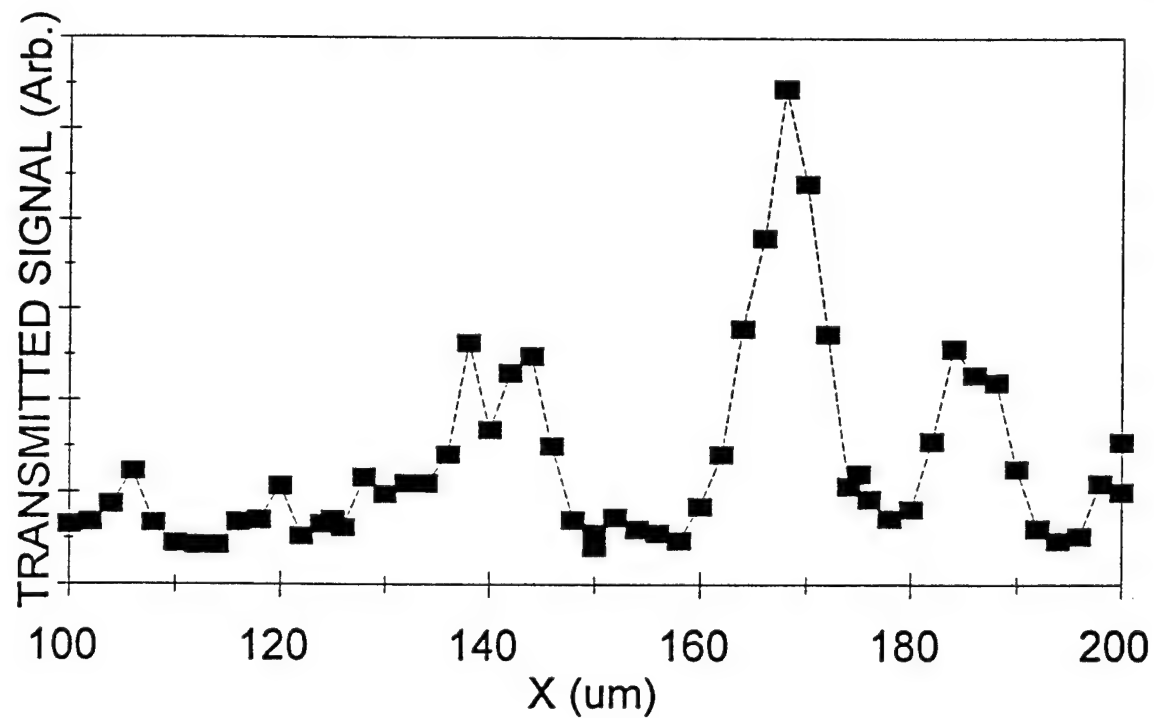


Figure 1. Transmission of a KN125 sample between crossed polarizers as a function of position. The sample is $15.4 \mu\text{m}$ thick and the laser wavelength 488 nm .

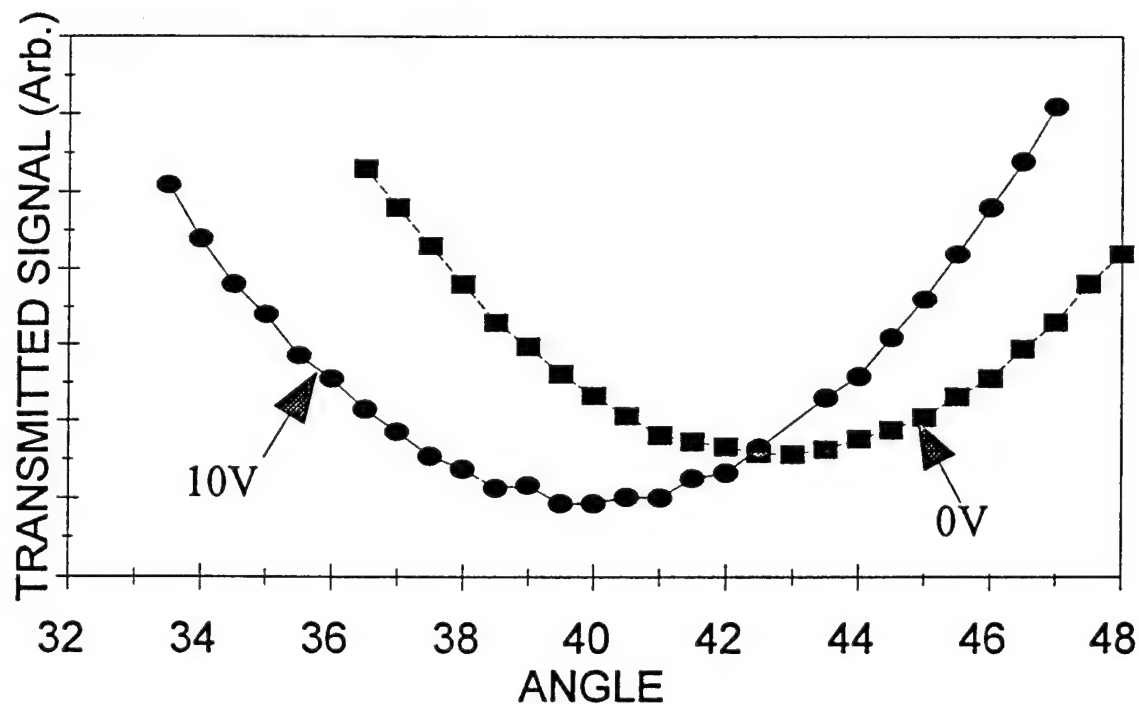


Figure 2. Angular variation of the transmission of a KN125 sample between crossed polarizers. The experiments are carried out near the valley of an x-scan at 488 nm and at the indicated applied voltages.

Thursday, March 16, 1995

Liquid Crystal: 2

LThD 3:30 pm-5:00 pm
Red Lion West

William Crossland, *Presider*
Cambridge University, U.K.

SPATIAL LIGHT MODULATORS: RUSSIAN RESEARCH, DEVELOPMENT AND APPLICATIONS

Igor N. Kompanets
P.N. Lebedev Physics Institute
53 Leninsky pr., 117924 Moscow, Russia
ph. (095) 132-5484; fax (095) 135-77880
e-mail: optoel@sci.fian.msk.su

New ferroelectric liquid crystals promising for the SLMs were created and investigated at P.N. Lebedev Physics Institute. Helical winding and chevrons were excluded all over the crystal volume, and low-energy molecular structures were recognized. Three types of FLC cells distinguished with the LC composition, layer thickness and boundary conditions were used for the light shutters and SLMs.

An achromatic hardly bistable modulator with 36 V voltage pulse of 2.5 μ s duration shows the optical contrast more than 50:1 (for white light). The 128x128 matrix with the period 20 μ m, LC layer thickness 1.5 μ m and passive addressing was fabricated to be used as the optical spatial phase-only filter in the image processing scheme.

An achromatic non-bistable FLC cell with the response time of 3.5 μ s and the optical contrast more than 50:1 (for white light) under 36 V of voltage is promising for fast shutters, arrays and image converters.

An achromatic modulator hardly bistable in a wide region of the aperture (tens of cm) and the LC thickness (from 12 to 40 μ m) shows the optical contrast more than 50:1 (for white light) under the voltage pulse of 36 V and 100 μ s duration. It can be used instead of supertwist nematic devices. Apparently, a multistable regime with gray scale could be realized in these modulators. It is possible to design TV format matrices on the basis of this principle, operating with close TV rate. The 128x128 matrix with the period of 165 μ m, the LC layer thickness 20 μ m and passive addressing was fabricated and used to input the images to the optical processing scheme.

An electrooptical effect in homeotropically aligned smectic C liquid crystal was discovered at the end of 80-ies at Lebedev Physics Institute, Moscow. The smectic C LC layers are parallel to limiting surfaces. Beside of a simple alignment technology, there are such advantages as an independence of the modulation on the LC thickness, achromatic initial (undisturbed by the electrical field) state, and a significant increase of the speed (by 2-3 times) at the same value of the electric field as for the effect in surface-stabilized FLC.

Recently, other electrooptical effects in the same geometry have been observed:

- a) achromatic light modulation via the waveguide mode light propagation along helix axes of smectic C liquid crystal;
- b) violation of the optical activity mode in smectic C LC with helix pitch (less than 0.3 μ m);
- c) wavelength selective reflection, which is shifted when the electrical field is applied.

An electrooptical effect in homeotropically aligned smectic C LC is somewhat promising for the development of gray-scale modulators, responding in 1-10 μs region, with the optical contrast as high as 100:1, and the uniformity of the initial state. As a result, Lebedev Physics Institute has developed, in collaboration with joint-stock company ESMA, a prototype of the 1-D array of 128 elements with 10 μs response.

Joint-stock company ESMA, with the science consulting of Lebedev Physics Institute, has also designed an optically addressed SLM on the base of the LC and gallium arsenide plate with a very wide region of sensitivity (due to the growth imperfections): from 600 to 1600 nm. Other parameters are: the threshold intensity, 10^{-6} W/cm^2 ; the resolution capability 20-50 lp/mm on the 50% of MTF; the frame rate 30 1/s.

This SLM was also connected, via the fibre plate, with a compact monochrome monitor (CRT with the dimensions 120x45x85 mm). Two of the hybrid devices were used in the optical/digital scheme of the image processing to input the images, and to form phase only-filters synthesized with the IBM PC AT/286.

The optically addressed SLM on the base of a photoconductor (CdS)-LC structure are fabricated at S.I.Vavilov State Optical Institute (St-Petersburg) in cooperation with Pilot Scale Production Factory. Their parameters are: the threshold sensitivity, 10^{-7} W/cm^2 ; the resolution capability up to 100 lp/mm; the frame rate, 10 1/s.

A new effective version of SLM based on silicon gel (elastomer) is investigated at Moscow Institute of Radiotechnics and Automation. This will be also discussed in the report.

Novel Electroclinic Liquid Crystal Materials for Spatial Light Modulators

B. R. Ratna and R. Shashidhar
Center for Bio/Molecular Science and Engineering
Code 6900, Naval Research Laboratory
Washington DC 20375

Electroclinic liquid crystal materials are promising for applications, such as spatial light modulators, that require analog phase modulation capability and fast response times¹.

The evolution of this technology greatly depends on the development of chiral smectic A materials with large induced tilt angles, field-independent and fast switching times and a broad operating temperature range. Development of such materials require a fundamental understanding of the molecular structure and its relation to the electrooptic performance.

Our efforts in this direction has led to the development of highly polar electroclinic materials which exhibit large electroclinic coefficient over a wide temperature range. In this presentation, the electrooptic performance of some of these new materials will be discussed, from the perspective of achieving some of the critical device requirements.

Since the demonstration of the electroclinic effect in chiral smectic A liquid crystals², efforts have been made to maximize the magnitude of the field induced tilt angle.

Application of an electric field parallel to the smectic layers induces a molecular tilt in a plane perpendicular to the applied field direction due to the coupling between the electric field and the transverse molecular dipole moment. The drawback of most of the previously known chiral smectic A materials is that relatively large values of the induced tilt angle are observed only on approaching the lower temperature ferroelectric smectic C* phase due to the pretransitional increase of the tilt susceptibility. This strong temperature dependence of the induced tilt angle imposes a stringent limitation on the operating

temperature range of a device, if the maximum dynamic range available in a given material is to be utilized without losing on the resolution of the device³. Further, the presence of the smectic C* phase results in a critical slowing down of the response time. Recent efforts have resulted in novel chiral smectic A materials with no underlying tilted phases exhibiting large induced tilt angles with no or weak temperature dependence over a broad temperature range extending to subambient temperatures. In this contribution, we present results of a systematic study of the effect of molecular structure on the electrooptic performance of a number of materials developed in our laboratory. We will discuss the physical properties desirable in a chiral smectic A liquid crystal and their effect on the device characteristics.

Finally, for most gray scale (analog) applications of the electroclinic effect, a large contrast ratio is essential. The contrast ratio, being defined as the ratio between the bright and dark states, is most sensitive to the nonuniformities in the alignment. One of the defect textures often reported for chiral smectic A materials is the quasibookshelf stripe deformation⁴. We will present a qualitative study of the effect of electric field on this stripe texture⁵ and its impact on the contrast ratio and soft mode (dynamic) behavior.

References:

1. K. M. Johnson, D. J. McKnight and I. Underwood, IEEE Journal of Quantum Electronics, 29, 699 (1993).
2. S. Garoff and R. B. Meyer, Phys. Rev. Lett., 38, 848 (1977).
3. A. B. Davey and W. A. Crossland, Ferroelectrics, 114, 101 (1991).
4. J. Povel and M. Glogarova, Liq. Cryst. 9, 87 (1991); K. Skarp, G. Andersson, T. Hirai, A. Yoshizawa, K. Hiraoka, H. Takezoe and A. Fukuda, Jap. J. Appl. Phys., 31, 1409 (1992).
5. G. P. Crawford, R. E. Geer, J. Naciri, R. Shashidhar and B. R. Ratna, Appl. Phys. Lett., 65, 2937 (1994).

Liquid Crystal Device Performance Degradation through Selective Adsorption of Ions by Alignment Layers

Stephen H. Perlmutter, David Doroski, and Garret Model

Department of Electrical and Computer Engineering
 Optoelectronics Computing Systems Center
 University of Colorado, Campus Box 425
 Boulder, Colorado 80309-0425
 Tel: (303) 492-1889, Email: model@boulder.colorado.edu

1. Introduction

We have found selective adsorption to be responsible for the observed increase in liquid crystal ion populations as test cells are driven. Increasing ion populations correlated well with evidence of increased shielding of an applied voltage. A number of different alignment layers were compared for their tendency toward selective absorption. To investigate the interaction between ions and the alignment layers, in addition to liquid crystals a number of alkane liquids with known ionic components were used in test cells. A computer-implemented simulation of ion behavior was developed and used to verify our interpretations of our experimental results.

Both nematic liquid crystals (NLCs) and ferroelectric liquid crystals (FLCs) have shown great promise for use in a wide range of optical devices [1, 2]. However, the tendency of the performance of these devices to degrade has been a significant barrier to practical applications, particularly for FLCs [3-6]. The most important cause of device performance degradation is the build-up of electric fields from ions within the liquid crystal itself. Selective adsorption of ions of only one charge-sign by the alignment layers and the resulting formation of ion double layers have already been used to explain the development of polar surface interactions responsible for changes in the anchoring energy in nematic liquid crystal cells [7]. Polar surface interactions have also been reported to be responsible for the creation of splayed states in FLC cells [8].

2. Experiment

The experiment consisted of periodic concurrent measurements of optical and integrated current hysteresis as a function of voltage as a test cell was subjected to a dc bias. A diagram of the experimental apparatus used is shown in Fig. 1. The liquid crystal cell and optics were contained in a light-tight box to preclude the generation of ions from ambient light. The cell was placed between a crossed polarizer and analyzer and illuminated with a laser diode (670 nm). The output beam from the laser was expanded and collimated to fill the ~2.25 cm diameter test cell area. The light transmitted through the analyzer was focused down into a photodiode. This measurement scheme provided the integrated optical response over the illuminated region of the test cell and was, therefore, insensitive to spatial variations.

The laser diode was turned on only for the duration of the hysteresis measurements, typically 5-10 msec, to minimize photogeneration of ions by the laser light. For the first hour after a change in the dc bias voltage, the hysteresis measurement was made every 30 seconds. Subsequently, the hysteresis was measured every 10 minutes until the dc bias was changed again. The entire process was controlled by an IBM AT-compatible computer through a National Instruments AT-MIO-16F-5 data acquisition card. The use of computer

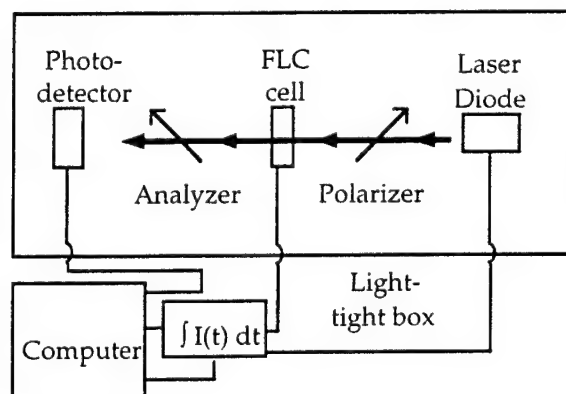


Figure 1: Experimental set up for measurement of optical and integrated current hysteresis as a function of voltage.

controlled data acquisition allowed experiments with different cells to be carried out under highly reproducible conditions.

The test cells themselves were fabricated by sandwiching the liquid crystal (or other test liquid) between two 1-inch optical flats, the inner surfaces of which were coated first with a thin layer of indium tin oxide (ITO) ($\sim 120\text{\AA}$) and then, optionally, with an alignment layer material.

3. Modeling Behavior of Ions in Liquid Crystal Cells

A description of ion dynamics in liquid crystals which takes into account thermal generation of ions from a neutral species, recombination of ions back to the neutral species, drift due to a uniform electric field, and diffusion was presented by Yang and Chieu [9] and used successfully by other researchers [6, 10] to explain results of liquid crystal ion studies. In this model, the liquid crystal mixture is treated as an electrolyte solution in which one or more neutral species can ionize due to thermal activation and recombine. We have developed and implemented on a computer a simulation of ion motion based on a finite element model which incorporates the thermal generation/recombination equations of Yang and Chieu, and additionally includes drift and diffusion of ions which are allowed to have a one dimensional variation in concentration along the thickness of the cell. We used the computer model to verify our interpretations of the following results.

4. Increasing Ion Populations in FLCs

Ion concentrations in FLCs were found to increase as the test cells were subjected to a dc bias and did not decrease even when the cells were allowed to sit for many hours with no applied driving field. Several aspects of the data collected with FLC cells consistently indicated this behavior.

A test cell with the FLC mixture SCE13 and rubbed nylon alignment layers was subjected to the pattern of dc biases shown in Fig. 2a. Fig. 2b shows the position of the center of the optical hysteresis curve as a function of time. The voltage excursions of the center of the hysteresis curve are seen to be gradually increasing. As the shift in hysteresis curve position is likely due to ionic shielding of the applied field then the increasing envelope indicates that the population of mobile ions, which are responsible for the shielding, is increasing.

Optical hysteresis curves measured at various times during periods of zero bias voltage with a 1 Hz triangle wave driving voltage show horizontal elongation of the hysteresis loop. This behavior is consistent with an increasing population of mobile ions in the liquid crystal which can drift to shield the applied field during the hysteresis measurement. The mobile ion population apparently increases even though the cell is allowed to sit with no driving voltage for periods of 6 hours.

Integrated charge hysteresis curves also indicate that there are permanently increasing ion populations. An identical cell to the one just discussed was also subjected to the pattern of dc biases shown in Fig. 2a, but with hysteresis measurements taken at 200 Hz. Fig. 3 shows the integrated current hysteresis curves halfway through several of the 0 V bias periods. The increasing area inside the curves indicates that the resistive component of the hysteresis is also increasing [11] after each dc bias even though the cell was biased at 0 V for periods of 6 hours during the experiment. These observations consistently

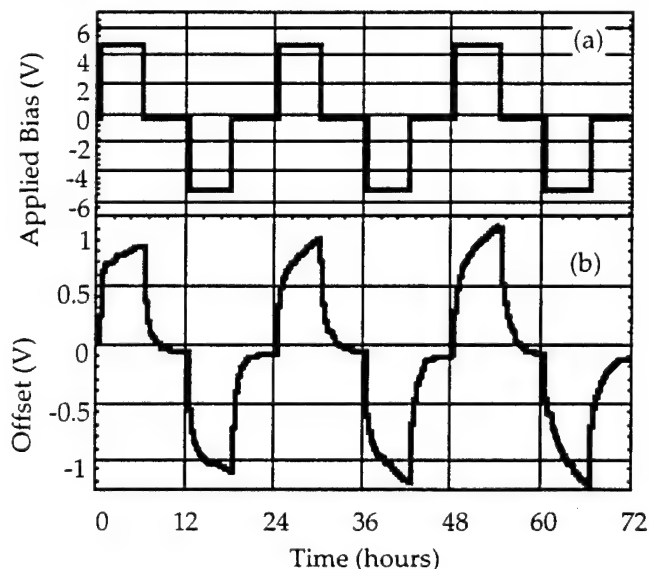


Figure 2: (a) Pattern of dc biasing across a test cell incorporating rubbed nylon alignment layers and filled with the FLC SCE13. (b) Central voltage of the optical hysteresis curve when the dc bias voltage shown in (a) is applied.

suggest that the mobile ion population increases as a result of dc bias on the cell. The increase in population results from the inability of the mobile non-adsorbed ions to recombine with the adsorbed ions. If the adsorption energy of both positive and negative ions were equal then the two ions would be treated symmetrically, and upon removal of the dc bias both ions would either remain trapped at the alignment layers or become free and recombine in the bulk of the cell. In either case, the population of mobile ions would not increase. Selective adsorption is required to explain the observed ion population increases.

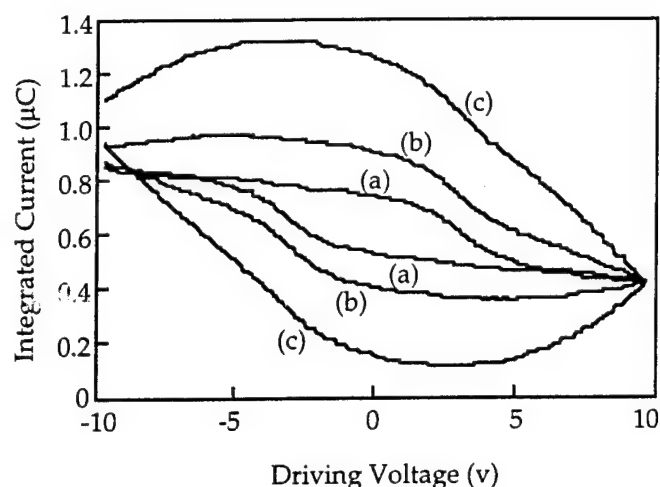


Figure 3: Integrated current hysteresis curves of a test cell incorporating rubbed nylon alignment layers and filled with the FLC ZLI3654. The curves were measured during the same experiment during which the data of Fig. 2 was measured. The curves of this figure were measured at (a) 1 hours, (b) 33 hours, (c) 69 hours.

5. Non-Liquid Crystal Cells

A better quantitative measurement of ion populations is facilitated by the elimination of the contributions to the integrated current hysteresis from the rotations of molecules having either dielectric anisotropy or spontaneous polarization. To this end, cells filled with three alkane liquids were studied: decane, 1-chlorodecane, 1-nonanoic acid. Decane has negligible intrinsic ion concentrations at room temperature, and so was useful in determining the contribution to the mobile ion population made by the alignment layers. The other two alkanes were chosen because each contained an ionic species that was likely to be found in liquid crystal mixtures. Also the differences in charge-sign and size between the reactive ions in the two alkanes (ionic chlorine in chlorodecane and ionic hydrogen in nonanoic acid) allowed the selective adsorption properties of ions with widely differing adsorption energies to be studied in cells incorporating a variety of different alignment layer materials.

Decane Decane cells were made with a number of alignment layer materials: rubbed nylon 6/6 ($\sim 300\text{\AA}$), silane ($\sim 10\text{\AA}$), and obliquely evaporated SiO ($\sim 80\text{\AA}$). In addition, cells were made with no alignment layers at all. All cells had effective resistances on the order of gigaohms, indicating that very low ion concentrations in the cells were present. The resistivity did not decrease when the cell was subjected for extended periods (hours) to a dc voltage. This result indicates that the alignment layers themselves are not responsible for contributing significantly to the ion population of the cell.

1-Chlorodecane Cells made with chlorodecane had significantly lower resistivities than the decane cells due to the presence of thermally generated chlorine ions. However, the resistivities of the cells decreased as the cells were subjected to dc voltage. The increase in ion concentrations responsible for the lower resistivity can be explained by a selective adsorption process which requires activation by an electric field. Of the alignment layers tested rubbed nylon showed the highest concentrations of mobile ions while non-rubbed nylon showed concentrations comparable to cells with no alignment layer at all. The process of buffing nylon alignment layers seems to increase the concentration of adsorption sites.

1-Nonanoic Acid Cells made with nonanoic acid showed behavior similar to that observed in the chlorodecane cells with the exception that a dc voltage did not cause as large a change in ion concentrations. This result indicates that either selective adsorption of ionic hydrogen does not occur or the selective adsorption sites are more rapidly saturated by ionic hydrogen than by ionic chlorine. Defining performance degradation as changes in liquid crystal operating characteristics, we can

conclude that ionic chlorine makes a greater contribution to gradual performance degradation than ionic hydrogen.

6. Conclusions

A dc component to a voltage which drives a liquid crystal can cause permanent damage by permanently increasing the population of mobile ions. This comes about through activation of selective adsorption sites on the alignment layers. Testing with alkane liquids indicated that the alignment layers themselves contributed negligibly to the mobile ion population. A consequence of selective adsorption is that liquid crystals with higher concentrations of intrinsic ionizable species will show greater degradation.

A dc component to a driving voltage signal can also cause asymmetrical trapping of ions in the alignment layers. Asymmetrical trapping has been shown through computer simulation to cause an offset to the field amplitude at the center of the cell. This offset, in turn, is responsible for an apparent voltage shift in the FLC's optical hysteresis curve, or more specifically, in the FLC's switching voltages after minutes to hours of operation under a dc voltage drive component.

Rubbed polymers are a common alignment layer material. Before rubbing, nylon alignment layers exhibited relatively low selective adsorption. However, after rubbing, the nylon alignment layers exhibited the highest levels of selective adsorption observed in this study. This may result from breaking polymer chains leaving highly reactive ends and/or from embedding static charges into the nylon from the material used to rub the nylon.

The best way to avoid performance degradation due to ions would be to find non-adsorptive alignment layers. In a cell with such alignment layers, ionic effects could be eliminated by periodically grounding the cell for a brief period (< 1 sec) to allow ion populations to uniformly distribute and excess populations (above thermal equilibrium) to recombine. Alternatively, alignment layers in which positive and negative ions have equal adsorption energies would at least not contribute to a net increase in mobile ion population. Given the likely significant size and chemical differences between the two ions, this alternative is probably the more difficult to achieve.

References

1. N.A. Clark and S.T. Lagerwall, "Introduction of ferroelectric liquid crystals," Chap. 1, in *Ferroelectric Liquid Crystals*, J.W. Goodby et al. Eds., (Gordon and Breach Science Publishers, Philadelphia, 1991) pp. 1-97.
2. G. Model, "Ferroelectric liquid crystal spatial light modulators," Chap. 6, in *Spatial Light Modulator Technology: Materials, Devices, and Applications*, U. Efron Ed., (Marcel Dekker, New York, 1994) pp. 287-359.
3. S.T. Lagerwall, J. Wahl, and N.A. Clark, "Ferroelectric liquid crystals for displays," Conference record of the 1985 International Display Research Conference, p.213-221 (1985).
4. S.H. Perlmutter, D. Doroski, P.R. Barbier, S. Wichart, and G. Model, "The influence of ion migration in ferroelectric liquid crystal on the performance of optically addressed spatial light modulators," OSA Annual Meeting, Vol. 23, *OSA Annual Meeting Technical Digest Series* (Optical Society of America, Washington, DC) p.82 (1992).
5. D. Doroski, S.H. Perlmutter, and G. Model, "Alignment layers for improved surface-stabilized ferroelectric liquid crystal devices," *Appl. Opt.* **33**, 2608-2610 (1994).
6. B. Maximus, E.D. Ley, A.D. Meyere, and H. Pauwels, "Ion transport in SSFLCD's," *Ferroelectrics* **121**, 103-112 (1991).
7. G. Barbero and G. Durand, "Ion adsorption and equilibrium distribution of charges in a cell of finite thickness," *J. Phys. France* **51**, 281-291 (1990).
8. M.A. Handschy and N.A. Clark, "Structures and responses of ferroelectric liquid crystals in the surface-stabilized geometry," *Ferroelectrics* **59**, 69-116 (1984).
9. T.C. Chieu and K.H. Yang, "Transport properties of ions in ferroelectric liquid crystal cells," *Jpn. J. Appl. Phys.* **28**, 2240-2246 (1989).
10. Z. Zou, N.A. Clark, and M.A. Handschy, "Ionic transport effects in SSFLC cells," *Ferroelectrics* **121**, 147-158 (1991).
11. S.H. Perlmutter, D. Doroski, and G. Model, "Analysis of ions in ferroelectric liquid crystals from hysteresis curves," *Ferroelectrics* **149**, 319-331 (1993).

Responses of a Spatial Light Modulator to Pulsed Electron Irradiations

E. W. Taylor, A. D. Sanchez, S. P. Chapman S. A. De Walt,
D. M. Craig, M. A. Kelly, M. F. Mitcham

AFMC Phillips Laboratory
PL/VTET Photonics Research Group
3550 Aberdeen Ave SE
Kirtland AFB, NM 87117-5776
(505) 846 - 4741, (505) 846 - 2561 (FAX)

The application of photonic technologies in space and enhanced environments has progressed steadily. The first survivable fiber optic point to point links were demonstrated in 1984¹, paving the way for other proposed experiments including acousto-optic devices². Radiation hardness studies of integrated³ and coupled wave optic⁴ devices have been performed. Photonic hardness standards are progressing from the studies of international round robin teams^{5,6}. However, limited data exists on the radiation responses of organic spatial light modulators⁷ (SLMs) or acousto-optic modulators in radiation environments. This paper partially addresses this issue by examining the radiation response of a SLM.

A ferroelectric liquid crystal light valve (FLCLV) consisting of a smectic C - liquid crystal film encased by cover plates of 7059 glass coated with Indium-Tin-Oxide (ITO) and a buffed polymer alignment layer is shown in Fig. 1.

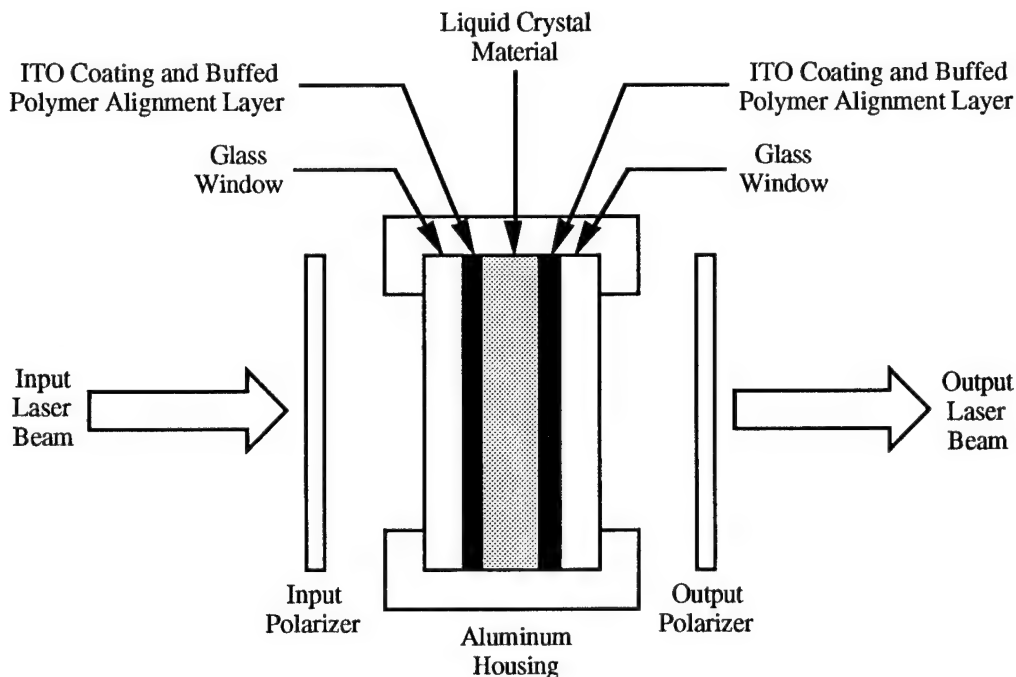


Figure 1. Liquid Crystal Light Valve Cross Section Components

The FLCLV was modulated at a frequency of 1 kHz while illuminated by a 1 mW optical beam of wavelength, $\lambda = 0.6328 \mu\text{m}$. As shown in Fig. 2, linearly accelerated electrons were directed at an angle of 45 degrees to the device, passing through the coated windows and liquid crystal film. The transient and steady state responses of the FLCLV before, during and after the irradiation were detected and recorded. The 15 MeV electron beam was applied at a duty cycle of 30 Hz, and consisted of individual ($1.0 \mu\text{s}$ FWHM) pulses, providing an average dose (D_e) of $D_e = 1.36 \text{ krad (Si)/pulse}$. All measurements were performed at a temperature of $21.4 \pm 2.0^\circ \text{C}$. Crossed polarizers, normally an integral part of the FLCLV, were separated and distanced from the FLC to prevent their exposure to the electron beam. The electron beam diameter was approximately 3 cm, and was directed at the 1 cm diameter input glass window of the FLC active area. The output from the laser beam was expanded and collimated to uniformly illuminate the input window of the FLCLV.

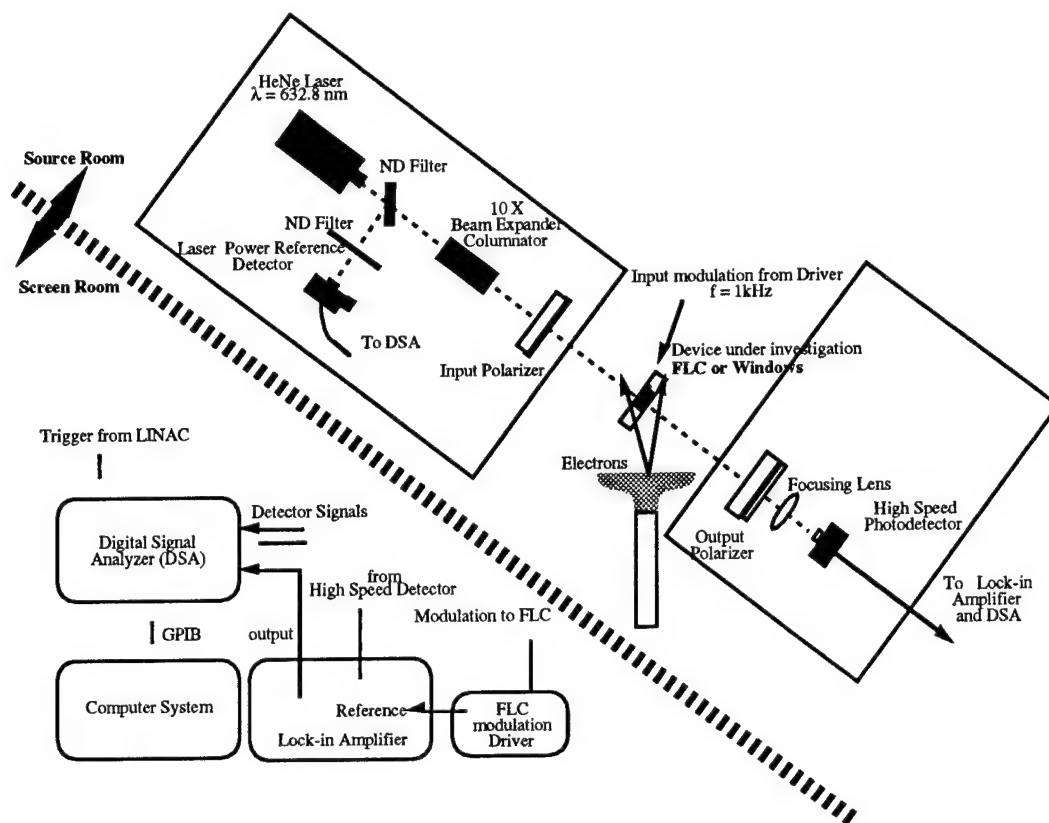


Figure 2. FLCLV Electron Exposure Arrangement

Shown in Fig 3 is the transient response of the FLCLV to the highest electron irradiation dose of $D_e = 401 \text{ krad(Si)}$.

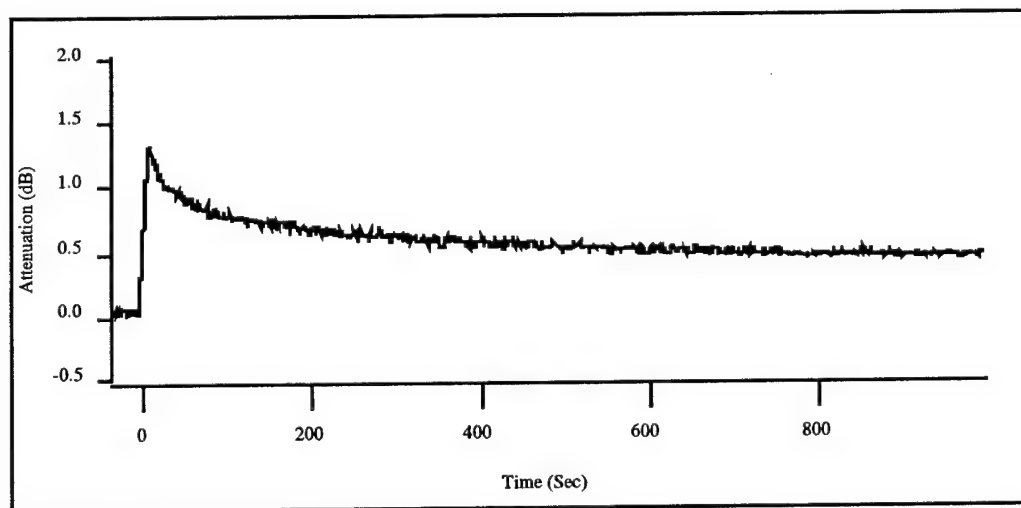


Figure 3. Peak Transient Attenuation and Recovery

The transmission of the optical signal was observed to attenuate rapidly, reaching a peak attenuation (α_p) value of $\alpha_p = 1.31$ dB. As may be observed, an exponential recovery from the peak attenuation persists to beyond 800 s. A series of these exposures was conducted over the range $66.0 \text{ krad(Si)} < D_e < 401 \text{ krad(Si)}$ and the measured peak induced attenuation is plotted as a function of the exposure dose as shown in Fig. 4. It was consistently observed that recovery of the optical signal was incomplete prior to the next radiation exposure. The time between exposures varied from 5 minutes to 20 minutes. Thus the residual attenuation (α_r) curve shown in Fig 4 is a measure of the long term attenuation present following a particular exposure. This residual attenuation is believed permanent since immediate examination of the FLCLV following the irradiation and some seven months later showed a distinctive darkening of the window regions indicating the presence of radiation induced color center damage.

A second set of exposures was conducted wherein the window components of the FLCLV were separately exposed to the pulsed electron beam, in order to differentiate the radiation induced responses of the liquid crystal film from the coated ITO windows, and the response of the ITO from uncoated glass windows. Both uncoated glass windows, and ITO coated glass windows were exposed invoking the same geometry and comparable radiation exposure conditions used during the FLCLV irradiation. However, in this instance, crossed polarizers were not used in the optical arrangement, since it was determined that no polarization-dependent responses were observed during the FLCLV exposures.

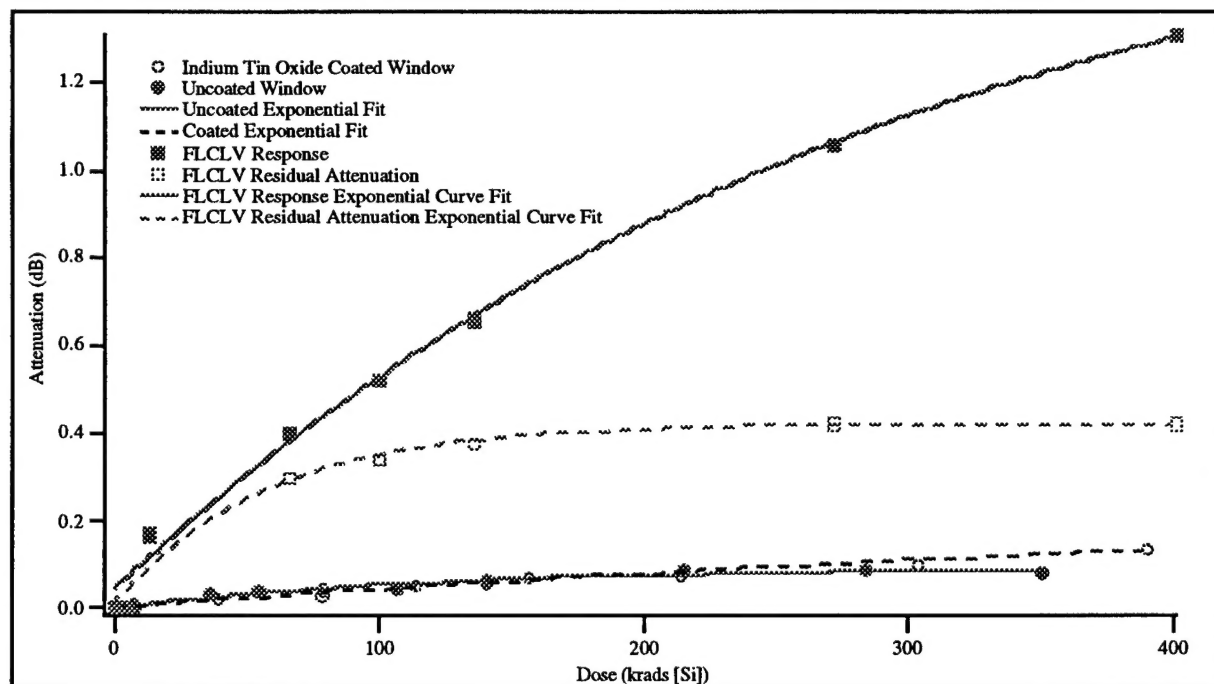


Figure 4. FLCLV and Window Responses to Electron Radiation

Shown in Fig. 4 are the data acquired for the FLCLV, an ITO coated glass window and the uncoated glass window responses to electron exposures. As an example, from the curve fit in Fig 4, a predicted FLCLV peak induced attenuation of $\alpha_p = 1.13$ dB occurs at $D_e = 300 \text{ krad(Si)}$, and corresponds to a predicted permanent (residual) attenuation of $\alpha_p = 0.417$ dB for the same dose. This residual attenuation appears to saturate at a dose of $D_e = 275 \text{ krad(Si)}$. For $D_e = 300 \text{ krad}$

(Si), each uncoated window and each ITO coated window would be expected to experience peak attenuations of 0.087 dB and 0.098 dB, respectively. Since the FLCLV is comprised of two coated windows, the peak induced attenuation (α_{pa}) attributed to the liquid crystal film and alignment layers may be calculated at $D_e = 300$ krad (Si), as:

$$\alpha_{pa} \text{ (LC film + alignment layers)} = \alpha_p \text{ (FLC)} - 2 \alpha_p \text{ (ITO Window)} \quad (1)$$

or $\alpha_{pa} = 0.934$ dB. The differences noted in the attenuation responses between the ITO coated and uncoated windows while small, show a saturation trend for the uncoated window at exposure levels for $D_e > 214$ krad (Si). A consideration that renders Eq. 1 to be a conservative estimate is the exposure geometry of the FLCLV. As a result of the electron beam incident on the FLCLV at an angle of 45 degrees, the FLCLV aluminum housing shielded a portion of the window, liquid crystal and buffed polymer alignment areas. These shielded regions decreased the measured attenuation by approximately 10 - 15%. Similar studies to measure the effects of gamma ray irradiation on the FLCLV and its components are underway. This research was sponsored by the AFMC Phillips Laboratory's In-House Independent Research, under ILIR 9217.

References

- [1] E. W. Taylor, "Performance of the First Operable Fiber Optic Systems in Prolonged Space Orbit," plenary paper presented at SPIE OE/Aerospace Sensing, Orlando FL, April 1992, *Proc. SPIE OE/Aerospace Sensing*, Vol. 1691.
- [2] D. J. Page, E. W. Taylor, K. T. Stalker, "Candidate Experiments for the Microelectronics and Photonics Test-Bed Satellite," presented at the SPIE Aerospace and Remote Sensing Conference - Photonics for Space Environments, 12-16 Apr 93, Orlando, FL, *Proc SPIE*, Vol. 1953, pp. 23-26
- [3] E. W. Taylor, "Ionization - Induced Refractive Index and Polarization Effects in LiNbO₃:Ti Directional Coupler Waveguides," *IEEE/OSA Journal of Lightwave Technology*, Vol. 9, No. 3, pp. 335-340 (March 1991)
- [4] E. W. Taylor, V. R. Wilson, et al., "Ionization Induced Nonequivalent Absorption in a Birefringent Silica Fiber," *IEEE Photonics Technology Letters*, Vol. 1, No. 8, pp. 248-249 (August 1989)
- [5] E. J. Friebele, E. W. Taylor, G. Turquet de Beauregard, J. Wall, and C. E. Barnes, "Interlaboratory Comparison of Radiation Induced Attenuation in Optical Fibers, I. Steady State Exposures," *IEEE/OSA, Jour of Lightwave Technology*, Vol. 6, No. 2, pp. 165-171 (February 1988)
- [6] E. W. Taylor, E. J. Friebele, H. Henschel, et al., "Interlaboratory Comparison of Radiation - Induced Attenuation in Optical Fibers. Part II: Steady State Exposures," *IEEE/OSA Journal of Lightwave Technology*, Vol. 8, No. 6, pp. 967-976 (June 1990)
- [7] E. W. Taylor, A. D. Sanchez, S. A. DeWalt, et al., "Radiation Induced Effects in Acousto Optic Devices", Presented at SPIE Integrated Optics Conference, *Proc SPIE* Vol. 1794, Sep 1992.

Agedal, Harald — LTuB1, LTuB2
 Agranat, Aharon J. — LThB1
 Anderson, Dana Z. — OWC2
 Arbet-Engels, V. — LThA5
 Athale, Ravindra A. — LWA2

Barbier, Pierre R. — LTuC4
 Bartoli, F. J. — LThC4
 Beth, Thomas — LTuB1, LTuB2
 Bowman, S. R. — LTuC6, LThB2
 Burdge, Geoff — LThA2
 Burns, D. C. — LTuC1

Caulfield, H. John — LTuC7
 Centanni, J. — LTuA3
 Chang, Wei — LTuA2, LThA5
 Chapman, S. P. — LThD4
 Chipman, Russell A. — LThB3
 Chirovsky, Leo M. F. — LTuA1
 Craig, D. M. — LThD4
 Crawford, G. P. — LThC4
 Crossland, William A. — LTuB3, LThD
 Cunningham, J. E. — LTuA3

De Walt, S. A. — LThD4
 Döhler, G. H. — LThA1
 Donley, Elizabeth — OWC2
 Doroski, David — LThD3
 Downie, John D. — LThB5

Efron, Uzi — LTuA, LTuA2, LThA5
 Esener, Sadik — LTuA2, LTuA4, LThA5, LThB
 Estes, Michael — LTuC9

Fan, Chi — LTuA2
 Flom, S. R. — LThC4
 Fukushima, Seiji — LThC2

Goossen, K. W. — LTuA3
 Gourlay, J. — LTuC1
 Gulden, K. H. — LThA1

Hahn, Tami — LThA3
 Hansen, Mark — LTuA2, LThA5
 Harvey, Phil — LTuA4
 Hibbs-Brenner, Mary — LThA
 Holder, Dave — LThA3
 Holmes, R. B. — LThA4
 Hossack, W. J. — LTuC1
 Huang, X. R. — LTuA5
 Huignard, Jean-Pierre — LTuB
 Hunt, J. H. — LThA4

Jan, W. Y. — LTuA3
 Johnson, Kristina M. — LThC, LThC1

Katzer, D. S. — LTuC6, LThB2
 Kelly, M. A. — LThD4
 Kiesel, P. — LThA1
 Kneissl, M. — LThA1
 Kompanets, Igor N. — LThD1
 Kurokawa, Takashi — LThC2
 Kyono, C. S. — LTuC6, LThB2

Lee, John N. — LWA
 Linder, N. — LThA1

Lindle, J. R. — LThC4
 Lohmann, Adolf W. — OWC1

Mansoorian, B. — LThB3
 McCallum, D. S. — LTuA5
 McKnight, Douglas J. — LThC1
 Mears, R. J. — LTuB3
 Miller, David A. B. — LWA1
 Mitcham, M. F. — LThD4
 Modell, Garret — LTuC3, LTuC5, LTuC8, LTuC9, LThA2, LThA3,
 LThD3
 Montemezzani, Germano — OWC2

Neto, Luiz Goncalves — LTuC2

O'Brien, Dominic C. — LTuC3, LTuC8

Parfenov, Alexander V. — LThC3
 Parker, M. C. — LTuB3
 Perlmutter, Stephen H. — LThD3
 Pezzaniti, J. Larry — LThB3

Rabinovich, W. S. — LTuC6, LThB2
 Ranganathan, R. — LThA5
 Ratna, B. — LThC4, LThD2
 Reichel, Frank — LTuB1, LTuB2, LTuB4
 Riel, P. — LThA1
 Roberge, Danny — LTuC2

Samus, S. — LTuC1
 Sanchez, A. D. — LThD4
 Schamschula, Marius P. — LTuC7
 Schmid, Michael — LTuB2
 Schuck, Miller H. — LThC1
 Schwarzer, Heiko — LTuB1, LTuB2
 Searcy, Paul — LThA3
 Sharpe, John P. — LTuC8
 Shashidhar, R. — LThC4
 Sheng, Yunlong — LTuC2
 Shih, David — LTuA2
 Shimizu, Norio — LThB4
 Smirl, Arthur L. — LTuA5
 Smith, J. S. — LThA1
 Sornsin, Elizabeth A. — LThB3
 Stevens, A. J. — LTuC1
 Sun, D. — LTuA5

Takei, Hiroyuki — LThB4
 Taylor, E. W. — LThD4
 Teiwes, Stephan — LTuB1, LTuB2
 Towe, E. — LTuA5

Vass, D. G. — LTuC1

Waldman, Gary — LThA3
 Wang, Li — LTuC5, LThA2, LThA3
 Warr, S. T. — LTuB3
 Wootton, John — LThA3
 Wu, X. — LThA1
 Wyrowski, Frank — LTuB2

Yablonovitch, Eli — LTuA2, LThA5

Zhang, Leo — LTuC7

**SPATIAL LIGHT MODULATORS AND APPLICATIONS
TECHNICAL PROGRAM COMMITTEE**

Garret Moddel, *General Chair*
University of Colorado, Boulder

Geoff Burdge, *Program Chair*
Laboratory for Physical Sciences

Allan Craig
U.S. Air Force Office of Scientific Research

William Crossland
Cambridge University, U.K.

Uzi Efron
Hughes Research Laboratory

Sadik C. Esener
University of California, San Diego

Mary K. Hibbs-Brenner
Honeywell, Inc.

Jean Pierre Huignard
Thomson CSF, France

Takashi Kurokawa
NTT, Japan

John N. Lee
U.S. Naval Research Laboratory

Anthony L. Lentine
AT&T Bell Laboratories

Alexander Parfenov
Lebedev Physical Institute, Academy of Sciences, Russia

Cardinal Warde
Massachusetts Institute of Technology